THE APPLICATION OF X-RAY DIFFRACTION LINE PROFILE ANALYSIS TO THE STUDY OF ANTI-PHASE DOMAINS IN LITHIUM FERRITE

A THESIS SUBMITTED FOR THE DEGREE OF
PHILOSOPHIAE DOCTOR
IN THE UNIVERSITY OF ASTON IN BIRMINGHAM

ROBERT WINSTON CHEARY, B.Sc.

Physics Department

December, 1971

ABSTRACT

X-ray diffraction patterns of lithium ferrite $LiFe_5O_8$ quenched from just below the temperature of its order-disorder transition were found to exhibit sharp lattice lines (h,k,l of similar parity) and superlattice lines (h,k,l, of mixed parity) whose breadths normally exceeded those of the lattice lines. Similar diffraction patterns were also obtained from specimens of lithium ferrite into which partial disorder was introduced by the substitution of a small fraction of Cr^{3+} ions for Fe^{3+} ions (i.e. $LiFe_{5-\frac{x}{4}}Cr_{\frac{x}{4}}O_8$, $x \leqslant 2$). The behaviour of these diffraction patterns is explained by assuming that the crystallites contain many small ordered regions which are generally referred to as anti-phase domains. In the present work a more precise picture of the anti-phase domains in these materials is developed through quantitative analysis of the X-ray line profiles.

Line positions are determined by the centroid method whilst line breadths are determined with the aid of Fourier, variance and two new methods of analysis. One of the new methods, namely that based on the variation of the function (truncated integrated intensity X range) versus range, is shown to have similar merits and limitations to variance for the analysis of broadened lines as well as being an accurate method for evaluating integrated intensities. The second new method, referred to as pseudo-variance, is a modification of variance in which the range dependence of the latter is corrected for the hyperbolic term. Prior to interpretation of the line profile parameters, consideration is given to the propagation of systematic errors. The influence of the $K\alpha$ satellite group on the parameters is eliminated by exploiting its intensity distribution with the aid of the centroid-range function. Justification for the background intensity levels obtained from variance analysis is given and the effects of non-linear range dependent terms on the measured variance slopes and intercepts are discussed. In the Fourier transform analysis, errors, particularly those resulting from profile truncation, are reduced by correction procedures. It is shown that good agreement is obtained between values for the Wilson parameter $J'(0)/J(0)$ determined from Fourier analysis and pseudo-variance. The conclusion is reached that the most reliable interpretation of the diffraction broadening is achieved with the parameters measured from the latter two methods of analysis.

Measurements of long range order parameters and lattice parameters indicate that the specimens prepared are slightly non-stoichiometric. Except for one special case, this did not appear to affect the breadths of the lattice lines which are accounted for by the emission profile, the instrumental aberrations and a small diffraction broadening contribution which seems to be independent of the stoichiometry and state of order of the specimens. Because of inconsistencies in the crystal structure of lithium ferrite proposed by Braun (1952), a redetermination is carried out with account being taken of non-stoichiometry. The new proposed structure is shown to be consistent with intensity results obtained from three specimens and previous published cation-anion distances.

The mean domain thicknesses obtained from the superlattice lines of the quenched and Cr^{3+} ion substituted lithium ferrite specimens are best accounted for by anti-phase domain boundaries on the $\{110\}$ planes. Evidence is presented to demonstrate that these are low energy boundaries. For some specimens, values of the domain thickness distribution $f(t)$ at $t = 0$, as estimated from pseudo-variance, are shown to be in very good agreement with those values predicted from the anti-phase domain model developed by Wilson in 1943. For other specimens an approximate agreement is found. The time and temperature dependence of domain growth in unsubstituted specimens of lithium ferrite indicate a rate process similar to grain growth in metals and a growth mechanism which is probably diffusion controlled. Agreement is obtained between measured and calculated values for the activation energy of the growth process. Anti-phase domains in the Cr^{3+} ion substituted specimens of lithium ferrite appear to exist in a state of thermal equilibrium. This condition is explained by assuming that all the Cr^{3+} ions lie on the domain boundaries and that domain growth is prevented by the immobility of these ions which arises from their crystal field stabilization energy.

Finally, a theory is developed which enables the complete domain thickness distribution to be evaluated from Fourier transform results. A practical evaluation of the distribution in some of the specimens is carried out. These and other results suggest that the domain thickness distribution approximates to a Gaussian curve during the earlier stages of domain growth and to a Cauchy curve during the later stages.

INDEX

Chapter 3 Experimental methods and analysis of data

CHAPTER 1.

PHASE TRANSITION BEHAVIOUR AND THE PROBLEM POSED BY LITHIUM FERRITE

1.1. Introduction

Phase transitions, especially the transformations of ice into water and boiling water into steam, must be among the first natural phenomena observed by man. The Aristotelian dogma concerning the constitution of matter rests it has been said, upon the observation that burning wood produced the basic elements of earth, air, fire and water. Indeed, the explanation of the "states of matter" was an important objective of the early atomists.

Much later, after the resurrection of the atomic hypothesis by Dalton, the subject continued to be of interest. The results from the classical experiments of Andrews (1869) on the transition from gaseous to liquid state in carbon dioxide are particularly significant, not only because they stimulated the search for equations of state such as that of van der Waal's (1873) and led ultimately to the development of low temperature physics, but also because of the discovery of the importance of critical phenomena in other branches of physics (see Domb, 1971).

When solids came to be investigated it was gradually realised that numerous other kinds of physical behaviour could be classified as a phase transition. For example, the change from paramagnetic to ferromagnetic behaviour, the ferroelectric transition, the metal to insulator and crystal structure transformations have all come to be recognised as specific examples of a more general phenomenon. At the same time, through the work of the theoreticians Ehrenfest (1933) and Landau (1937b) it was recognised that important differences could be distinguished between certain cases on the basis of the Gibbs free energy. In particular, phase changes in which the first order derivatives of the latter change discontinuously, are found to exhibit discontinuities in entropy and volume and are accompanied by a latent heat. Most of the familiar phase transitions such as melting and vapourisation are of this type. In other cases however, the first order derivatives of the Gibbs function change continuously as the substance passes from one phase to the other and it is the second order derivatives which exhibit the discontinuities. The paramagnetic to ferromagnetic and liquid helium II to liquid helium I behavioural changes are examples of second order phase transitions. Yet more complicated types of phase transition behaviour have been recognised (see for example, Pippard (1964) for a careful review), but these will be neglected here.

1.2 Order - disorder behaviour in homogeneous alloys

Among the most interesting of transitions exhibited by crystalline solids are those in which the structure undergoes a change, with increasing temperature, from an ordered to a disordered arrangement in which some or all of the atoms of the substance become randomly distributed over the original set of atomic locations. Two examples of this kind of transformation taken from among the metal alloys are illustrated in Fig.1.1.

In β - brass (Fig.1.1a) the ordered structure has a primitive cubic lattice with the copper atoms at (0, 0, 0,) and the zinc atoms at ($\frac{1}{2}$, $\frac{1}{2}$, $\frac{1}{2}$) whilst the disordered structure has body centred cubic lattice, each of the ordered locations being allocated equally to the copper and zinc atoms.

In ordered Cu_3Au (Fig.1.1b), which again is primitive cubic,

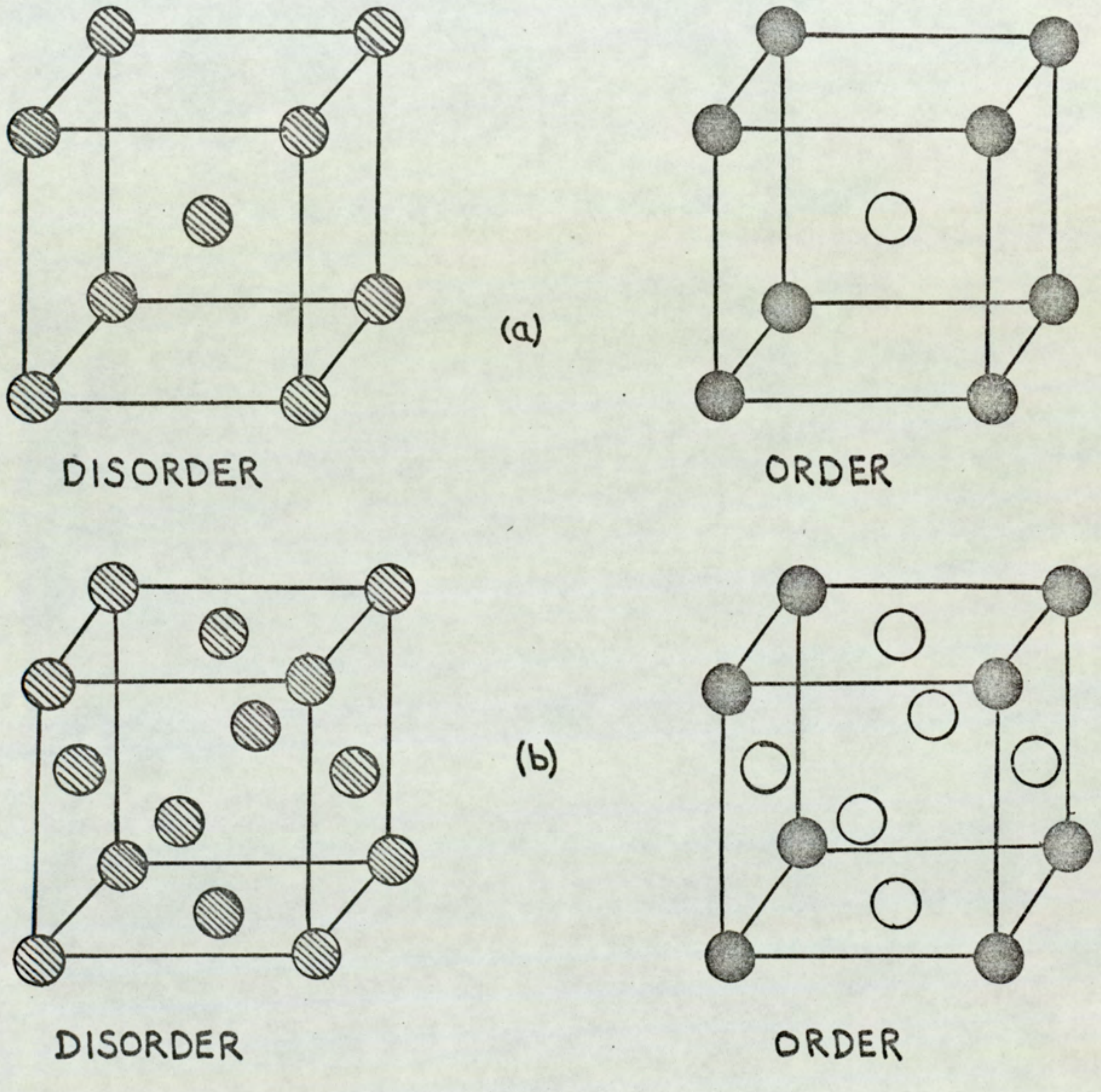

Fig.1.1 Ordered and disordered structures of two alloys

(a) β - brass, CuZn, ● Cu, ○ Zn, ▨ $\frac{1}{2}$Cu$\frac{1}{2}$Zn;

(b) Cu$_3$Au, ● Au, ○ Cu, ▨ $\frac{1}{4}$Au$\frac{3}{4}$Cu gold atoms occupy the cube corners and copper atoms the face centres of the unit cells, whilst in the completely disordered state each ordered location is occupied on average by $\frac{1}{4}$ of a gold atom and $\frac{3}{4}$ of a copper atom so that the lattice is statistically face centred cubic.

Order-disorder transitions such as the examples described have been much studied by X-ray diffraction. Fig.1.2 shows the manner in which the diffraction pattern from a polycrystalline sample can reveal structural changes of the kind which occur in Cu_3 Au alloy. As the temperature is lowered the diffraction lines of the disordered phase, termed lattice lines (h,k,l of similar parity), are augmented below a certain critical temperature by a number of additional lines commonly called the superlattice lines. The Miller indices of the latter do not correspond to the characteristics of the face centred lattice, for these lines arise through a reduction of the symmetry of the crystal structure.

The transition, under equilibrium conditions, from disordered to ordered state is rarely if ever completed at the critical temperature. The initial situation is one of partial order which becomes more completely ordered as the temperature is decreased below the critical temperature. Various parameters have been proposed to describe the intermediate condition of which the long range order parameter introduced by Bragg and Williams (1934) is the most practically convenient. If the fully ordered state is characterised by a fraction X_A lattice sites of type α occupied by A atoms and a fraction X_B lattice sites ($X_B = 1 - X_A$) of type β occupied by B atoms then the long range order parameter S is defined as

$$S = \frac{P - X_A}{1 - X_A}$$

where P represents the fraction of α sites occupied by A atoms

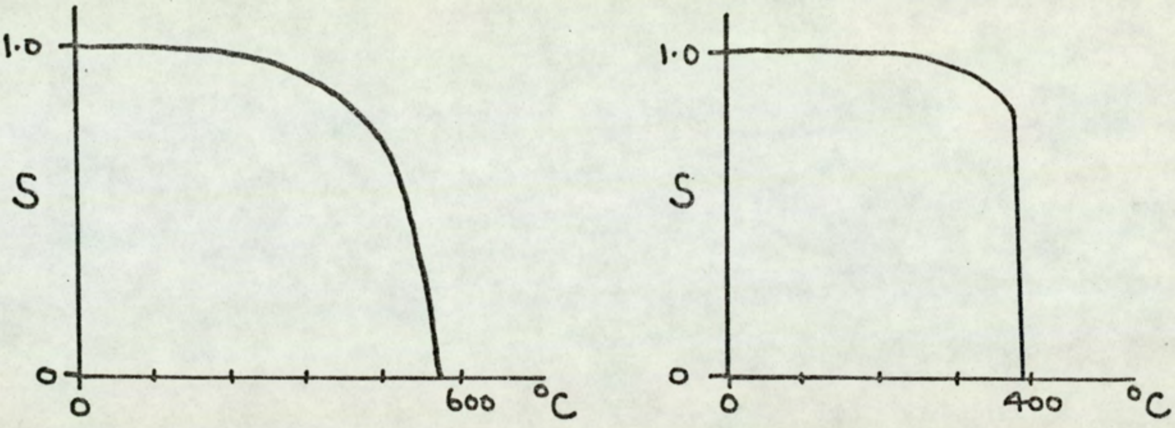

(a) β-brass (b) Cu_3Au

<u>Fig.1.3</u> Temperature dependence of long range order parameters in β- brass (after Chipman and Warren, 1950) and Cu_3Au alloy (after Keating and Warren, 1951).

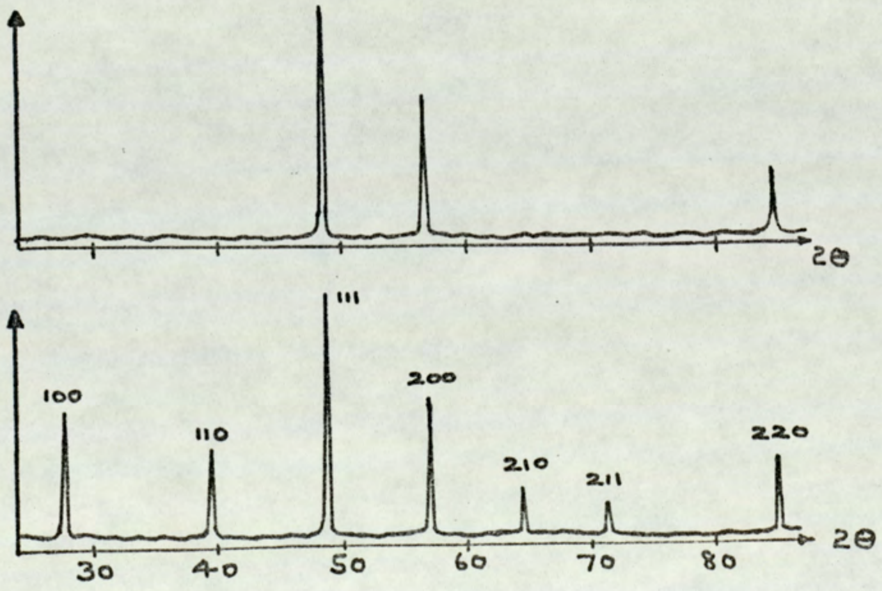

<u>Fig.1.2</u> Diffractometer tracings of powdered Cu_3Au using CuKα radiation (after Warren, 1969). Upper pattern obtained by quenching at 600°C. Lower pattern: ordered form obtained by annealing for 20 days at 365°C and 40 days at 280°C.

in the partially ordered state. Thus, S will be unity for complete order and zero for the disordered state. Unlike the alternative parameters of order (see Bethe (1935) and Cowley (1950)), the long range order parameter S may be estimated with comparative ease as the integrated intensities of superlattice lines from AB or A_3B alloys are given by

$$I = KS^2(f_A - f_B)^2$$

where f_A and f_B are the atomic scattering factors corresponding to the atomic species A and B, and K is a constant which may be determined with the aid of the integrated intensities of the lattice lines (see for instance Warren, 1969).

Typical of the variations of the long range order parameter in alloys as a function of temperature are those determined for β - brass (Chipman and Warren, 1950) and Cu_3Au alloy (Keating and Warren, 1951) illustrated in Fig.1.3. For β - brass (Fig.1.3a) the long range order parameter decreases uniformly to zero as a function of temperature. For Cu_3Au alloy (Fig.1.3b), the rate of decrease of S is rather slow up until a few degrees before the transition temperature whereupon S falls abruptly to zero. The uniformity of the variation in β - brass and the abruptness of the variation in Cu_3Au alloy is attributed to the former transition being a second order phase transition and the latter a first order phase transition (Krivoglaz and Smirnov, 1964). These conclusions are supported by the observations that at their transition temperatures the lattice parameters of Cu_3Au (Betteridge, 1949) and β - brass (Keating and Warren, 1951) are discontinuous and continuous respectively, and that Cu_3Au appears to exhibit a latent heat effect (Jones and Sykes, 1936) whilst β - brass exhibits a sharp change in specific heat, but no latent heat (Sykes and Wilkinson, 1937).

The first successful microscopic theory to explain these phenomena was developed by Bragg and Williams (1934) in terms of the long range order parameter. In this work, it was assumed that,

(a) the total configurational energy W of a partially ordered alloy could be expressed as the sum of all the nearest neighbour interactions,

i.e. $$W = -(N_{AA}V_{AA} + N_{BB}V_{BB} + N_{BA}V_{BA})$$

where $-V_{AA}$, $-V_{BB}$ and $-V_{BA}$ are the potential energies of the bonds and N_{AA}, N_{BB} and N_{BA} are the number of each type of nearest neighbour.

(b) the alloy system could be represented by a single energy level namely the average energy $\overline{W}$ so that the partition function Z could be reduced to a single term,

i.e. $$Z = g(\overline{W})e^{-\overline{W}/kT}$$

where $g(\overline{W})$ is the thermodynamic probability of the system.

Under these conditions it was a simple matter to express $\overline{W}$ as a function of S,

i.e. $\overline{W} = W_o - 2NVS^2$ for an AB alloy

and $\overline{W} = W_o - \frac{9NVS^2}{2}$ for an A_3B alloy where N is the total number of atoms, W_o is the configurational energy at the transition temperature and V is the ordering energy defined as

$V = V_{AB} - (V_{AA} + V_{BB}) / 2$ which must be positive for ordering to occur. As the partition function determines the thermodynamic state of a system Bragg and Williams were able to generate expressions for the thermodynamic properties of AB and A_3B alloys.

From these expressions it was predicted that for AB alloys the change in long range order parameter should be continuous with temperature and that the specific heat should exhibit a sharp variation in the vicinity of the transition temperature, but no latent heat effect. For A_3B alloys there should be a discontinuous change in the long range order parameter at the transition temperature together with a latent heat effect. Qualitatively, these results are in agreement with the experimental results described earlier. Quantitatively, however, this description is far from complete as the comparison between the theoretical and experimental temperature dependence of the long range order parameter given in Fig.1.4 for Cu_3Au demonstrates.

Developments since the Bragg-Williams theory have been mainly concerned with

(a) making allowance for long range interactions,

(b) generalising the evaluation of the partition function,

(c) making allowance for lattice vibrations.

Unfortunately, the incorporation of these factors into one theory is not a simple matter and as such only partial generalisations of the Bragg-Williams theory have been developed. It is noticeable however,

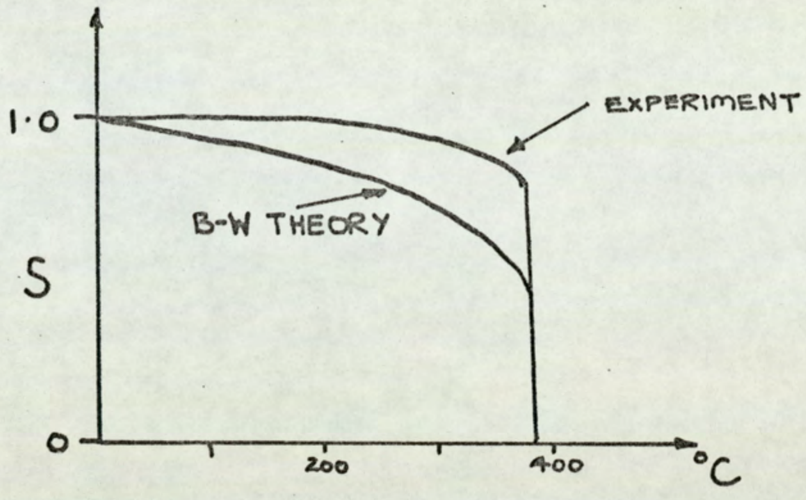

Fig.1.4 Comparison of the theoretical and experimental variations of the long range order parameter in Cu_3Au alloy.

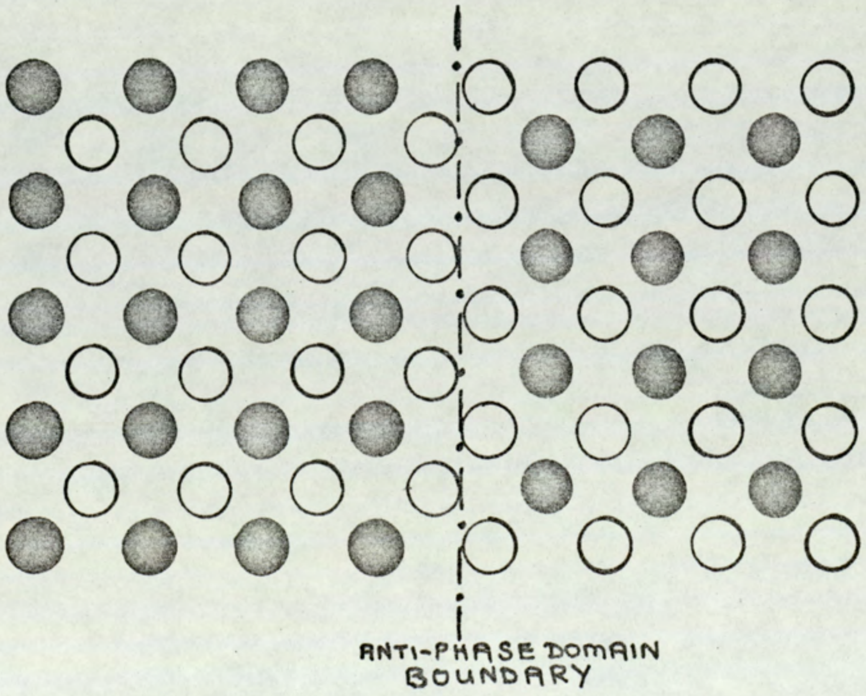

Fig.1.5 Anti-phase domains in a two dimensional AB structure.

that each generalisation results in improved agreement with experiment, but that discrepancies are still evident (see for instance the reviews of Guttman (1956) and Krivoglaz and Smirnov (1964)).

1.3 Mechanism of ordering: anti-phase domains.

In some alloys, notably of the type A_3B , ordering starts at a large number of locations throughout the crystal. As the transformations are typically from a compound lattice to a primitive lattice structure it is pure chance which of the equivalent lattice sites, at each of the ordering locations, will be occupied by the B atom. Hence the possibility arises of two neighbouring regions of order being "out of step". This condition is illustrated in Fig.1.5 with a two dimensional AB structure in which the left hand half is "out of step" with the right hand half by half the face diagonal. Such regions are called anti-phase domains and the boundary between two regions is called an anti-phase domain boundary. In disordered Cu_3Au for example, the lattice is statistically face centred cubic thus four different types of domain are possible (i.e. gold atom occupying corner or face-centre position of the cell). Each anti-phase domain boundary in this material is associated with a shift of the structure of half of the face diagonal of the unit cell in one of the $\langle 110 \rangle$ directions.

This concept of the ordering process was first inferred by Jones and Sykes (1938) who observed that the superlattice lines from partially ordered Cu_3Au are broadened whilst the lattice lines are sharp and substantially unaffected by the state of order. An analysis of the superlattice line breadths by Wilson (1943) and electron microscopy studies by Marcinkowski and Fisher (1960) confirmed the interpretation of Jones and Sykes. As this aspect of the ordering process is the main theme of the present work and as much of the interpretation is based on X-ray line broadening data further discussion is deferred until chapter 2.

1.4 Phase transitions among the spinel group of compounds

1.4.1 Introduction

Although order-disorder phenomena and anti-phase domain structures probably exist among numerous types of crystalline substances it is a remarkable fact that almost all experimental work to date has been devoted to the study of the metallic systems. This is very understandable in view of the complexities of the phenomena, but it does mean that our knowledge is still largely restricted to the very simplest cubic structures and to metal alloys. The former restriction is advantageous for experimental work and is probably not significant for an appreciation of physical principles. On the other hand, it is clearly desirable to study other types of compound for which different energies play the important rôle during the ordering transition.

A particularly interesting group of materials displaying a wide variety of phase transition behaviour including order-disorder transitions exists among the compounds related to the mineral spinel, $MgAl_2O_4$. Some of these, such as $NiCr_2O_4$, $CuFe_2O_4$ and Fe_3O_4, undergo transitions from cubic to tetragonal or lower symmetry as a result of the presence of certain transition metal ions subject to the Jahn - Teller effect (Dunitz and Orgel, 1957). Many more, containing magnetic ions exhibit spin ordering behaviour (Goodenough, 1963) and at least six different types of order-disorder change are known among the spinels.

Lithium ferrite ($LiFe_5O_8$), the subject of this study, is one of these compounds which undergoes an order-disorder transition and it is convenient here to briefly describe the crystallography of the spinel system so as to explain how the ordering phenomena arises.

1.4.2 The spinel structure

The crystal structure for the mineral spinel was originally determined independently by Bragg (1915) and by Nishikawa (1915). Related compounds tend to have a molecular formula of the form AB_2O_4 in which A and B are metal ions. In each such compound the crystal structure corresponds to an approximately closed packed cubic arrangement of the oxygen ions with the metal ions occupying selected "tetrahedral sites" (surrounded by 4 oxygen ions) and "octahedral sites" (surrounded by 6 oxygen ions) - see Plate 1.6. The space group to which the structure is usually referred is Fd3m and the atomic positions in the unit cell are:

(i)	32 oxygen ions	$u, u, u; \frac{1}{4} - u, \frac{1}{4} - u, \frac{1}{4} - u;$
		$u, \bar{u}, \bar{u}; \frac{1}{4} - u, \frac{1}{4} + u, \frac{1}{4} + u;$
		$\bar{u}, u, \bar{u}; \frac{1}{4} + u, \frac{1}{4} - u, \frac{1}{4} + u;$
		$\bar{u}, \bar{u}, u; \frac{1}{4} + u, \frac{1}{4} + u, \frac{1}{4} - u;$
		+ f. c. c. translations
(ii)	16 metal ions	$\frac{5}{8}, \frac{5}{8}, \frac{5}{8}; \frac{5}{8}, \frac{7}{8}, \frac{7}{8};$
	(octahedral sites)	$\frac{7}{8}, \frac{5}{8}, \frac{7}{8}; \frac{7}{8}, \frac{7}{8}, \frac{5}{8};$
		+ f. c. c. translations
(iii)	8 metal ions	$0, 0, 0; \frac{1}{4}, \frac{1}{4}, \frac{1}{4};$
	(tetrahedral sites)	+ f. c. c. translations

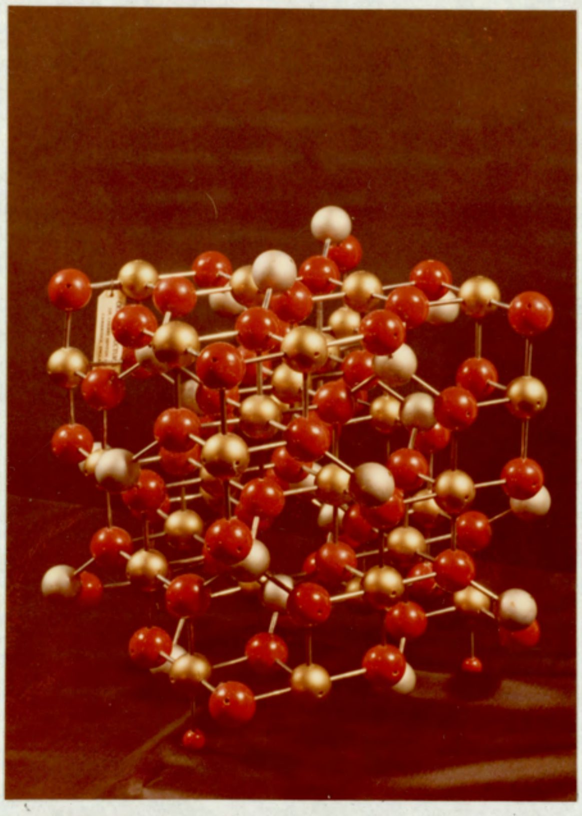

Plate 1.6 Unit cell of $MgAl_2O_4$.

The deviation of the oxygen ions from ideal cubic close packing, in which $u = -\frac{1}{8}$ (or $\frac{3}{8}$), is realized as a movement of the oxygen ions in the $\langle 111 \rangle$ directions away from their nearest neighbour tetrahedral site ion. By themselves, the eight tetrahedral site ions form a diamond structure with the equivalent cell edges parallel to the $\langle 100 \rangle$ directions. The structural arrangement of the octahedral site ions may be visualised as tetrahedral groups of ions connected at their apexes (see Fig.1.7a) or alternatively, as rows of ions laid down in the $\langle 110 \rangle$ directions in successive (100) planes, a/4 apart, with rows in adjacent planes being right angles (see Fig.1.7b).

In a "normal" spinel (eg. $MgCr_2O_4$), the 8 A ions (Mg) occupy the 8 tetrahedral sites and the 16 B ions (Cr) the octahedral sites. In an "inverse" spinel (eg. $NiFe_2O_4$), 8 of the B ions (Fe) occupy the tetrahedral sites whilst the remainder and the 8 A ions (Ni) are distributed over the octahedral sites. Cation distributions also occur which are intermediate to the above cases. In $NiAl_2O_4$ for instance, the nickel and aluminium ions tend to distribute themselves randomly over the tetrahedral and octahedral sites. X-ray and theoretical investigations (Verwey, deBoer and van Santen, 1948) have shown that the cation distribution is determined mainly by the Coulomb energy and by an individual preference of a number of ions for four - or six - fold co-ordination. In some cases, the latter can determine the form of the structure. For example, the chromites always form normal structures because of the overwhelming preference of the Cr^{3+} ion for the octahedral site (McClure, 1957).

In the case of inverse or partially inverse structures it was originally assumed that the distribution of different cations over a shared crystallographic site was random. It has since been shown however, that a large number of spinels have ordered cation distributions,

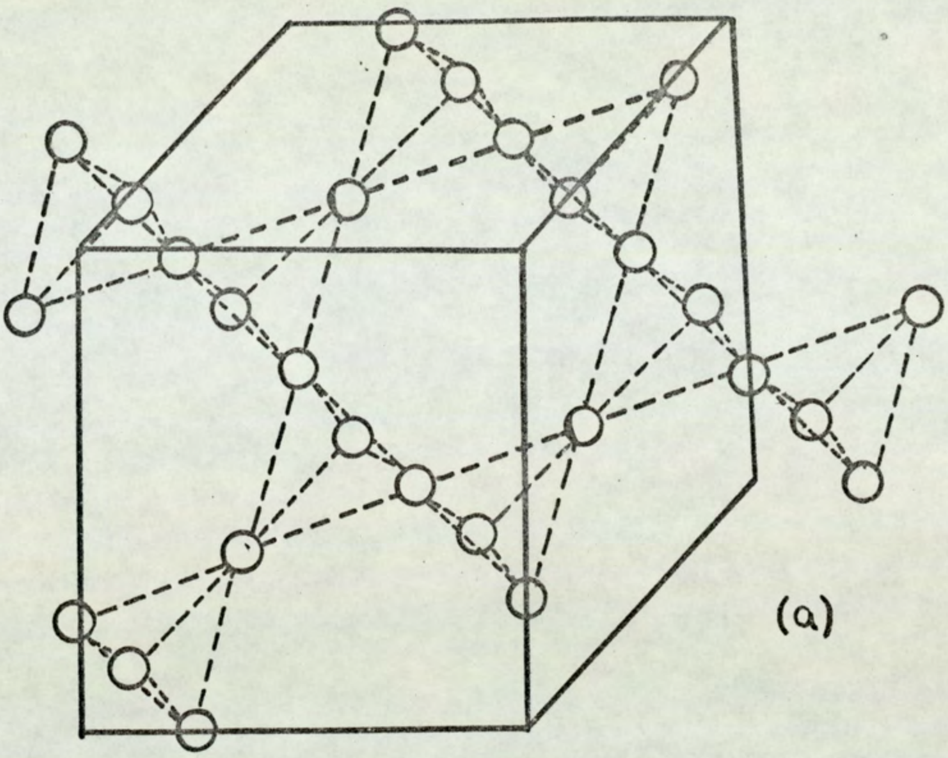

Fig.1.7 Octahedral ion structure in spinel structures.

(a) viewed as linked tetrahedrons

(b) projected on (100) plane.

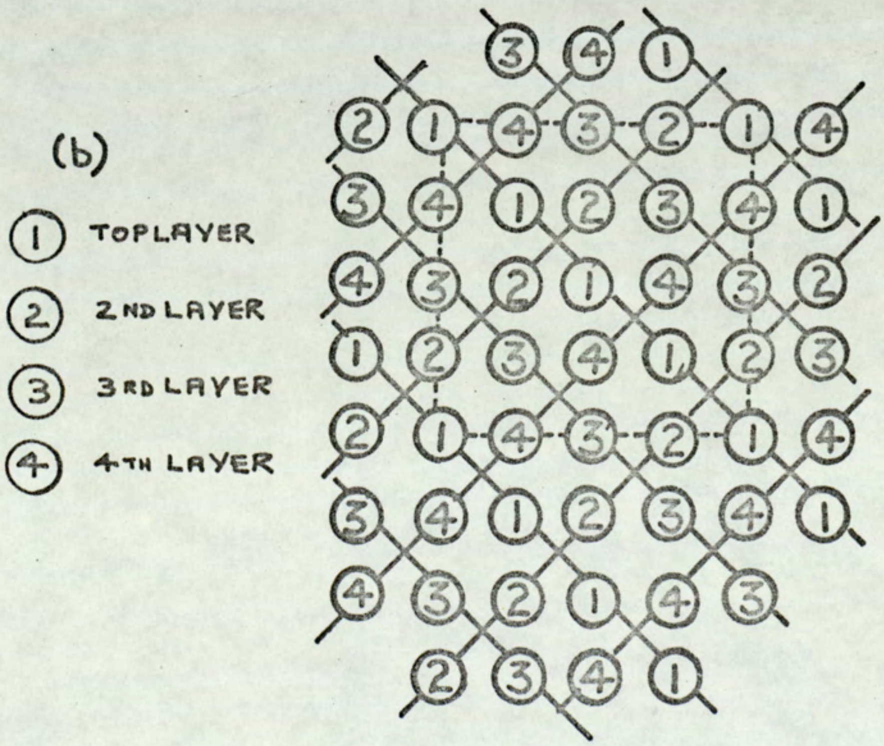

on one or other of the sites, of which lithium ferrite is an example. Six types of ordered arrangement have so far been identified as being associated with order-disorder transitions;

(a) 1:1 order on the octahedral sites. This type occurs in $Zn(Li\,Nb)O_4$ where the Li^+ and Nb^{5+} form into alternate positions in the ⟨110⟩ rows of octahedral sites (Blasse, 1964).

(b) 1:3 order on the octahedral sites. Many examples of this type of ordering exist (see for instance Blasse, 1964) of which $LiAl_5O_8$ and $LiFe_5O_8$ (lithium ferrite) were the first to be investigated. In $LiAl_5O_8$ (Datta and Roy, 1963) for instance, the 4 Li^+ ions and 12 Al^{3+} ions order themselves on the octahedral sites below 1295°C and in so doing reduce the lattice symmetry to primitive cubic.

(c) 1:5 order on the octahedral sites. γ-Fe_2O_3 and γ-Al_2O_3 (Oosterhout and Rooymans, 1958) are interesting examples of this type where some of the normally occupied octahedral sites contain vacancies which are ordered and as a result the lattice type is tetragonal with $c = 3a$ (a = lattice constant of disordered structure)

(d) 1:1 order on the tetrahedral sites. $LiFeCr_4O_8$ (Gorter, 1954) is an example of this type. The ordered arrangement consists of Li^+ ions at (0, 0, 0,) + f.c.c. translations and Fe^{3+} ions at $(\frac{1}{4}, \frac{1}{4}, \frac{1}{4})$ + f.c.c. translations; the lattice type of the ordered structure retains face-centred cubic symmetry.

(e) 1:2 order on the tetrahedral sites. An example of this type is β-In_2S_3 . This has a spinel structure above 420°C (sulphur occupying oxygen positions) in which vacancies are distributed randomly over the tetrahedral sites. Below 420°C the vacancies take up an ordered arrangement and the lattice type becomes body centred tetragonal with $c = 3a$; a being the face diagonal of the disordered unit cell. (Rooymans (1959), King 1962)).

(f) 1:1 order on tetrahedral sites and 1:3 order on the octahedral sites has been observed in $\mathrm{LiZn(LiMn_3)O_8}$ (Blasse (1963), Joubert and Durif (1964)). Below 720°C the Li^+ and Mn^{3+} ions are ordered on the octahedral sites. Below 400°C the Li^+ and Zn^{2+} ions are ordered on the tetrahedral sites.

1.4.3 Lithium ferrite - $\mathrm{LiFe_5O_8}$

Lithium ferrite was originally recognised as having a spinel structure by Hoffman (1938) and this was later confirmed by Braun (1952). The unit cell of this compound is unusual in that the octahedral sites are shared between 4 Li^+ ions and 12 Fe^{3+} ions while the eight tetrahedral sites are occupied exclusively by the remaining Fe^{3+} ions. According to Braun's structural analysis the the Li^+ ions appear to be distributed randomly over the octahedral sites above 755°C and the space group corresponds to that of a standard spinel (i.e. $Fd3m$). Below this temperature the Li^+ ions order themselves on the octahedral sites and the space group becomes cubic $P4_332$. The positions of the atoms in the unit cell according to the nomenclature of volume I of the International Tables for X-ray Crystallography (1952) are

4 Li^+ ions at $\frac{5}{8}, \frac{5}{8}, \frac{5}{8}; \frac{1}{8}, \frac{7}{8}, \frac{3}{8}; \frac{3}{8}, \frac{1}{8}, \frac{7}{8}; \frac{7}{8}, \frac{3}{8}, \frac{1}{8}$.
12 Fe^{3+} ions (octahedral sites) at 12(d) with $x = \frac{3}{8} + \Delta_1$,
8 Fe^{3+} ions (tetrahedral sites) at 8(c) with $x = 0 + \Delta_2$,
24 O^{2-} ions at 24 (e) with $x = \frac{1}{8} + \Delta_3$, $y = -\frac{1}{8} - \Delta_4$, $z = \frac{1}{8} + \Delta_5$,
8 O^{2-} ions at 8(c) with $x = -\frac{1}{8} - \Delta_6$ (or $\frac{3}{8} + \Delta_6$).

Braun's results from single crystals and powders indicated that the oxygen ion positions may be described with $\Delta_3 = \Delta_4 = \Delta_5 = \Delta_6 = 0.007$

which is equivalent to a spinel parameter u = - 0.132 (or 0.382). The Fe^{3+} ions on the octahedral and tetrahedral sites are shifted slightly in the ⟨110⟩ and ⟨111⟩ sets of directions, respectively, relative to their spinel positions. The ordered positions of the Li^{+} ions are such that the nearest neighbour octahedral ions are always Fe^{3+} ions.

Reported values for the lattice parameter of lithium ferrite vary from 8.314 Å to 8.37 Å (see von Aulock, 1965). Much of this variation however, can be attributed to the preparation technique (Pointon and Saull (1969) and Ridgley, Lessoff and Childress (1970)) which normally consists of sintering lithium carbonate and α- iron oxide between 1000°C and 1200°C. These authors demonstrated that above 1000°C lithium ferrite undergoes an irreversible loss of lithium and oxygen which results in the precipitation, to a varying degree, of α- Fe_2O_3 as a second phase and the formation of a product which is equivalent to a solid solution of lithium ferrite and Fe_3O_4 (i.e. $Li_{1-x}Fe^{2+}_{2x}Fe^{3+}_{5-x}O_8$ - where x is approximately proportional to the excess temperature above 1000°C). For stoichiometric lithium ferrite, Ridgley et al. (1970) estimated the lattice parameter to be 8.3296 ± 0.0005 Å at 28°C.

The change in the crystal structure of lithium ferrite has the characteristics of a first order phase transition in that at the transition temperature the volume of the unit cell and the long range order parameter change discontinuously (Kato (1956), Brunel and Bergevin (1964) and Vishnevskii et al. (1969)). All these workers agree that the transition temperature T_c lies between 735°C and 767°C. Kato's value of 750°C appears to be the most acceptable as the effects of non-stoichiometry and heating rate were taken into account in this work.

The difference in Coulomb energy between the ordered and randomly disordered form of lithium ferrite has been calculated as 9.76 e.v. (de Boer, van Santen and Verwey, 1950). As this energy is large compared with the thermal energy at the transition temperature the latter authors inferred that short range ordering persists in the disordered structure. Later, Anderson (1956) demonstrated theoretically that the thermodynamic free energy of the disordered structure is probably minimised by a state of short range order in which each tetrahedral group of octahedral site ions consists of one Li^+ ion and three Fe^{3+} ions (this condition is normally referred to as tetrahedral charge invariance). X-ray diffuse scattering measurements (Brunel and Bergevin, 1966) have since confirmed that tetrahedral charge invariance is rigidly adhered to in disordered lithium ferrite. A theoretical analysis of the latter measurements by Yamada and Yoshimori (1967) has indicated that range of interaction extends further than nearest neighbours. The strength of the interactions in lithium ferrite is also indicated by the rapidity with which the equilibrium long range order parameter achieves a value of unity as the temperature is reduced (see Fig.1.8).

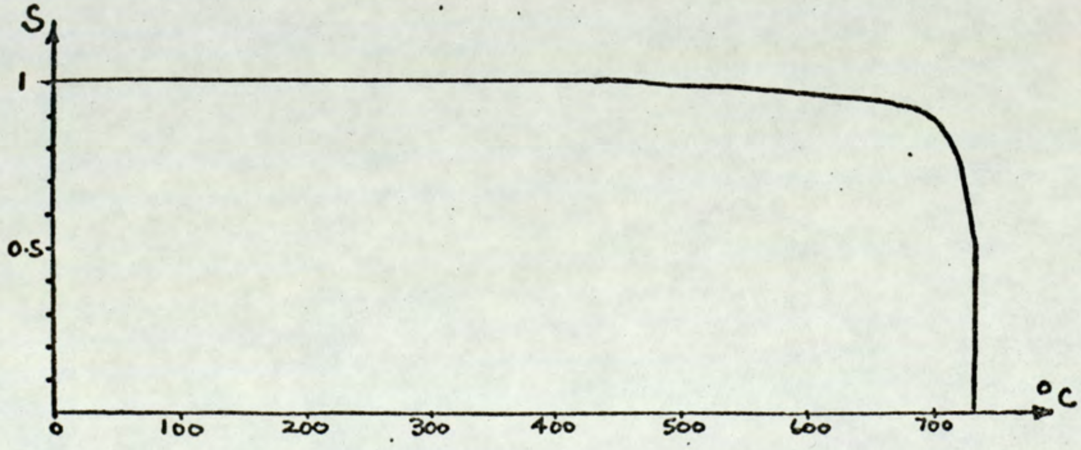

<u>Fig.1.8</u> Temperature dependence of long range order parameter in lithium ferrite(after Brunel & Bergevin,1964).

1.5 Scope of the present work

In a preliminary investigation, X-ray diffraction patterns from lithium ferrite samples which were either quenched from just below the transition temperature or partially disordered by the substitution of a small number of Cr^{3+} ions for Fe^{3+} ions were found to include superlattice lines whose breadths exceeded those of the lattice lines (see Fig.1.9a). Further work on the unsubstituted specimens showed that the breadth of the superlattice lines decreased as a function of the time for which the samples were annealed before quenching. When the latter samples were cooled slowly from the transition temperature the superlattice lines were found to be as well resolved as the lattice lines (see Fig.1.9b). These observations together with the fact that the phase transition in lithium ferrite has similar thermodynamic characteristics to the transition in Cu_3Au alloy, led to the conclusion that ordering occurs through the formation of anti-phase domains. As disordered lithium ferrite has a face centred cubic lattice similar to Cu_3Au there will be four types of domain ; each domain boundary being associated with a shift in the structure of half the face diagonal of the unit cell in one of the $\langle 110 \rangle$ directions.

The work described in this thesis is principally concerned with elucidating the nature of these anti-phase domains through an analysis of the X-ray diffraction line profiles from partially ordered specimens of lithium ferrite. The analysis of the line breadths was carried out by the Fourier transform method of Stokes (1948), the newer variance technique (Tournarie (1956 a & b), Wilson (1962 a & b, 1963 a)) and two new methods somewhat similar to variance. Line positions were analysed by the centroid method of Pike and Wilson (1959).

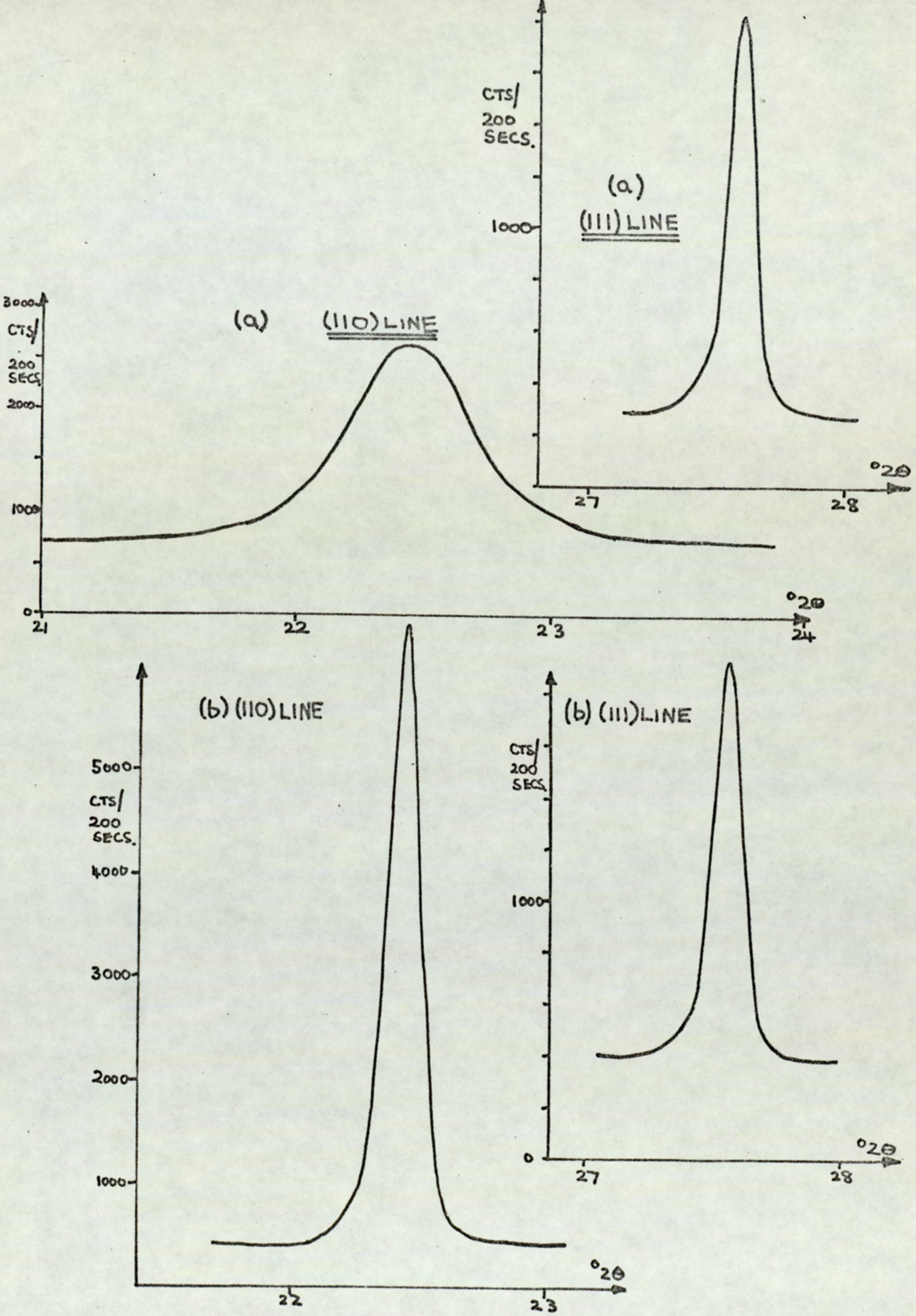

Fig.1.9 (110) superlattice line and nearby (111) lattice line.

Lithium ferrite (a) quenched from 745°C,

(b) allowed to cool slowly to room temperature.

The experiments divide themselves into three groups:-

In the first, specimens of lithium ferrite were quenched from just below the transition temperature (the annealing time not being measured). These specimens were used not only to investigate the anti-phase domains (i.e. nature of boundary planes and domain thickness distribution), but also to redetermine the crystal structure for lithium ferrite and estimate the non-stoichiometry resulting from the preparation technique. Analysis therefore, was performed on the lattice lines as well as the superlattice lines.

In the second group of experiments, samples of lithium ferrite were annealed just below the transition temperature for different periods of time before quenching. X-ray line breadth analysis of the superlattice lines from these samples was used to investigate the growth rate of the anti-phase domains and the domain thickness distribution after different periods of time.

A final group of experiments was concerned with the question of the mechanisms by which Cr^{3+} ions affect the development of anti-phase domains. For this analysis, samples of lithium ferrite were prepared with up to two Cr^{3+} ions per unit cell substituted for Fe^{3+} ions (i.e. $LiFe_{5-\frac{x}{4}}Cr_{\frac{x}{4}}O_8$, $x \leqslant 2$). Chromium was originally chosen as the substitutional ion because of its known tendencies to occupy octahedral sites (see section 1.4.2) and reduce the state of order (Gorter, 1954). The investigation was performed principally through analysis of the broadened superlattice lines although some additional information was obtained from lattice parameters and order parameters derived with the aid of the stronger lattice lines.

CHAPTER 2

ANALYSIS OF X-RAY DIFFRACTION LINE PROFILES

2.1 Measurement of line profile parameters

The observed intensity distribution across an X-ray diffraction line profile is given by the convolution of the intrinsic line profiles of each independent source of broadening or aberration which contributes to the observed profile (see for instance Klug and Alexander, 1954). For two independent sources of broadening with intrinsic profiles H(s) and L(s), a case examined experimentally by Jones (1938), the result of convolution I(s) is given by

$$I(s) = \int_{-\infty}^{\infty} L(s')H(s - s')ds' = \int_{-\infty}^{\infty} L(s - s')H(s')ds'$$

where s is a reciprocal space variable defined as $s = \frac{2\sin\theta}{\lambda} - \frac{1}{d}$, θ being the angle of diffraction and d the interplanar spacing associated with the reflection. As a consequece of this relation the Fourier transform of I(s), defined as $Z(t) = \int_{-\infty}^{\infty} I(s)e^{2\pi jst}ds$ where t is a vector length perpendicular to the plane of reflection, is equal to the product of the Fourier transforms of L(s) and H(s). Thus the correction of a diffraction broadened intensity profile for instrumental effects may be rigourously carried out through analysis of its Fourier transform provided the intensity distribution of the corresponding "instrumental" profile is known (Stokes, 1948). In this respect therefore, it is convenient to express the intensity function I(s) in terms of the transform Z(t),

$$\text{i.e.}\quad I(s) = \int_{-\infty}^{\infty} Z(t)e^{-2\pi jst}dt$$

or, as modified by Wilson (1962b),

$$I(s) = 2K\int_{0}^{\infty}\left(A(t)\cos 2\pi st - B(t)\sin 2\pi st\right)dt$$

where K is a slowly varying function of θ which may be assumed to be constant across an individual profile and $Z(t) = K(A(t) - jB(t))$. In the present work, the transform symbols used for the various sources of broadening are $A(t) - jB(t)$ for the general case, $V(t)$ for particle size broadening, $J(t) - jK(t)$ for diffraction broadening resulting from anti-phase domains, strain or stacking faults and $X(t) - jY(t)$ for instrumental broadening.

The Fourier integral representation of the intensity function is also convenient from an interpretation point of view as the transforms $V(t)$ and $J(t) - jK(t)$ are definable in terms of the physical causes of diffraction broadening (see Wilson, 1962c). $V(t)$, the particle size transform for the (hkl) diffraction line, is the volume common to a crystal and its exact replica displaced a distance t perpendicular to the (hkl) plane. $J(t) - jK(t)$ is the mean value FF^* of the structure factors of a pair of cells separated by a translation t perpendicular to the reflecting planes.

The applicability of Fourier transform methods to the analysis of diffraction broadened profiles was first demonstrated by Stokes (1948) using line profiles from cold worked copper and annealed copper. In this work the transform $J(t) - jK(t)$ arising solely from the effects of cold working was calculated as,

$$J(t) - jK(t) = \frac{\text{Transform of (hkl) profile (cold worked Cu)}}{\text{Transform of (hkl) profile (annealed Cu)}}$$

As intensity measurements are normally taken at discrete values of s or 2θ the practical evaluation of $J(t) - jK(t)$ necessitates approximating the Fourier integral representation by a Fourier series. This however, is only valid if $J(t) - jK(t)$ decreases to zero within $t = 1/\Delta$ where Δ is the step size in s between each intensity measurement (Stokes (1948), Young, Gerdes and Wilson (1967)). Despite its theoretical merits the use of Fourier transform analysis is frequently unwarrented as

(a) the theoretical apparatus for interpreting the whole of the transform function is not always sufficiently well developed (e.g. line broadening due to the effect of stacking faults - see Warren (1969)).

(b) only one parameter may be required from the line breadth analysis (e.g. mean particle size)

(c) the transform function $V(t)$ say, is highly sensitive to the presence of random and systematic errors in the intensity profile (Kukol (1962); Young, Gerdes and Wilson (1967)). Consequently, accurate and reliable data is required.

The measures of breadth most frequently used in line profile analysis are the half width, integral breadth and variance. The half width (Scherrer, 1918) has been used extensively in the past as it is an easily obtained and convenient measure of breadth. As quantitative interpretations based on this parameter are generally unreliable, it will not be given further consideration. The integral breadth β of a line profile (von Laue, 1926) is defined as

$$\beta = \frac{\text{Integrated Intensity}}{\text{Peak Height of Profile}}$$

$$= \frac{A(0)}{2\int_0^\infty A(t)dt} \qquad \text{provided the}$$

profile is reasonably symmetrical (i.e. $B(t) = 0$). Unfortunately, the absolute interpretation of this parameter (corrected for instrumental effects) is not a simple matter as the relationship between the real part of the transform function (e.g. $J(t)$) and the physical cause of the broadening is required in order to evaluate $\int_0^\infty J(t)dt$.

A measure of line breadth which has come into use more recently is the variance measured over a deliberately restricted range of a line profile (Tournarie (1956 a & b), Wilson (1962 a & b, 1963 a), Langford and Wilson (1963)). For the range of profile $s = -\sigma_1$ to σ_2 (reciprocal space parameters), the variance may be defined using either the total or the truncated integrated intensity as a normalising factor,

i.e. Variance type 1 $\quad W_\infty(\sigma_1, \sigma_2) = \int_{-\sigma_1}^{\sigma_2}(s - \langle s\rangle_\infty)^2 I(s)ds \Big/ \int_{-\infty}^{\infty} I(s)ds$

and Variance type 2 $\quad W(\sigma_1, \sigma_2) = \int_{-\sigma_1}^{\sigma_2}(s - \langle s\rangle)^2 I(s)ds \Big/ \int_{-\sigma_1}^{\sigma_2} I(s)ds$

where the centroid shift terms $\langle s\rangle_\infty$ and $\langle s\rangle$ are defined by

$$\langle s\rangle_\infty = \int_{-\sigma_1}^{\sigma_2} sI(s)ds \Big/ \int_{-\infty}^{\infty} I(s)ds$$

$$\langle s\rangle = \int_{-\sigma_1}^{\sigma_2} sI(s)ds \Big/ \int_{-\sigma_1}^{\sigma_2} I(s)ds$$

In practice, the second definition of variance is favoured as the total integrated intensity is generally unknown. By expressing each of the definitions in terms of the general transform function A(t) - jB(t) and by taking the range symmetrically about the centroid values (i.e. $\sigma_1 \simeq \sigma_2 \simeq \sigma$) the variance-range characteristics, $W_\infty(2\sigma)$ and $W(2\sigma)$, approximate closely to linear functions of 2σ in the region corresponding to the tails of a line profile,

i.e. $$W_\infty(2\sigma) = -\frac{1}{2\pi^2}\cdot\frac{A'(0)}{A(0)}\cdot 2\sigma \; - \frac{1}{4\pi^2}\cdot\left(\frac{A''(0)}{A(0)} + \left(\frac{B'(0)}{A(0)}\right)^2\right)$$

,Wilson (1962 b)

and $$W(2\sigma) = -\frac{1}{2\pi^2}\cdot\frac{A'(0)}{A(0)}\cdot 2\sigma \; - \frac{1}{4\pi^2}\cdot\left(\frac{A''(0)}{A(0)} + \left(\frac{B'(0)}{A(0)}\right)^2\right) + \frac{1}{\pi^4}\cdot\left(\frac{A'(0)}{A(0)}\right)^2$$

,Wilson (1965)

The parameters determined from the variance method, namely the slope and intercept of the linear part of either $W_\infty(2\sigma)$ or $W(2\sigma)$, have the particularly useful properties of being,

(i) easily and accurately corrected for the contributions arising from instrumental broadening,

(ii) susceptible of simple physical interpretation, when corrected for instrumental effects, for the three main causes of diffraction broadening (Wilson (1962b, 1963a)).

Provided the profiles considered are not excessively broadened the variance-range characteristics when converted to "2Θ space" (range 2ϕ) or "wavelength space" (range, $\Delta\lambda$) will remain linear in the tails of the profile and related to $W(2\sigma)$ (or $W_\infty(2\sigma)$) as follows:—

$$W(2\phi) = W(2\sigma)\cdot\left(\frac{\lambda}{\cos\theta}\right)^2 \qquad \text{and } 2\sigma = 2\phi\cdot\frac{\cos\theta}{\lambda},$$

$$W(\Delta\lambda) = W(2\sigma)\left(\frac{\lambda}{d}\right)^2 \text{ and } 2\sigma = \frac{d}{\lambda}\cdot\Delta\lambda$$

$$\text{also } W(\Delta\lambda) = W(2\phi)\left(\frac{\lambda\cot\theta}{2}\right)^2 \text{ and } \Delta\lambda = \frac{\lambda\cot\theta}{2}\,2\phi$$

The first stage in a practical evaluation of any line breadth parameter is the elimination of the background scatter contribution to the observed intensity profile. The earliest and probably still most popular method is to assume a linear background variation, the slope and mean value of which are estimated by inspection of the intensity levels at large ranges either side of the observed profile. However, as this method of estimation is to a large extent subjective it cannot be considered as being satisfactory particularly when extensive diffraction broadening is present. Langford and Wilson (1963) have developed an objective method of estimation which is based on the principle that the correct background has been subtracted from the intensity profile when the variance-range characteristic $W(2\phi)$ of the corrected profile is linear in the tails (see Fig.2.1). When the background level is wrongly chosen $W(2\phi)$ is supplemented by a cubic term in 2ϕ,

$$\text{i.e. } W(2\phi) = S.2\phi + I + D(2\phi)^3$$

where $D \simeq$ Background Error/12.Integrated Intensity.

In practice, great care must be exercised in using the latter method as,

(i) the absorption edge of the β filter restricts the upper limit of linearity (see Fig.2.2). For low angle lines however, it is possible to use the region outside the absorption edge without the effects of statistical

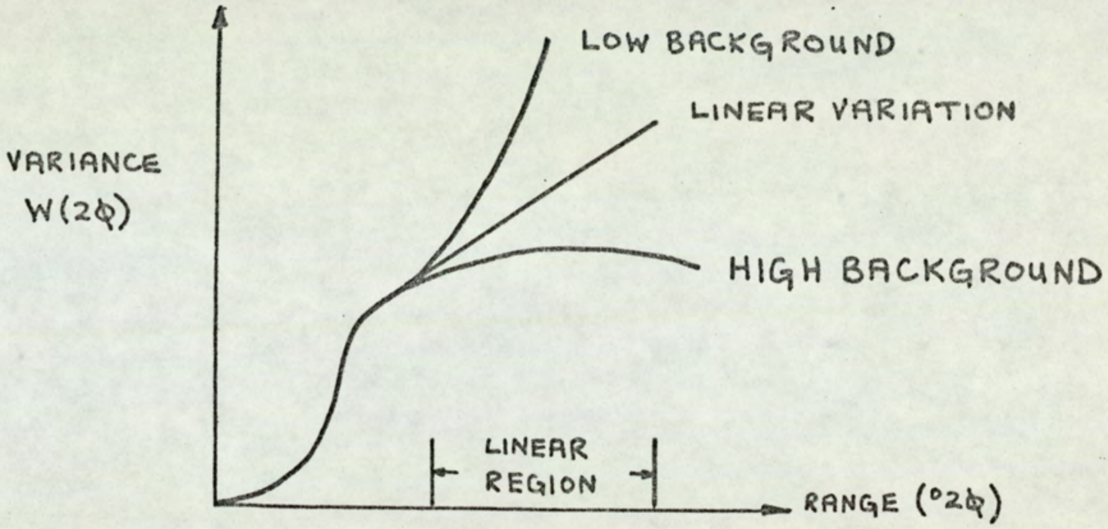

Fig.2.1 Effect of background level on the variance-range characteristic of a line profile.

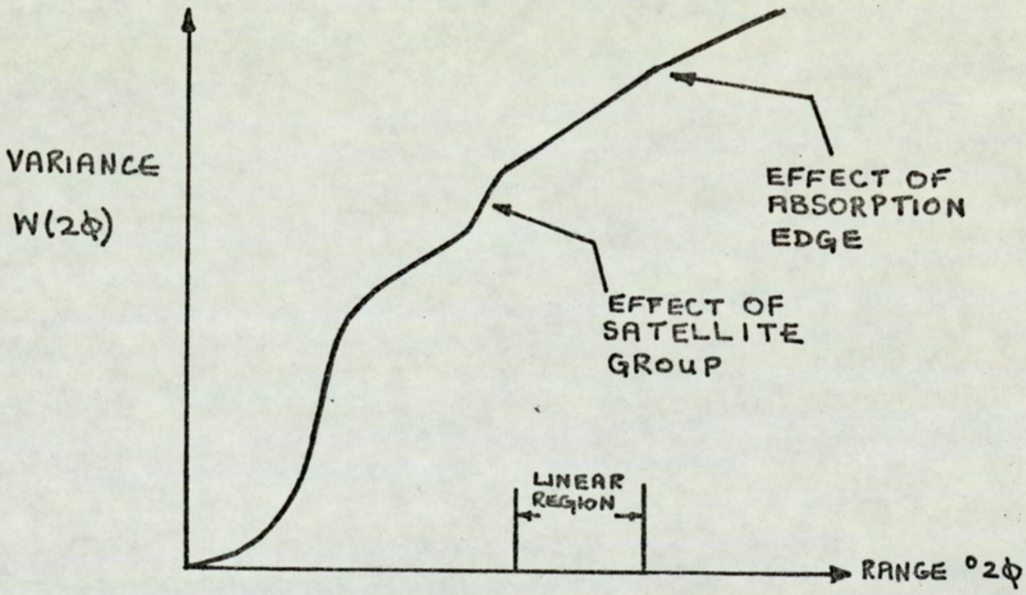

Fig.2.2 Effect of Kα satellite group and absorption edge of β filter on the variance-range characteristic.

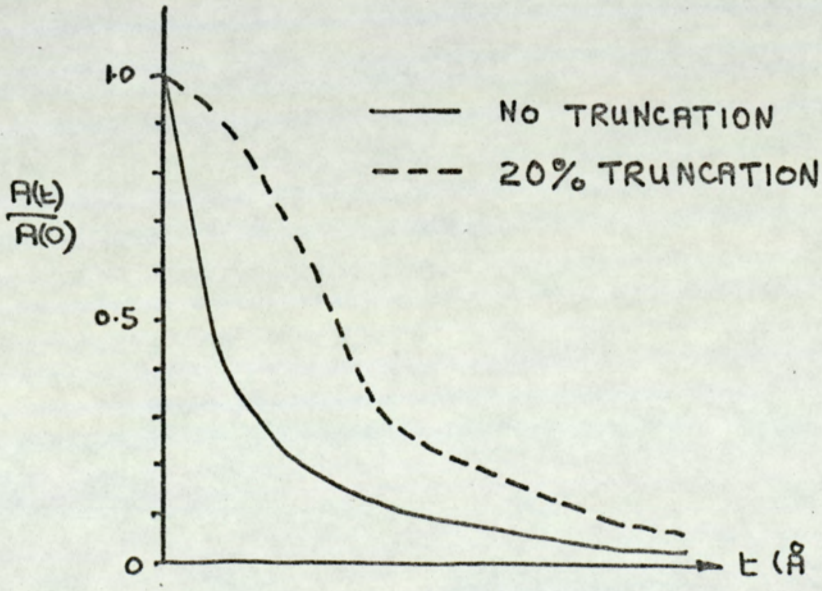

Fig.2.3 Effect of truncation of a line profile on the Fourier transform (after Young, Gerdes and Wilson, 1967).

fluctuations in the intensity data being particularly evident.

(ii) the Kα satellite group of emission lines lies between the start of the expected linear region and the range of the absorption edge (Langford (1968a), Edwards and Toman (1969, 1970a)). For sharp profiles, the effect of these lines is seen as a step like change in W(2ϕ) (see Fig.2.2.) and as such the linear region is reduced to the ranges between the satellite group and the absorption edge. Methods of eliminating the influence of the satellite group have been described by Edwards and Toman (1970a).

In addition to subtracting the correct background level, it is also important in Fourier transform analysis to ensure that the intensity profile is not truncated as otherwise the measured transform A(t) will exhibit Gibbs oscillations and A(0) will be underestimated (Bertaut (1952), Kukol (1962), Young, Gerdes and Wilson (1967)). An illustration of the effect of truncation is given in Fig.2.3.. The relation between the measured and true values of A(t) when the transform is evaluated over the reduced range $-\alpha/2$ to $\alpha/2$ is

$$(A(t))_{\text{measured}} = \int_{-\infty}^{\infty} A(t)\frac{\sin(\pi\alpha(t-x))}{\pi(t-x)}dx \qquad \text{, Bertaut (1952).}$$

Wagner (1966) has pointed out that the corrected transform, J(t) - jK(t) say, will also exhibit oscillatory effects when the transforms of the sharp and broadened profiles are determined about values of s, the reciprocal space parameter, which are not equivalent with respect to s = o, i.e. $(J(t) - jK(t))_{\text{measured}} = (J(t) - jK(t))e^{\pm 2\pi j t s_o}$

where s_o is the difference in the origins of measurement. This may be avoided if the lattice parameters of the annealed sample and the sample giving the diffraction broadened lines are known or if the corrected transform is known to be either real or imaginary. In the latter case $|(J(t) - jK(t))_{\text{measured}}|$ will give the true transform function.

To correct the various measures of line breadth for instrumental contributions it is usual to adjust the results from each broadened profile with the aid of corresponding results from a profile, at a similar Bragg angle, in which the diffraction broadening is negligible (i.e. sharp profile). If the sharp and broadened profiles are both Cauchy shaped (i.e. $a/(b+s^2)$) or both Gaussian shaped (i.e. ae^{-bs^2}) the corrected integral breadth β is given by

$$\beta = (\beta_{\text{broad line}} - \beta_{\text{sharp line}}) \text{ for the Cauchy case}$$

$$\text{and } \beta^2 = (\beta^2_{\text{broad line}} - \beta^2_{\text{sharp line}}) \text{ for the Gaussian case}$$

(Warren and Biscoe, 1938). Most experimental profiles however, lie somewhere between the above curves. Wagner and Aqua (1964) for instance, have found that the empirical correction given by

$$\beta = \beta_{\text{broad line}} - \beta^2_{\text{sharp line}}/\beta_{\text{broad line}}$$

is more appropriate to the profiles they measured. The only rigourous method of determining the corrected integral breadth is to evaluate the Fourier transform $J(t)$ and then calculate $J(0)/\int_0^\infty J(t)dt$.

In variance analysis, correcting the observed slopes and intercepts for instrumental effects is a relatively simple matter (see Wilson, 1970). This follows from the fact that the Fourier transform $A(t) - jB(t)$ is given by the product of the instrumental transform $X(t) - jY(t)$ and the diffraction broadening transform $J(t) - jK(t)$,

$$\text{i.e. } A(t) - jB(t) = (X(t) - jY(t)).(J(t) - jK(t)) \ ,$$

so that

$$\frac{A'(0)}{A(0)} = \frac{X'(0)}{X(0)} + \frac{J'(0)}{J(0)}$$

$$\text{and } \left(\frac{B'(0)}{A(0)}\right)^2 + \frac{A''(0)}{A(0)} = \frac{X''(0)}{X(0)} + \frac{J''(0)}{J(0)} + \frac{2J'(0)}{J(0)}\frac{X'(0)}{X(0)} + \left(\frac{Y'(0)}{X(0)} + \frac{K'(0)}{J(0)}\right)^2$$

Consequently, as the terms $X'(0)/X(0)$ and $X''(0)/X(0) + (Y'(0)/X(0))^2$ are proportional to the variance slope and intercept of the sharp profile and as $K'(0)/J(0)$ and $Y'(0)/X(0)$ may be determined independently from centroid shifts, it is possible to determine the parameters associated with the diffraction broadening (i.e. $J'(0)/J(0)$ and $J''(0)/J(0)$. In this connection it is worth remarking that the centroid of a line profile also has the property of being easily corrected for instrumental effects as the total centroid shift of a sharp line is the sum of the shifts of the component instrumental aberrations (Wilson, 1963b).

Besides the serious reduction of the linear region caused by the absorption edge and the satellite lines, the only other feature limiting the accuracy of variance is the assumption that $W(2\emptyset)$ (or $W_\infty(2\emptyset)$) is a linear function of $2\emptyset$ in the tails of a profile.

It has recently been shown (Edwards and Toman (1970b), Wilson (1970)) that $W(2\sigma)$ and $W_\infty(2\sigma)$ are more accurately represented in the practical linear region by expressions of the form

$$W_\infty(2\sigma) = \left(W_\infty(2\sigma)\right)_{\text{linear}} - \frac{1}{2\pi^4} \cdot \frac{A'''(0)}{A(0)} \cdot \frac{1}{2\sigma}$$

and $$W(2\sigma) = \left(W(2\sigma)\right)_{\text{linear}} - \frac{1}{2\pi^4} \cdot \left(\frac{A'''(0)}{A(0)} - \frac{A'(0)}{A(0)}\left(\frac{A''(0)}{A(0)} + \left(\frac{B'(0)}{A(0)}\right)^2\right)\right) \cdot \frac{1}{2\sigma}$$

Edwards and Toman (1970b) concluded that if a straight line is fitted to the variance - range characteristic of a simulated Cauchy profile in the practical linear region, the subsequent discrepancy in the measured slope is only a few per cent whilst the discrepancy in the measured intercept is several tens per cent. As yet no work appears to have been published on the influence of the hyperbolic term in experimental variance - range characteristics. Its influence cannot be very large however, as reasonably comparable values for the crystallite size are given from instrumentally corrected slopes and intercepts obtained by assuming $W(2\phi)$ to be linear (Langford, 1968b).

2.2 Interpretation of diffraction broadening

In the present work the prime concern is interpretation of line broadening effects due to the presence of anti-phase domains in lithium ferrite. Consequently, in the following sections the interpretation of diffraction broadening due to small crystallites, strain and stacking faults is only given superficial considerations.

2.2.1 Diffraction broadening arising from small crystallites

Stokes and Wilson (1942, 1944a) put the analysis of crystallite size broadening in a systematic form by defining the transform $V(t)$

the variation of which, as a function of t, they calculated for single crystallites with selected polyhedral shapes. In order to define the crystallite size p by a single parameter they set the volume of the crystallite V(0) equal to p^3. The initial portion of V(t) for a single crystallite is generally given by

$$\frac{V(t)}{V(0)} = 1 - \frac{K}{p}.t + \frac{L}{p^2}.\frac{t^2}{2} = 1 + \frac{V'(0)t}{V(0)} + \frac{V''(0)t^2}{V(0)2}$$

where K, the Scherrer constant, and L, the taper parameter, are functions of the plane of reflection and, $^p/_K$ is normally termed the apparent particle size. Consequently, the variance - range characteristic $W_\infty(2\phi)$, in 2θ space, is given by,

$$W_\infty(2\phi) = \frac{K\lambda}{2\pi^2 p\cos\theta} \cdot (2\phi) - \frac{L\lambda^2}{4\pi^2 p^2\cos^2\theta} \qquad \text{,Wilson (1962b)}$$

In general all the lines in a diffraction pattern are broadened by this cause.

Unfortunately, the above results only apply when the crystallites are all the same size. Bertaut (1950), by expressing the problem in terms of columns of unit cells perpendicular to the (hkl) plane, was able to formulate a generalized form for V(t) namely,

$$V(t) = \int_t^\infty (T - t)f(T)dT$$

where f(t) is the distribution of column lengths over all the crystallites. From this relation he demonstrated that V''(t) is proportional to f(t). The relation of the initial portion of V(t) to the true average crystallite size p is given in general by

$$\frac{V(t)}{V(0)} = 1 - \frac{K\langle p^2\rangle}{\langle p^3\rangle}.t + \frac{L\langle p\rangle}{\langle p^3\rangle^2}.\frac{t^2}{}$$

2.2.2 Diffraction broadening arising from strained crystallites

In a strained crystallite the varying distortion of the unit cells is responsible for the X-ray line broadening. Under the assumption that the relative positions of the atoms in any unit cell are negligibly disturbed it has been shown (Stokes and Wilson, 1944b) that

$$J(t) - jK(t) = F^2\left\langle e^{2\pi jS_o te}\right\rangle = F^2\int_{-\infty}^{\infty}\Psi(t,e)e^{2\pi jS_o te}de$$

where e is the mean strain in the [hkl] direction at a distance t between two cells, $S_o = 2\sin\theta/\lambda$ and $\Psi(t,e)$ is the fraction of crystallites with a strain e to e+de over a distance t. For small values of t,

$$\frac{J(t)}{J(0)} = 1 - 4\pi^2S_o^2\langle e^2\rangle t^2 = 1 + \frac{J''(0)}{J(0)}\frac{t^2}{2}$$

and $\frac{K(t)}{J(0)} = 2\pi S_o\langle e\rangle t.$

Thus, according to Wilson (1963a), the effects of strain are observed only in the variance intercept

i.e. $W_\infty(2\phi) = \tan^2\theta(\langle e^2\rangle - \langle e\rangle^2)$

The presence of line broadening arising from strain is more evident in the high angle diffraction lines and hardly observable in the very low angle lines.

2.2.3 Diffraction broadening arising from stacking faults

Cold working a metal or alloy induces not only strain, but also, in many cases, stacking faults. For small values of t the transform $\frac{J(t)}{J(0)} = 1 - \frac{t}{D}$ where D, the apparent particle size, is proportional to the mean distance between the stacking faults. When more than one type of stacking fault is present $\frac{1}{D} = \frac{1}{D_1} + \frac{1}{D_2} \ldots\ldots$ where D_1, D_2 etc. are proportional to average distances between each type of stacking fault. In some ways the effect of stacking faults on the diffraction pattern is similar to the effects of small crystallites except that for some types of stacking fault centroid shifts occur and also the variation of the apparent particle size as a function of the plane of reflexion tends to be irregular. For reviews of this aspect of line broadening the reader is referred to Wagner (1966) and Warren (1969).

2.2.4 Diffraction broadening arising from anti-phase domains

Theory

Although the theory of X-ray diffraction from materials containing anti-phase domains existed in an implicit form through the works of Landau (1937a), Lifschitz (1937) and Hendricks and Teller (1942) it was Wilson (1943) who first expressed it in an explicit form. In Wilson's formulation, the Fourier transform J(t) - jK(t) is given, by

$$J(t) - jK(t) = \sum_{i} g_i F_i \left[\sum_{j} p(t, j/i) F_j^* \right]$$

where the summations are carried out over all possible type of unit cell structure, F_i is the structure factor of an i type unit cell structure (F^* represents complex conjugate of F), g_i is the fraction of i type unit cell structures in the crystallite, and $p(t,j/i)$ is the probability of a unit cell structure of type j at a distance t in the [hkl] direction from a unit cell structure of type i. As anti-phase domains in materials other than Cu_3Au alloy have not been investigated to any great extent, the form of $J(t) - jK(t)$ will be developed in terms of Cu_3Au alloy. Most of the results for this alloy however, are sufficiently general to apply to any material (including lithium ferrite) in which the phase transition is from a face-centred cubic lattice to a primitive cubic lattice.

In partially ordered Cu_3Au alloy, the gold atoms may occupy one of four positions in the unit cell which shall be designated A,B,C and D (see Fig.2.4). Thus the possible structure factors are

$$F_A = f_{Au}e^{\pi j(k+l)} + f_{Cu}\left(e^{\pi j(h+l)} + e^{\pi j(h+k)} + 1\right),$$

$$F_B = F_A e^{\pi j(h+k)} = F_A(-1)^{h+k},$$

$$F_C = F_A e^{\pi j(h+l)} = F_A(-1)^{h+l},$$

$$F_D = F_A e^{\pi j(k+l)} = F_A(-1)^{k+l}$$

Fig.2.4 Location of gold atoms in each type of unit cell

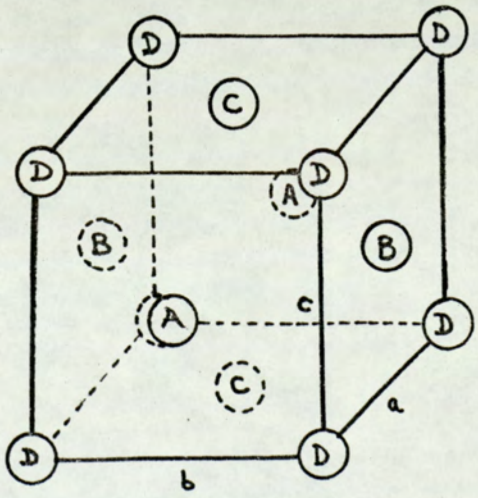

For the lattice lines (h,k,l all odd or all even), $F_A = F_B = F_C = F_D = (3f_{Cu} + f_{Au})$ and J(t) = constant. These lines therefore, are unbroadened by the presence of anti-phase domains in the structure. For each h,k,l corresponding to a superlattice line the structure factor F_i(i = A,B,C or D) is $(f_{Au} - f_{Cu})$ or $-(f_{Au} - f_{Cu})$ so that $F_iF_j^*$ can be $+F^2$ or $-F^2$. By considering the types of structural change that may occur at a boundary between two adjacent cells, it has been shown (Wilson and Zsoldos, 1966) that the following sets of change are structurally equivalent:

(i) A to B and C to D,

(ii) A to C and B to D,

(iii) A to D and B to C.

Consequently, as each type of unit cell is expected to be equally abundant ($g_i = {}^1/_4$) and as all the possible values of $F_iF_j^*$ are known, the equation for J(t)(K(t) = 0) may be reduced to

$$J(t) = F^2((-1)^{k+l}.p(t,A/D) + (-1)^{h+l}.p(t,B/D)$$

$$+ (-1)^{h+k}.p(t,C/D) + p(t,D/D)).$$

To calculate P(t,i/D), Wilson (1943) and Wilson and Zsoldos (1966) assumed a model,hereinafter referred to as the random model, in which the probability of an anti-phase domain boundary between any two adjacent cells is independent of boundaries between other cells (i.e. a domain thickness distribution $f(t) = \frac{1}{D} . e^{-t/D}$ where D is the mean domain thickness). Under this condition the forms of J(t) for the superlattice lines are given by

$J(t) = F^2 e^{-2(\beta+\gamma)t}$ for k and l of similar parity

$J(t) = F^2 e^{-2(\alpha+\gamma)t}$ for h and l of similar parity

$J(t) = F^2 e^{-2(\alpha+\beta)t}$ for h and k of similar parity

where α, β and γ are the probabilities of changes A to D, B to D and C to D, respectively, per unit length. In lithium ferrite, as in Cu_3Au, the shift of the structure at the domain boundaries is half the face diagonal of the unit cell in one of the $\langle 110 \rangle$ directions. The possible structure factors, therefore, are +F and -F. Consequently, the above equations for J(t) also apply to lithium ferrite.

The set or sets of planes defining the anti-phase domain boundaries are reflected into J(t) through the dependence of α, β and γ on h,k and l, the Miller indices of the reflecting planes. Wilson (1943) calculated this dependence for a number of models, but neglected to account for the multiplicity of the boundary planes. This has since been rectified however, by Wilson and Zsoldos (1966). Two classes of boundary model must be distinguished:—

<u>Class I</u> No restrictions are placed on the type of adjacent domain. Thus for instance, a domain of type D cells may be followed with equal probability by a domain of type A,B or C cells (i.e. $\alpha = \beta = \gamma$). Expressions for α, β and γ when the domain boundaries are on the $\{100\}$, $\{110\}$ or $\{111\}$ have been derived by Wilson and Zsoldos (1966). For this class of domain boundaries J(t) may be expressed as a function of p(t,D/D) since $p(t,i/D) = \frac{1}{3}(1-p(t,D/D))$ when $i \neq D$,

$$\text{i.e. } J(t) = F^2\left[\frac{4}{3} \cdot p(t,D/D) - \frac{1}{3}\right]$$

<u>Class II</u> Restrictions are placed on the possible types of adjacent domain so that in general, $\alpha \neq \beta \neq \gamma$. Most of these models are variations on the principle that domain

boundaries in Cu_3Au alloy for which the gold atoms are nearest neighbours are more unstable (high energy boundaries) than boundaries for which gold atoms are not nearest neighbours (low energy boundaries). Low energy and high energy boundaries on the $\{100\}$ and $\{110\}$ sets of planes have been examined by Wilson and Zsoldos (1966). Various combinations of class I and class II boundaries have been examined by Wilson (1943), Batterman (1956) and Mikkola and Cohen (1966).

Wilson (1958) and Wilson and Zsoldos (1966) have expressed concern for the physical reality of the random model of domain sizes. Unfortunately, the calculation of J(t) from a physical model ofdomain formation is not a simple matter. A special case corresponding to a one dimensional domain structure has been calculated by Lifschitz (1937). In this work the domains arise from small ordered nuclei which, at temperatures below the transition temperature, grow until they meet other growing nuclei. The domain size distribution for this model is approximately given by $f(t) = \frac{t}{D^2}e^{-t/D}$. No analytical extensions of this model to three dimensional growth appear to have been achieved. Roessler and Flinn (1967) on the other hand, have shown that if the domain thickness distribution f(t) is known, J(t) can be calculated provided the function J_k , the mean value of FF^* for cells separated by k domain boundaries, is independent of the domain thickness distribution. Reformulating their equations in the reverse manner they came to the conclusion that

$$f(t) = \frac{D9}{16} \frac{J''(t)}{J(0)}$$

where D is the mean domain thickness. However, if applied to the random model with class I boundaries (i.e. $J(t)/J(0) = e^{-4t/3D}$ and

$f(t) = \frac{1}{D} \cdot e^{-t/D}$) this equality is not satisfied.

Wilson (1963a), extending an argument of Strijk and MacGillavry (1946), formulated J'(0)/J(0) and J''(0)/J(0) in a form sufficiently general to apply to any anti-phase domain structure namely,

$$\frac{J'(0)}{J(0)} = \frac{J_a - J_s}{DJ_s}$$

$$= -\frac{4}{3D} \text{ for a random model with class I boundaries}$$

and $$\frac{J''(0)}{J(0)} = \frac{(2J_a - J_s - J_n)f(0)}{DJ_s}$$

$$= \frac{16}{9D^2} \text{ for a random model with class I boundaries}$$

where J_s, J_a and J_n are the mean values of FF* for cells in the same domain, adjacent domains and next but one domains, respectively, f(0) is the domain thickness distribution at t = o and D, as before, is the mean domain thickness. As the possible structure factors are either +F or -F the parameter $J_a = \alpha F^2 - (1-\alpha)F^2$ where α is the fraction of adjacent domains having structure factors of the same sign. Consequently, the initial variation of J(t) will always be of the form

$$\frac{J(t)}{J(0)} = 1 - \frac{2\alpha t}{T}$$ whatever the nature of the domain thickness distribution (Wilson, 1958).

Experimental electron microscopy and X-ray diffraction work on anti-phase domains.

Electron microscope observations of large anti-phase domains

(> 500 Å) in Cu_3Au by Marcinkowski and Fisher (1960) revealed that the domain boundaries are primarily on the {100} planes. In a similar study on the growth of domains. Yamaguchi, Watanabe and Ogawa (1961) concluded that

(i)during the early stages of growth the boundary planes are not clearly defined on {100} planes and that lower symmetry planes assume a boundary role.

(ii)the {100} boundaries are primarily of the type for which gold atoms do not come into contact (i.e. low energy boundaries). This conclusion was reached by analysing the image contrast at the boundaries for different orientations of the specimen.

These conclusions are in accordance with X-ray measurements. Wilson (1943) showed that the observed variation of the apparent particle sizes with the indices of reflection could be adequately accounted for by a combination of low energy {100} boundary planes and boundary planes for which the average inter-boundary separation distance is independent of crystallographic direction. Poquette and Mikkola (1969) on the other hand, accounted for their apparent particle sizes by a combination of class I {111} boundary planes and low energy {100} boundary planes. The discrepancy between these observations probably arises from the fact that different methods wereused to estimate the apparent particle sizes. An argument in favour of the latter model is that {111} boundaries are expected to be second most stable boundary type (Flinn, 1960); the most stable being low energy {100} boundaries.

To test the random model against experiment, Fourier transform analysis has been carried out by a number of workers. In these analyses (Mac Gillavry and Strijk (1946) and Edmunds and Hinde (1952) on Cu_3Au, and Steeple and Edmunds (1956) on Mg_3Cd) it was found that the form of J(t) approximated to a Gaussian function (i.e. $J(0)e^{-bt^2}$).

The reality of this result however, for small values of t is difficult to accept even though the analyses were performed with considerable care as

(i) $J'(0)/J(0) \neq 0$ for a strictly anti phase domain structure (Wilson, 1958)

(ii) systematic errors in the initial portion of $J(t)$ are almost unavoidable (Kukol, 1962)

(iii) a negative value for $J''(0)/J(0)$ implies that $f(t)$ has a negative value at $t=o$

Graphical values of $J(t)$ given in Poquette and Mikkola (1969) indicate that for $t > 20\text{Å}$, $J(t)/J(0)$ lies slightly closer to e^{-at} than e^{-bt^2}. Nevertheless, it must be assumed that the random model does not explain these or the previous Fourier transform results.

Using thermal techniques, Jones and Sykes (1936) demonstrated that the growth of anti-phase domains in Cu_3Au is a two stage process. Their interpretation was that small domains nucleate and then grow until all the domain boundaries are in contact whereupon some domains grow at the expense of others. Further support for this model is given by short range order measurements on disordered Cu_3Au which indicate the presence of isolated regions of ordered structure distributed throughout the disordered matrix (Moss (1966), Cohen and Gehlen (1965)). Taylor, Hinde and Lipson (1951) however, suggest that the ordering process starts at all points simultaneously such that gold atoms tend to avoid one another, hence the low energy domain boundaries.

From an analysis of the apparent particle size D as a function of annealing time (x) at various fixed temperatures (T), Poquette and Mikkola (1969) demonstrated that the rate process of domain growth in Cu_3Au is very similar to that of ideal grain growth in metals (see Cahn, 1970) as the relationship

$D^2 - D_0^2 = Kx$ could be fitted to the results. No such relationship was indicated in similar analyses by Jones and Sykes (1938) and Owen and Mac Arthur Sim (1947). Poquette and Mikkola (1969) were also able to demonstrate that domain growth is diffusion controlled and that the activation energy is in good agreement with values obtained from diffusion measurements.

CHAPTER 3

EXPERIMENTAL METHODS OF ANALYSIS OF DATA

3.1 Preparation of lithium ferrite samples

In the present experiments the samples were prepared from reagent grade Li_2CO_3,α-Fe_2O_3 and, in the case of the chromium substituted samples, Cr_2O_3. The technique used to prepare each sample followed, to a large extent, that of previous workers (e.g. Gorter (1954), Blasse (1964)) in that calculated amounts of the constituent materials (dried at 150°C prior to use) were combined, ground together in an agate mortar for 15 to 20 minutes, moulded under pressure into the form of a pellet, and sintered at 1150°C in a vertical tubular furnace (note: at the time of preparation the fact that lithium ferrite prepared above 1000°C is slightly non-stoichiometric (Pointon and Saull (1969), Ridgley et al.(1970)) was unknown to the author). To avoid losses of Li_2CO_3 (melting point 618°C) by evaporation the reaction was allowed to proceed at 600°C for a few hours before raising the temperature to 1150°C. Subsequent heat treatment of the samples consisted of either cooling slowly (approximately 20°C/hr.) to room temperature or quenching into liquid nitrogen from just below the transition temperature. Identification was carried out with the aid of X-ray powder diffraction photographs of the samples, using either CoKα or CrKα radiations.

The full details of the heat treatments given to the three groups of samples prepared (see section 1.5) were as follows:-

<u>Group 1</u> This group consisted four lithium ferrite samples quenched from temperatures between 725°C and 745°C (no record kept of annealing time at the quenching temperature, but of the order of 1 to 15 minutes).

Sample Designation	Initial Heat Treatment	Secondary Heat Treatment	Preset (Quenching) Temperature
LF-725	(i) 3 hrs.at 600°C (ii) 6 hrs. at 1150°C (iii) cooled slowly to room temp.(approx. 20°C/hr)	(i) Reheated to 900°C (ii) Maintained approx. 30mins (iii) Cooled and held at preset temp (iv) Quenched in liquid N_2	725°C
LF-735			735°C
LF-740			740°C
LF-745			745°C

To investigate the decomposition of lithium ferrite into α-Fe_2O_3, as indicated by Pointon and Saull (1969) and Ridgley et al. (1970), sample LF-740 (after line profile analysis) was refired at 950°C in an oxygen atmosphere for 24 hours and then allowed to cool slowly to room temperature. This sample was designated LF-DEC.

<u>Group 2</u> In this group, nine lithium ferrite samples were quenched from 700°C, the lower limit of the transition region, after various times of annealing.

Sample Designation	Heat Treatment	Preset Time (mins.) (Annealing Time)
LF700,0		0
LF700,$\frac{1}{2}$	(i) 3 hrs at 600°C	$\frac{1}{2}$
LF700,1	(ii) 6hrs at 1150°C	1
LF700,5	(iii) cooled to 700°C	5
LF700,10	and held for a	10
LF700,20	preset time before	20
LF700,40	quenching in liquid	40
LF700,60	nitrogen	60
LF700,140		140

Special care was taken over the preparation of these samples to ensure that their stoichiometric conditions were equivalent,

(i) a prefiring mixture of approximately 200gms. was made up from which the sample aliquots of 6gms. were taken,

(ii) each pellet was formed at the same pressure (i.e. 3 tons/sq.in.),

(iii) the heating and cooling cycle of each sample followed the same pattern; monitoring of the temperature being carried out with the aid of a chromel-alumel thermocouple held against the face of each sample,

(iv) the same location in the hot zone of the furnace was used to ensure that the temperature distribution throughout each sample was similar.

Group 3 This group consisted of six lithium ferrite samples in which a small number of Cr^{3+} ions were substituted for Fe^{3+} ions (i.e. $LiFe_{5-x/4}Cr_{x/4}O_8, x \leqslant 2$). These samples were prepared simultaneously.

Sample Designation	Average No. of Cr^{3+} ions/unit cell	Heat Treatment
CR$\frac{1}{4}$	$\frac{1}{4}$	
CR$\frac{1}{2}$	$\frac{1}{2}$	(i) 3 hrs at 600°C
CR$\frac{3}{4}$	$\frac{3}{4}$	(ii) 6 hrs at 1150°C
CR1	1	(iii) cooled slowly to
CR1$\frac{1}{2}$	1$\frac{1}{2}$	room temperature
CR2	2	

A 'standard' sample of fully ordered unsubstituted lithium ferrite, designated LF-S, was also prepared. The heat treatment given to this sample was the same as that given to the chromium substituted samples.

Analysis of X-ray powder photographs

X-ray powder diffraction photographs of the products were indexed and the crystalline phases identified as lithium ferrite ($LiFe_5O_8$). In all the photographs, except those of the 'standard' sample LF-S and LF-DEC, the superlattice lines were diffuse and not observable at high angles whilst the lattice lines were well resolved and comparable with the lattice lines from the 'standard' sample LF-S. Further, the resolution of the lattice and superlattice lines from the 'standard' sample was comparable with the resolution of the diffraction lines from well crystallized specimens of $MgCr_2O_4$.

The photographs from samples LF735, LF740 and LF-DEC showed the presence of α-Fe_2O_3 although in the former two samples it was only possible to observe the strongest line associated with α-Fe_2O_3 (i.e.(104)line). Further discussion of the presence of α-Fe_2O_3 is deferred until Chapter 4. X-ray photographs from samples LF700,60 and LF700,140 contained very weak (220) and (440) lines due to an $FeAl_2O_4$ phase. This was attributed to packing the lithium ferrite pellets in alumina powder during preparation. Fortunately, the $FeAl_2O_4$ phase was identified only on the surface of the pellets as X-ray photographs of the interiors of the pellets gave no indication of the phase. No other impurity phases were observed.

It is also worth mentioning that attempts to produce disordered lithium ferrite were not successful. Even when samples were quenched from 300°C above the transition temperature it was still possible to observe the (210) superlattice line.

3.2 Diffractometer alignment and measurement procedure

The X-ray line profiles were measured with a Philips powder diffractometer (see Plate 3.1) which in a simple schematic form is represented by Fig.3.2. For a discussion of the principles and design of diffractometers the reader is referred to Klug and Alexander (1954), Wilson (1963b) or Parrish (1965). Besides the features illustrated in the above figures, the diffractometer system also included,

(i) facilities for automatic step-scanning across the line profiles,

(ii) standard counting equipment including pulse height analyser,

(iii) a printer and eight hole punch tape outputs to register measured intensity values.

The alignment of the X-ray beam and slit system was carried out according to the procedures described by Parrish (1965); single and double knife edges being used for 'zeroing' the

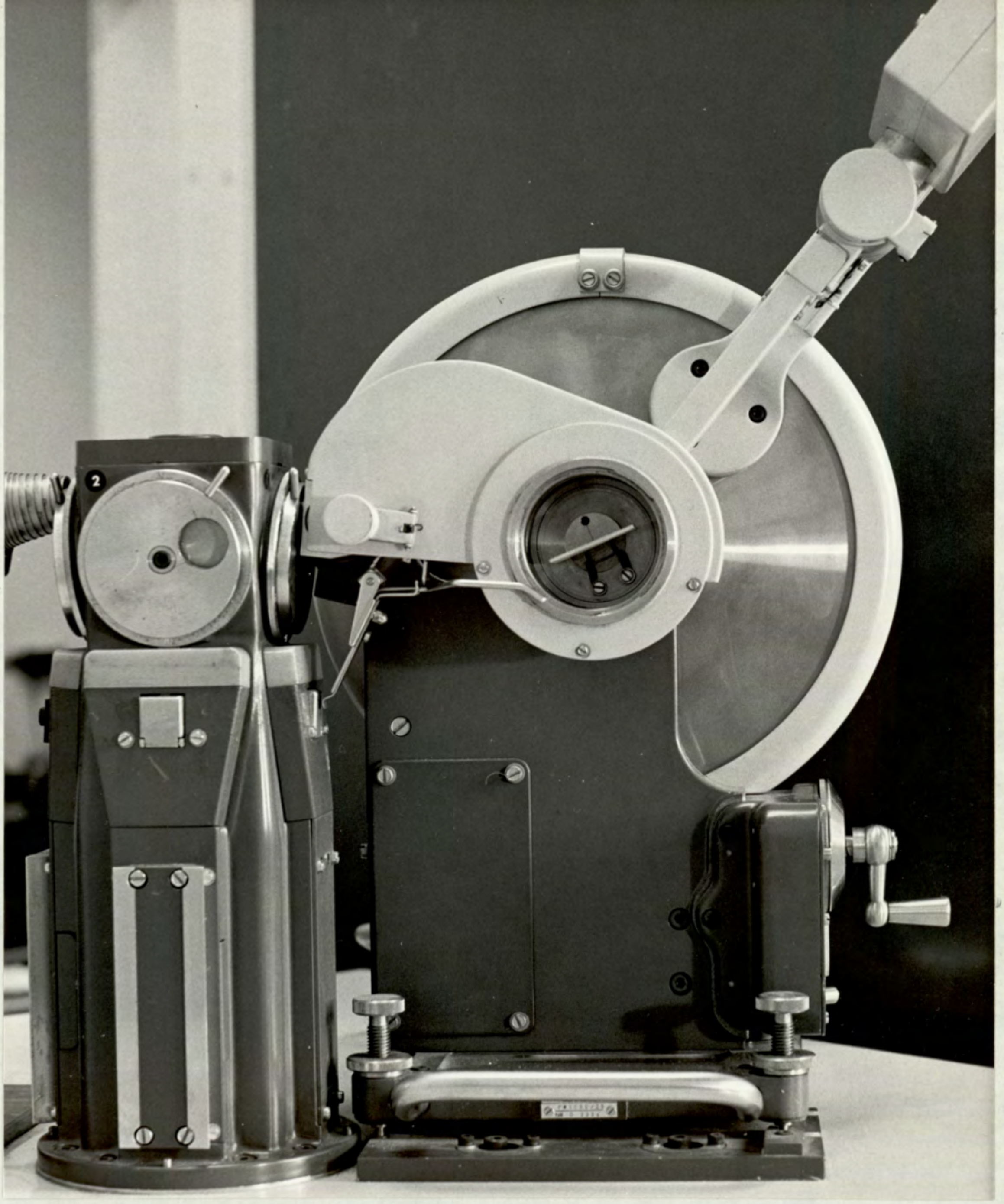

Plate 3.1 A Philips powder diffractometer (PW 1050).

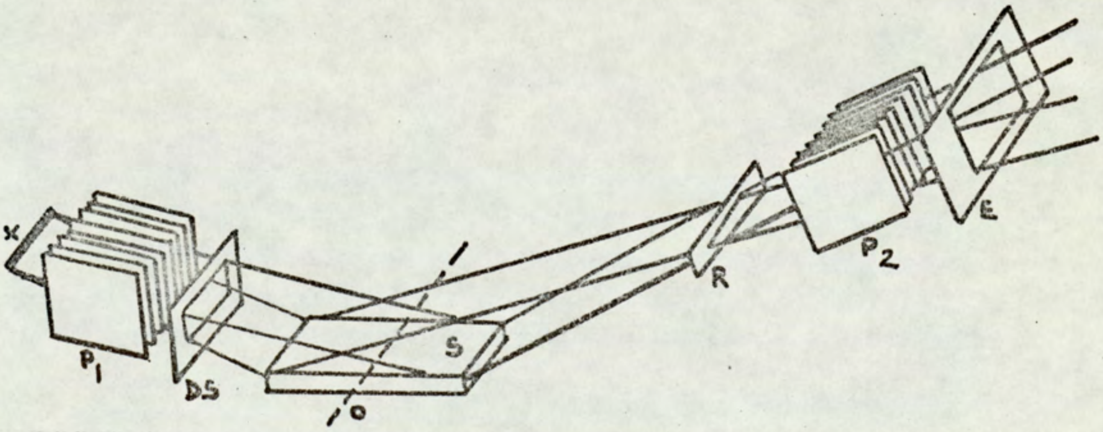

Fig.3.2 A typical powder diffractometer arrangement. X focal line of X-ray tube, P_1 and P_2 Soller slit assemblies, DS divergence slit, O goniometer axis of rotation, S powder sample, R receiving slit, E anti-scatter slit (after Parrish, 1965).

receiving slit and 2:1 setting, respectively. A discrepancy in the zero 2θ position, as estimated with the single knife edge in its normal and inverse positions, was attributed to a 0.025mm. displacement of the goniometer axis outside the focussing circle. The experimental conditions of the diffractometer system are given in Table 3.1.

During the optimisation of the pulse height analyser settings, using lithium ferrite as the specimen, it was found that approximately 80% of the background scatter comprised FeK radiation as a result of fluorescence from the interaction of the sample with the white radiation in the incident beam. Unfortunately, only 75% of the measured fluorescence could be eliminated by pulse height discrimination owing to overlap with the voltage pulses of the CrK radiation. A further reduction of the measured fluorescence was achieved when the two standard vanadium β- filters (i.e. CrKα intensity reduced by half) were placed between the counter and the sample as opposed to the manufacturer's arrangement of one filter before and one filter after the sample. The primary purpose of two filters however, was to completely eliminate the CrKβ diffraction lines which tended to coincide with the tails of lower order CrKα lines.

The intensity profiles were obtained by step-scanning procedures. For the measurement of the low angle lines from standard sample LF-S a step size of $0.01^{\circ}2\theta$ was used. The high angle lines from this sample and all the lines from the other samples were measured at $0.02^{\circ}2\theta$ intervals. For convenience purposes a fixed time counting scheme was adopted. To realise a statistical error of less than 5% of the measured integrated intensities a time of 200 secs/intensity measurement was found to be adequate for

Table 3.1 Experimental conditions of the diffractometer system (For a fuller description of what these conditions mean see Wilson 1963b)

Radiation	CrKα - vanadium β filter
X-ray tube supply	30kV,30mA.
Angle of take-off	6°
Divergence slit	1°
Size of X-ray source	1.6mms.by 12mms.
Sample size	2cms. x 1cm. x 0.2 cms.
Aperture of Sollerslits	2.25°
Receiving slit	0.1mm.
Source to sample distance	17.3cms.
Anti-scatter slits	1°
X-ray counter	Xenon proportional counter
Displacement of receiving slit from focussing circle	<1mm.
Inclination of specimen plane to goniometer axis	Unknown, but small
Angular mis-setting of 2:1 ratio	Unknown, but small
Displacement of goniometer outside focussing circle	0.025mms.
Angular mis-setting of receiving slit	Unknown, but small
Angular mis-setting of centroid of X-ray beam	Probably $<\frac{1}{4}^{\circ}$

most of the lattice lines and the stronger sharp superlattice lines. To obtain a similar accuracy for the intensity measurements from the broadened superlattice lines it was necessary to use longer counting times (e.g. 400 and 600 secs.). In the case of the chromium substituted sample CR2 a time of 1000 secs/intensity measurement was necessary as the superlattice lines were very weak and the background level very high owing to CrK fluorescent radiation.

Each sample prepared for the diffractometer was ground, sieved and microscopically examined until the average particle size was between 5 and 10 microns, at which point the resulting powder was manually pressed into a sample holder. Great care was taken to ensure that the surface of the sample was flat. Negligible preferred orientation was believed to be present as tests with powder discs formed at pressures ranging from 0 to 20tons/sq.in. revealed negligible changes in the relative intensities of the diffraction lines.

To help decide the range over which to step-scan, a preliminary chart recording of each profile was made. For most of the sharp lines it was found that a range of scan of approximately $\pm 2^{\circ} 2\theta$ about the centroid was sufficient to encompass the statistically acceptable regions of the profile tails. On the basis of step scanning measurements carried out on the first sample prepared (i.e. LF740) the policy was adopted with the broadened lines of scanning over a range of at least five half widths of each profile; a preliminary estimate of the half width being made from the chart recording.

In all, approximately 200 line profiles were measured of which 80 were broadened superlattice lines. The large proportion of lattice lines in this group reflects, primarily, the measurements from the Group 1 samples as these samples were used not only for investigating the anti-phase domains, but also for determining the average crystal structure, the lattice parameters and the stoichiometry of lithium ferrite as well as the instrumental contribution to the line breadths of the broadened superlattice lines. In the cases of the annealed and chromium substituted samples the emphasis was placed on measuring superlattice lines although for the latter samples some of the stronger lattice lines were measured for the purpose of determining accurate lattice parameters.

To illustrate the extent of the broadening of the superlattice lines and also to give a general impression of the accuracy of the data, a selection of weak and strong, lattice and superlattice line profiles from sample LF725 is given in Figs.3.3(a) to 3.3(e). Sample LF725 was chosen for this illustration because the extent of the line broadening associated with its superlattice lines was intermediate to the range of broadening observed.

In the following sections of this chapter an account is given of the ways in which the positions, breadths and integrated intensities of the line profiles were estimated. In each case systematic errors are discussed together with the correction procedures employed. Most of the numerical work involved in determining the line profile parameters was performed on the I.C.L. 1905 computer at Aston university.

3.3 Determination of line profile positions and lattice parameters

In the present analysis the centroid (Pike and Wilson, 1959) is used as the measure of line position. This measure has the advantages of being statistically accurate and easily corrected for the effects of instrumental aberrations (Wilson, 1963b). To

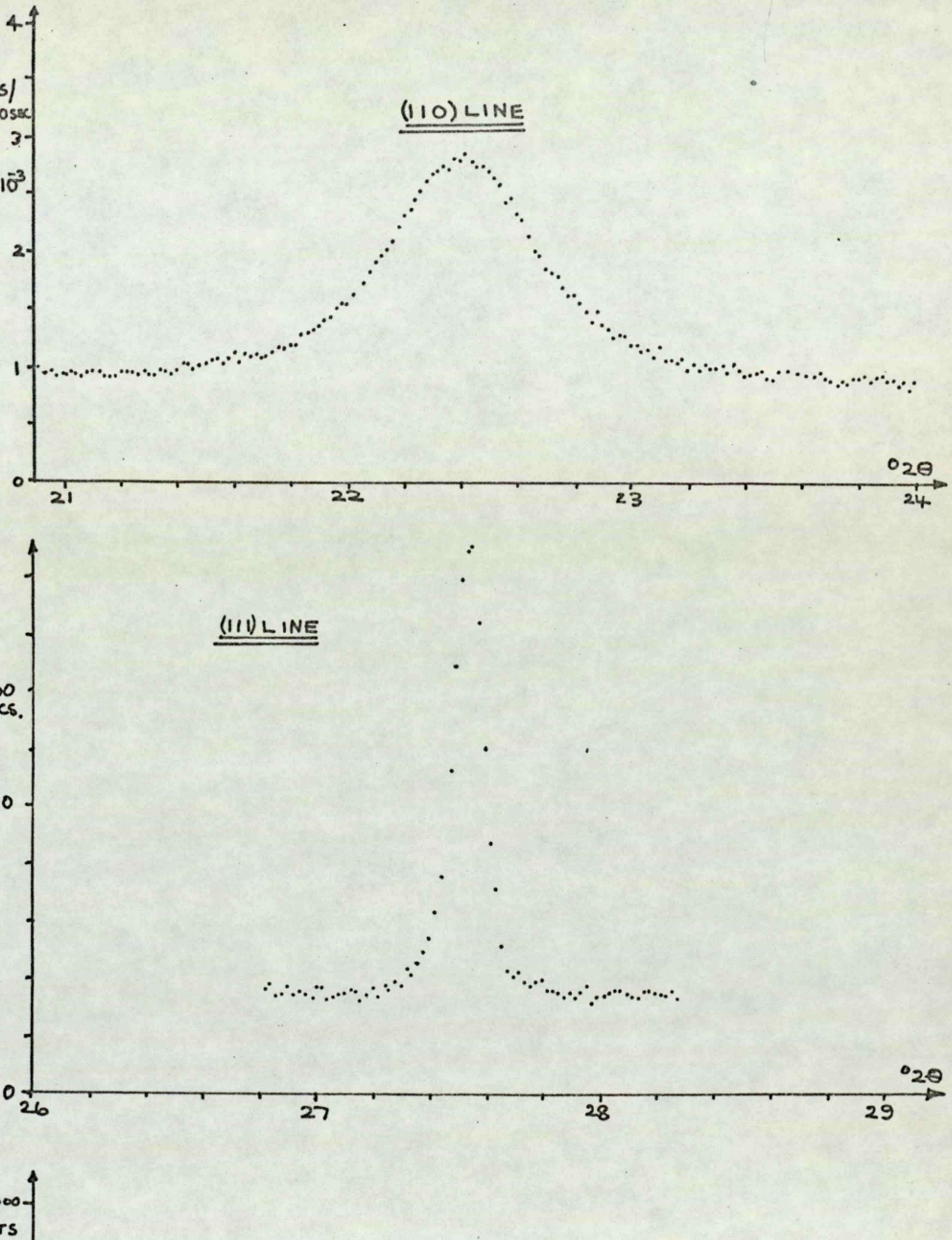

Fig.3.3(a) Intensity profiles from the lithium ferrite sample LF725.

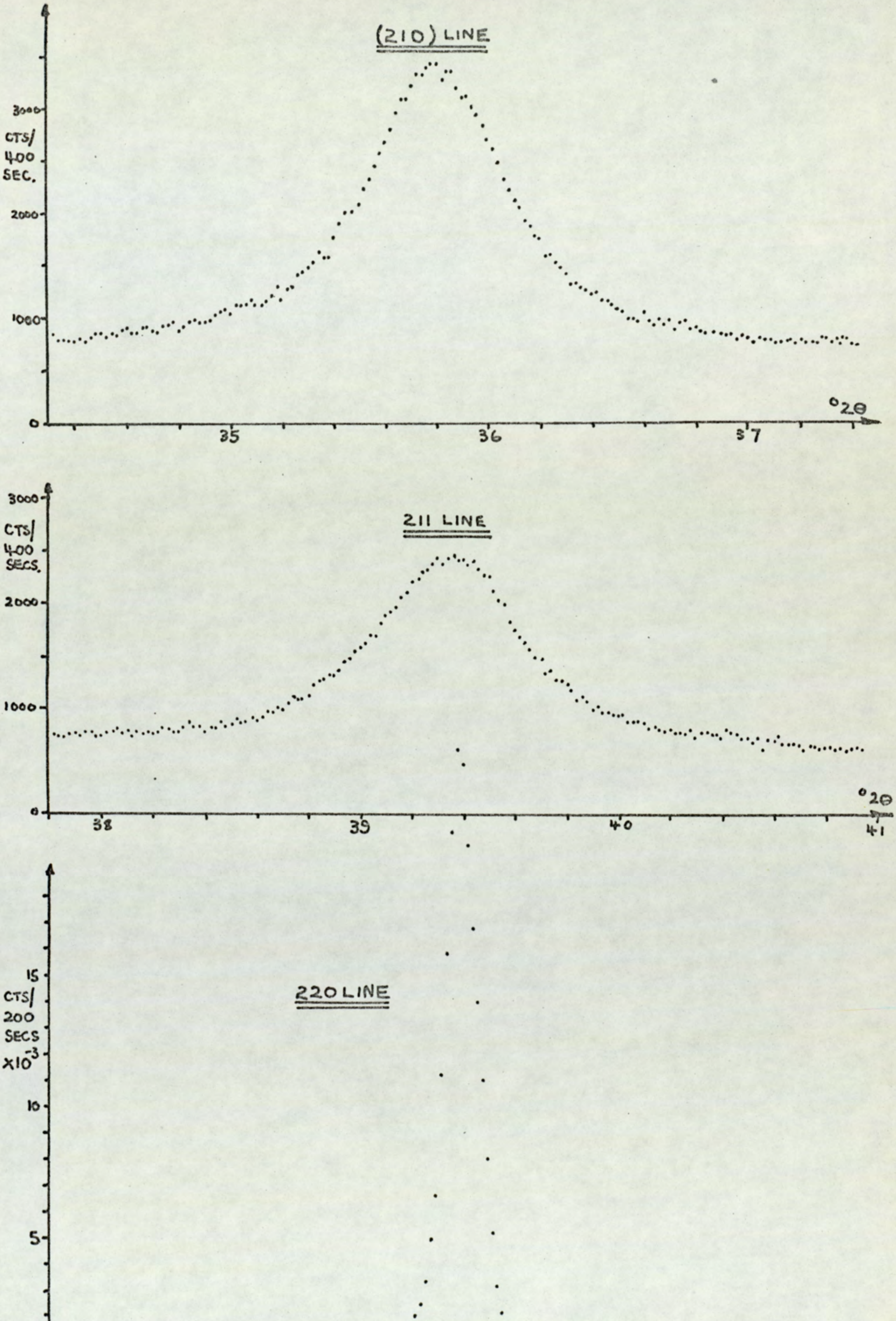

Fig.3.3(b) Intensity profiles from the lithium ferrite sample LF725

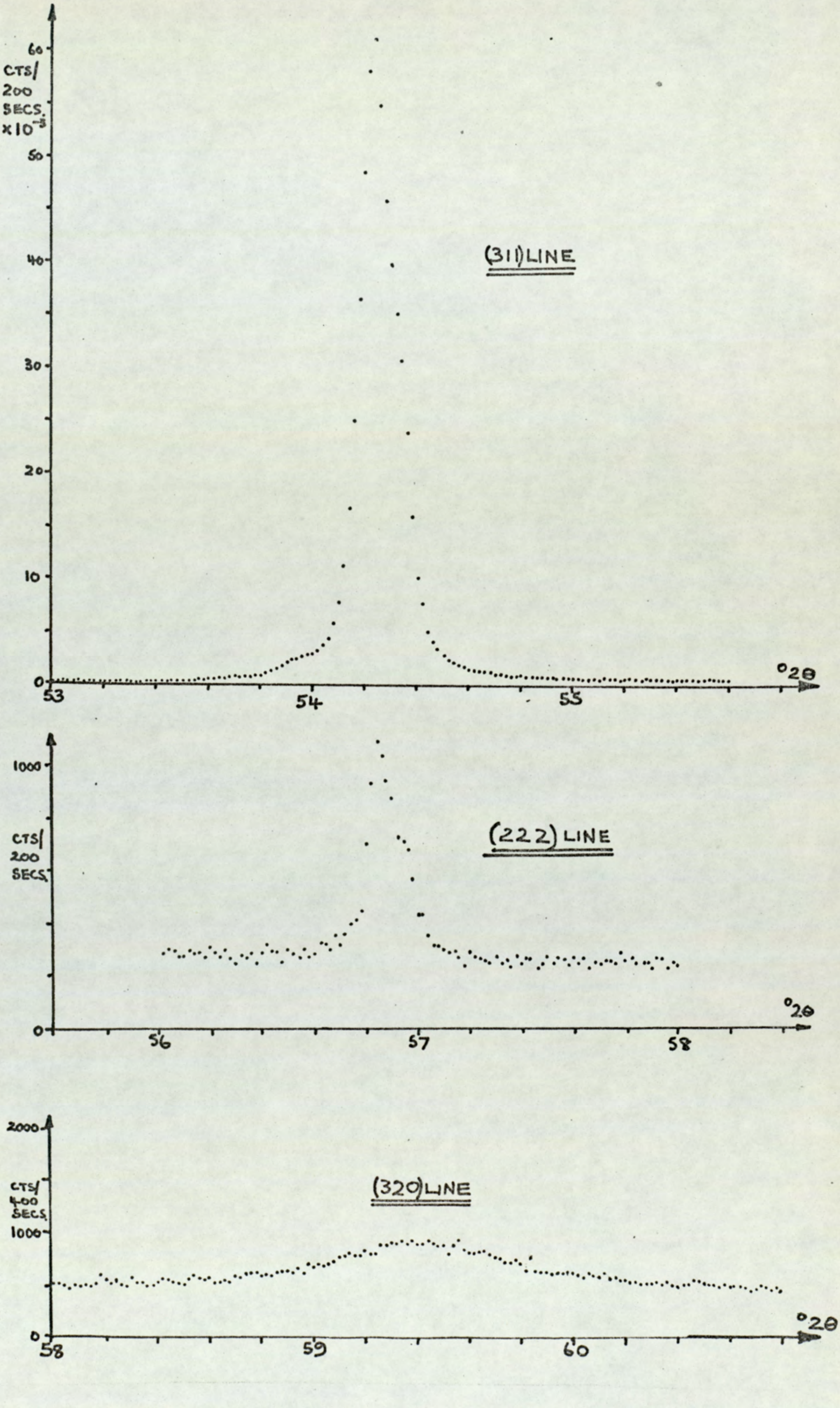

Fig.3.3(c) Intensity profiles from the lithium ferrite sample LF725

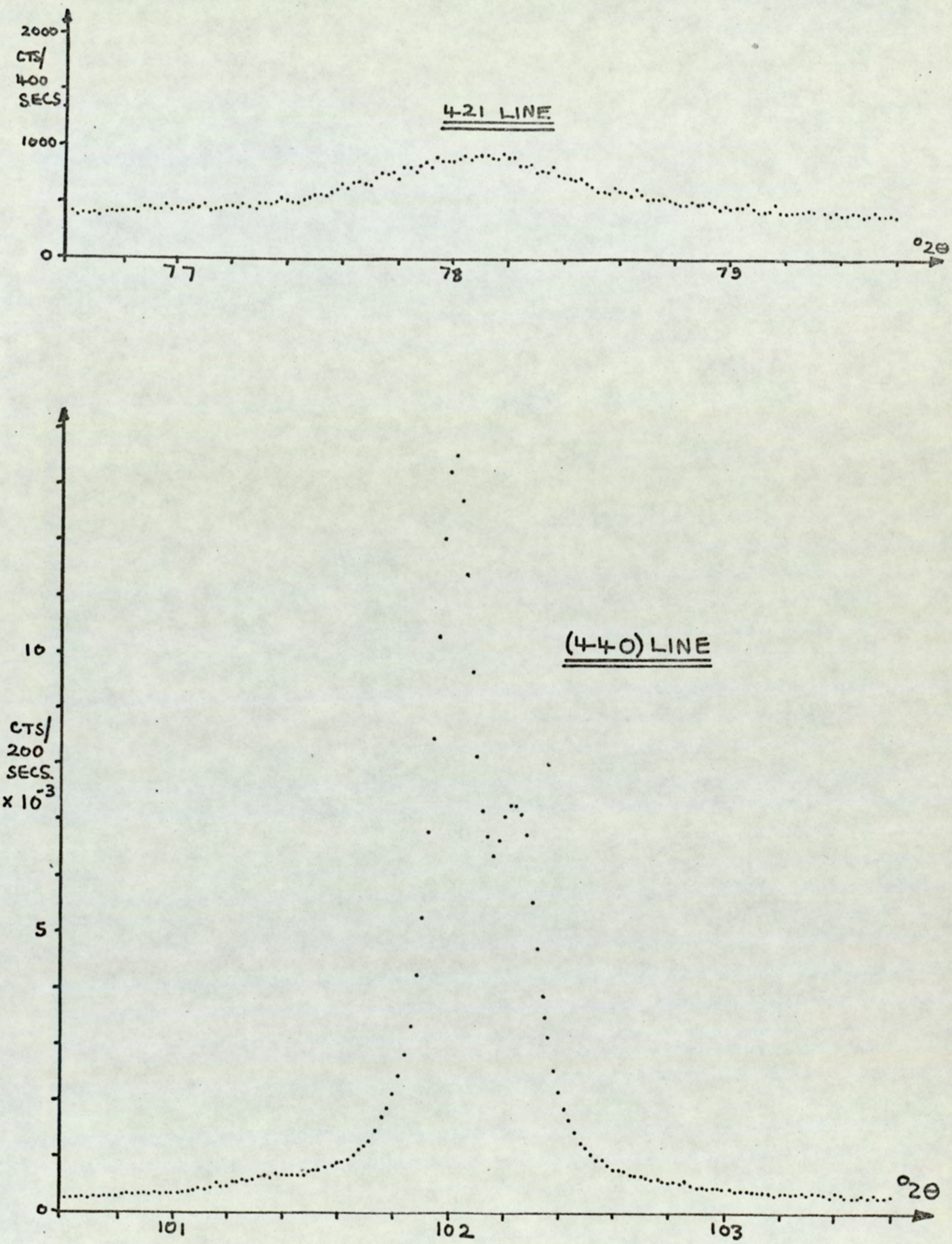

Fig.3.3(d) Intensity profiles from the lithium ferrite sample LF725

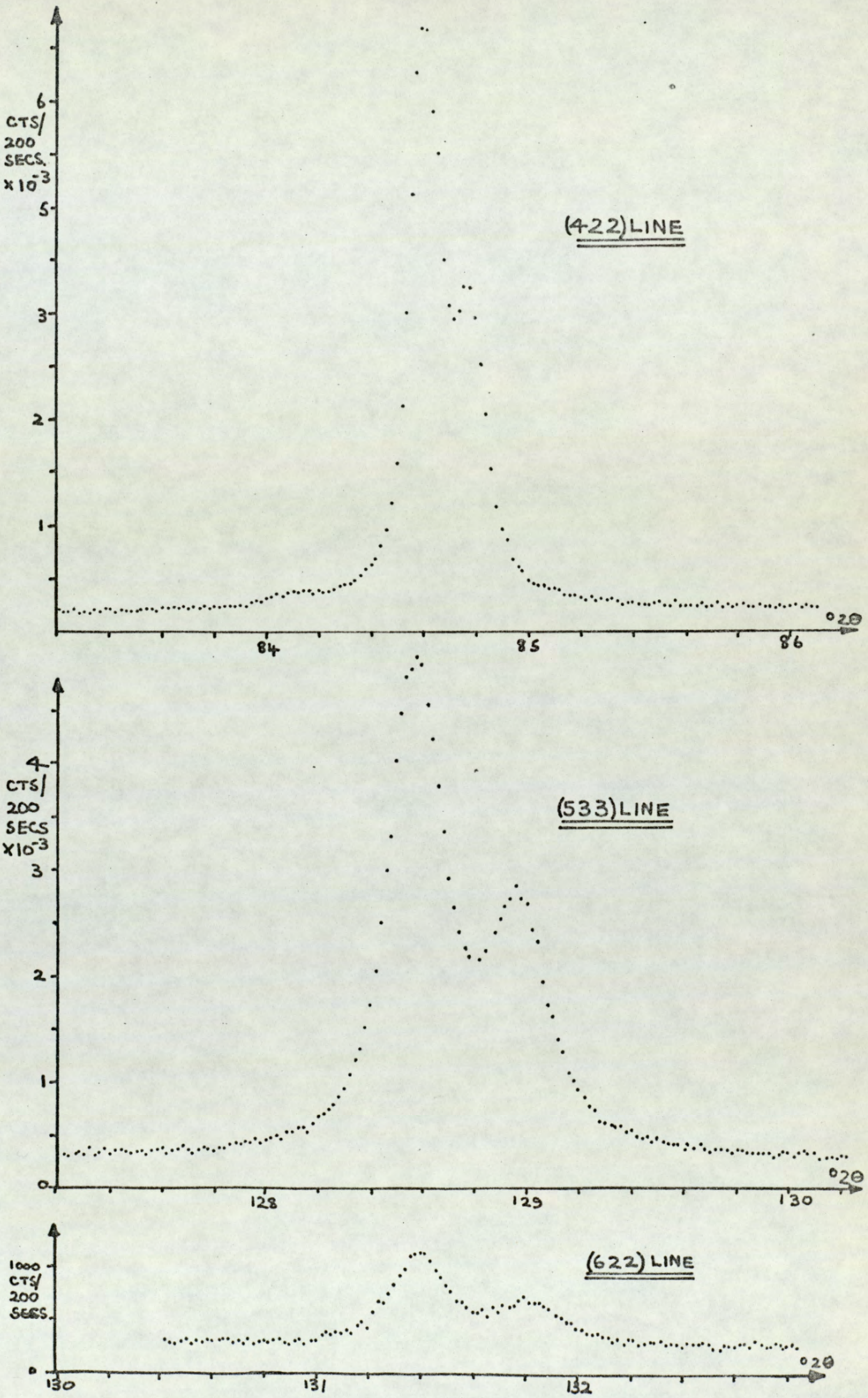

Fig.3.3(e) Intensity profiles from the lithium ferrite sample LF725

determine lattice parameters from centroid values however, it is necessary to know the centroid wavelength, λ_o, of the particular radiation being used. In the case of CrKα radiation this value is unknown and as such it was necessary to resort to the approximate value given by the weighted mean of the Kα_1 and Kα_2 wavelengths,

i.e. $$\lambda_o = (\lambda_{K\alpha_1} + C.\lambda_{K\alpha_2})/(1 + C)$$

$$\lambda_o = 2.29095\text{Å}.$$

where C, the ratio of the intensities Kα_2/Kα_1, $\lambda_{K\alpha_1}$ and $\lambda_{K\alpha_2}$ were taken from the International Tables for X-ray Crystallography III (1962).

Unfortunately, the above value of λ_o approximates to the centroid wavelength of a CrKα emission profile which is free of the Kα satellite group of lines and the discontinuity resulting from the absorption edge of the β filter. Nevertheless, Pike and Wilson (1959) have demonstrated, using an experimentally measured profile (CuKα radiation), that when the centroid is determined as a function of the range of truncation in a manner similar to variance, the subsequent centroid-range characteristic exhibits a plateau prior to the range corresponding to the satellite lines which would indicate that the weighted mean wavelength is probably appropriate to that region. A similar behaviour was also observed in the present analysis of centroid-range characteristics, but only for high angle lines ($2\theta > 100^{o}$).

3.3.1 Centroid analysis of simulated emission profiles

To gauge the influence of the satellite lines a pair of CrKα

emission profiles was simulated, one of which contained a satellite distribution, by Cauchy curves from which the centroid wavelengths, $\lambda_c(\Delta\lambda)$, were calculated as a function of the range of truncation $\Delta\lambda$ according to the equation

$$\lambda_c(\Delta\lambda) = \frac{\int_{-\frac{\Delta\lambda}{2}}^{+\frac{\Delta\lambda}{2}}(\lambda-\lambda_0)f(\lambda-\lambda_0)\,d(\lambda-\lambda_0)}{\int_{-\infty}^{\infty}f(\lambda-\lambda_0)\,d(\lambda-\lambda_0)}$$

where $f(\lambda - \lambda_0)$ represents the intensity distribution across either of the emission profiles about the weighted mean wavelength λ_0 of the $K\alpha_1$ and $K\alpha_2$ components. The results of these calculations, presented in Fig.3.4, assumed a description of the $CrK\alpha$ emission profile approximating to that given by Parratt (1936) (i.e. a $K\alpha_1$ - $K\alpha_2$ peak separation of 3.9 MÅ, an integrated intensity ratio $K\alpha_2/K\alpha_1$ of 0.5, half widths of 0.80MÅ and 0.90MÅ for $K\alpha_1$ and $K\alpha_2$ components, respectively, and a satellite distribution, comprising 1.1% of the total integrated intensity of the emission profile, represented by two Cauchy profiles each with a half width of 1MÅ and separated from λ_0 by 11.7MÅ and 13.3MÅ). From Fig.3.4 it is clear that the presence of the satellite lines in experimental profiles could easily prove to be troublesome in the estimation of reliable lattice parameters especially when low angle diffraction lines are employed.

In order to reduce the uncertainty in centroid determination brought about by the satellite lines a correction was made for their effect by subtracting an experimentally determined satellite distribution from the line profiles before proceeding with analysis. Before describing the procedure used to determine this distribution it is necessary to describe the procedures used to generate the

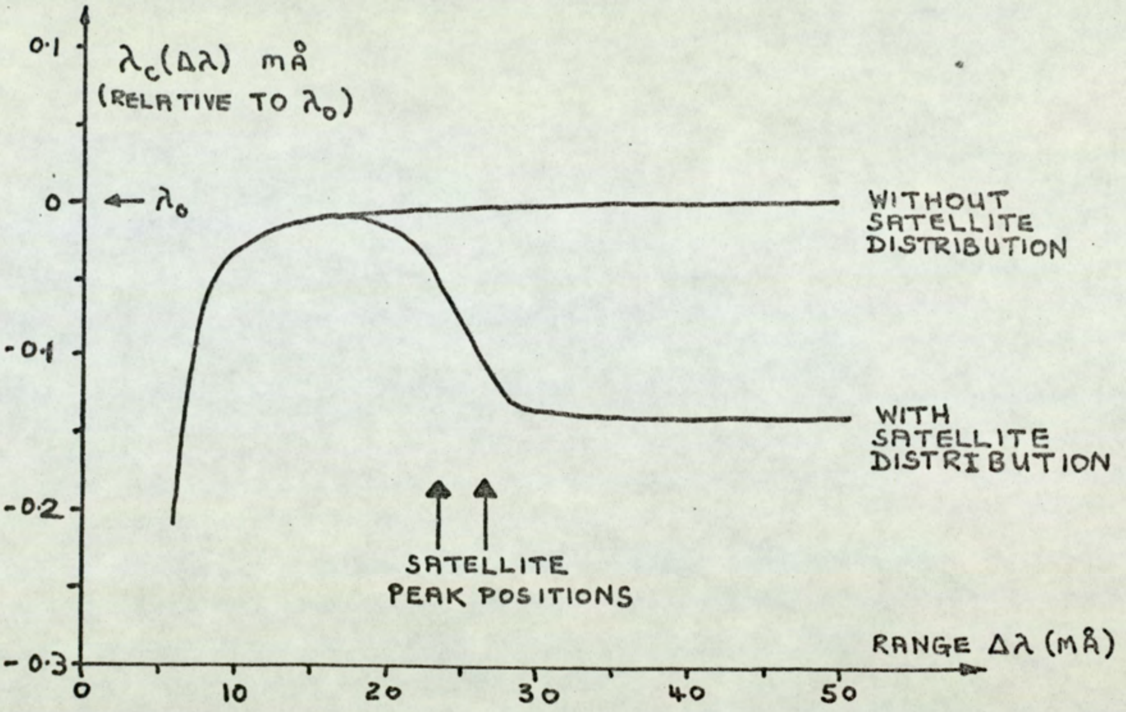

Fig.3.4 Centroid wavelength as a function of the range of integration - simulated CrKα emission profiles.

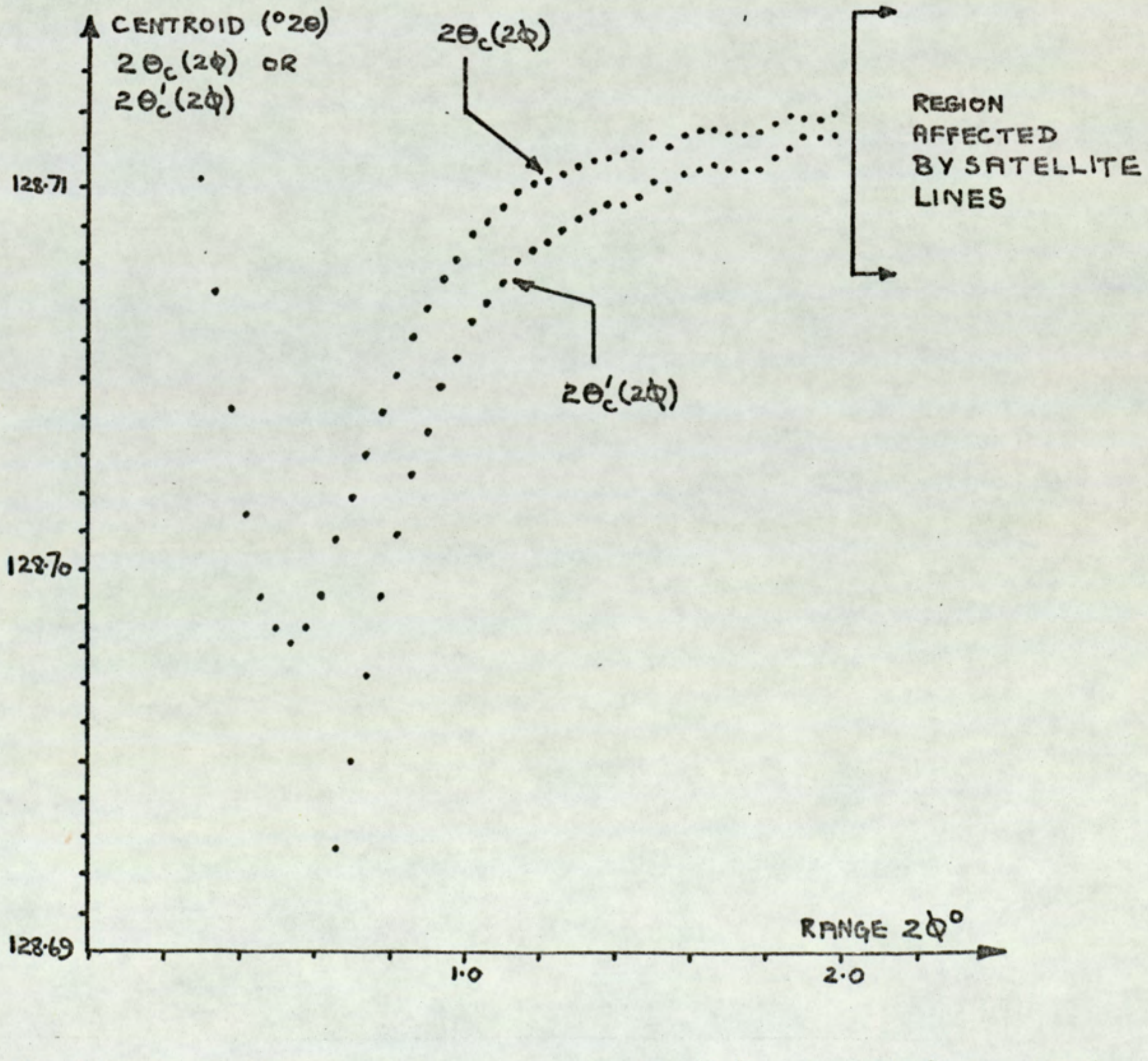

Fig.3.5 Centroid-range characteristics $2\theta_c(2\phi)$ and $2\theta_c'(2\phi)$ for (533) line from sample LF725.

centroid-range characteristics of the experimental profiles.

3.3.2 Determination of experimental centroid-range characteristics

First of all the observed intensities $G(2\theta_i)$ at each angle $2\theta_i$ were corrected for the background contribution. The mean background level was determined by the variance method of Langford and Wilson (1963)(discussed in section 3.5) whilst the background slope was estimated by inspection of the intensity levels at large ranges either side of the line profile. When 'weak' overlapping on either of the profile tails was evident, a correction was made for the contribution of the offending line profile. This was achieved by assuming the intensity of an offending line $H(2\theta_j)$ depreciated as $A/(2\theta_j - \langle 2\theta \rangle)^2$ (Wilson, 1965) where A is a constant and $\langle 2\theta \rangle$ is the centroid of the offending line which was estimated by inspection, so that by plotting $H(2\theta_j)$ against $(2\theta_j - \langle 2\theta \rangle)^{-2}$ in that part of the offending profile tail least affected by overlapping, it was possible to estimate A and subtract off the overlap contribution to the profile under examination. Subsequent to background correction an approximate overall centroid of the profile, 2θmax, was computed and the nearest angle of measurement, $2\theta_k$ say, to 2θmax taken as an origin. The centroid was then calculated as a function of the range of truncation $-\phi$ to $+\phi$ according to the following,

$$2\theta_c(2\phi) = 2\theta_k + \frac{\Delta 2\theta}{I_T} \sum_{2\theta_i = 2\theta_k - \phi}^{2\theta_k + \phi} (2\theta_i - 2\theta_k) I(2\theta_i)$$

where $\Delta 2\theta$ is the step size between each intensity measurement, $I(2\theta_i)$ is the intensity at $2\theta_i$ corrected for the background contribution, and I_T is the total integrated intensity which was determined independently from the slope of the function (truncated integrated intensity X range) against range (see section 3.5). This definition of $2\theta_c(2\phi)$ was used because it was found to converge slightly more rapidly to the plateau region than the alternative definition based on the use of the truncated integrated intensity as a normalising factor (Pike and Wilson, 1959),

$$\text{i.e. } 2\theta_c'(2\phi) = 2\theta_k + \frac{\displaystyle\sum_{2\theta_i=2\theta_k-\phi}^{2\theta_k+\phi}(2\theta_i-2\theta_k)I(2\theta_i)}{\displaystyle\sum_{2\theta_i=2\theta_k-\phi}^{2\theta_k+\phi}I(2\theta_i)}$$

This is demonstrated in Fig.3.5 where the $2\theta_c(2\phi)$ and $2\theta_c'(2\phi)$ characteristics of the high angle (533) profile from sample LF725 (this profile is given in Fig.3.3) are plotted as a function of 2ϕ.

Estimates were also made of the statistical error of each value of $2\theta_c(2\phi)$ using the equation for the standard error, $\sigma(2\theta_c(2\phi))$, given by Wilson (1967),

$$\text{i.e. } \sigma(2\theta_c(2\phi)) = \frac{\left[(\Delta 2\theta)^2\sum_i(2\theta_i-2\theta_k)^2G(2\theta_i) + (2\phi)^4\cdot\left(\sigma^2(B(2\theta_k+\phi)+\sigma^2(B(2\theta_k-\phi)))/144\right]^{\frac{1}{2}}}{I_T}$$

where $\sigma^2(B(2\theta_k + \phi))$ and $\sigma^2(B(2\theta_k - \phi))$ are the mean square errors of the estimated background levels at $2\theta_k + \phi$ and $2\theta_k - \phi$ which, for convenience, were assumed to be equal to the estimated background levels at those angles in accordance with a Poisson distribution of measured intensities. It is worth remarking that the standard error of $2\theta_c(2\phi)$ increases with the range of observation 2ϕ and as such it is advantageous to use as short a range as is consistent with including the essential features of the profile. For the well-resolved low angle lines from lithium ferrite, such as the (220) and (311) lines, $\sigma(2\theta_c(2\phi)) \simeq 10^{-4}\,{}^\circ 2\theta$ in the 'plateau region' of 2ϕ. Even for the weak (622) line at $2\theta \simeq 132^\circ$ the value of $\sigma(2\theta_c(2\phi))$ was always less than $0.01^\circ 2\theta$ at $2\phi = 2.5^\circ$ (i.e. satellite range).

3.3.3 Determination of the satellite distribution.

To provide initial conditions on which to base a later refinement, approximate values for the peak position of the CrKα satellite group relative to the K$\alpha_1\alpha_2$ centroid and its relative contribution to the total integrated intensity were estimated, using the (400) line from a single crystal of sodium chloride (see Fig.3.6), as 12.8 milliangstroms and 1.4%, respectively. In obtaining these values it was assumed that the intensity variation in the tails of the K$\alpha_1\alpha_2$ profile alone is approximately symmetrical about the centroid inside the range of the absorption edge, so that the intensity on the high angle side of the profile could be subtracted from the low angle side leaving the satellite distribution as a residual. On the basis of work on simulated Kα doublets it was calculated that the error introduced into the estimated integrated intensity of the satellite lines by making this assumption is not more than 10%.

Refinement of the approximate satellite parameters was achieved with the aid of the centroid-range characteristics of the (440) lines from the lithium ferrite samples LF725 and LF735. Firstly, it was assumed that the centroid-range characteristic of a K$\alpha_1\alpha_2$ profile alone is reasonably range independant and not

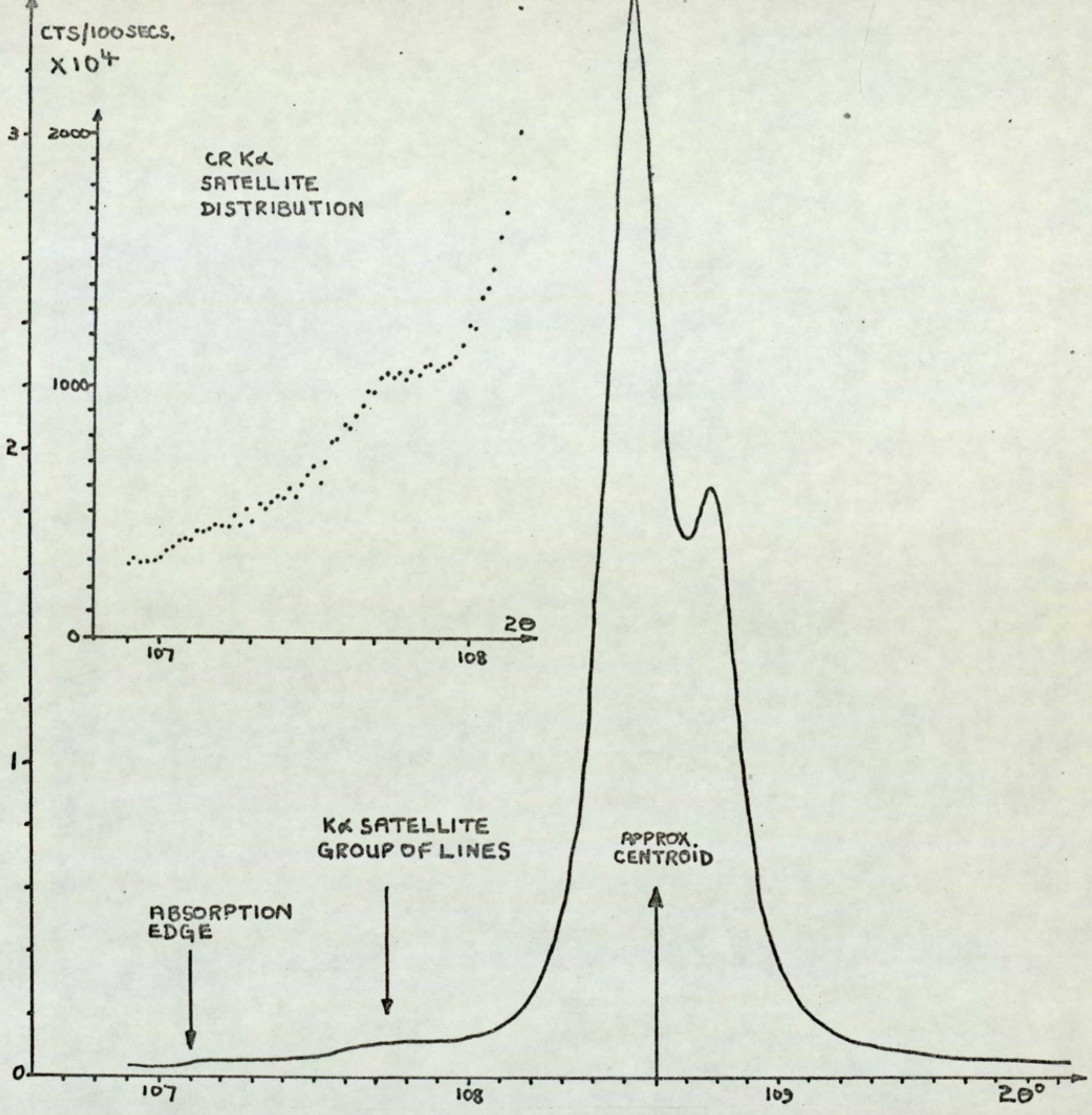

Fig.3.6 (400) line from a single crystal of NaCl

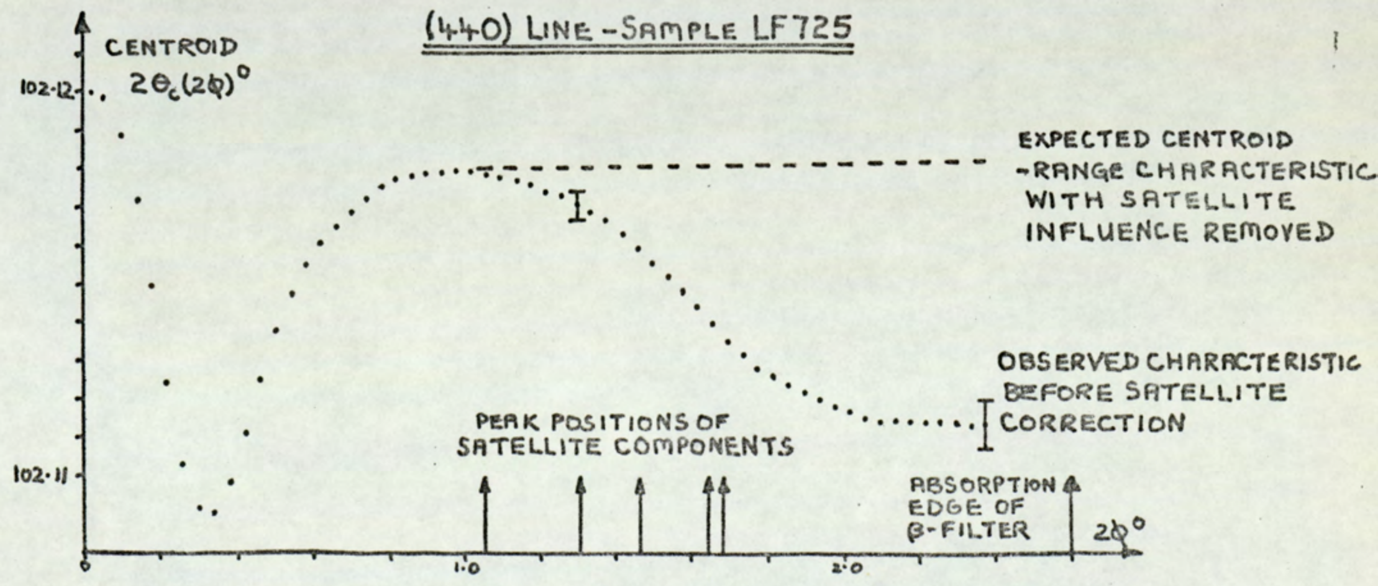

Fig.3.7 Estimation of centroid-range characteristic corrected for the influence of satellite lines.

decreasing in the range beyond the 'plateau region' (see Fig.3.7), as observed with the simulated emission profiles and as expected theoretically (Wilson 1962b), so that the rate of change of the observed characteristics $2\theta_c(2\phi)$ with range 2ϕ may be attributed to the satellite distribution $P(\phi)$ as follows:-

$$\frac{d(2\theta_c(2\phi))}{d(2\phi)} = -\frac{\phi.P(\phi)}{I_T}$$

The satellite intensity distribution was assumed to arise from five Cauchy profiles, representing the five components of the satellite group (Parratt, 1936). Refinement therefore, consisted of adjusting the parameters defining the Cauchy profiles by trial and error until the overall distribution fitted reasonably well to the $P(\phi)$ distributions estimated from the variations of $d(2\theta_c(2\phi))/d(2\phi)$. The parameters obtained from this procedure are given in table 3.2. The (440) line was chosen for this analysis because it is well resolved and exhibits a 'plateau region' of approximately $0.2^\circ 2\phi$ on which to base the corrected $2\theta_c(2\phi)$ variation. Also the effect of errors in the background slopes was small as tests with badly mis-set but acceptable background slopes showed that the centroids never changed by more than $0.0005^\circ 2\theta$ for a range $2\phi = 1.5^\circ$.

Table 3.2 Parameters of Optimized Satellite Distribution

Relative Integrated Intensity of Satellite Group to $K\alpha$ group 1.3%

Half Width of Component Satellites 3MÅ

% contribution of components to satellite group	2	20	39	31	8
Displacement, in MÅ, of components from $K\alpha_1\alpha_2$ centroid	-8.60	-10.60	-11.90	-13.40	-13.70

The optimized half widths, relative to the measured $K\alpha_1$ or $K\alpha_2$ half widths, and distribution of the satellite components agreed approximately with Parratt's values. The discrepancy between the present value of 1.3% for the relative integrated intensity of the satellites and his value of 0.9% is attributed to the different methods of correcting for the $K\alpha_1\alpha_2$ tail. In Parratt's graphical data the satellite intensity decreases to zero in approximately two overall half widths which suggests that some degree of overestimation was made of the level of the $K\alpha_1\alpha_2$ tail. Support for the present satellite distribution was given by the centroid-range characteristics of the (311) and (440) lines from samples other than LF725 and LF735. When corrected with the optimised distribution these characteristics were reasonably range independent beyond the 'plateau region' (see Fig.3.8).

The procedure was adopted therefore, of correcting all the experimental profiles with negligible diffraction broadening using the satellite parameters given in Table 3.2 with approximate integrated intensity values and centroid values being used for the purposes of

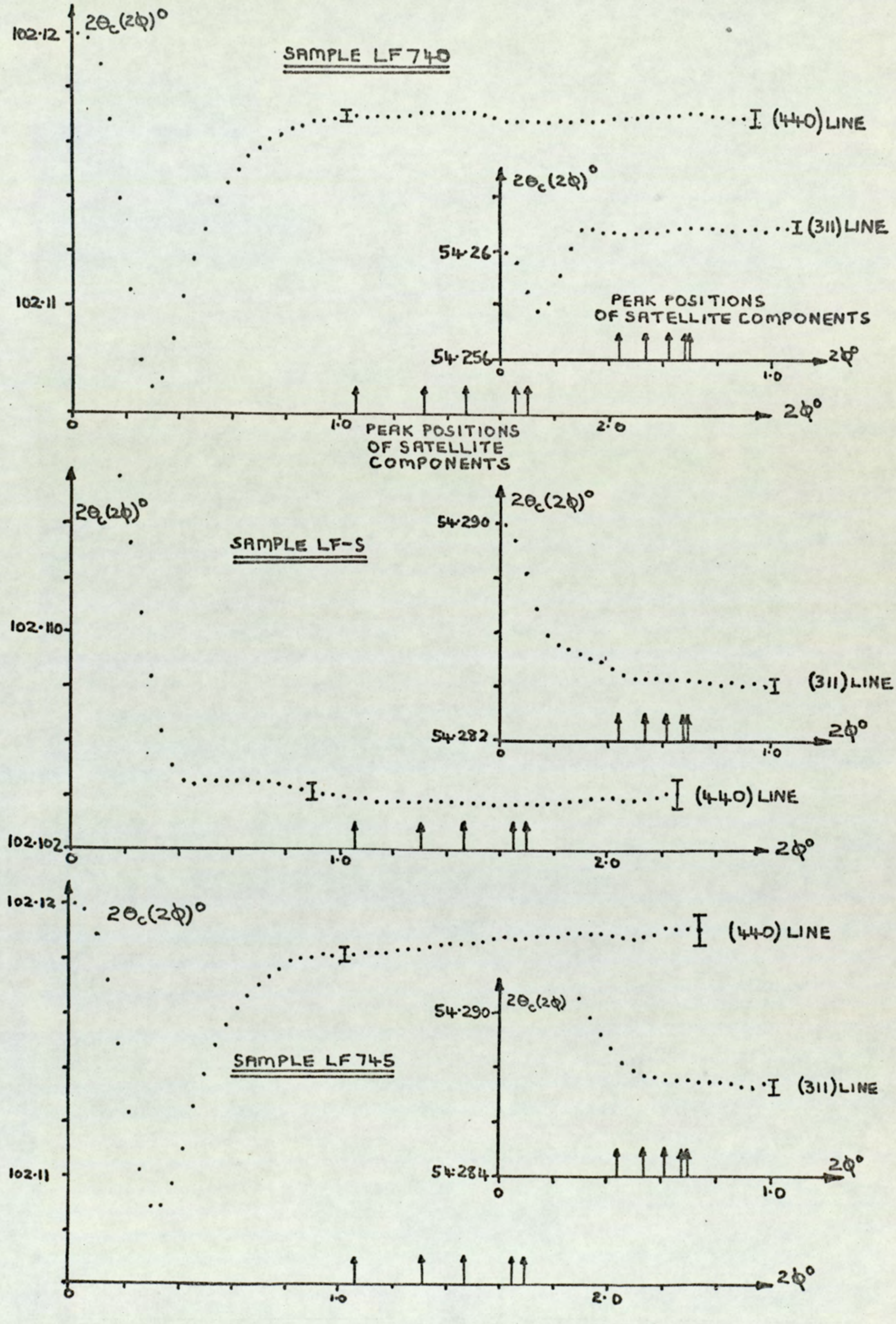

Fig.3.8 Centroid-range characteristics corrected for the influence of the satellite distribution.

scaling and locating the satellite intensity distribution. To modify the satellite distribution to the cases of profiles containing diffraction broadening, the half width of each Cauchy component was increased by the same value as the estimated increase in the $K\alpha_1\alpha_2$ half width.

3.3.4 Determination of lattice parameters

Each centroid value chosen for this purpose was taken to be the average value of $2\theta_c(2\phi)$ over the region in 2ϕ corresponding to the peak positions of the satellite components. This choice was based on the results from the simulated profiles which show that this region corresponds accurately to the weighted mean wavelength λ_o. Also, it was necessary to have a region which could be reproduceably determined and which was at low 2ϕ values to minimise statistical errors.

The procedure used to determine the lattice parameters accurately followed closely that suggested by Wilson (1963b). In broad outline this consisted of,

(i) subtracting calculated centroid shifts due to various instrumental and physical aberrations from the estimated centroid values.

(ii) calculating apparent values for the lattice parameter (a_{meas}) from each corrected centroid value, i.e.

$$a_{meas} = \frac{\lambda_o(h^2 + k^2 + l^2)^{\frac{1}{2}}}{2\sin\theta_c}$$

(iii) plotting a_{meas} against an appropriate linear extrapolation function $f(\theta)$ and determining the intercept a_o corresponding to $\theta = 90^o$. This value was assumed to be the fully corrected lattice parameter.

Centroid shifts resulting from the following instrumental and physical aberrations were calculated:

(a) axial divergence,

(b) specimen transparency (thick specimen),

(c) flat specimen error,

(d) refraction (wavelength effect),

(e) Lorentz-polarisation factor,

(f) differential wavelength absorption of the X-ray beam in its path from the X-ray source to the counter,

(g) dispersion.

The theoretical expressions used to calculate these shifts were taken from Wilson (1963b) with the geometric parameters of the diffractometer system given in Table 3.1 and a value for W_λ, the mean square breadth of the emission profile, equal to $5 \times 10^{-6} (\text{Å})^2$ being used for their evaluation. For the calculation of the shift due to specimen transparency the density of each lithium ferrite powder sample was measured. On average, this was found to be approximately 0.40(± 0.05) of the bulk density (4.76gm/cc.) from which the linear absorption coefficient was estimated as 155cms^{-1} for CrKα radiation. The result of these calculations is given in Fig.3.9 where the total centroid adjustment $\delta(2\theta)$ due to the above aberrations is plotted as a function of 2θ.

The measured values of the lattice parameter are related to a_o, the fully corrected lattice parameter, through

$$a_{meas} = a_o\left(1 - \frac{\cot\theta}{2} \cdot \delta(2\theta)\right)$$

where $\delta(2\theta)$ represents the residual centroid displacement resulting from incomplete correction. As most of the instrumental aberrations

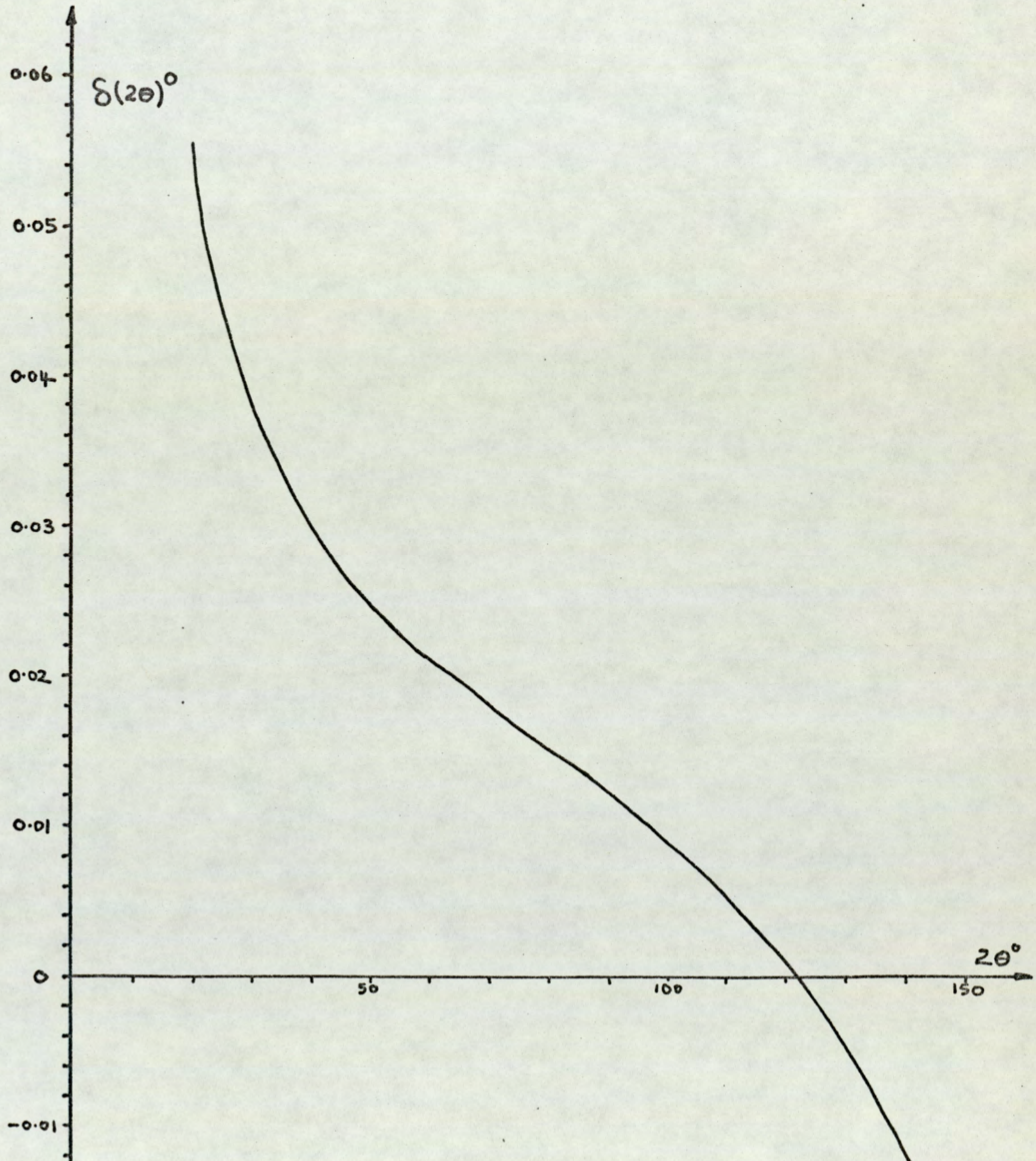

Fig.3.9. Centroid correction for instrumental and physical aberrations (to be added to measured centroid).

result in centroid shifts which are proportional to either $\cos\theta$ or $\cot\theta$ (Wilson 1963b) the appropriate linear extrapolation function $f(\theta)$ should be $\cos\theta\cot\theta$, $\cot^2\theta$ or some intermediate function. The policy was adopted therefore, of plotting the measured lattice parameters against $\cot^2\theta$ and $\cos\theta\cot\theta$ with the corrected lattice parameter a_o being determined from the extrapolation plot closest to a straight line. Examples of the extrapolation plots for two of the lithium ferrite samples are given in Fig.3.10 where in one case $\cot^2\theta$ gives linearity and in the other $\cos\theta\cot\theta$ gives linearity.

3.4 Determination of line breadths

I Fourier transform method

Fourier transform analysis was carried out by the method of Stokes (1948). As this method of analysis is extremely susceptible to the effects of systematic errors and as a great deal of the information concerning the anti-phase domains may be obtained more reliably from variance analysis ,only the most intense broadened superlattice line, namely the (210) line, was considered for analysis with the (210) line from the standard sample LF-S being used to correct for instrumental broadening. Further analysis was also undertaken to understand and, in some cases, minimise the effects of the following errors:-

(i) Truncation of the line profiles,

(ii) Error in the choice of the origins of broadened and sharp superlattice lines,

(iii) Error in the mean background level,

(iv) Statistical errors,

(v) Deviations from the convolution principle.

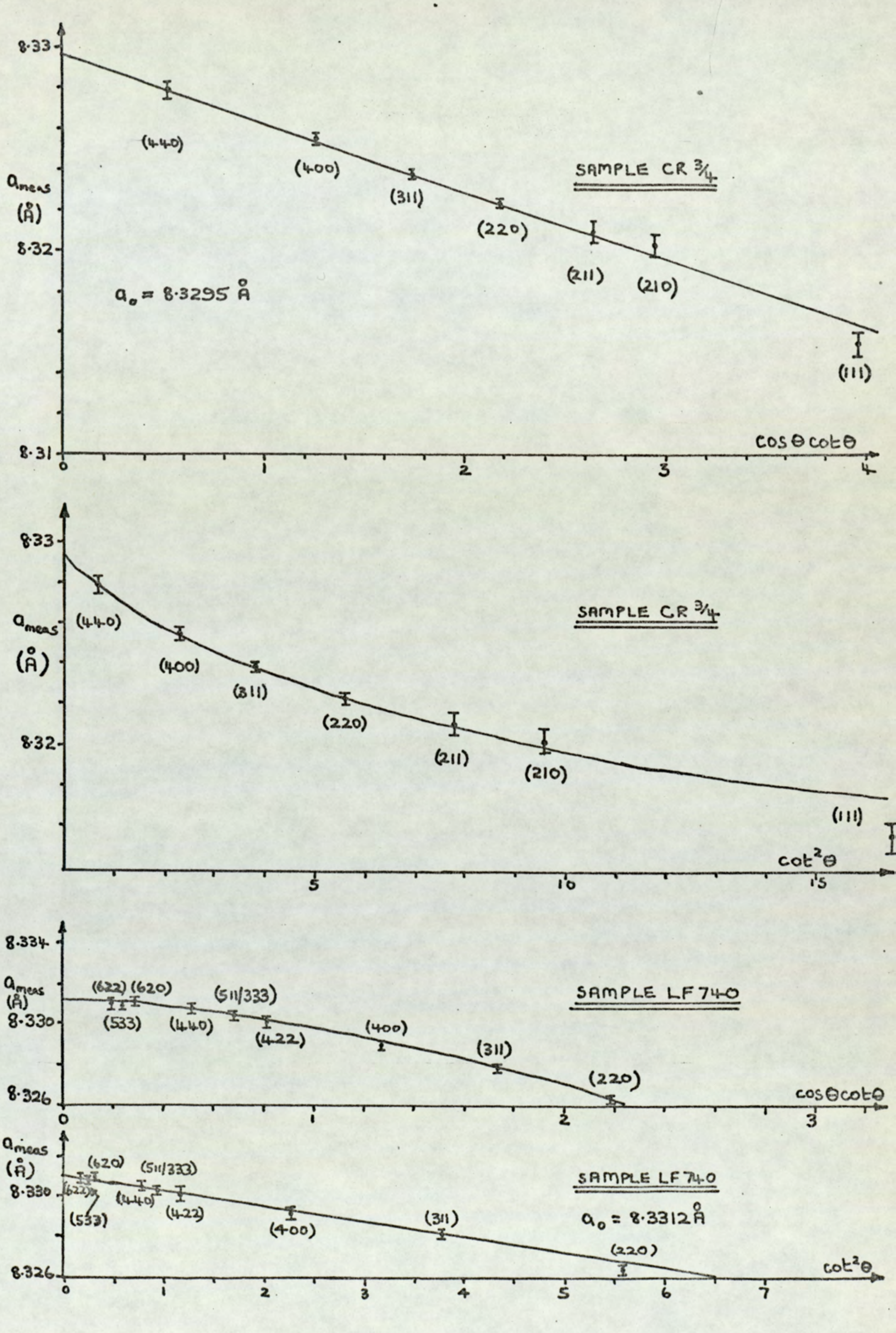

Fig.3.10 Extrapolation plots for two of the lithium ferrite samples

3.4.1 Description of numerical evaluation of transform functions

The background contribution and the overlap contribution of the (211) tail were corrected for by similar methods to those described in the evaluation of the centroid-range characteristics. Each profile was normalized so that $A(0) = X(0) = 1$($A(t) - jB(t)$ representing the transform of the broadened profile and $X(t) - jY(t)$ representing the transform of the sharp profile) and the real and imaginary parts of the transforms calculated as a function of t about $2\theta_k$, the overall centroid, according to the Fourier series approximation,

$$\text{i.e. Real Part } (A(t) \text{ or } X(t)) = \frac{\sum\limits_{2\theta_i = 2\theta_{start}}^{2\theta_{end}} I(2\theta_i) \cos\left(\frac{\pi^2 t \cos\theta_k (2\theta_i - 2\theta_k)}{4.5\lambda}\right)}{\sum\limits_{2\theta_i = 2\theta_{start}}^{2\theta_{end}} I(2\theta_i)}$$

$$\text{and Imaginary Part } (B(t) \text{ or } Y(t)) = \frac{\sum\limits_{2\theta_i = 2\theta_{start}}^{2\theta_{end}} I(2\theta_i) \sin\left(\frac{\pi^2 t \cos\theta_k (2\theta_i - 2\theta_k)}{4.5\lambda}\right)}{\sum\limits_{2\theta_i = 2\theta_{start}}^{2\theta_{end}} I(2\theta_i}$$

where $2\theta_i$ is in degrees, λ and t are in Å, and $2\theta_{start}$ and $2\theta_{end}$ are the lower and upper angular limits of the profile. The corrected transform $J(t) - jK(t)$ was obtained from

$$J(t) - jK(t) = \frac{A(t) - jB(t)}{X(t) - jY(t)} \qquad \text{,Stokes (1948)}$$

3.4.2 Analysis of the random and systematic errors

(i) Truncation errors

If the Fourier transform is determined from an intensity profile which is given over the range -R/2 to +R/2, in 's' space, then

$$(A(t))_{\text{measured}} = \int_{-\infty}^{\infty} A(x) \frac{\sin(\pi R(t-x))dx}{\pi(t-x)} \quad \text{(Bertaut, 1950)}$$

where A(t) is the correct transform. Young, Gerdes and Wilson (1967) have shown that with only 5% truncation of an intensity profile it is possible to overestimate the apparent crystallite size (determined from J'(0)/J(0)) by approximately 40%. Other equally unsatisfactory interpretations are possible unless measures are taken to correct for truncation.

In the present analysis, it was estimated that the broadened profiles were truncated by approximately 5%. Consequently, a curve fitting procedure was applied to the tails of all the profiles. For the broadened profiles it was found that a function of the form $\alpha/((2\theta_i - 2\theta_k)^2 \pm \beta)$ could be fitted to the tails and that α and β could be estimated from the intercepts and slopes of the plots of $I(2\theta_i) \times (2\theta_i - 2\theta_k)^2$ against $I(2\theta_i)$. For the sharp profile a more general function of the form $I(2\theta_i) = \sum_{n=1}^{4} A_n/(2\theta_i - 2\theta_k)^n$ was fitted to the tails where the values of A_n were estimated by least squares analysis. Utilising these results, the ranges of the measured intensity profiles were extended to ± 12° in the broadened cases and ± 6° in the sharp case.

The change in the transform functions on making a truncation correction was quite marked. This is demonstrated in Fig.3.11 where the corrected and uncorrected values of $|J(t) - jK(t)|$ are given for the (210) line from sample LF740 (apparent crystallite

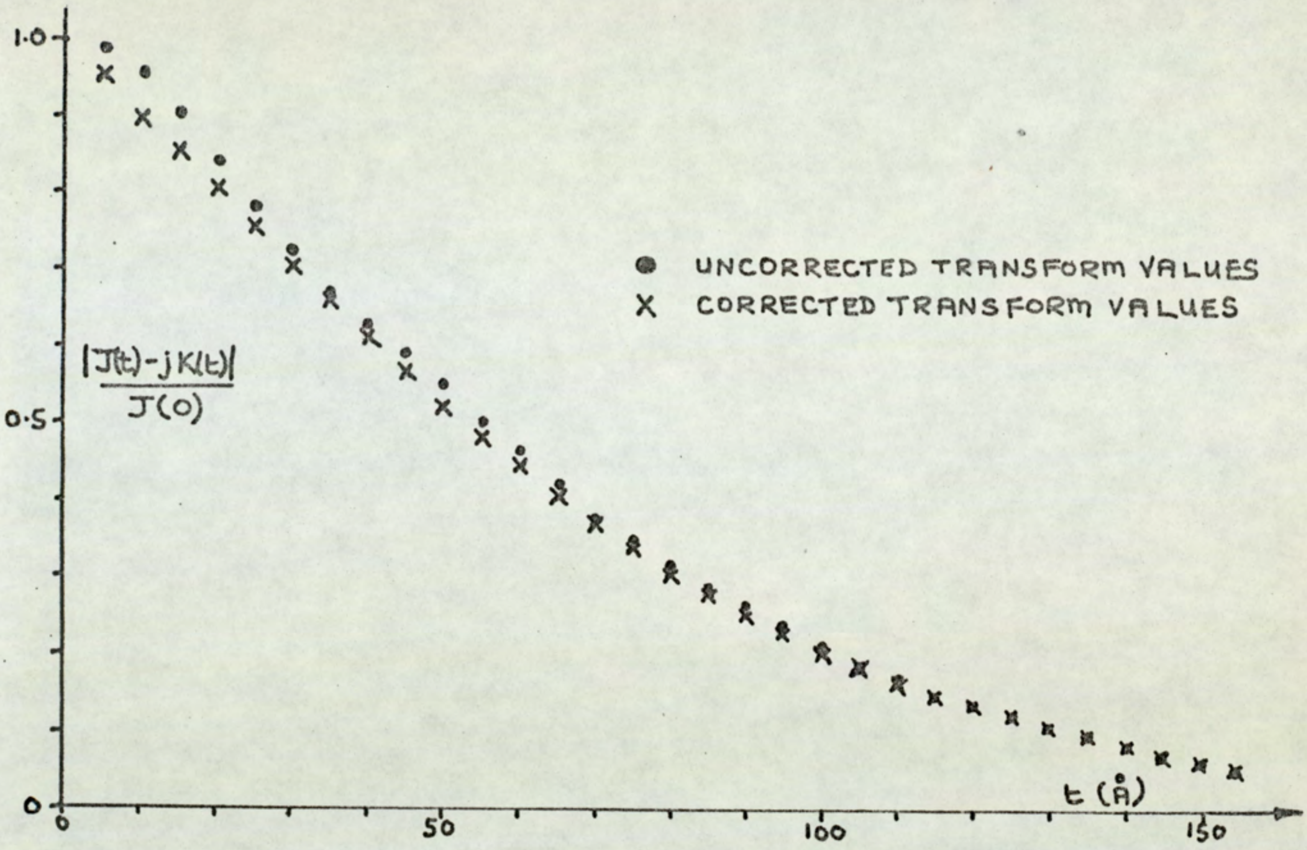

Fig.3.11 Effect of correcting J(t) - jK(t) for truncation errors - (210) line, sample LF740.

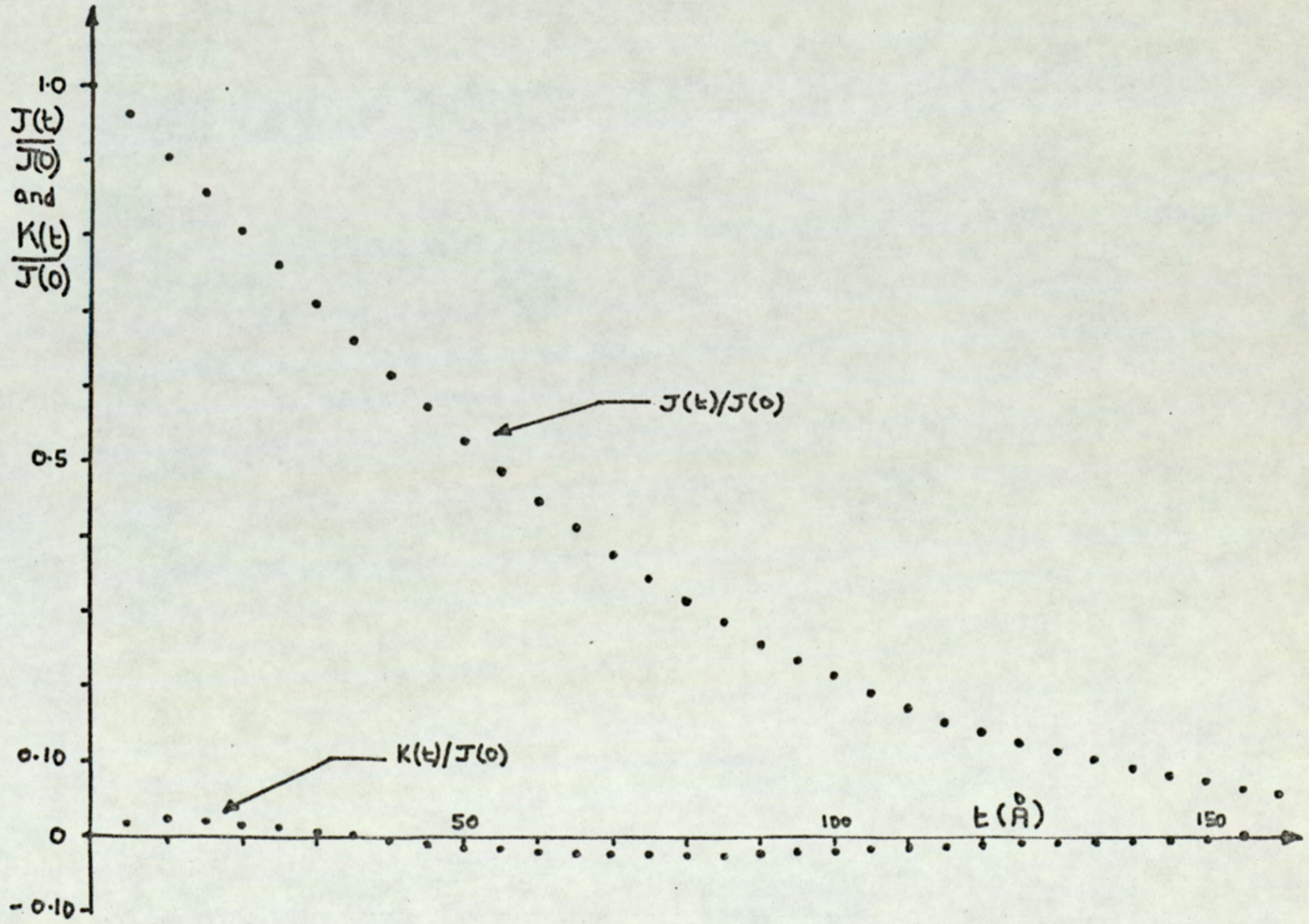

Fig.3.12 J(t) and K(t) determined from the (210) line of sample LF740.

size approximately 75Å).

(ii) Error in the choice of origins of broadened and sharp profiles

If the origins chosen for the sharp and broadened profiles correspond to different values of s relative to s = o, an oscillatory term is superimposed on to the correct transform function (Wagner, 1966),

$$\text{i.e. } (J(t) - jK(t))_{\text{measured}} = e^{\pm 2\pi j s_o t}(J(t) - jK(t))$$

where s_o is the difference in chosen origins. Fortunately, the diffraction broadening appeared to be symmetrical (i.e. K(t) = 0) as

(a) the ratio of the integrated intensity above the peak angle to below the peak angle of each of the broadened profiles was comparable to the ratio of the sharp profile,

(b) the peak displacements of the broadened (210) profiles relative to the (111) and (220) profiles were negligible,

(c) K(t) for the (210) line from sample LF740 was found to be small when a correction for the oscillatory term was made using a value of s_o determined from the difference in centroid values given by the fully corrected lattice parameters of sample LF740 and the standard sample LF-S. (see Fig.3.12)

Consequently, J(t) was determined by evaluating $|J(t) - jK(t)|$ as this function is independent of the choice of origins.

(iii) Error of the mean background level.

The normalising factor of a transform function will be changed by an amount proportional to the error of the estimated background level and as a result of this the values of $A(t)$ for $t>0$ will be shifted up or down in value, depending on the sign of the error, by a constant factor. Truncation of a line profile coupled with a background error b adds, besides the normal truncation, a further error to $A(t)$.

For this case,

$$(A(t) - jB(t))_{meas} = \int_{-\frac{R}{2}}^{+R/2} (I(s) + b)e^{2\pi jst}ds \Bigg/ \int_{-R/2}^{+R/2} (I(s) + b)ds$$

which may be re-expressed as

$$(A(t) - jB(t))_{meas} = \frac{(A(t)' - jB(T)')}{1 + Rb/I_T} + \frac{b}{Rb + I_T} . \frac{\sin(\pi Rt)}{\pi t}$$

where $I_T = \int_{-R/2}^{+R/2} I(s)ds$ and $A(t)' - jB(t)'$ is the transform with a pure truncation error. The first term above is the expected background error effect combined with a truncation, whilst the second term is an extra effect which superimposes a ripple on $A(t)$ at small values of t. In view of these effects a great deal of emphasis has been placed on justifying the chosen background levels. The measurement and discussion of this aspect however, is deferred until the next section on variance and related methods of analysis.

(iv) Statistical errors

Random noise in an intensity profile shows itself as fluctuations in the measured transform functions, $J(t) - jK(t)$, particularly at large values of t. To reduce the effects of noise each profile was smoothed with the aid of a five point formula such that the smoothed intensity value $G'(2\theta_i)$ at $2\theta_i$ (before background correction) was given by

$$G'(2\theta_i) = \frac{17.G(2\theta_i) + 12.(G(2\theta_{i+1}) + G(2\theta_{i-1})) - 3.(G(2\theta_{i+2}) + G(2\theta_{i-2}))}{35}$$

where $G(2\theta_i)$ are the measured intensities. Also to determine the range in t over which the $|J(t) - jK(t)|$ values are expected to be reliable, rough estimates were made of the standard errors, $\sigma(|J(t) - jK(t)|)$, using the method of estimation given by Stokes (1948),

$$\text{i.e. } \sigma(|J(t) - jK(t)|) = \frac{1}{|X(t) - jY(t)|}\sqrt{\frac{1}{I_{TB}} + \frac{|J(t) - jK(t)|}{I_{TS}}}$$

where I_{TB} and I_{TS} are the normalizing factors for the broad and sharp lines respectively (i.e. $\sum_i I(2\theta_i)$) and $|X(t) - jY(t)|$ is the modulus of the transform function of the sharp line. The magnitude of these errors, which are more or less the same for all the present set of transform results, is demonstrated in Fig.3.13 as a function of t.

(v) Deviations from the convolution principle

Deviations from the convolution principle occur when the shape of a line profile varies rapidly as a function of its centroid angle (Klug and Alexander, 1954). A comparison, by inspection, of the (210) and (211) lines however, did not indicate any large scale differences in shape. Nevertheless, the precaution was taken of correcting for one of the effects that cause deviations namely the variation of the Lorentz - polarisation across a line profile (at the position of the (210) line (i.e. $2\theta \simeq 36^\circ$) this factor has a value of 17.5 and a differential coefficient with respect to 2θ of -1). The correction was applied by multiplying each intensity value

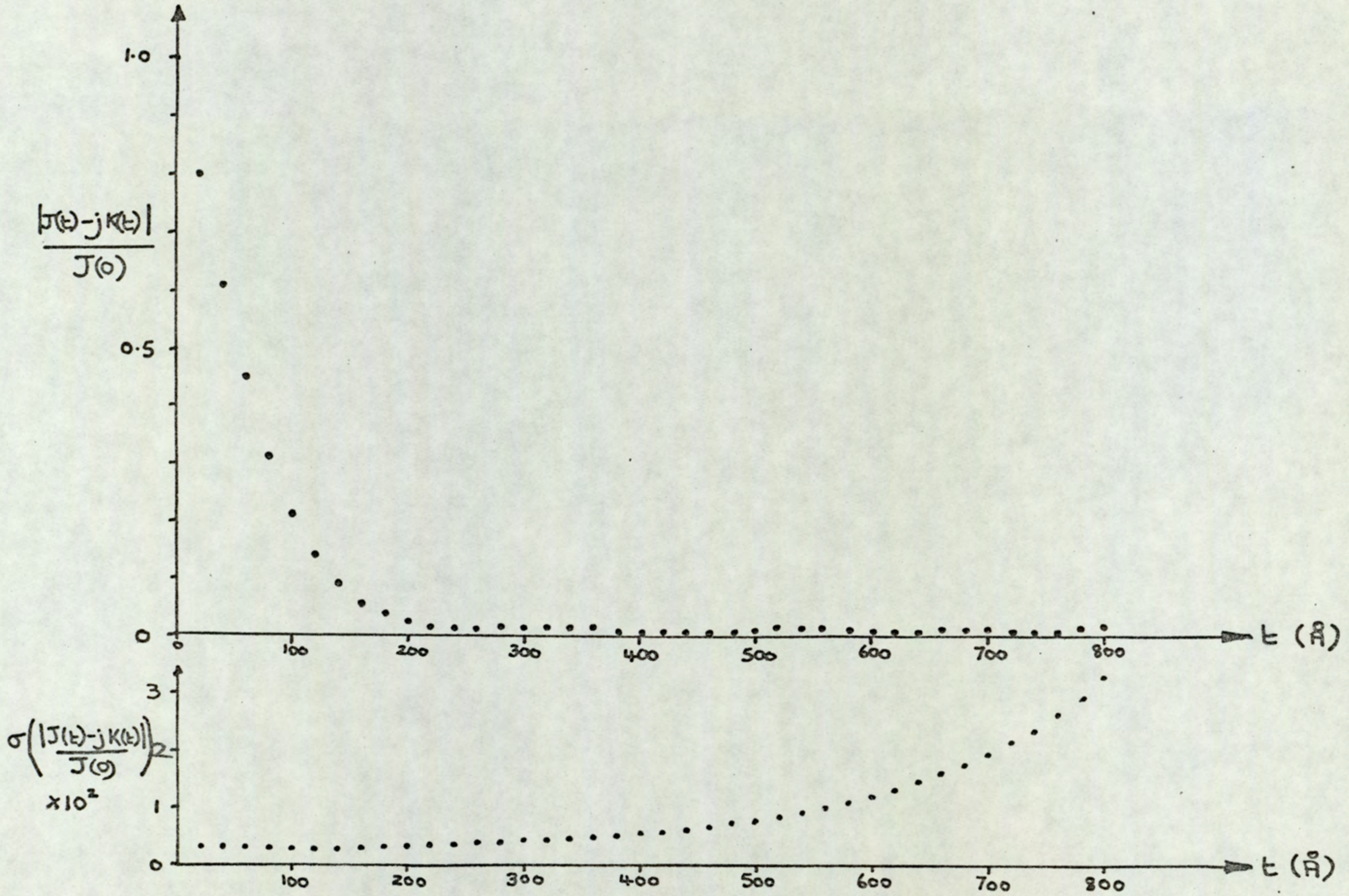

Fig.3.13 Estimates of the statistical errors of $J(t) - jK(t)$ as a function of t.

$I(2\theta_i)$ by $\sin^2\theta_i \cos\theta_i/(1 + \cos^2 2\theta_i)$. The changes in the measured transforms on making this correction were small and observable only at small values of t as the comparison of corrected and uncorrected values of $|J(t) - jK(t)|$ in table 3.3 demonstrates.

Table 3.3 Comparison of $|J(t) - jK(t)|$ values before and after correction for the Lorentz-polarisation factor - sample LF740.

t(Å)	UNCORRECTED $\lvert J(t) - jK(t)\rvert$	CORRECTED $\lvert J(t) - jK(t)\rvert$
0	1	1
5	0.9627	0.9602
10	0.9066	0.9036
15	0.8602	0.8583
20	0.8083	0.8064
30	0.7109	0.7099
40	0.6167	0.6162
50	0.5293	0.5294
100	0.2128	0.2129

3.5 Determination of line breadths

II Variance and related methods

Of the methods available for line breadth analysis, variance appears to be the most reliable method of obtaining easily corrected parameters which are susceptible of simple physical interpretation for the three main causes of diffraction broadening. Even variance however, has limitations. These arise primarily because of the hyperbolic term in the variance-range characteristic $W(2\phi)$ and the presence of the satellite group of lines. If left uncorrected for these factors will not only affect the reliability of estimated line breadth parameters, but also, in principle, the estimated background levels when they are determined with the aid of variance (Langford and Wilson, 1963). As these matters are of direct concern to the present interpretations, investigations were undertaken with the aim of improving the reliability of the parameters obtained from variance namely, $J'(0)/J(0)$ and $J''(0)/J(0)$. In doing so, two alternative methods of determining these parameters were examined. The first of these is based on the variation of the function (truncated integrated intensity X range), symbolized as $Z(2\phi)$, with range 2ϕ. The other method is based on a modification of variance, termed pseudo-variance, in which the hyperbolic term is eliminated by forming the function $SW(2\phi) = d(2\phi.W(2\phi))/d(2\phi)$.

3.5.1 Theory

The intensity distribution across a line profile may be expressed as a Fourier integral,

$$\text{i.e. } I(s) = 2.K \int_0^\infty (A(t)\cos 2\ st - B(t)\sin 2\ st)dt.$$

where K represents parameters such as the Lorentz-polarization factor which may be assumed to be constant over a line profile without loss of generality.

For $|s|>0$, $I(s)$ may be expanded as an infinite series by continuous integration by parts to obtain

$$I(s) = 2K\left[-\frac{A'(0)}{(2\pi s)^2} + \frac{A'''(0)}{(2\pi s)^4} - \frac{A^{V}(0)}{(2\pi s)^6} + \ldots\ldots\ldots\ldots\right]$$

$$+ 2K\left[\frac{B''(0)}{(2\pi s)^3} - \frac{B^{iv}(0)}{(2\pi s)^5} + \ldots\ldots\ldots\ldots\ldots\right]$$

The total integrated intensity of a line profile is K.A(0) so that the integrated intensity for the limited range $-\sigma_1$ to σ_2 is

$$T(\sigma_1, \sigma_2) = KA(0) - \int_{-\infty}^{-\sigma_1} I(s)ds - \int_{\sigma_2}^{\infty} I(s)ds$$

or in terms of the series expansion, (Wilson 1969),

$$T(\sigma_1,\sigma_2) = K\left[A(0) + \frac{2.A'(0)}{(2\pi)^2}\left(\frac{1}{\sigma_1} + \frac{1}{\sigma_2}\right) - \frac{2.A'''(0)}{3.(2\pi)^4}\left(\frac{1}{\sigma_1^3} + \frac{1}{\sigma_2^3}\right) + \ldots\ldots\ldots\right]$$

$$+ K\left[\frac{2.B''(0)}{2.(2\pi)^3}\left(\frac{1}{\sigma_1^2} - \frac{1}{\sigma_2^2}\right) - \frac{2.B^{iv}(0)}{4.(2\pi)^5}\left(\frac{1}{\sigma_1^4} - \frac{1}{\sigma_2^4}\right) + \ldots\ldots\ldots\ldots\ldots\right]$$

If the truncation is symmetrical with respect to s = 0 so that $\sigma_1 = \sigma_2 = \sigma$, this equation reduces to

$$T(2\sigma) = K\left[A(0) + \frac{2}{\pi^2} . \frac{A'(0)}{2\sigma} - \frac{2}{3\pi^4} . \frac{A'''(0)}{(2\sigma)^3} + \ldots\ldots\ldots\ldots\right]$$

The function (truncated integrated intensity X range) is therefore given by

$$Z(2\sigma) = 2\sigma.T(2\sigma)$$

$$= K\left[A(0).2\sigma + \frac{2}{\pi^2} .A'(0) - \frac{2}{3\pi^4} . \frac{A'''(0)}{(2\sigma)^2} + 0\left(\frac{1}{\sigma^4}\right)\right]$$

which is a linear function of 2σ when the range is sufficiently large. The slope of the linear part of $Z(2\sigma)$ gives the integrated intensity K.A(0) whilst the intercept obtained by extrapolation to zero range gives $2K.A'(0)/\pi^2$. Thus, the parameter $A'(0)/A(0)$ is given from the ratio of intercept to slope. It is also worth noting that a small inequality between σ_1 and σ_2 leads to a modification of the term in $1/(2\sigma)^2$ and higher order terms, but that the first two terms remain unaffected.

The relation of the pseudo-variance function to the range of integration, 2σ, may be deduced quite easily from the form of W(2), the variance-range function, which is given in the tails of a profile by

$$W(2\sigma) = -\frac{1}{2\pi^2}\cdot\frac{A'(0)}{A(0)}2\sigma - \frac{1}{4\pi^2}\left(\frac{A''(0)}{A(0)} + \left(\frac{B'(0)}{A(0)}\right)^2\right) + \frac{1}{\pi^4}\left(\frac{A'(0)}{A(0)}\right)^2$$

$$- \frac{1}{2\sigma}\cdot\frac{1}{2\pi^4}\left(\frac{A'''(0)}{A(0)} - \frac{A'(0)}{A(0)}\left(\frac{A''(0)}{A(0)} + \left(\frac{B'(0)}{A(0)}\right)^2\right)\right)$$

$$+ O\left(\frac{1}{(2\sigma)^2}\right)$$

so that

$$SW(2\sigma) = \frac{d(2\sigma . W(2\sigma))}{d(2\sigma)}$$

$$= -\frac{1}{\pi^2}\cdot\frac{A'(0)}{A(0)}\cdot 2\sigma - \frac{1}{4\pi^2}\cdot\left(\frac{A''(0)}{A(0)} + \left(\frac{B'(0)}{A(0)}\right)^2\right) + \frac{1}{\pi^4}\left(\frac{A'(0)}{A(0)}\right)^2 + O($$

When analysis is carried out in 2θ space for an overall range 2ϕ with a background error b the functions are modified as follows:-

$$W(2\phi) = \left(\frac{\lambda}{\cos\theta}\right)^2 . W(2\sigma) + D.(2\phi)^3$$

$$SW(2\phi) = \left(\frac{\lambda}{\cos\theta}\right)^2 SW(2\sigma) + 4.D.(2\phi)^3$$

$$Z(2\phi) = \left(\frac{\lambda}{\cos\theta}\right)^2 Z(2\sigma) + b.(2\phi)^2$$

where $D \simeq b/(12.\text{Integrated Intensity})$

and θ is the Bragg angle.

Correction of the estimated values of $A'(0)/A(0)$ and $A''(0)/A(0) + (B'(0)/A(0))^2$ for instrumental broadening was carried out using the relations given in Chapter 2 section 1,

i.e. $$\frac{A'(0)}{A(0)} = \frac{J'(0)}{J(0)} + \frac{X'(0)}{X(0)}$$

and $$\frac{A''(0)}{A(0)} + \left(\frac{B'(0)}{A(0)}\right)^2 = \frac{X''(0)}{X(0)} + \frac{J''(0)}{J(0)} + 2.\frac{J'(0)}{J(0)}.\frac{X'(0)}{X(0)} + \left(\frac{Y'(0)}{X(0)} + \frac{K'(0)}{J(0)}\right)^2$$

where $X''(0)/X(0) + (Y'(0)/X(0))^2$ and $X'(0)/X(0)$ were determined from the sharp superlattice and lattice line profiles. As no centroid shifts were observed as a result of the broadening of the superlattice lines, $K'(0)/J(0)$ was assumed to be zero.

3.5.2 Practical evaluation of line breadth characteristics

As apreliminary to the numerical analysis, the effects of overlapping lines and the satellite group of lines were eliminated from the line profiles by the methods described in section 3.3. Each of the characteristics was computed with $2\theta_k$, the overall centroid, as an origin $2\phi = 0$.

$$\text{i.e. } Z(2\phi) = 2\phi.\Delta 2\theta \sum_{2\theta_j = 2\theta_k - \phi}^{2\theta_k + \phi} \left(G(2\theta_j) - b(2\theta_j)\right)$$

$$W(2\phi) = \frac{2\phi.\Delta 2\theta}{Z(2\phi)} \sum_{2\theta_j = 2\theta_k - \phi}^{2\theta_k + \phi} \left(2\theta_j - 2\theta_c'(2\phi)\right)^2 \left(G(2\theta_j) - b(2\theta_j)\right)$$

$$W_\infty(2\phi) = \frac{\sum_{2\theta_j = 2\theta_k - \phi}^{2\theta_k + \phi} \left(2\theta_j - 2\theta_c(2\phi)\right)^2 I(2\theta_j)}{\sum_{2\theta_j = -\infty}^{\infty} I(2\theta_j)}$$

where $G(2\theta_j)$ is the measured intensity at $2\theta_j$,

$I(2\theta_j)$ is the measured intensity corrected for the optimized background determined from analysis $Z(2\phi)$,

$b(2\theta_j)$ is an assumed background level at $2\theta_j$,

$\Delta 2\theta$ is the step size between intensity measurements,

and $2\theta_c(2\phi)$ and $2\theta_c'(2\phi)$ are the centroid values for the range 2ϕ determined using the total integrated intensity and the truncated integrated intensity, respectively, as normalizing factors.

The $Z(2\phi)$ and $W(2\phi)$ characteristics were computed for a range of mean background levels whilst $W_\infty(2\phi)$ was computed only for the optimized background level as determined from $Z(2\phi)$ (see below) with $\sum_{-\infty}^{\infty} I(2\theta_j)$ also being determined from $Z(2\phi)$. For each $W(2\phi)$

characteristic a pseudo-variance characteristic was derived using the relation

$$SW(2\phi) = \frac{d(2\phi.W(2\phi))}{d(2\phi)} = W(2\phi) + 2\phi.\frac{dW(2\phi)}{d(2\phi)}$$

As small statistical fluctuations in $W(2\phi)$ tend to be magnified in $SW(2\phi)$, the derivative of $W(2\phi)$ at $2\phi_i$ was calculated by the least squares fitting of a parabola to the five points $W(2\phi_{i-2})$ to $W(2\phi_{i+2})$

i.e. $$\left.\frac{dW(2\phi)}{d2\phi}\right|_{2\phi_i} = \frac{2(W(2\phi_{i+2}) - W(2\phi_{i-2})) + (W(2\phi_{i+1}) - W(2\phi_{i-1}))}{20.\Delta 2\theta}$$

Estimates of the mean background level under each profile were obtained by applying the method of Langford and Wilson (1963) (see Chapter 2, section I) to the variance-range and also to the $Z(2\phi)$-range characteristics (i.e. two estimates of the background level). In each case least squares analysis was performed over the 'linear region' to determine the mean background levels b_z and b_W at which the linearity of $Z(2\phi)$ and $W(2\phi)$, respectively, was optimized. Each optimised mean background level was taken to be the 'true' mean background level for its associated characteristic. The slope and intercept values of the characteristics were determined from the following relations,

$$\text{Slope} = \frac{\langle Y.2\phi\rangle - \langle 2\phi\rangle.\langle Y\rangle}{\langle (2\phi)^2\rangle - \langle 2\phi\rangle^2}$$

$$\text{Intercept} = \frac{\langle Y\rangle.\langle (2\phi)^2\rangle - \langle Y.2\phi\rangle.\langle 2\phi\rangle}{\langle (2\phi)^2\rangle - \langle 2\phi\rangle^2}$$

where Y represents either $W(2\phi)$ or $Z(2\phi)$, and $\langle Y \rangle$ represents the mean value of Y over the chosen linear region. Under these conditions the form of the characteristics is given by

$$Z(2\phi) = Z_o + m.2\phi$$

and $W(2\phi) = W_o + k.2\phi$

The statistical errors of the variance slope k and variance intercept W_o were also estimated. The equations relating these errors to the observed data are derived in the appendix.

A selection of experimental $W(2\phi)$ and $Z(2\phi)$ characteristics corresponding to weak and strong, lattice and superlattice lines, is given in Fig.3.14. (The intensity profiles corresponding to these characteristics are given in Fig.3.3).

3.5.3 Line breadth analysis of simulated profiles

To gain some idea of the errors resulting from non-linear terms in $Z(2\phi)$, $W(2\phi)$ and $SW(2\phi)$, an analysis was carried out on $K\alpha$ doublets simulated by pairs of Cauchy curves. The results presented in Tables 3.4, 3.5 and 3.6 assumed a $K\alpha_1\alpha_2$ doublet separation of 3.9MÅ., a $K\alpha_1/K\alpha_2$ integrated intensity ratio of 2 and initial half widths for the $K\alpha_1$ and $K\alpha_2$ components of 0.80MÅ and 0.90MÅ, respectively; these values correspond quite closely to the description of the $CrK\alpha$ doublet given by Parratt (1936). Various degrees of breadth were realized by stepping the half widths of the $K\alpha_1$ and $K\alpha_2$ components from the initial values up to 18.80MÅ and 18.90MÅ., respectively, in units of 2MÅ. After plotting out the functions $Z(\Delta\lambda)$, $W(\Delta\lambda)$ and $SW(\Delta\lambda)$ the respective slopes and intercepts were derived by fitting a straight line

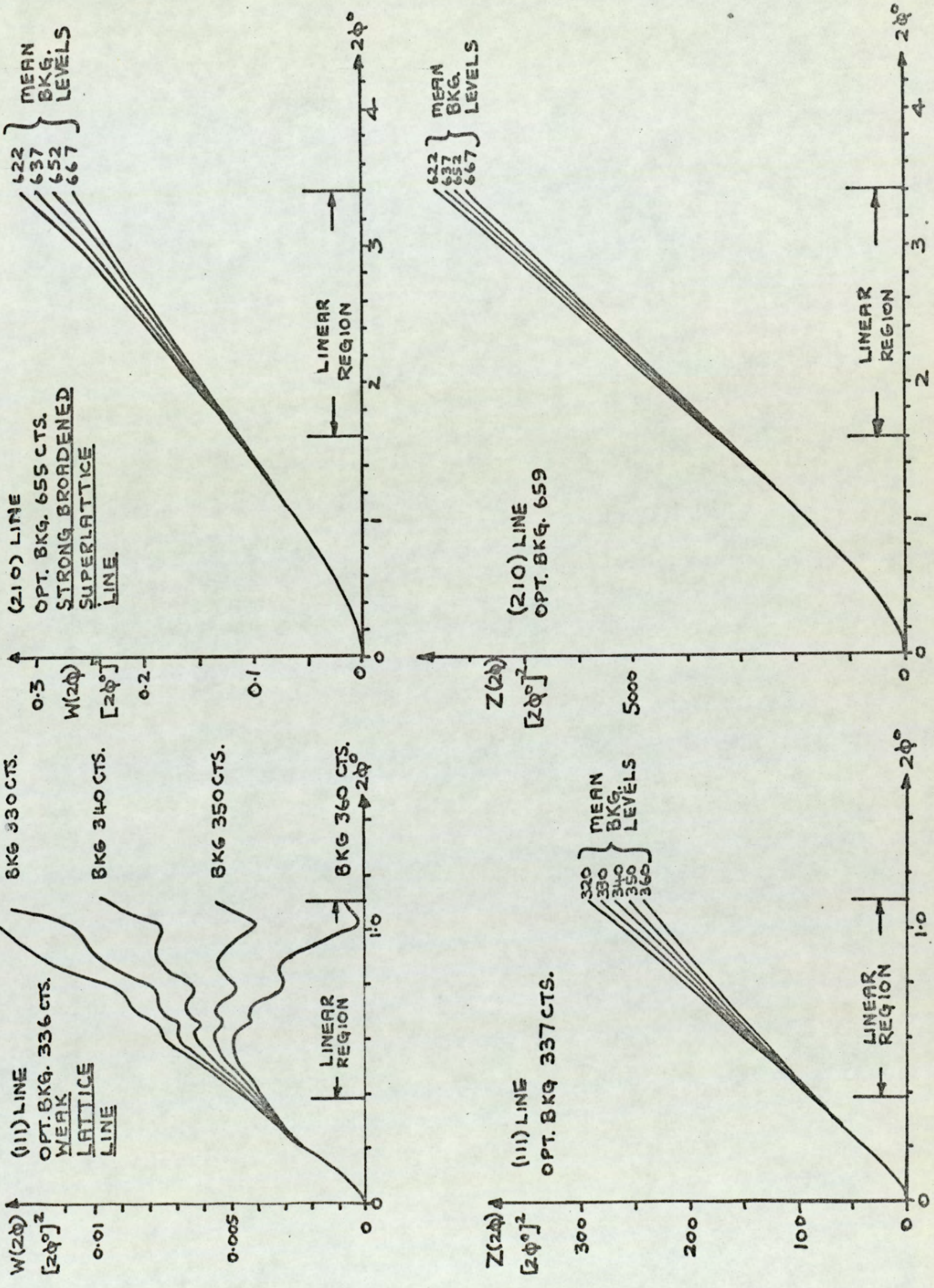

Fig.3.14(a) W(2Ø) and Z(2Ø) characteristics for a range of background levels —— Sample LF725.

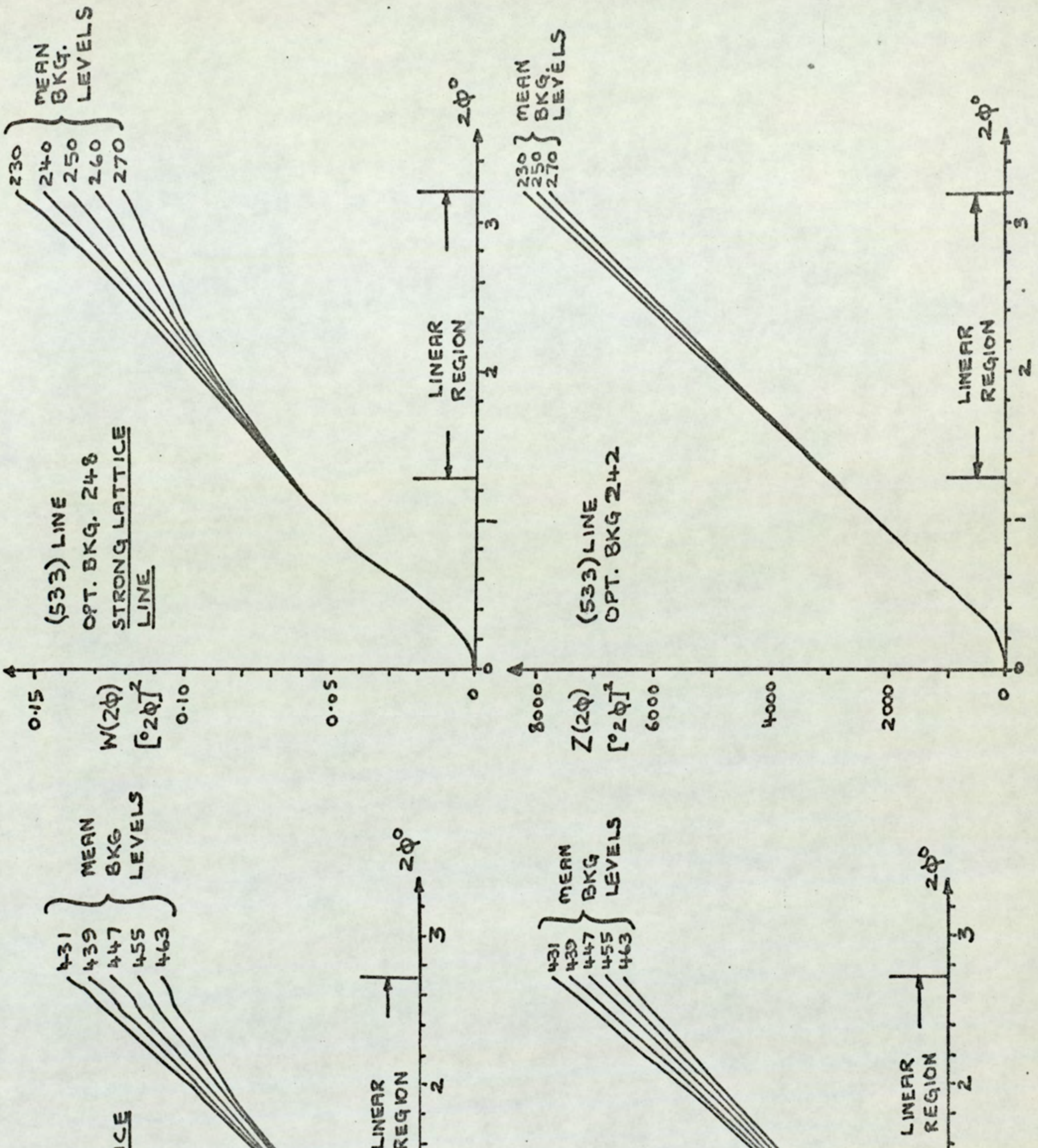

<u>Fig.3.14(b)</u> $W(2\phi)$ and $Z(2\phi)$ characteristics for a range of background levels ——— Sample LF725.

in the region $\Delta\lambda = 3$ to 5 overall half widths of the simulated Kα doublets. The theoretical counterparts of the measured slopes and intercepts were calculated from the asymptotic forms for the breadth functions,

i.e.

$$Z(\Delta\lambda) = (3\pi.I\alpha_2).\Delta\lambda - 4I\alpha_2.(2\alpha_1 + \alpha_2)$$

$$W(\Delta\lambda) = \left(\frac{2\alpha_1 + \alpha_2}{3\pi}\right).\Delta\lambda + \frac{1}{3}.\left(\frac{2}{3}.\beta^2 - 2\alpha_1^2 - \alpha_2^2\right)$$

where I is the peak height of the Kα_2 component

$2\alpha_1$ and $2\alpha_2$ are the half widths of the Kα_1 and Kα_2 components in MÅ,

and β is the separation of the peaks in MÅ,

Table 3.4 Comparison of the measured and theoretical parameters of $Z(\Delta\lambda)$ from simulated profiles.

α_1 (MÅ)	α_2 (MÅ)	Theoretical slope (MÅ)	Measured Slope(M) (MÅ)	Theoretical Intercept $(\text{MÅ})^2$	Measured Intercept (Z_o) $(\text{MÅ})^2$	Range of Linearity in $\Delta\lambda$(MÅ)	Profile Number
0.80	0.90	989	992	-524	-592	15-25	1
2.80	2.90	989	991	-1785	-1864	20-30	2
4.80	4.90	989	990	-3040	-3080	20-30	3
6.80	6.90	989	988	-4300	-4233	30-40	4
8.80	8.90	989	987	-5560	-5408	40-50	5
10.80	10.90	989	986	-6820	-6601	50-60	6
12.80	12.90	989	985	-8080	-7700	50-60	7
14.80	14.90	989	982	-9320	-8744	50-60	8
16.80	16.90	989	982	-10580	-9944	60-70	9
18.80	18.90	989	980	-11850	-10958	60-70	10

Table 3.5 Comparison of the theoretical and measured variance slopes from W(Δλ), SW(Δλ) and equivalent of variance slope from Z(Δλ) which is given by $-Z_o/4m$ (Units MÅ)

Theoretical Slope	Measured Slope(k) from W(Δλ)	Discrepancy of k	Slope from Z(Δλ)	Discrepancy of $-Z_o/4m$	Slope from SW(Δλ)	Discrepancy of SW(Δλ) slope	Profile Number
0.133	0.147	10.5%	0.149	12%	0.132	-0.7%	1
0.451	0.472	4.7%	0.470	4.4%	0.451	0	2
0.770	0.795	3.2%	0.778	1.0%	0.770	0	3
1.089	1.097	0.9%	1.069	-1.9%	1.089	0	4
1.407	1.404	-0.2%	1.368	-2.8%	1.407	0	5
1.723	1.713	-0.6%	1.672	-3.0%	1.725	0	6
2.043	2.016	-1.6%	1.955	-4.3%	2.044	0	7
2.361	2.313	-2.1%	2.222	-5.9%	2.362	0	8
2.680	2.624	-2.3%	2.530	-5.6%	2.679	0	9
2.995	2.915	-2.7%	2.792	-6.6%	2.997	0	10

Table 3.6 Comparison of the theoretical and measured variance intercepts from W(Δλ) and SW(Δλ). (Units MÅ^2)

Theoretical Variance Intercept	Measured Variance Intercept W_o	Measured Variance Intercept From SW(Δλ)	Profile Number
3.216	2.958	3.492	1
2.187	1.395	2.463	2
-0.080	-1.086	0.156	3
-3.572	-3.848	-3.275	4
-8.200	-7.622	-7.892	5
-12.630	-12.386	-13.386	6
-21.050	-17.668	-20.669	7
-29.690	-23.411	-28.831	8
-38.470	-30.850	-38.084	9
-49.020	-37.844	-48.501	10

It is clear from the variance slope and intercept values determined from the pseudo-variance-range functions that the significant non-linear contribution in the variance functions arises from the hyperbolic term. As far as the variance slope k from $W(\Delta\lambda)$ and its equivalent from $Z(\Delta\lambda)$ are concerned the effect of non-linear terms is not markedly different. When the variance slope was measured from $W_{\infty}(\Delta\lambda)$ it was found to be almost the same as the value estimated from $Z(\Delta\lambda)$ (Note: this was done only for the sharpest and broadest profile). Consequently, the slightly improved linearity of $W(\Delta\lambda)$ for the broader profiles may be attributed to the truncated integrated intensity being used as a normalising factor. The estimated intercept values from $W(\Delta\lambda)$ are far from being reliable as Edwards and Toman (1970b) have already remarked. As the breadth of the simulated profiles increases the signs of the $1/(\Delta\lambda)^2$ and $1/(\Delta\lambda)$ terms in $Z(\Delta\lambda)$ and $W(\Delta\lambda)$, respectively, change from negative to positive. Coincident with these changes are changes in the sign of the discrepancies of the measured parameters. Despite the non-linear terms, the visual appearance of the line breadth functions in the tails of the profiles is decidedly linear over local regions of 20 to 30 MÅ at a time (see Fig.3.15).

3.5.4 Effect of satellite lines

The importance of the satellite group of lines in variance analysis was first emphasized by Langford (1965) and later, by Edwards and Toman (1969,1970a) and Langford and Edwards (1971). Their remarks concerning the CuKα and FeKα satellite group are especially significant in the present case because the CrKα satellite group is relatively stronger and occupies a similar unsatisfactory position relative to the linear regions of line breadth characteristics. To overcome the problems posed by these lines, the satellite correction

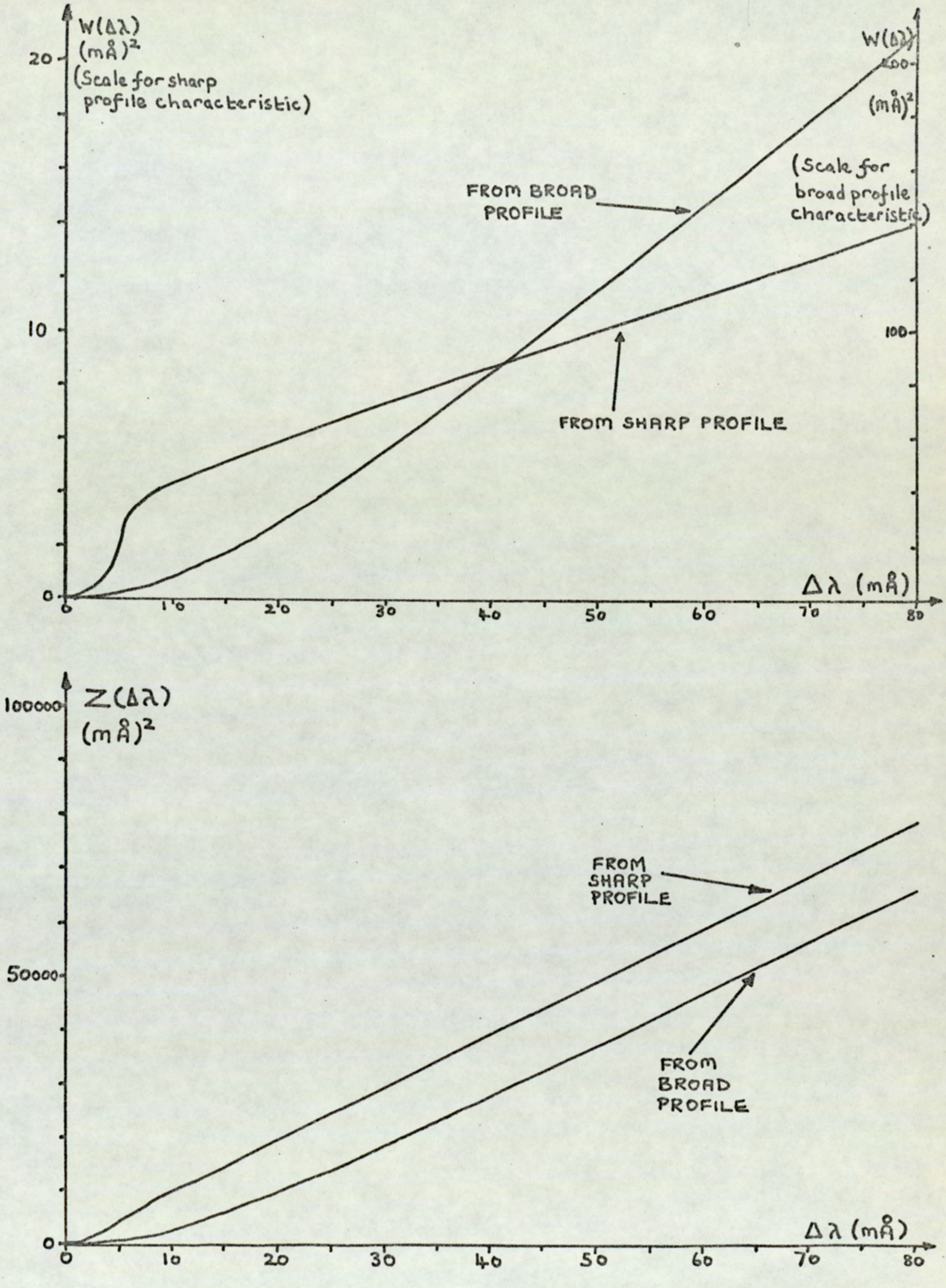

Fig.3.15 W(Δλ) and Z(Δλ) characteristics of the sharpest and broadest of the simulated CrKα emission profiles.

described earlier (section 3.3) was employed and found to be very satisfactory. Fig.3.16 shows the effect of this correction on the variance-range characteristic of the (440) line from sample LF-725 (this profile is given in Fig.3.3). The optimum background levels, b_W and b_Z, were determined after correction for the satellite lines.

3.5.5 Choice of linear region

Because of the discontinuity in the emission profile caused by the absorption edge of the β filter, careful attention was paid to the choice of the 'linear regions'. The 'linear regions' of the variance-range and $Z(2\phi)$-range characteristics of profiles with negligible diffraction broadening were chosen between the satellite group peak position and the absorption edge except for diffraction lines at $2\theta < 40^\circ$ where the linear region was taken from the absorption edge up to a 2ϕ value dictated by the accuracy of the intensity data. For diffraction broadened lines the linear region was chosen by inspection with an initial value for $2\phi \simeq 3$ half widths of the diffraction profile.

3.5.6 Background errors and inverse range dependent terms

The optimum background level determined by assuming that either $W(2\phi)$ or $Z(2\phi)$ is linear should not correspond to a zero background error owing to the inverse range dependent terms. Originally, it was hoped that $Z(2\phi)$ would provide a more satisfactory means of background estimation than variance as the dominant inverse range term varies as $1/(2\phi)^2$ as opposed to $1/2\phi$. Unfortunately, this gain is compensated for by the fact that an error in the background level for variance is $(2\phi)^3$ dependent whilst that for $Z(2\phi)$ is only $(2\phi)^2$ dependent. A comparison of the optimum background levels determined independently, by variance and $Z(2\phi)$ analysis (i.e. b_W and b_Z), given in Fig.3.17,

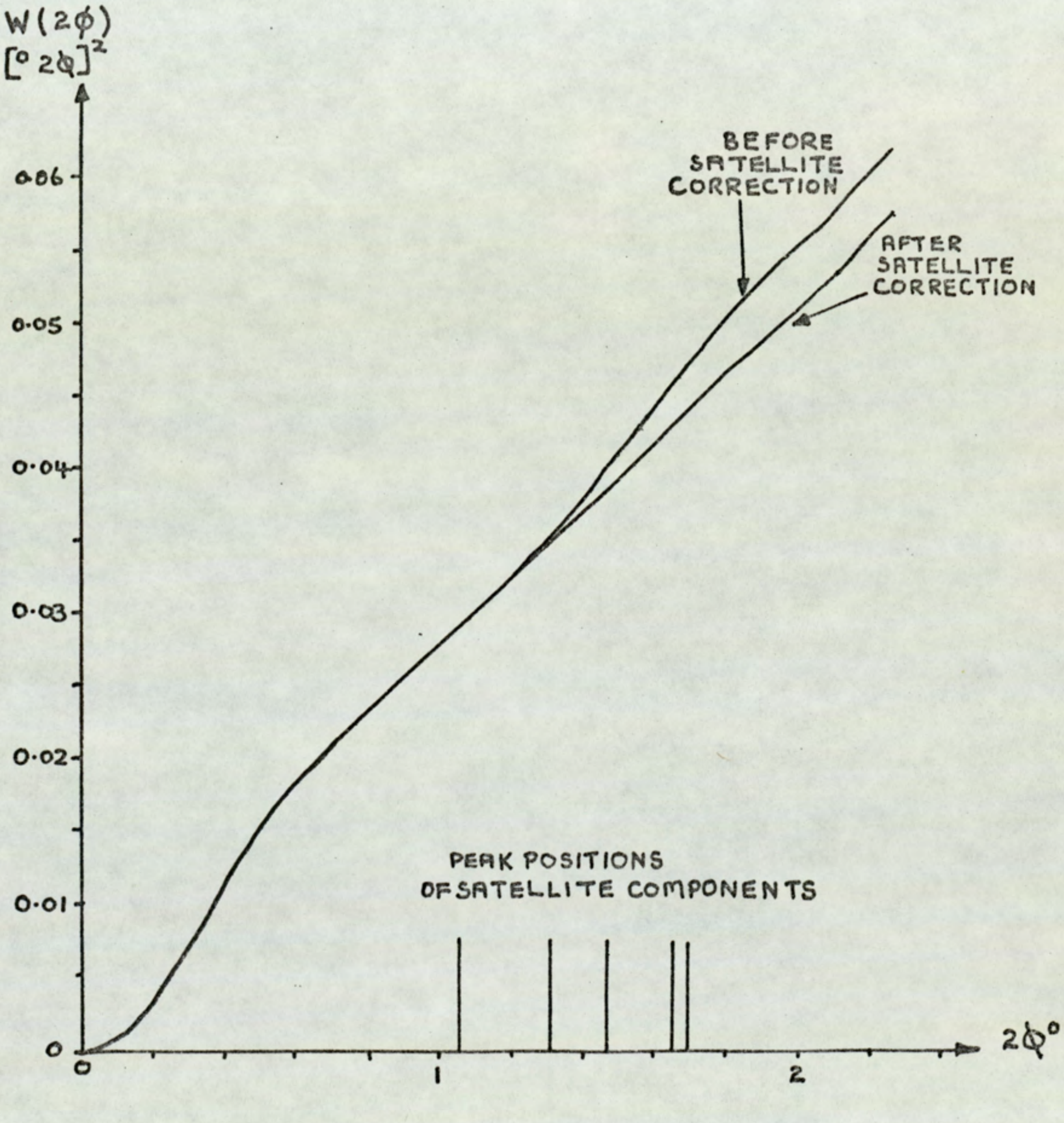

Fig.3.16 Effect of satellite correction on the variance-range characteristic of the (440) line from sample LF725.

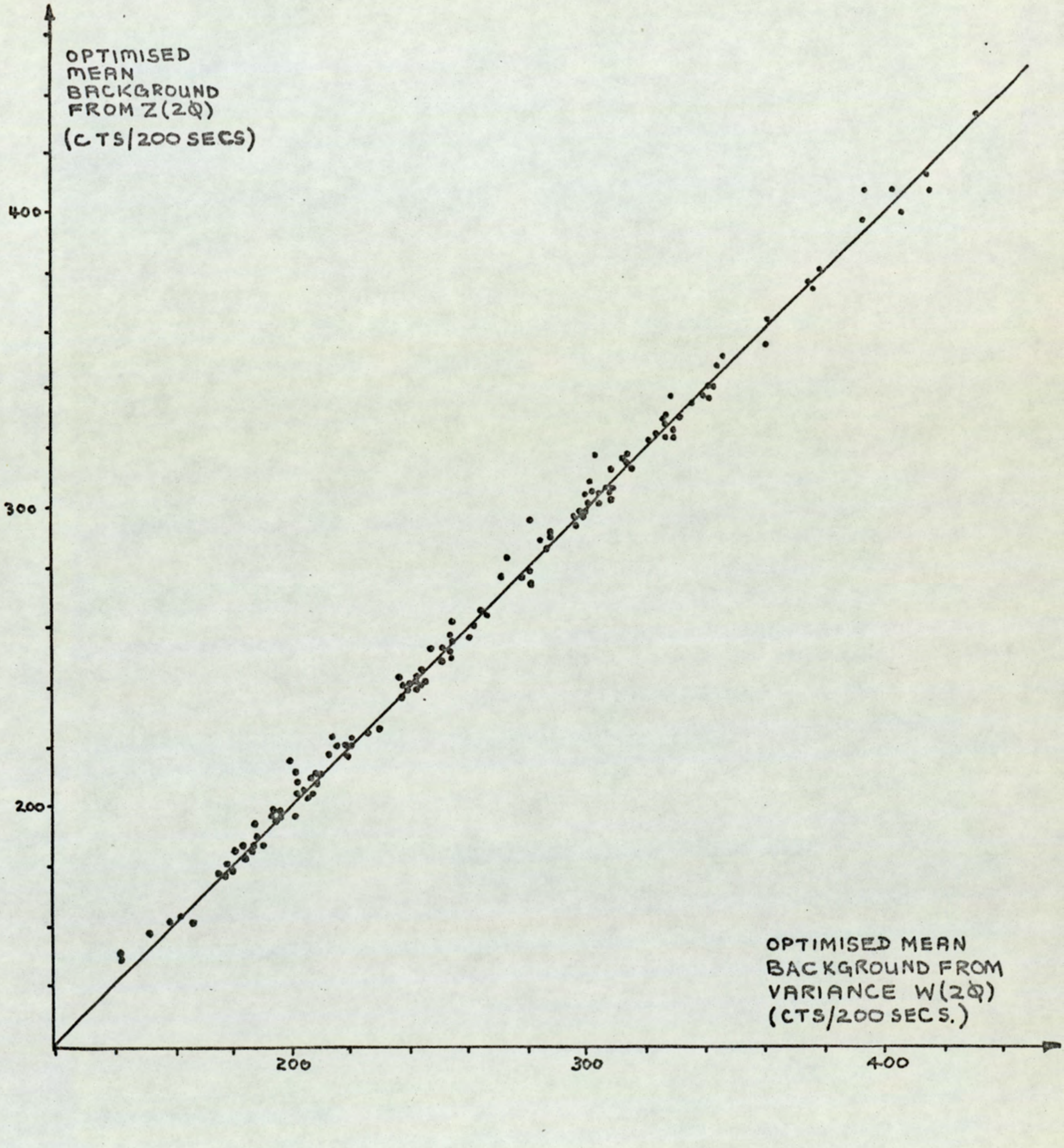

Fig.3.17 Comparison of mean background levels determined from Z(2θ) and variance analysis (exact agreement is indicated by the solid line).

shows that they are in good agreement for all ranges of breadth. A further comparison of the measured variance slopes with their equivalents from $Z(2\phi)$(i.e. $- Z_0/4m$), given in Fig.3.18, shows that these are also in good agreement except for lines exhibiting strong diffraction broadening where there is a tendency for the variance slope to be slightly greater than its equivalent from $Z(2\phi)$. When the variance slope was measured from the alternative definition of variance (i.e. $W_\infty(2\phi)$) the latter discrepancy was almost eliminated. As the parameters obtained from variance and $Z(2\phi)$ are very similar it must be concluded that the limitations imposed on their interpretation by inverse range dependent terms and background errors are very similar.

It was also thought that the background could be optimised using $SW(2\phi)$. In practice, $SW(2\phi)$ turns out to be a rather poor function to use in this way owing to its high sensitivity to intensity fluctuations and minor residuals left by over or under estimation of the satellite group. For those cases in which an attempt was made to determine the optimized background level, obviously erroneous values were obtained. It was found however, that if the background is optimized using $W(2\phi)$, a good straight line may be fitted to the 'linear region' of the (pseudo-variance)-range function. This is demonstrated in Fig.3.19 with the (pseudo-variance)-range characteristics derived from the optimized variance-range characteristics given in Fig.3.14. In view of the linearity of these functions at the optimized background levels it was inferred that the errors in the background levels were fairly small.

Further support for the variance optimized background levels was given by comparing the variance slopes and intercepts, k and W_0, respectively, with their counterparts, k' and W_0' from pseudo-variance

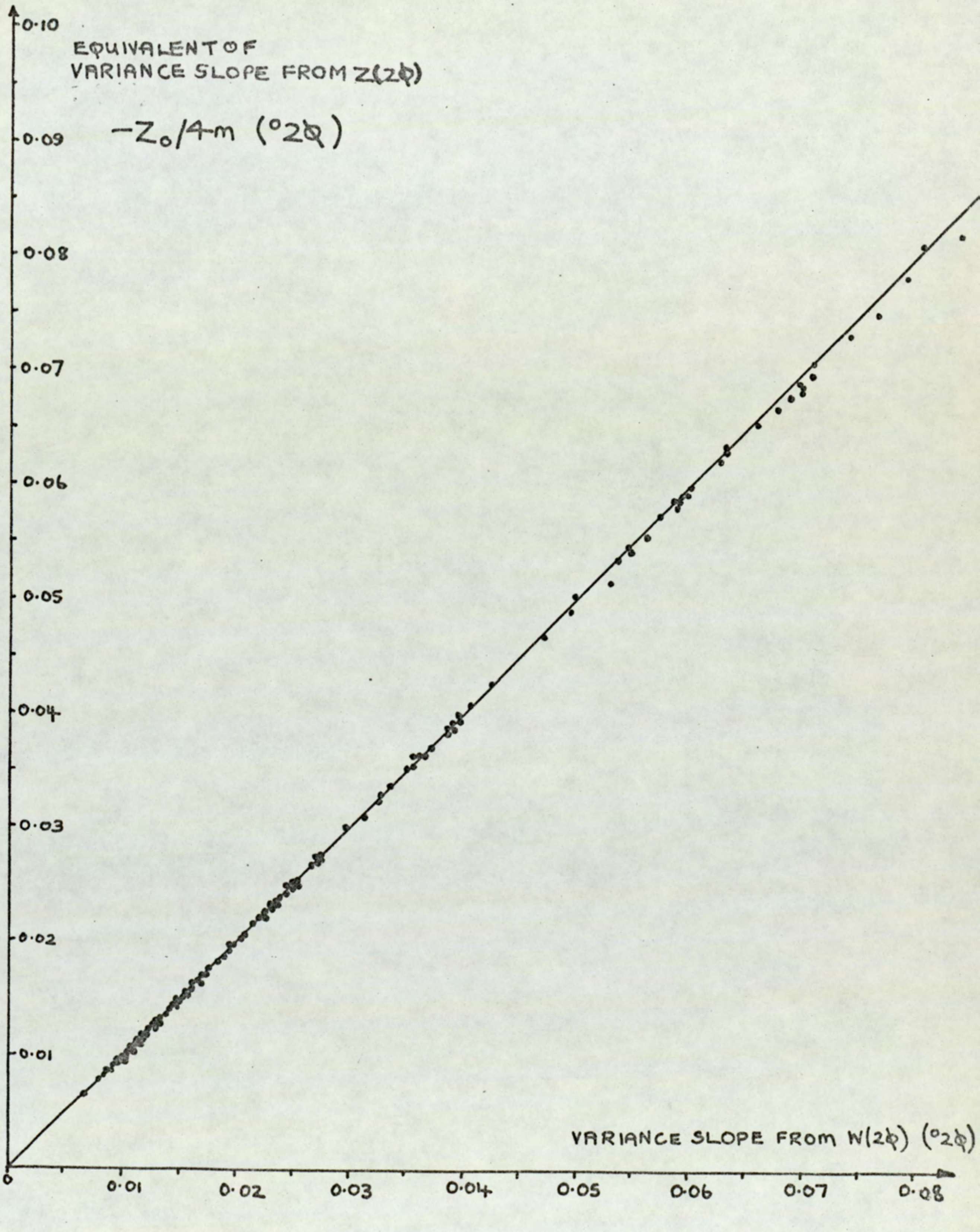

Fig.3.18 Comparison of $-Z_0/4m$ derived from $Z(2\phi)$ analysis with variance slope. (exact agreement is indicated by the solid line).

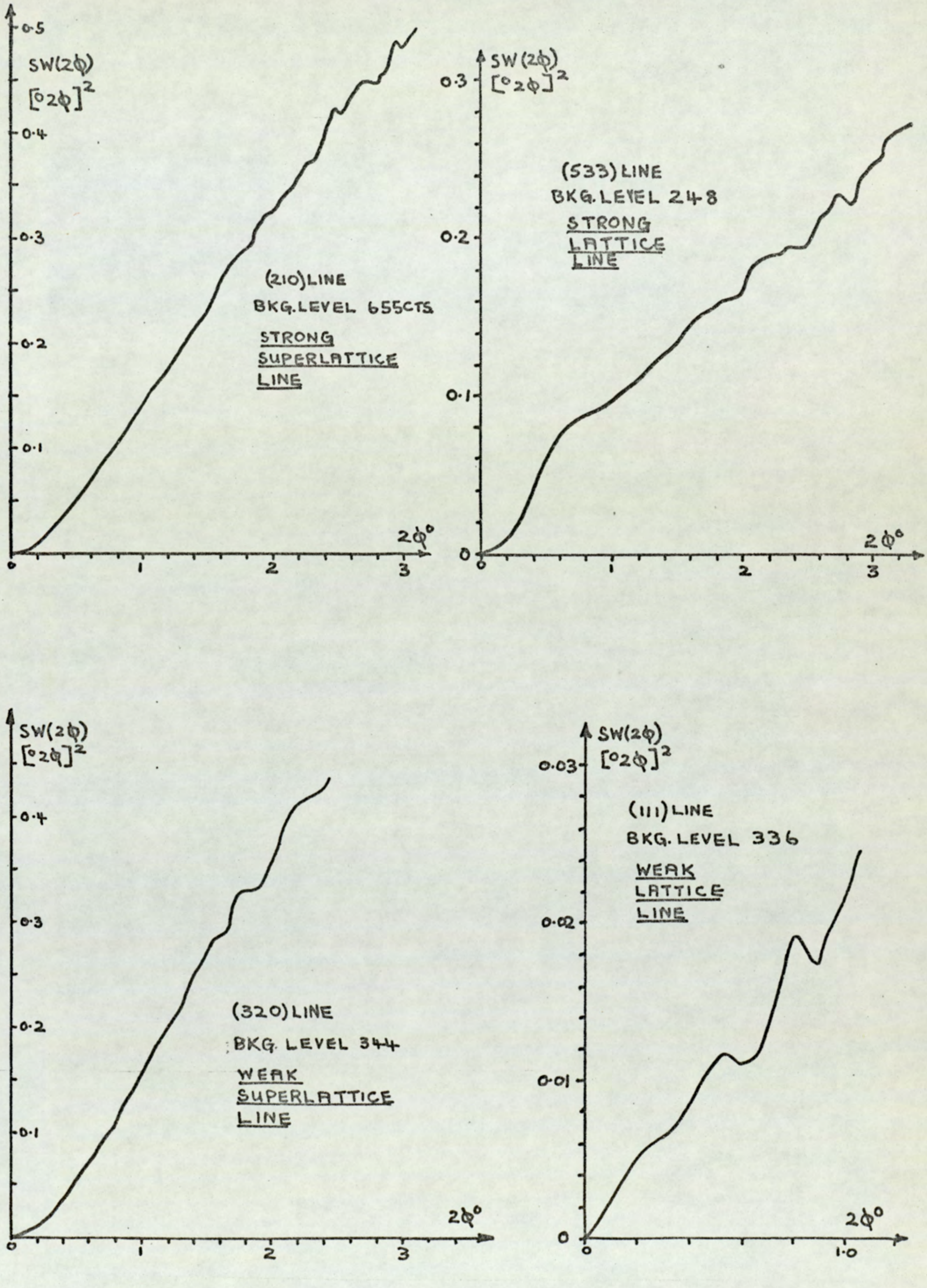

Fig.3.19 Pseudo-variance-range characteristics at variance optimized background levels - sample LF725.

using, in both cases, the variance optimized background levels. These comparisons are presented in Figs.3.20,3.21,3.22 and 3.23. The general trends in the above figures may be summarised as follows:-

(i) For sharp lines, $k > k'$ and $W'_o > W_o$

(ii) For diffraction broadened lines $k' > k$ and $W_o > W'_o$.

These results concur with the results obtained from the simulated profiles (see Tables 3.5 and 3.6) where the coefficient of the hyperbolic term in $W(\Delta\lambda)$ is negative for sharp profiles and positive for broadened profiles.

According to Wilson (1970) the variance and consequently pseudo-variance are quite accurately represented in the tails of a line profile by expressions of the form

$$W(2\theta) = S.2\theta + I + C/2\theta + D.(2\theta)^3$$

and

$$SW(2\theta) = 2S.2\theta + I + 4D.(2\theta)^3$$

where $D \simeq$ Background Error/12.Integrated Intensity.

In least squares analysis the measured slopes, k and k', and intercepts W_o and W'_o from variance and pseudo variance are related to S,C and D through the following relations,

$$k = S + \frac{D.(\langle x^4\rangle - \langle x^3\rangle.\langle x\rangle)}{\langle x^2\rangle - \langle x\rangle^2} - \frac{C.(\langle x\rangle.\langle x^{-1}\rangle - 1)}{\langle x^2\rangle - \langle x\rangle^2} ,$$

$$W_o = I - \frac{D.(\langle x^4\rangle.\langle x\rangle - \langle x^3\rangle.\langle x^2\rangle)}{\langle x^2\rangle - \langle x\rangle^2} + \frac{C.(\langle x^2\rangle.\langle x^{-1}\rangle - \langle x\rangle)}{\langle x^2\rangle - \langle x\rangle^2} ,$$

$$k' = S + \frac{2D.(\langle x^4\rangle - \langle x^3\rangle.\langle x\rangle)}{\langle x^2\rangle - \langle x\rangle^2} ,$$

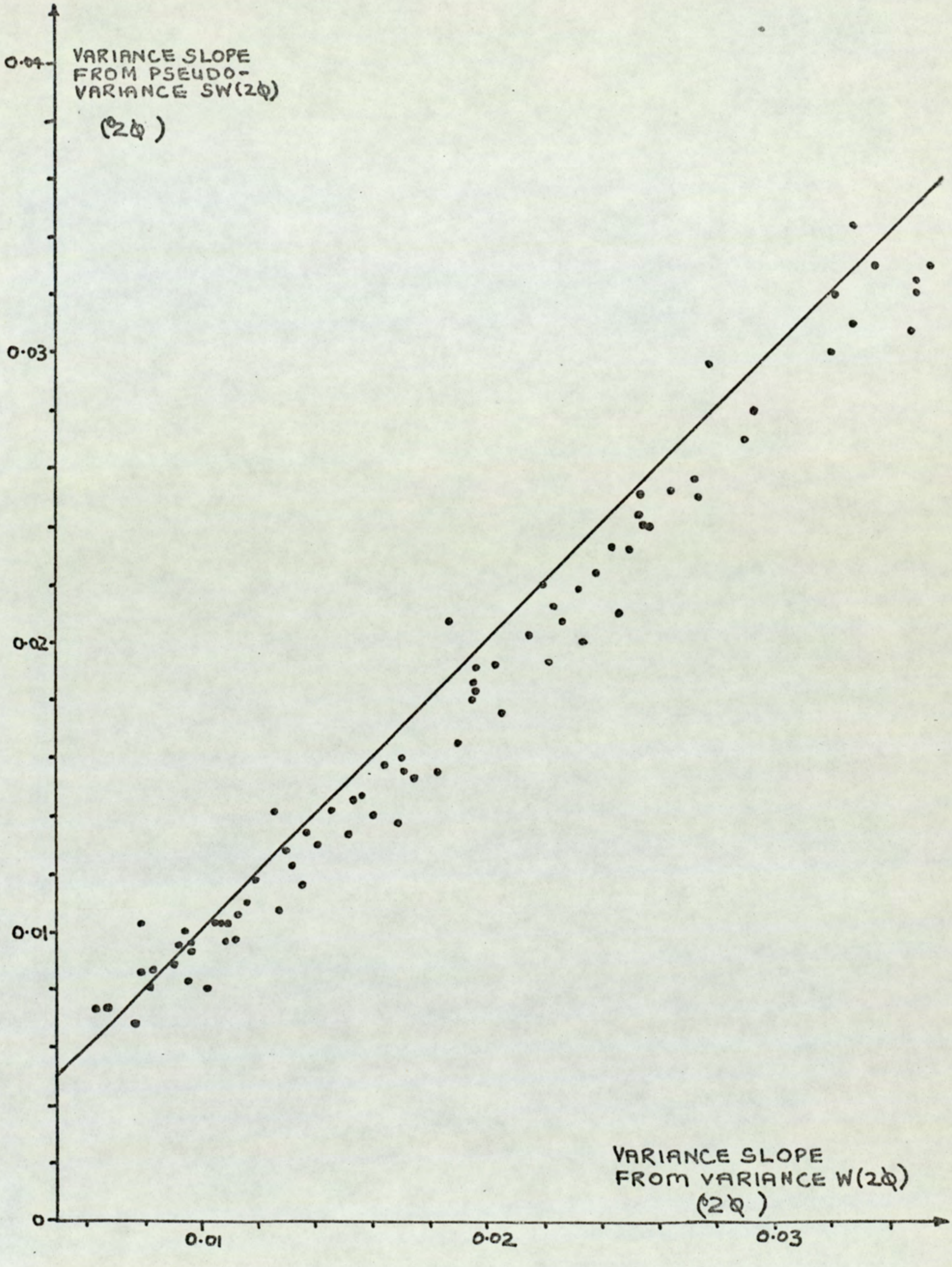

Fig.3.20 Comparison of variance slope with its equivalent derived from pseudo-variance for lattice lines. (exact agreement is indicated by the solid line).

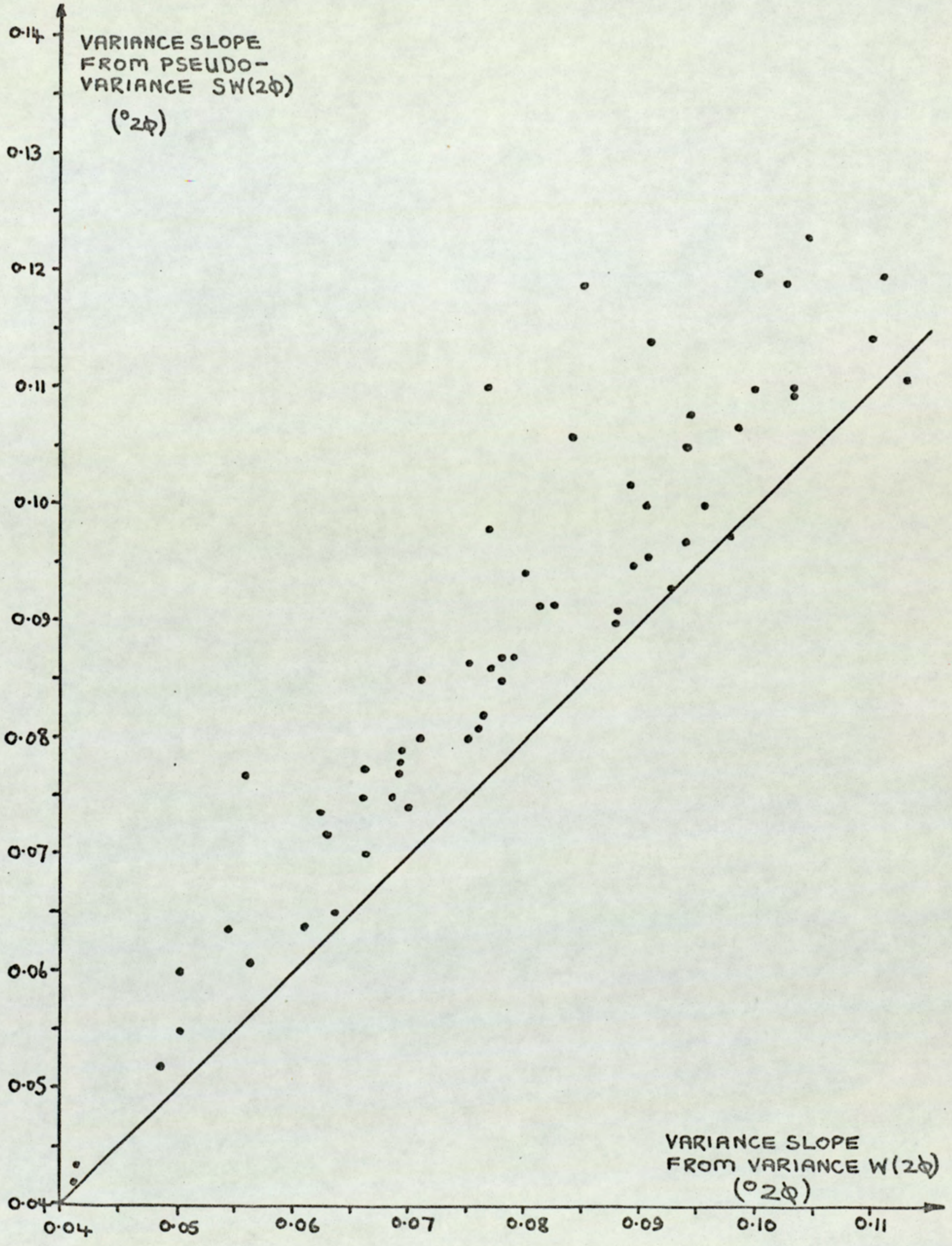

Fig.3.21 Comparison of variance slope with its equivalent derived from pseudo-variance for broadened superlattice lines (exact agreement is indicated by the solid line).

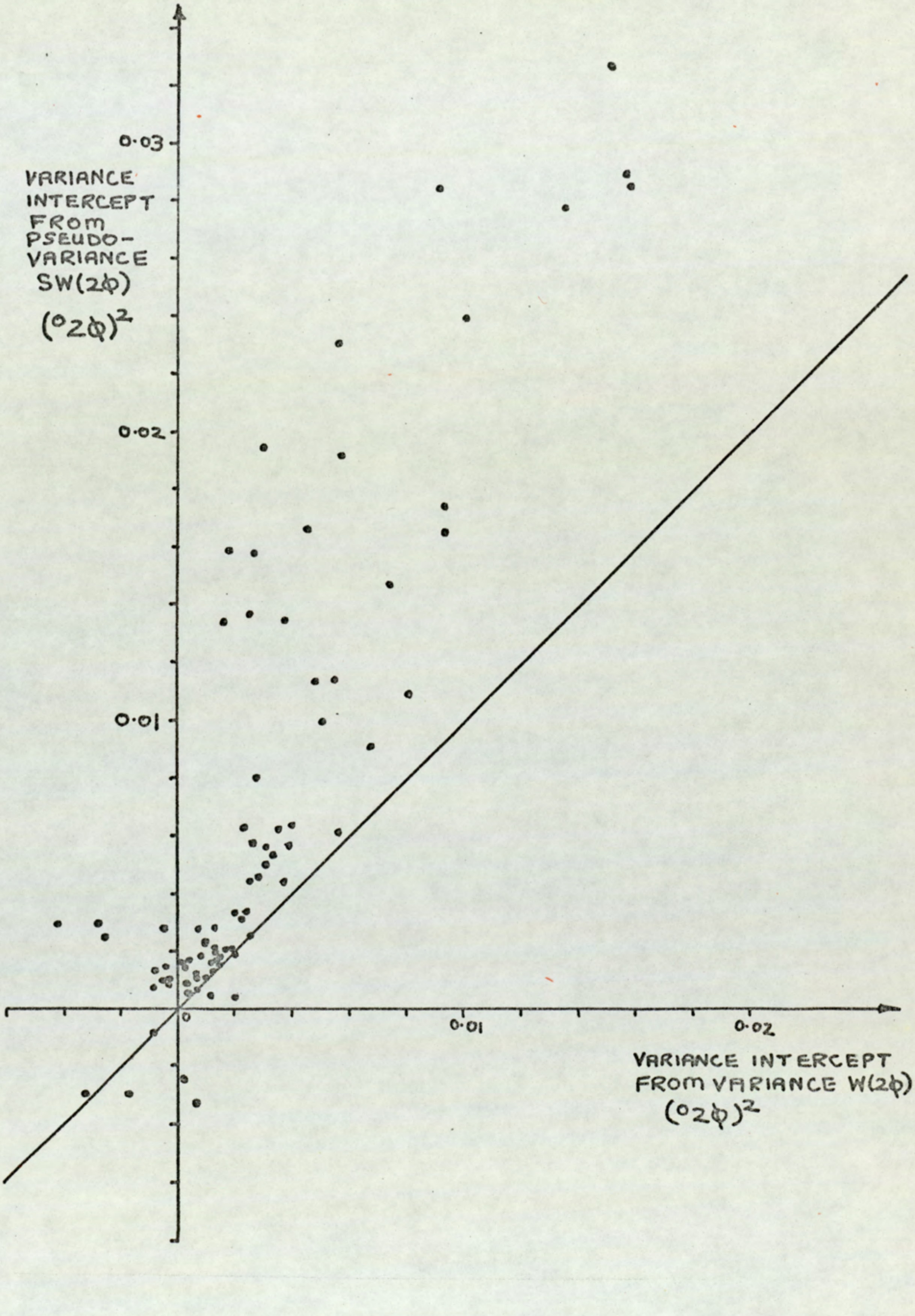

Fig.3.22 Comparison of variance intercept with its equivalent derived from pseudo-variance for lattice lines (exact agreement is indicated by the solid line).

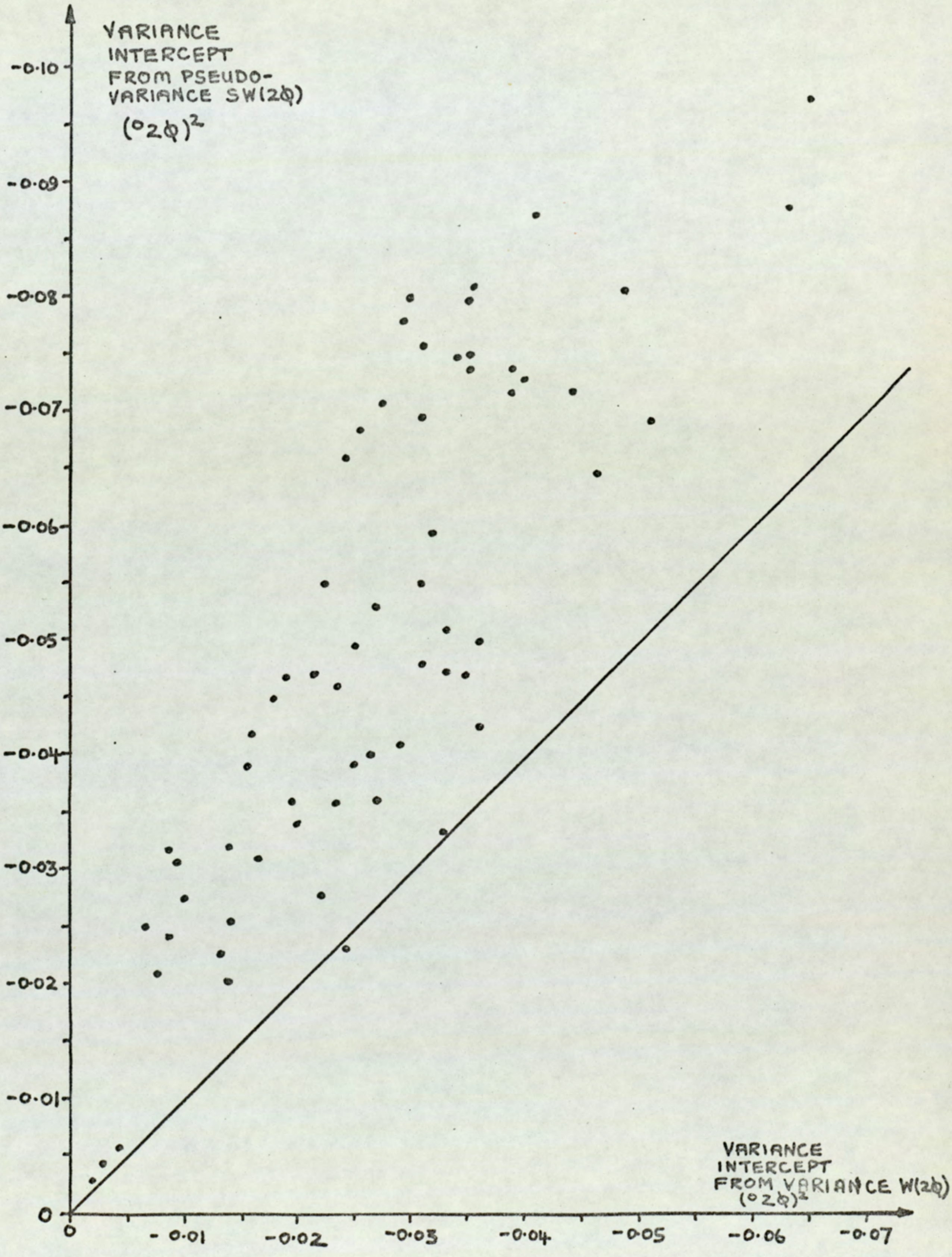

Fig.3.23 Comparison of variance intercept with its equivalent derived from pseudo-variance for broadened superlattice lines (exact agreement is indicated by the solid line).

$$W'_o = I - \frac{2D.(\langle x^4\rangle.\langle x\rangle - \langle x^3\rangle\langle x^2\rangle)}{\langle x^2\rangle - \langle x\rangle^2}$$

$$\text{i.e. } k' - k = \frac{C.(\langle x\rangle.\langle x^{-1}\rangle - 1)}{\langle x^2\rangle - \langle x\rangle^2} + \frac{D.(\langle x^4\rangle - \langle x^3\rangle.\langle x\rangle)}{\langle x^2\rangle - \langle x\rangle^2}$$

$$\text{and } W'_o - W_o = -\frac{C.(\langle x^2\rangle\langle x^{-1}\rangle - \langle x\rangle)}{\langle x^2\rangle - \langle x\rangle^2} - \frac{D.(\langle x^2\rangle.\langle x^3\rangle - \langle x^4\rangle.\langle x\rangle)}{\langle x^2\rangle - \langle x\rangle^2}$$

where $\langle x^n\rangle$ = expected value of $(2\phi)^n$ over the chosen linear region and the coefficients of C and D>0. For the diffraction broadened lines the sign of C is almost certainly positive since

(i) $d^2W(2\phi)/d(2\phi)^2$ is always positive in the region preceding the linear region,

(ii) the slope derived from the variance normalised with respect to the total integrated intensity is nearly always greater than the slope of the variance normalised with respect to the total integrated intensity (see Fig.3.24). In the former the hyperbolic term proportional to $-A'''(0)/A(0)$ is supplemented by a term proportional to $A'(0)/A(0).A''(0)/A(0)$ which, in this instance, is negative. Thus it must be inferred that $-A'''(0)/A(0)>0$ since the measured variance slopes from $W(2\phi)$ are increased by the extra term.

For the strong lattice lines C appears to be negative as

(i) curve fitting analysis of some of the variance-range characteristics gave C as negative,

(ii) $d^2W(2\phi)/d(2\phi)^2$ is always negative in the region preceding the linear region,

(iii) the inequalities $k>k'$ and $W'_o>W_o$ are maintained in some cases (e.g.(220),(311),(440) lines) for a large range of background levels.

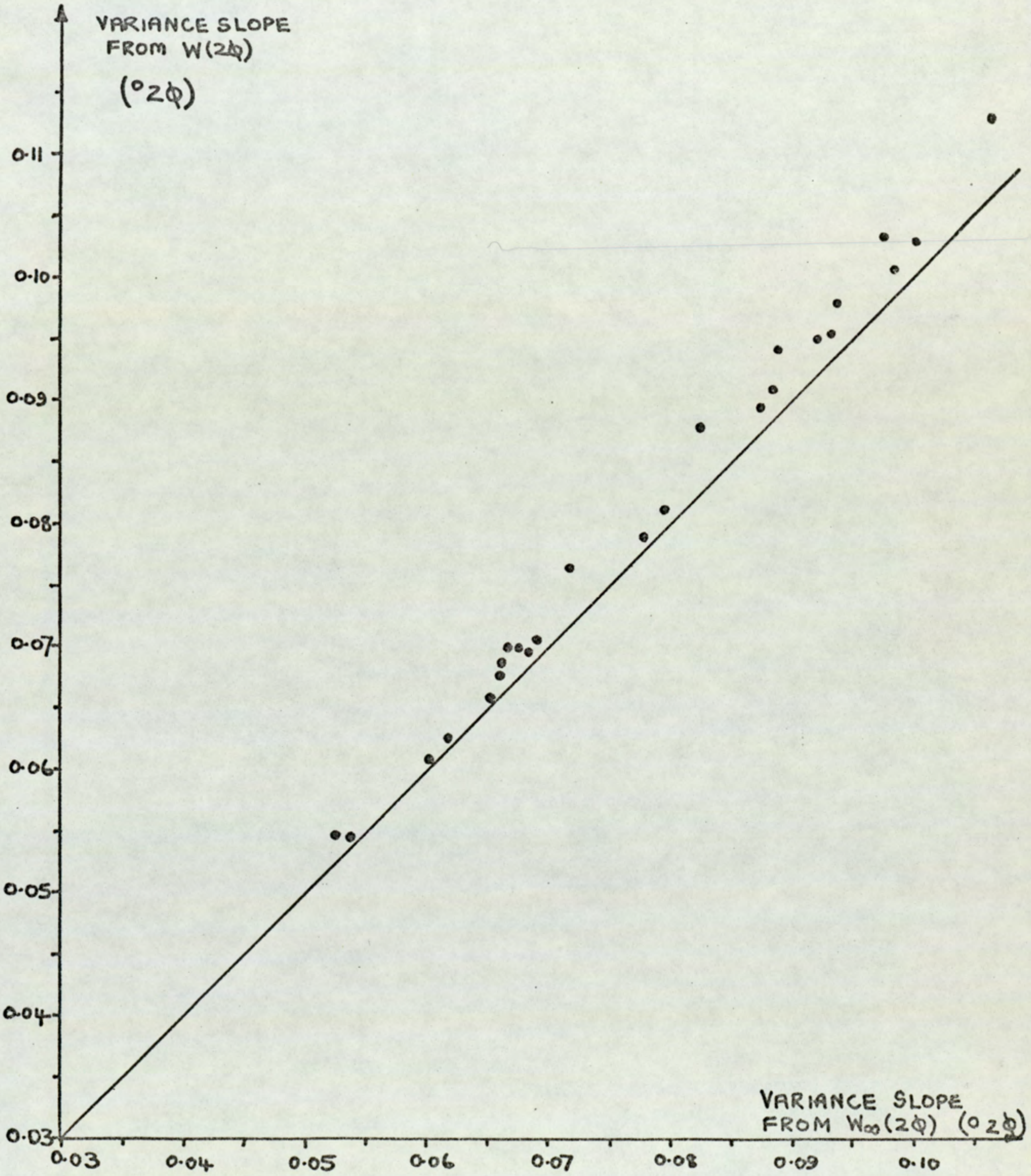

Fig.3.24 Comparison of variance slope from $W(2\phi)$ with that derived from $W_{\infty}(2\phi)$ (Exact agreement is indicated by the solid line).

Now for an optimized variance-range function $dW(2\phi)/d(2\phi)$ should be comparable at each end of the chosen linear region (i.e. $2\phi_1$ to $2\phi_2$) so that $D \simeq - C/3.(2\phi_1)^2.(2\phi_2)^2$. It follows therefore that the sharp lines are optimized with $D \gtrsim 0$ and the diffraction broadened lines with $D \lesssim 0$. Thus, in all the experimental ranges of breadth considered,

$$|k' - k| = |\text{hyperbolic effect}| - |\text{background error effect}|$$

and

$$|W_o' - W_o| = |\text{hyperbolic effect}| - |\text{background error effect}|,$$

which indicates that not only is the effect of the hyperbolic term dominant over the background error effect, but also that errors in background estimation are small as the values of the measured slopes k and k' would otherwise differ from S by an unreasonably large extent.

The results of Fourier transform also indicate that errors in background estimation are small because

(i) the values of $- J'(0)/J(0)$, determined by curve fitting $J(t)$ between $t = 5$ and 20Å, were comparable with the corresponding values derived from the instrumentally corrected pseudo variance slopes (see Table 3.7)

(ii) in no case did the measured and extrapolated values of $J(0)$ differ by more than 1.5% (see Figs.6.4(a) to (j) in Chapter 6).

Table 3.7 Comparison of $-J'(0)/J(0)$ determined from pseudo variance and Fourier analysis.

$-J'(0)/J(0) \times 10^4(\text{Å}^{-1})$ (Fourier)	84	98	108	107	123	132	140	163	156	202
$-J'(0)/J(0) \times 10^4(\text{Å}^{-1})$ (Pseudo-Variance)	88	99	105	110	125	132	146	106	166	202

It was noted during analysis of the simulated profiles that the hyperbolic term behaves almost as a linear modification to the variance over local regions of $\Delta\lambda$. As the ranges of the linear regions considered very rarely exceeded $3^\circ\ 2\phi$ the idea of a linear modification could possibly account for the apparently small background errors. The broadened superlattice lines for instance, are relatively weak and as such only small background errors would be required to rectify the non-linearity of the hyperbolic terms. Conversely, the rate of change of the variance slopes and intercepts of the strong lattice lines with background level was small enough to allow a large background error without affecting the measured slope and intercept values to any great extent. For example, the average change in slope k of the (311) lines for a change of one standard deviation in the background level (i.e. $(b_W)^{\frac{1}{2}}$) is approximately $0.0002(^\circ 2\phi)$ in $0.0100(^\circ 2\phi)$.

3.5.7 Conclusions

It is evident that the influence of the inverse range dependent terms on the estimation of $A'(0)/A(0)$ and $A''(0)/A(0)$ from variance analysis and $A'(0)/A(0)$ from $Z(2\phi)$ analysis is not negligible. Consequently, the interpretation of the diffraction broadening was based on the variance slope and intercept values derived from the (pseudo-variance)-range characteristics at the variance optimized background levels. Adopting this procedure has resulted in a decrease in statistical accuracy of the observed parameters, but this decrease should be counterbalanced by the improved reliability of the parameters, particularly the intercept values.

3.6. Measurement of Integrated Intensities

The integrated intensities of the line profiles were determined from the slopes of the $Z(2\phi)$ functions at the optimized background levels. This is a useful approach as truncation errors are reduced particularly for the cases of diffraction broadened lines and high angle lines. Estimates of the statistical errors $\sigma(I)$ of the integrated intensity values were made according to the equation

$$\sigma(I) = \Delta 2\theta . \left(\sum_{2\theta_j = 2\theta_k - \phi_2}^{2\theta_k + \phi_2} G(2\theta_j) \right)^{\frac{1}{2}}$$

where $G(2\theta_j)$ is the observed intensity level at $2\theta_j$, and $2\phi_2$ is the upper limit of the chosen linear region. This equation is an approximation of the equation given in Wilson (1967).

For the purpose of crystal structure analysis each integrated intensity was corrected for the multiplicity of reflection planes and the trigonometrical factor (i.e. $(1 + \cos^2 2\theta)/(\sin^2\theta\cos\theta)$). The effects of some systematic errors were also considered:

(i) Preferred Orientation

This effect was assumed to be negligible as the crystallites were irregular and experiments with powder discs formed at pressures ranging from 0 - 20tons/sq.in. revealed no significant changes in relative intensities of the diffraction lines.

(ii) Instrumental Aberrations

From the calculations of Jennings and Suortti (1971), it was estimated that the angular correction to the integrated intensities was constant to within 1%.

(iii) Porosity

The average value of μt (μ = linear absorption coefficient for CrKα, t = crystallite size) for the lithium ferrite samples was estimated as 0.3. According to Trucano and Batterman (1970) this value corresponds to an effective powder absorption factor which varies by approximately 1% from $2\theta = 20^\circ$ to 140°. Therefore, no correction was made for porosity.

(iv) Thermal Diffuse Scatter

An approximate estimate of the percentage contribution, Q, of thermal diffuse scatter to the integrated intensities was made according to the calculation of Chipman and Paskin (1959)

$$\text{i.e. } Q = \frac{B.\sin 2\theta.(2\phi)}{240\lambda^2}$$

where B is the temperature factor in $(\text{Å})^2$ and 2ϕ is the range in degrees over which the integrated intensity is measured. In this instance 2ϕ was chosen as the upper limit of the linear region. For lithium ferrite $B \simeq 0.5\text{Å}^2$ (assuming Debye temperature given by Pollack and Atkins (1962)) and a = 8.33Å (Braun,1952) thus at high angles thermal diffuse scatter comprises approximately 1% of the integrated intensity.

CHAPTER 4

ANALYSIS OF STOICHIOMETRY AND AVERAGE CRYSTAL STRUCTURE OF THE LITHIUM FERRITE SAMPLES

4.1 Stoichiometry of lithium ferrite samples

Recently, Pointon and Saull (1969) have demonstrated that above 1000°C lithium ferrite undergoes an irreversible loss of lithium and oxygen which results in the formation of Fe^{2+} ions and, to a varying degree, the precipitation of αFe_2O_3 as a second phase. According to these authors the decomposition of lithium ferrite occurs in two stages:-

Stage 1 lithium and oxygen are lost and Fe_3O_4 is formed,

$$LiFe_5O_8 \rightarrow (1-x)LiFe_5O_8 + \frac{5x}{12}O_2\uparrow + \frac{x}{2}Li_2O\uparrow + \frac{5x}{3}Fe_3O_4$$

Stage 2 some or all of the Fe_3O_4, depending on the temperature and the time of firing, is oxidised by the atmosphere to give αFe_2O_3,

$$(1-x)LiFe_5O_8 + \frac{5x}{3}Fe_3O_4 + \frac{5xy}{12}O_2 \longrightarrow$$

$$(1-x)LiFe_5O_8 + \frac{(1-y)5x}{3}Fe_3O_4 + \frac{5xy}{2}Fe_2O_3$$

According to Ridgley, Lessoff and Childress (1970) the products formed after the first stage of decomposition are equivalent to a solid solution of Fe_3O_4 and lithium ferrite (i.e. $Li_{1-x}Fe^{2+}_{2x}Fe^{3+}_{3-x}O_8$) and that reasonable estimates for the Fe^{2+} ion concentration may be obtained from the lattice parameter a_x by assuming Vegard's law to hold for compositions between lithium ferrite and Fe_3O_4,

$$\text{i.e.} \qquad x = (a_x - a_{LiFe_5O_8})/(a_{Fe_3O_4} - a_{LiFe_5O_8})$$

On the basis of these papers the presence of Fe^{2+} ions in the present lithium ferrite samples is a distinct possibility especially as they were all prepared above 1000°C.

The first indication that some of the samples were not stoichiometric lithium ferrite was given by the presence of weak X-ray diffraction lines associated with αFe_2O_3. No lines due to other iron oxide phases, γFe_2O_3 and Fe_3O_4 in particular, were observed. From the calibration of the peak intensity of the (104) line from αFe_2O_3 relative to the (220) line from $LiFe_5O_8$ given by Ridley et al.(1970), it was possible to estimate approximate values for the volume fraction of αFe_2O_3 in each of the samples. These values are presented in table 4.1.

Table 4.1 Estimates of the αFe_2O_3 content in the group I samples of $LiFe_5O_8$.

Sample	LF-S	LF725	LF735	LF740	LF745	LF-DEC
$\% \alpha Fe_2O_3$	not detectable	not detectable	$\ll 2$	$\ll 2$	$\ll 2$	5.8
I(104)/I(220)	-	-	0.0058	0.0090	0.0028	0.1260

In all the samples except LF-DEC, which was specifically prepared to induce the precipitation of αFe_2O_3, the αFe_2O_3 content was estimated to be very small.

Further evidence that Fe^{2+} ions were present in the structure was given by measurements of the long range order parameter S. As the integrated intensity of the (220) line from lithium ferrite is dependent almost entirely on the tetrahedral site ions (Vishnevskii et al.,1970) and independent therefore of lithium and oxygen losses, reliable values for S are given by

$$S^2 = \left[\frac{I_{hkl}}{I_{220}}\right]_{\substack{\text{PARTIAL}\\ \text{ORDER}}} \Big/ \left[\frac{I_{hkl}}{I_{220}}\right]_{\substack{\text{COMPLETE}\\ \text{ORDER}}}$$

where the I's represent integrated intensities. With the standard sample LF-S as the ordered sample, S was determined from the 3 strongest superlattice lines of the group I lithium ferrite samples. The results are presented in table 4.2.

Table 4.2 Estimates of the long range order parameters from the group I lithium ferrite samples. Statistical accuracy of S~3%.

hkl	LF725	LF735	LF740	LF745
110	0.970	1.045	1.080	1.010
210	0.985	1.055	1.065	1.035
211	0.995	1.060	1.020	1.050

For stoichiometric partially ordered lithium ferrite an order parameter which is greater than unity is physically meaningless. However, if it is assumed that Fe^{2+} ions enter the Li^{+} ion sites during preparation and that the standard sample LF-S contains the highest concentration of these ions, the possibility arises of the order parameter exceeding a value of unity. This follows because the mean atomic scattering factor of Li^{+} ion sites will be increased by the presence of Fe^{2+} ions and as a result the integrated intensities of the superlattice lines, given approximately by $k(f_{Fe\ Site} - f_{Li\ Site})^2$, will be reduced.

The information inferred from observations of the long range order parameter is supported to some extent by the lattice parameters of the samples which are given with their estimated errors in table 4.3. Comparison of this data with the room temperature lattice parameter derived for stoichiometric lithium ferrite according to Ridgley et al. (1970) (i.e. 8.3295 Å) leads to the Fe^{2+} ion concentrations given in the final column if we assume Vegard's law and that a_o for Fe_3O_4 is 8.3940 Å (Abrahams and Calhoun, 1953). The graphs of a_{hkl} against $f(\theta)$, the extrapolation function, from which the lattice parameters were determined are given in Fig.4.1.

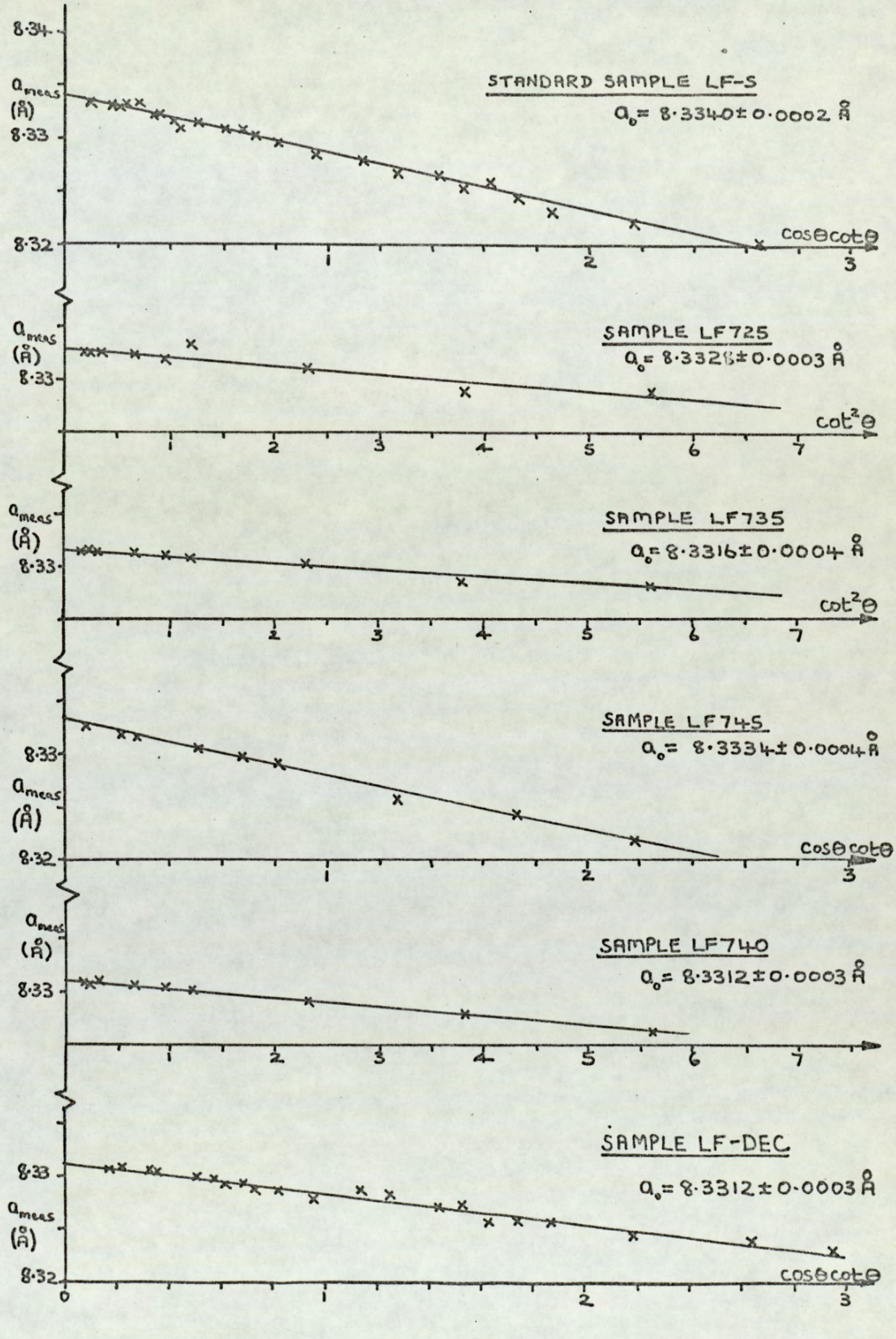

Fig. 4.1 Plots of a_{hkl} versus f(θ) for the group I lithium ferrite samples.

Table 4.3 Lattice parameters of group I lithium ferrite samples together with the estimated Fe^{2+} ion concentrations (nominal temperature of measurement 22°C)

Sample	a(Å)	Δa(Å)	% Li Sites occupied by Fe^{2+} ions
LF-S	8.3340	0.0002	6.9
LF725	8.3328	0.0003	5.1
LF735	8.3316	0.0004	3.2
LF740	8.3312	0.0004	2.6
LF745	8.3334	0.0003	6.0
LF-DEC	8.3312	0.0003	2.6

As expected the lattice parameters are all greater than the stoichiometric lithium ferrite value of 8.3295 Å. If a correction for the presence of Fe^{2+} ions is applied to the measured long range order parameters in table 4.2 by assuming

(a) the estimated Fe^{2+} ion concentrations given in the table of lattice parameters,

(b) random mixing of the Fe^{2+} ions and Li^{+} ions, and Fe^{2+} ions and Fe^{3+} ions on their respective sites so that,

$$f_{Li^+ \text{sites}} = x f_{Fe^{2+}} + (1-x) f_{Li^+}$$

and

$$f_{Fe^{3+}\text{sites}} = \frac{x}{3} f_{Fe^{3+}} + \left(1 - \frac{x}{3}\right) f_{Fe^{2+}}$$

where x is the fraction of Li^{+} ion sites occupied by Fe^{3+} ions,

(c) $|F_{hkl}| \simeq k\left(f_{Fe^{3+}\text{sites}} - f_{Li^+\text{sites}}\right)$ for the superlattice lines so that,

$$S_{\text{CORRECTED}} \simeq S_{\text{MEASURED}} \cdot \frac{|F_{\text{CALC}}|_{\text{CORRECTED}}}{|F_{\text{CALC}}|_{\text{UNCORRECTED}(x=0)}}$$

the values for the long range order parameter become more acceptable (see table 4.4).

Table 4.4 Long range order parameters given in table 4.2 corrected for the influence of Fe^{2+} ions.

hkl	LF725	LF735	LF740	LF745
110	0.940	0.995	1.010	1.000
210	0.955	1.005	1.005	1.025
211	0.965	1.010	0.965	1.040

As the present results are internally consistent and consistent with published work the view has been taken that the present lithium ferrite samples are each equivalent to a solid solution of Fe_3O_4 and lithium ferrite. The variability of the estimated Fe^{2+} ion concentrations is attributed to differences in the individual preparation procedures (e.g. firing temperatures slightly different, samples held at different positions in furnace).

When sample LF740 was reheated to induce the precipitation of αFe_2O_3 (i.e. sample LF-DEC) no change was observed in the lattice parameter which would indicate that although extensive decomposition occured it did so on the surface of the crystallites leaving the interiors stoichiometrically unchanged. This is corroborated by the results from line breadth analysis (see chapter 5, section 1).

4.2 Redetermination of the average crystal structure for lithium ferrite

According to Braun (1952) the space group of lithium ferrite is $P4_332$ (Cubic) and therefore the atomic positions of all the ions except lithium, are incompletely specified. In the present work the symbols accorded to the unspecified parameters are as follows:-

(i) Fe^{3+} ions on the tetrahedral sites: t,

(ii) Fe^{3+} ions on the octahedral sites: b,

(iii) O^{2-} ion parameters: x, y, z and u.

An illustration of part of the lithium ferrite structure is given in Fig. 4.2 to demonstrate the relation between these parameters and the atomic positions.

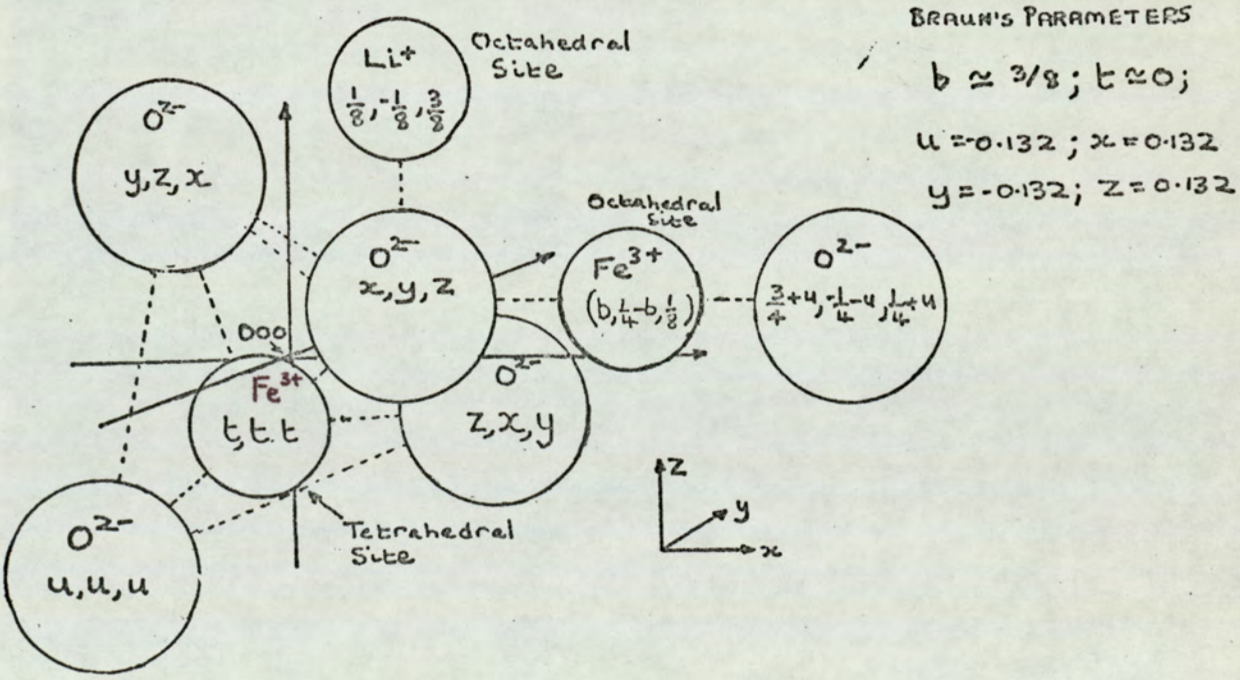

Fig.4.2 An illustration of the unspecified parameters for lithium ferrite given by the space group $P4_332$.

Braun's values for these unspecified parameters are $x = -y = z = -u = 0.132$, $t = \Delta_1$ where $0<\Delta_1<0.007$, and $b = 0.375 + \Delta_2$ where $0<\Delta_2<0.007$. The validity of these estimates however, is questionable because

(i) diffuse X-ray scattering measurements by Brunel and Bergevin (1966) on disordered lithium ferrite indicated that the Fe^{3+} ions on the octahedral sites are shifted from their ideal spinel positions where $b = 0.375$ to positions corresponding to $b = 0.365$,

(ii) the $Li^{+} - O^{2-}$ distance calculated from the x, y and z parameters and lattice parameter is 0.09 Å smaller than any published $Li^{+} - O^{2-}$ distance in similar coordinations conditions (for a bibliography of the publications see Shannon and Prewitt, 1969).

In view of these discrepancies and the possibility that shifts of the ions from their ideal spinel positions introduce distorted anti-phase domain boundaries a redetermination of the structure parameters has been carried out on the basis of the space group proposed by Braun.

According to the theory of X-ray diffraction from powders in the form of a thick slab, the integrated intensity I_{OBS} of an (hkl) profile corrected for the angular and multiplicity factors is given by

$$I_{OBS} = K|F_{hkl}|^2 e^{-2B\sin^2\theta/\lambda^2} \qquad \text{(James, 1948)}$$

where K is a constant of proportionality, $|F_{hkl}|$ is the modulus of the (hkl) structure factor and B is the overall temperature factor. This relation shows that when the structure parameters are optimised and used to calculate the structure factors F_{hkl}, the graph of $\log_e(|F_{calc}|^2/I_{OBS})$ against $(h^2 + k^2 + l^2)$ should be linear. It was therefore assumed that this condition could be employed to determine the structure parameters, deviations from linearity being interpreted as arising from errors in one or more of these parameters. The atomic scattering factors used in the computer calculations of $|F_{CALC}|^2$ were taken from volume 3 of the International Tables for X-ray Crystallography (1962) in the cases of the Fe^{2+}, Fe^{3+} and Li^+ ions and from Klug and Alexander (1954) in the case of the O^{2-} ions. Corrections were made for the dispersion effects of Cr Kα radiation (International Tables for X-ray Crystallography (1962), Vol.3).

Initially the structure factors were calculated according to the parameters given by Braun (1952). It was immediately obvious however from the $\log_e(|F_{CALC}|^2/I_{OBS})$ versus N plot ($N = h^2 + k^2 + l^2$) for the standard sample LF-S (see Fig.4.3a) that these parameters were in error. Substantial discrepancies existed even when the atomic scattering factors were corrected for the presence of Fe^{2+} ions (see Fig.4.3b) as described in section 4.1. From an estimate of the scaling constant K obtained by fitting a straight line through the lattice line values of $\log_e(|F_{CALC}|^2/I_{OBS})$ the calculated structure factors for the (211) and (320) superlattice lines, in particular, differed from the observed values by more than 40%. These discrepancies were significant for they were also observed with other lithium ferrite samples.

From an approximate analysis of the variation of the calculated structure factors as a function of the parameters t,b,u,x,y, and z it was clear that agreement with observation could be improved by adjustment of Braun's parameters. Refinement of Braun's structural parameters was achieved by a form of linear analysis on the results of the standard sample LF-S. In this analysis, it was assumed that the values of $\log_e(|F_{CALC}|^2/I_{OBS})$ for the lattice lines were reasonably correct even though the structural parameters were in error, for these lines are relatively insensitive to small structural changes. On this basis a straight line was fitted to the lattice line values of $\log_e(|F_{CALC}|^2/I_{OBS})$ versus N. Discrepancies D_{hkl} were estimated for

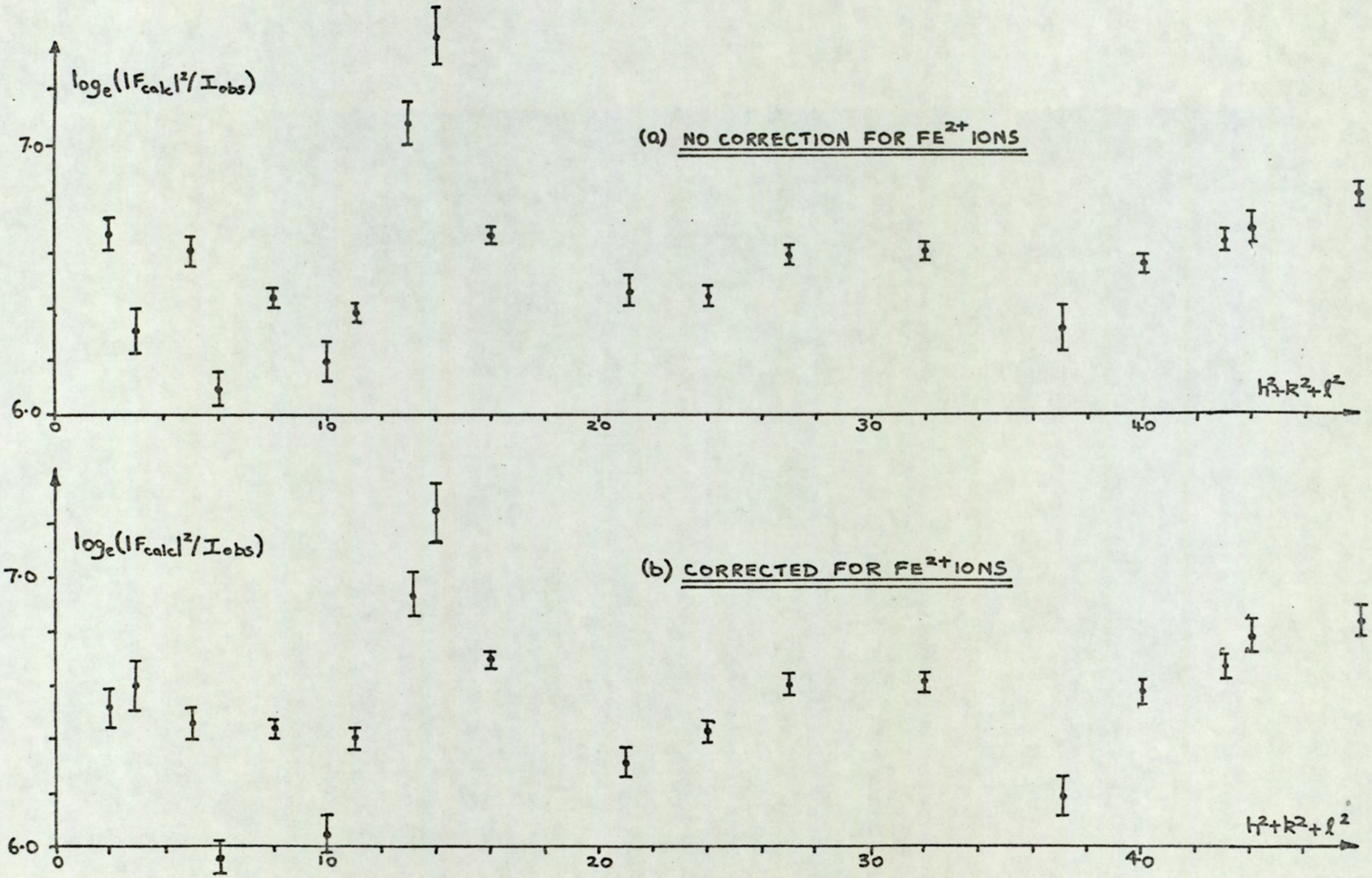
(a) NO CORRECTION FOR FE^{2+} IONS

(b) CORRECTED FOR FE^{2+} IONS

<u>Fig. 4.3</u> $\mathrm{Log}_e(|F_{CALC}|^2/I_{OBS})$ versus $(h^2 + k^2 + 1^2)$ for the lithium ferrite standard sample LF–S. Structural parameters: $t = 0$, $b = 0.375$, $x = -y = z = -u = 0.131$,

these plotted values and those for the superlattice lines. As approximate values for the structural parameters were known, these discrepancies for six reflexions particularly dependent on the structural parameters were expressed as linear equations in the corrections δu_i ($i = 1,2,3,4,5$ and 6) to the parameters,

$$D_{hkl} = \log_e(|F_{OBS}|^2/I_{OBS}) - \log_e(|F_{CALC}|^2/I_{OBS})$$

$$= \sum_{i=1}^{6} \frac{\partial \log_e(|F_{CALC}|^2/I_{OBS})}{\partial u_i} \,.\, \delta u_i$$

where the differential coefficients were calculated numerically. Improved values for the parameters were obtained by solving the six equations. This procedure was repeated, but with a varying set of six reflections until the corrections δu_i were smaller than the estimated errors of the parameters. The reason for using six reflections in the refinement arises from the fact that the linear equations were solved manually to enable a subjective allowance to be made for statistical errors in the observed integrated intensities.

Without a correction for the presence of Fe^{2+} ions it was found that

(i) the calculated structure factors would not converge to an R factor $\left(\text{i.e.} \sum_{hkl} \big||F_{OBS}|-|F_{CALC}|\big| \Big/ \sum_{hkl} |F_{OBS}| \right)$ of better than 8%,

(ii) the parameters obtained at this optimum R factor were not compatible with published inter-ionic distances.

Consequently, the atomic scattering factors were corrected as described in section 4.1 for the presence of Fe^{2+} ions in the octahedral sites. The convergence of the R factor and sensibility of the results was thereby much improved. The structure factors of most of the reflections tend to be least dependent on the oxygen ion parameters and as a result improved agreement with experiment was achieved primarily by adjusting the unspecified octahedral and tetrahedral site ion parameters (i.e. t and b). The reliability of the parameters obtained from the refinement procedure carried out on the standard sample LF-S is demonstrated by the consistency of the optimised $\log_e(|F_{CALC}|^2/I_{OBS})$ versus N graph for this sample, given in Fig.4.4a, with similar graphs for samples LF735 and LF740, given in Fig.4.4b and c, using the same values for the structure parameters (the latter samples were used for structure analysis because their corrected order parameters were very close to unity - see table 4.4). The values of $|F_{OBS}|^2$ and $|F_{CALC}|^2$ at the optimised parameters are given together with the R factors (expressed as percentages) and temperature factors in table 4.5 (for mixed reflections $|F|^2$ is given as $m_1F_1^2 + m_2F_2^2$ and for R factor calculation $|F|$ taken as $((m_1F_1^2 + m_2F_2^2)/(m_1 + m_2))^{\frac{1}{2}}$).

The structure parameters obtained through the refinement procedure were as follows:-

$b = 0.368 \pm 0.002,$

$t = -0.003 \pm 0.002,$

$u = -0.135 \pm 0.004,$

$x = 0.131(5) \pm 0.004,$

$y = -0.129(5) \pm 0.004$

$z = 0.123 \pm 0.004,$

where the errors were estimated by varying the optimised parameters separately until it was clear that the $\log_e(|F_{CALC}|^2/I_{OBS})$ versus N graph for sample LF-S was no longer linear. Additional justification for the measured parameters is given by,

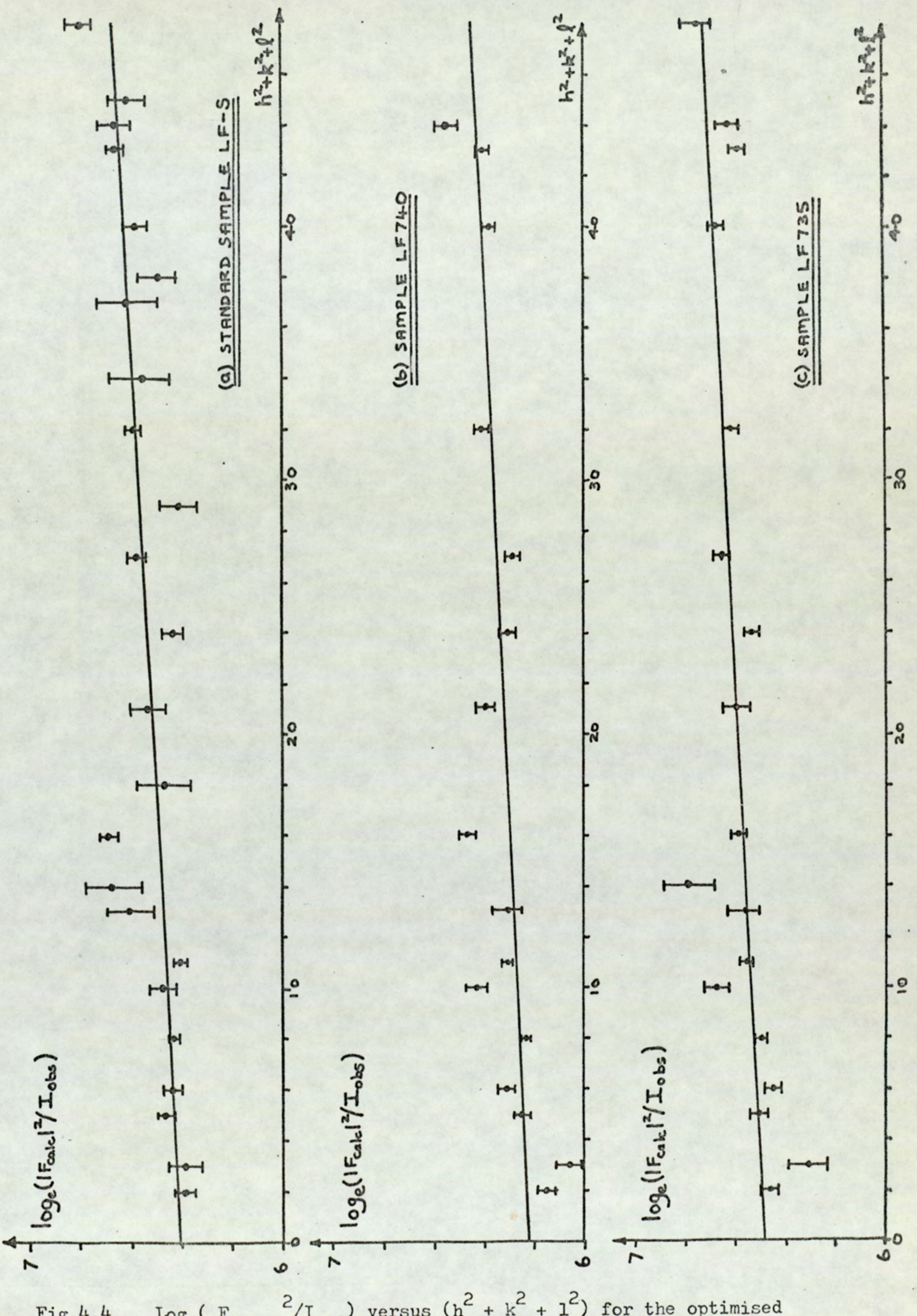

Fig.4.4 $\log_e(F_{CALC}{}^2/I_{OBS})$ versus $(h^2 + k^2 + l^2)$ for the optimised structural parameters b = 0.368, t =-0.003, u =-0.135, x = 0.1315, y =-0.1295 and z = 0.123. (a) standard sample LF-S (b) sample LF740 (c) sample LF735.

Table 4.5 $|F|^2_{OBS}$ and $|F|^2_{CALC}$ values together with the R factors and temperature factors (B) for lithium ferrite.

	Sample LF-S		Sample LF740		Sample LF735	
hkl	F^2_{CALC}	F^2_{OBS}	F^2_{CALC}	F^2_{OBS}	F^2_{CALC}	F^2_{OBS}
110	1065	1090	1190	1260	1160	1180
111	630	650	545	640	560	670
210	2230	2150	2470	2420	2420	2510
211	1750	1745	1900	1760	1870	1960
220	22810	23400	22810	23000	22810	23300
310	1470	1440	1591	1360	1570	1340
311	45550	48700	44900	42900	45030	43800
320	1260	1110	1420	1380	1380	1350
321	480	400	-	-	530	410
400	53270	43900	51970	43300	52230	50200
411 330	21390	22400	-	-	-	-
421	1780	1740	1940	1850	1910	1870
422	14890	16550	14890	15300	14890	15800
511 333	1045000	1011000	1029000	1110000	1031500	983000
520 432	79100	91200	-	-	-	-
440	154270	150000	152250	147000	152820	155000
530 433	46300	46800	-	-	-	-
610	1560	1530	-	-	-	-
611 532	59150	67700	-	-	-	-
620	10720	11050	10720	11150	10720	10650
533	22210	21550	21900	22100	21960	24400
622	4540	4400	4260	3710	4320	4590
542 630	60590	62500	-	-	-	-
444	18590	16200	-	-	18160	17100
Temp. Factor (B)	0.70 ± 0.10 Å^2		0.65 ± 0.15 Å^2		0.65 ± 0.10 Å^2	
R Factor	3.25%		3.10%		2.30%	

(a) the agreement of the inter-ionic distances with previous published distances - see table 4.6. A bibliography of these publications has been collected by Shannon and Prewitt (1969)

(b) the approximate agreement between the Debye temperature estimated from each temperature factor and the Debye temperature estimated from the low temperature specific heat of lithium ferrite (Pollack and Atkins, 1962) - see table 4.6.

Table 4.6 Comparison of the measured inter-ionic distances and Debye temperatures from the present analysis with the average values from previous published data.

		PRESENT ANALYSIS	PUBLISHED DATA
$Li^+ - O^{2-}$ (xyz) type		2.10 ± 0.03Å	2.13 ± 0.05Å
Fe^{3+}(Oct) - O^{2-}(uuu) type		2.06 ± 0.04Å	2.02 ± 0.02Å
Fe^{3+}(Oct) - O^{2-}(xyz)type		1.97 ± 0.04Å	2.02 ± 0.02Å
Fe^{3+}(tet) - O^{2-}(uuu)type		1.90 ± 0.04Å	1.87 ± 0.01Å
Fe^{3+}(tet) - O^{2-}(xyz)type		1.87 ± 0.03Å	1.87 ± 0.01Å
Debye Temperatures	LF-S	410 ± 70°K	512°K
	LF735	440 ± 70°K	
	LF740	440 ± 100°K	

The positions of the ions in lithium ferrite as estimated in the present analysis are not markedly different from those of a spinel structure. The "distortions" seem to be explainable purely on the basis of the sizes of the constituent ions. The shifts of the Fe^{3+} ions on the tetrahedral and octahedral sites from spinel positions are 0.04Å in ⟨111⟩ directions and 0.08Å in ⟨110⟩ directions respectively. In spite of these shifts the cations still retain, within

0.02Å, centre of gravity positions in the oxygen polyhedra. In each of the tetrahedral groups three of the oxygen ions are located from the parameters x, y and z, the other one being located from the parameter u. In each of the octahedral groups associated with Fe^{3+} ions two of the oxygen ions are located from the parameter u (these ions are in the same plane as the Fe^{3+} ion shift) whilst the other four are located from the parameters x, y and z. The remaining octahedral groups, which are associated with the Li^{+} ions, contain oxygen ions located from the parameters x, y and z. Table 4.6 in fact, gives a complete list of nearest neighbour cation-anion distances in lithium ferrite.

CHAPTER 5

RESULTS FROM PSEUDO-VARIANCE ANALYSIS OF LINE PROFILES

5.1 Pseudo-variance analysis of sharp diffraction line profiles

Before examination of the diffraction broadened profiles it was necessary to consider the instrumental contribution to their line breadths. This was done through analysis of the stronger lattice line profiles from the lithium ferrite samples LF-S, LF725, LF735, LF740 and LF745. The variance slopes and intercepts determined from the (pseudo-variance)- range characteristics of these profiles together with their mean standard errors due to counting statistics are given in tables 5.1 and 5.2. Also given in these tables are the variance results for the sample LF-DEC.

The variance results obtained from the lattice lines of the standard sample LF-S are comparable with variance results obtained from the lines of well crystallised powders of the "normal" spinel $MgCr_2O_4$ (Hilleard (1969), Waters (1969)). The deviations of the variance results obtained for the lattice lines of samples LF725, LF740 and LF745 relative to the variance results for the standard sample LF-S did not exhibit any significant correlations with either the estimated Fe^{2+} ion content or the mean anti-phase domain thickness. Consequently, structural distortions caused by the Fe^{2+} ions or the anti-phase domain boundaries not being ideally continuous with respect to the atomic coordinates were assumed to be, at most, of second order importance in the breadth of the lattice lines.

A feature which did appear to affect the lattice line breadths was the precipitation of αFe_2O_3. After sample LF740 was annealed at 950°C to form sample LF-DEC definite increases in the variance slopes and decreases in the variance intercepts were observed together with

Table 5.1 Variance slopes x$10^4(2\theta^{o})$ of lattice lines of lithium ferrite.

hkl	Sample LF-S	Sample LF725	Sample LF735	Sample LF740	Sample LF745	Sample LF-DEC	Estimated Error
220	85	89	96	81	82	110	3
311	93	96	103	103	97	134	2
400	140	147	121	145	130	224	5
422	160	187	188	174	193	251	8
511/333	212	192	221	180	192	252	6
440	202	220	219	233	236	330	6
620	325	349	296	244	330	-	18
533	348	362	326	347	343	407	12
440	550	495	453	-	545	-	30

Table 5.2 Variance intercepts x$10^4((2\theta^{o})^2)$ of lattice lines of lithium ferrite.

hkl	Sample LF-S	Sample LF725	Sample LF735	Sample LF740	Sample LF745	Sample LF-DEC	Estimated Error
220	15	16	4	16	8	11	2
311	20	22	14	16	21	10	1
400	21	20	34	17	21	-30	2
422	45	16	20	25	24	-14	4
511/333	45	64	14	54	62	15	4
440	91	84	63	64	81	0	3
620	175	132	137	232	167	-	3
533	279	240	286	290	337	80	5
444	705	715	713	-	670	-	12

a large increase in the αFe_2O_3 content and no change in the lattice parameter (see Chapter 4, section 1). As the changes in the variance slopes and intercepts varied approximately with θ as secθ and sec$^2\theta$, respectively, the broadening was attributed to the crystallites being small (approximately 1300Å). This result reinforces the earlier conclusion that αFe_2O_3 forms on the surfaces of the lithium ferrite crystallites leaving the crystal structure of the interiors of the crystallites unaffected.

Of the other samples LF725 is the only one for which the variance slopes and intercepts tend to be consistently greater and less respectively than those for the standard sample LF-S. The variance results for samples LF735, LF740 and LF745 tend to be scattered evenly about those of the standard sample even though traces of αFe_2O_3 were detected in each of them. Despite the consistency, the deviations of the results for sample LF725 (equivalent to an apparent particle size in the region of 6000Å) were not considered significant because,

(i) the extent of the deviations showed no strong tendencies to increase with θ as would be expected if the broadening were caused by strain, stacking faults or small crystallites,

(ii) no signs of lines due to αFe_2O_3 were evident in the diffraction patterns.

As the breadths of the lattice lines of each sample (except LF-DEC) were apparently uncorrelated with any "extraneous" physical effect, it was concluded that the scatter of the observed variance results was statistical in origin. Thus, for the purpose of instrumental correction the variance slope and intercept of each lattice line was taken to be the mean value given by averaging over all the results in table 5.1 except those for sample LF-DEC. These values are listed in table 5.3 together with the standard errors due to the scatter of the original results. It is to be noted that the original values for the standard error were underestimated. This is to be expected as they were calculated solely for the effect of random fluctuations in the measured intensity values. It must be accepted that errors will also be propagated as a result of correcting the variance results for the influences of the satellite group and the hyperbolic term, variations in the conditions of the powder samples (e.g. surface roughness, presence of large crystallites) and time varying parameters such as atmospheric conditions. Besides raising the levels of standard error, the averaging procedure also results in smooth variations for the variance slope and intercept as functions of 2θ (see Fig.5.1). Even so, this does not preclude the possibility of there being some small "extraneous" line broadening associated with some of the specimens. However, as the standard errors of the variance results of the broadened profiles (given in next section) tend to exceed the maximum scatter of each lattice line result, the reliability of the instrumentally corrected variance results will not be unduly impaired by slightly mis-represented lattice line results. In consequence, the variance slopes and intercepts attributed to the sharp superlattice lines were taken from the smooth curves given in Fig.5.1.

Table 5.3 Mean variance slopes $\langle k \rangle$ and intercepts $\langle Wo \rangle$ of the lattice lines (values in brackets represent errors given in tables 5.1 and 5.2).

hkl	$\langle k \rangle x10^{4}(20^{\circ})$	$\sigma(\langle k \rangle)x10^{4}(20^{\circ})$	$\langle Wo \rangle x10^{4}(20^{\circ})^{2}$	$\sigma(\langle Wo \rangle)x10^{4}(20^{\circ})^{2}$
220	87	6(3)	12	5(2)
311	98	4(2)	19	3(1)
400	136	10(5)	23	6(2)
422	180	12(8)	26	10(4)
511/333	200	15(6)	46	18(4)
440	222	12(6)	77	11(3)
620	309	31(18)	168	27(8)
533	345	10(12)	286	31(5)
444	505	34(30)	695	18(11)

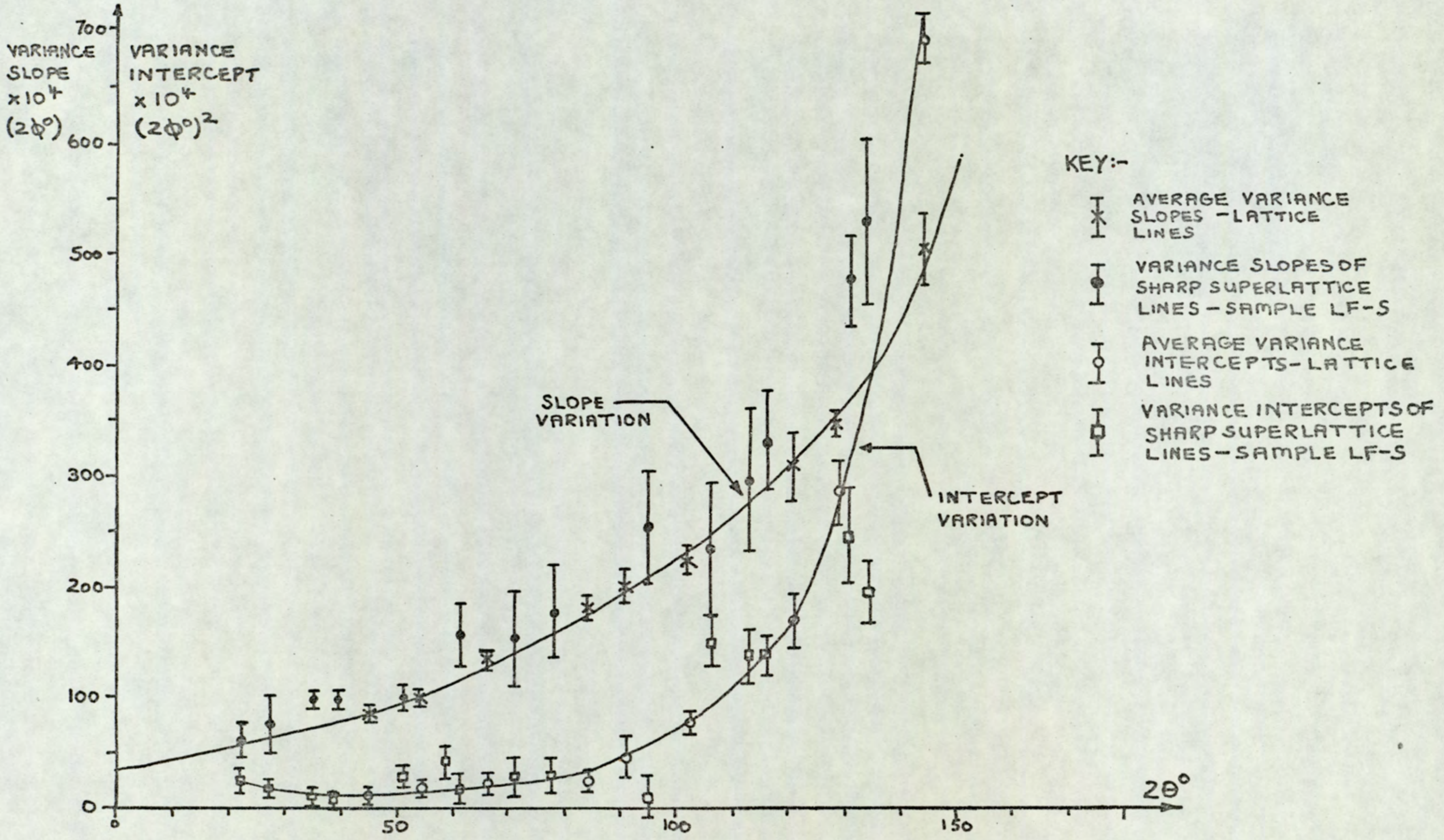

Fig.5.1 Variation of variance slope and intercept as a function of 2θ for the sharp diffraction lines - CrK .

To investigate how well the variance results given in table 5.3 were accountable for by the contributions of the instrumental aberrations and the emission profile, variance analysis was performed on the (200) and (400) line profiles diffracted from a single crystal of sodium chloride (the (400) profile is given in Fig.3.6). Owing to the higher peak/background ratios ($\sim 10^4$ and 10^3 for (200) and (400), respectively) of these profiles compared with the lattice line profiles of lithium ferrite, a correction was applied to each measured intensity value for the response time of the proportional counter. It was also necessary to correct for the influence of the satellite group with a slightly modified distribution to the one described earlier. Furthermore, the mean background level and slope were determined from an average of the intensity levels at large ranges either side of the profiles. The variance slopes and intercepts obtained from the (pseudo-variance)-range characteristics are given in table 5.4 together with errors that represent the range of values which fitted the characteristics.The effect of background errors was small as varying the background level over an acceptable range of values changed the measured slopes and intercepts by smaller amounts than the standard errors quoted in table 5.4.

Table 5.4 Variance slopes (k) and intercepts (W_o) of the (200) and (400) lines from a single crystal of sodium chloride - CrKα radiation.

hkl	Centroid $2\theta_c$	$k \times 10^4 (2\theta^o)$	$W_o \times 10^4 (2\theta^o)^2$
200	47.90°	73 ± 2	25 ± 3
400	108.61°	220 ± 10	175 ± 15

The contributions of the individual instrumental aberrations to the variance of a line profile are finite and additive and as such their effect is observed only in the intercept term (Wilson, 1963b). Consequently, the variance slope of a profile exhibiting no diffraction broadening is almost entirely dependent on the characteristics of the emission profile. Under this condition the slope k varies with θ as $k = A\tan\theta$ where A is a constant. Langford (1968a), using annealed nickel and aluminium powders of good grain size, demonstrated that a much better fit to his variance slopes was given by $k = A\tan\theta + B\sec\theta$, which indicated that diffraction broadening was present despite the apparent perfection of his samples. This behaviour was also observed with the lithium ferrite results as a plot of $k\cos\theta$ against $\sin\theta$ (see Fig. 5.2) gave a reasonable straight line from which A and B were estimated as $(0.0150 \pm 0.0030)^\circ 2\theta$ and $(0.0025 \pm 0.0015)^\circ 2\theta$, respectively. From a similar plot with the sodium chloride results (see Fig.5.2) A and B were estimated as $(0.0155 \pm 0.0010)^\circ 2\theta$ and $(0.0005 \pm 0.0010)^\circ 2\theta$, respectively. As $B \simeq 0$ for the latter results it was inferred that no source of broadening other than the emission profile was contributing to the variance slopes. By comparison, it was evident that the emission profile was also responsible for the $\tan\theta$ dependence of the variance slopes associated with the lithium ferrite results. The $\sec\theta$ dependence associated with latter results is definitely significant as values for B determined from the results of individual samples were more or less equal to the above value. This effect cannot be explained by a crystallite size effect as microscopical examination revealed quite clearly crystallites of the order of a few microns in size. A possible explanation is thermal diffuse scatter as its effect would tend to be invariant with the types of heat treatment given to the present samples. Other effects

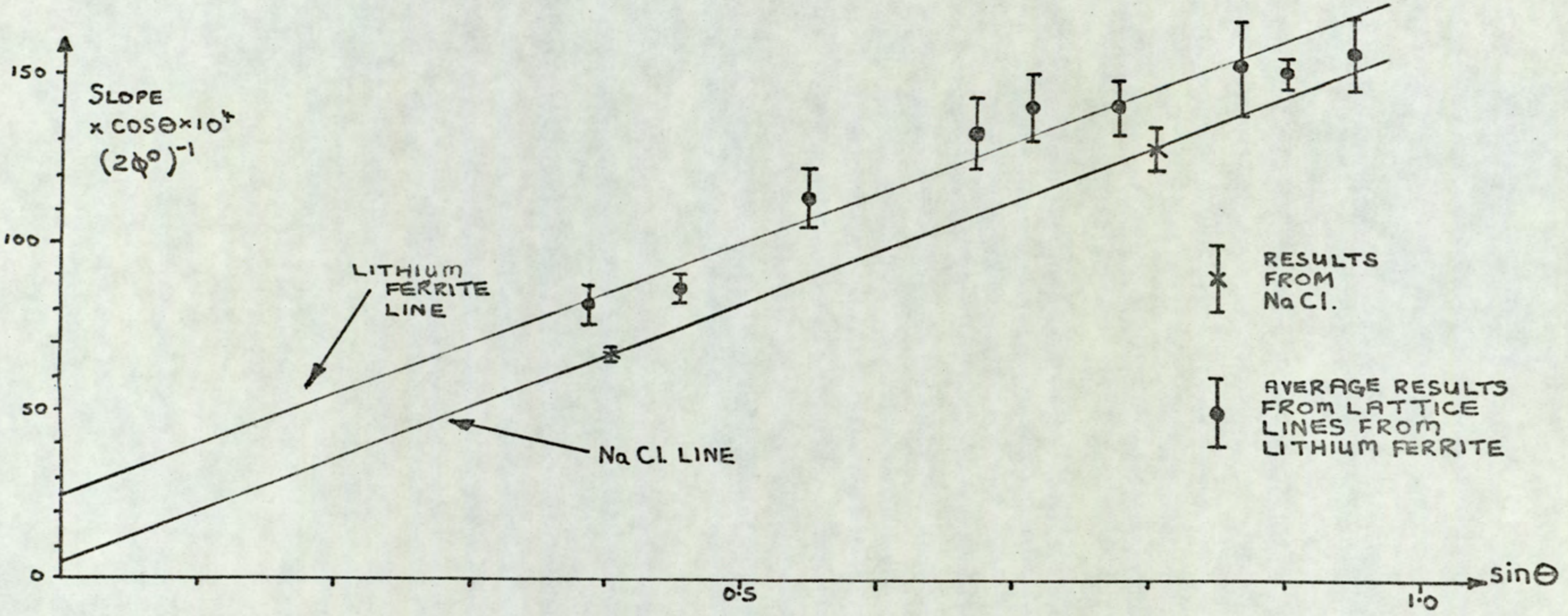

Fig.5.2 Variance slope x cosθ versus sinθ for lithium ferrite and sodium chloride results.

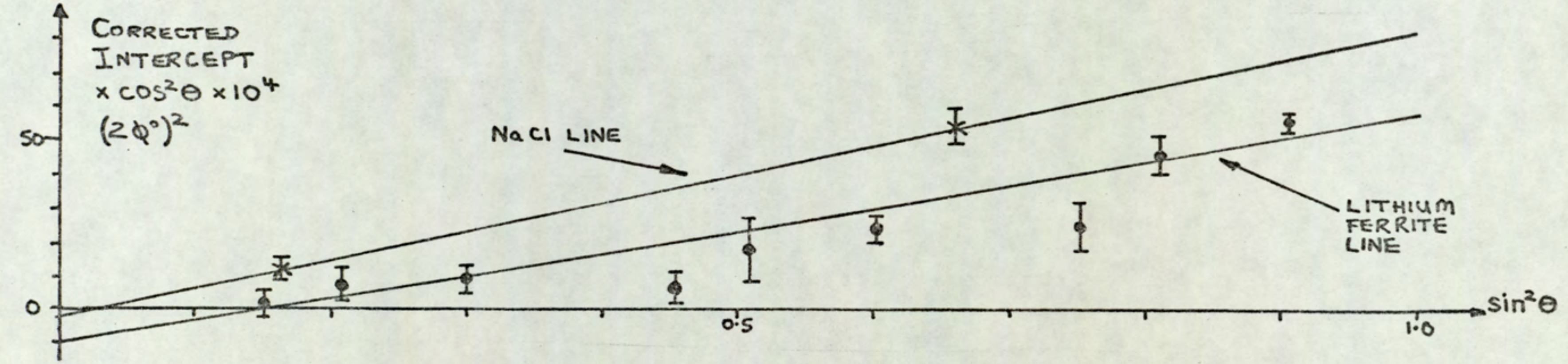

Fig.5.3 Corrected intercept x $\cos^2\theta$ versus $\sin^2\theta$ for lithium ferrite and sodium chloride results.

such as those arising from stacking faults and dislocations would tend to vary with heat treatment.

For a comparison between the variance intercepts of the sodium chloride and lithium ferrite reflections to be meaningful and to investigate whether the equivalent of a crystallite size effect could be detected it was necessary to make corrections to both sets of measured intercept values. These included the subtraction of:-

(a) a calculated instrumental contribution,

(b) the contribution proportional to $(A'(0)/A(0))^2$ arising from the use of variance normalised with respect to a truncated integrated intensity (Wilson, 1965),

(c) the extra non-additive term proportional to $(J'(0)/J(0).X'(0)/X(0))$ in the lithium ferrite intercepts that results from the presence of two contributions in the variance slopes (Wilson, 1970).

The instrumental aberration contribution used in the above correction was calculated as the sum of the contributions arising from specimen refraction, axial divergence, flat specimen error, finite receiving slit width, specimen transparency and finite focal line width using the data for the diffractometer system given in table 3.1 and the equations given by Wilson (1963b). Assuming the instrumental aberrations are fully corrected for the corrected intercepts should vary with θ as $W_o = A'\tan^2\theta + B'\sec^2\theta$ if the contributions arise from the emission profile (represented by A') and a crystallite size effect (represented by B') Graphs of $W_o\cos^2\theta$ versus $\sin^2\theta$ are given in Fig.5.3 for the lithium ferrite and sodium chloride results. The graph for the sodium chloride reflexions gave $A' = 0.0084 \pm 0.0008(2\theta^{\circ})^2$ and $B' = -0.0002 \pm 0.0004(2\theta^{\circ})^2$.. As $B \simeq 0$ it was inferred that the emission profile determines these corrected values of Wo and that the instrumental aberration contribution was adequately accounted for during the correction stage. In the case of the lithium ferrite reflections a linear fit was obtained with $A' = 0.0068 \pm 0.0010(20^{\circ})^2$ and $B' = -0.0010 \pm 0.0005(20^{\circ})^2$. In view of the large error in the estimated value of A' it was not possible to decide whether its deviation from the emission profile value of A' was significant. It did appear however, as if the B' value was significantly different from the emission profile value.

To complete this section of analysis the values of A and A' determined from the measured emission profile are compared with those derived from simulated CrKα emission profiles (i.e. overlapping Cauchy curves) based on the published half width data of Bearden and Shaw (1935) and Parratt (1936) - see Table 5.5. The marked disagreement between the measured and calculated values of A is attributed to the slow decay of the measured emission profile relative to the simulated profiles. On the other hand, the agreement in the values of A' is attributed to the fact that the central portion of the measured emission profile is represented quite accurately by the simulated profiles. Similar conclusions were reached by Langford and Wilson (1963) for the case of the CuKα emission profile.

Table 5.5 Comparison of A and A' determined from measured and simulated CrKα emission profiles.

		$A \times 10^4 (20^{\circ})$	$A' \times 10^4 (20^{\circ})^2$
Measured Profile		155 ± 10	84 ± 8
Simulated Profiles	Bearden and Shaw (1935)	88	77
	Parratt (1936)	84	78

5.2 Results from pseudo-variance analysis of broadened superlattice lines

As many of the broadened superlattice lines, particularly those at high angles, were either very weak (e.g. (221), (411/330)) or overlapping onto a neighbouring superlattice line (e.g. (521) on (520/432) and vice versa) or lattice line (e.g. (611/532) on (620)), pseudo-variance analysis could only be carried out with reasonable accuracy on a restricted number of profiles (i.e. (110), (210), (211), (310), (320), (321) and (421)). In certain cases even some of these profiles could not be analysed. For some of the lithium ferrite samples annealed at 700°C only the (210) profile was measured. This was done for the purpose of confirming trends, as a function of annealing time, indicated by the more fully analysed samples of this group.

To convert the measured variance slopes and intercepts given by pseudo-variance into a form suitable for interpretation, corrections were made for angular factors, instrumental broadening, the contribution to the variance intercept arising from the use of the truncated integrated intensity as a normalising factor, the non-additive cross term proportional to $(X'(0)/X(0).J'(0)/J(0))$ in the intercept and constant factors. These were carried out according to the relations given in chapter 3, sections 5.1 and 5.2. The standard errors of $J'(0)/J(0)$ and $J''(0)/J(0)$ were taken to be double the values estimated on the basis of counting statistics being the only source of error. This was done because the standard errors estimated from the scatter of the lattice line results tended to be double the standard errors due to counting statistics (see table 5.3). The corrected pseudo-variance results for the superlattice lines of the quenched samples are given together with the estimated errors in tables 5.6 and 5.7. The corresponding results

Table 5.6 Experimental values of $J'(0)/J(0) \times 10^4 (\mathring{A}^{-1})$, together with errors of measurement, determined from the superlattice lines of the quenched lithium ferrite samples.

Sample Designation	(110)	(210)	(211)	(310)	(320)	(321)	(421)
LF725	-118(10)	-125(7)	-117(9)	-130(9)	-129(20)	-	-120(18)
LF735	-85(5)	-88(5)	-81(6)	-88(11)	-86(13)	-90(19)	-90(11)
LF740	-134(6)	-132(6)	-123(7)	-135(11)	-127(15)	-	-135(11)
LF745	-97(8)	-99(6)	-102(7)	-95(19)	-92(19)	-104(23)	-88(13)
LF700,0	-169(18)	-202(14)	-164(17)	-165(27)	-	-	-174(26)
LF700,½	-	-166(14)	-	-	-	-	-
LF700,1	-136(14)	-160(11)	-142(12)	-148(20)	-	-	-139(24)
LF700,5	-147(16)	-146(13)	-132(17)	-136(24)	-	-	-144(26)
LF700,10	-	-143(12)	-	-	-	-	-
LF700,20	-	-137(12)	-	-	-	-	-
LF700,40	-	-132(9)	-	-	-	-	-
LF700,60	-127(13)	-110(10)	-116(15)	-132(20)	-	-	-114(19)
LF700,140	-100(9)	-150(7)	-108(10)	-95(12)	-	-	-115(18)

Table 5.7 Experimental values of $J''(0)/J(0) \times 10^6(\text{Å}^{-2})$, together with errors of measurement, determined from superlattice lines of the quenched lithium ferrite samples.

Sample Designation	(110)	(210)	(211)	(310)	(320)	(321)	(421)
LF725	145(11)	154(9)	136(10)	178(16)	152(27)	-	141(20)
LF735	81(4)	68(4)	72(6)	85(10)	69(11)	84(18)	84(11)
LF740	131(8)	137(7)	117(8)	145(15)	135(18)	-	147(14)
LF745	80(7)	108(6)	94(7)	86(17)	94(17)	97(25)	65(12)
LF700,0	262(27)	402(28)	251(25)	225(35)	-	-	270(47)
LF700,$\frac{1}{2}$	-	271(21)	-	-	-	-	-
LF700,1	209(18)	286(18)	226(16)	267(27)	-	-	238(32)
LF700,5	234(22)	236(18)	204(22)	217(30)	-	-	236(35)
LF700,10	-	216(16)	-	-	-	-	-
LF700,20	-	217(16)	-	-	-	-	-
LF700,40	-	184(13)	-	-	-	-	-
LF700,60	183(16)	133(11)	136(17)	188(25)	-	-	151(20)
LF700,140	106(9)	117(8)	133(12)	127(11)	-	-	155(22)

Table 5.8 Experimental values of $J'(0)/J(0) \times 10^4(\mathring{A}^{-1})$, together with errors of measurement, determined from superlattice lines of the chromium substituted lithium ferrite samples, designated CRx where x represents the average number of Cr^{3+} ions/unitcell.

Sample Designation	(110)	(210)	(211)	(310)	(421)
CR$\frac{1}{4}$	-26(7)	-28(5)	-25(7)	-26(12)	-28(11)
CR$\frac{1}{2}$	-67(9)	-69(7)	-63(9)	-64(13)	-67(14)
CR$\frac{3}{4}$	-77(12)	-77(10)	-74(12)	-86(23)	-73(28)
CR1	-119(26)	-102(16)	-118(23)	-104(31)	-139(43)
CR1$\frac{1}{2}$	-136(30)	-142(25)	-132(37)	-	-
CR2	-226(21)	-206(20)	-237(29)	-	-

Table 5.9 Experimental values of $J''(0)/J(0) \times 10^6(\mathring{A}^{-1})$, together with errors of measurement, determined from superlattice lines of the chromium substituted lithium ferrite samples designated CRx where x represents the average number of Cr^{3+} ions/unitcell.

Sample Designation	(110)	(210)	(211)	(310)	(421)
CR$\frac{1}{4}$	7.0(2)	8.1(2)	6.9(2)	9.1(4)	9.8(5)
CR$\frac{1}{2}$	67(7)	53(5)	52(8)	52(10)	72(10)
CR$\frac{3}{4}$	75(9)	96(8)	56(9)	77(19)	63(19)
CR1	198(30)	144(16)	173(28)	121(31)	203(64)
CR1$\frac{1}{2}$	206(36)	219(30)	199(46)	-	-
CR2	491(40)	532(42)	633(64)	-	-

for the chromium substituted samples of lithium ferrite are given in tables 5.8 and 5.9. To avoid round-off error the values are given as computed. Omissions in the tables indicate that pseudo-variance analysis was not carried out.

The remaining sections of this chapter are concerned with the interpretation of the measured values of $J'(0)/J(0)$ and $J''(0)/J(0)$. This has been carried out in terms of the following:-

(i) the set(s) of $\{HKL\}$ planes defining the anti-phase domain boundaries,

(ii) the domain thickness distribution,

(iii) the rate of growth of the domains in the unsubstituted specimens as a function of temperature and time.

(iv) the relationship between anti-phase domain formation and Cr^{3+} ion substitution.

5.3 Determination of the planes defining the anti-phase domain boundaries

The variation of $J'(0)/J(0)$ as a function of (hkl), the plane of reflexion, is determined by the set or sets of $\{HKL\}$ planes defining the anti-phase domain boundaries and by the nature of adjoining domains. Theoretical calculations of this variation have been carried out by Wilson and Zsoldos (1966) for a large range of anti-phase domain boundary models. Although their method of determining $J(t)$ is based on a geometric distribution of domain thicknesses (i.e. the random model) this in no way invalidates their calculations of $J'(0)/J(0)$ which is independent of the domain thickness distribution (Wilson (1958), Roessler and Flinn (1967)). The results of the calculations of $J'(0)/J(0)$, for boundary models in which there are no restrictions on the nature of adjoining domains, are as follows:-

(i) domain boundaries for which the mean domain thickness is independent of direction

$$\frac{J'(0)}{J(0)} = -\frac{4}{3T}$$

where T is the mean domain thickness,

(ii) domain boundaries on the {100} set of planes

$$\frac{J'(0)}{J(0)} = -\frac{4(h+k+l)}{3T_{100}\sqrt{N}}$$

(iii) domain boundaries on the {110} set of planes

$$\frac{J'(0)}{J(0)} = -\frac{8(2h+k)}{3T_{110}\sqrt{2N}}$$

(iv) domain boundaries on the {111} set of planes

$$\frac{J'(0)}{J(0)} = -\frac{16h}{3T_{111}\sqrt{3N}} \quad \text{for } h \geqslant k+l$$

$$\frac{J'(0)}{J(0)} = -\frac{8(h+k+l)}{3T_{111}\sqrt{3N}} \quad \text{for } h < k+l$$

where T_{100}, T_{110} and T_{111} are the mean distances between adjacent (100), (110) and (111) boundary planes, respectively, in the [100], [110] and [111] directions, respectively; the positive values of the indices are arranged in the order $h \geqslant k \geqslant l$ and $N = h^2 + k^2 + l^2$. For all these anti-phase domain boundary models $J'(0)/J(0) = -4/3D_{hkl}$ where D_{hkl} is the mean domain thickness in the [hkl] direction.

In Cu_3Au alloy, the factor restricting the types of adjoining domain appears to be that gold atoms tend to avoid one another. According to Anderson (1956) and Brunel and Bergevin (1966) an analogous restriction exists in lithium ferrite in that each tetrahedron of octahedral ions must contain one Li^+ ion and three Fe^{3+} ions - a condition referred to as the principle of tetrahedral invariance. This means that the six nearest neighbour octahedral ions to a Li^+ ion must always be Fe^{3+} ions. A study has therefore been carried out to determine the restrictions tetrahedral invariance imposes on the nature of adjoining domains for {100}, {110} and {111} type anti-phase domain boundary planes.

Each of the domains in lithium ferrite may assume one of four possible arrangements of the Li^+ and Fe^{3+} octahedral ions. The co-ordinates of the Li^+ ions for these arrangements are as follows:-

A type Li^+ ions at $\frac{5}{8},\frac{5}{8},\frac{5}{8};\frac{1}{8},\frac{7}{8},\frac{3}{8};\frac{3}{8},\frac{1}{8},\frac{7}{8};\frac{7}{8},\frac{3}{8},\frac{1}{8}$:
B type Li^+ ions at $\frac{1}{8},\frac{5}{8},\frac{1}{8};\frac{5}{8},\frac{7}{8},\frac{7}{8};\frac{7}{8},\frac{1}{8},\frac{3}{8};\frac{3}{8},\frac{3}{8},\frac{5}{8}$:
C type Li^+ ions at $\frac{1}{8},\frac{1}{8},\frac{5}{8};\frac{5}{8},\frac{3}{8},\frac{3}{8};\frac{7}{8},\frac{5}{8},\frac{7}{8};\frac{3}{8},\frac{7}{8},\frac{1}{8}$:
D type Li^+ ions at $\frac{5}{8},\frac{1}{8},\frac{1}{8};\frac{1}{8},\frac{3}{8},\frac{7}{8};\frac{3}{8},\frac{5}{8},\frac{3}{8};\frac{7}{8},\frac{7}{8},\frac{5}{8}$:

where B, C and D domains are equivalent to A domains when their origins are translated by $\frac{1}{2},0,\frac{1}{2};\frac{1}{2},\frac{1}{2},0$ and $0,\frac{1}{2},\frac{1}{2}$, respectively. In contrast to Cu_3Au alloy, lithium ferrite has sixteen ions participating in the ordering process and a large unit cell and as such an anti-phase domain boundary can occur at a number of different positions in an individual unit cell. This is illustrated for (100), (101) and (111) type boundaries in Fig.5.4. With a (100) type boundary for instance, a change in structure can occur across any one of the (100) planes

(i) (100) boundary positions.
[Structure represented by oxygen ions on (010) plane at $y \simeq -1/8$]

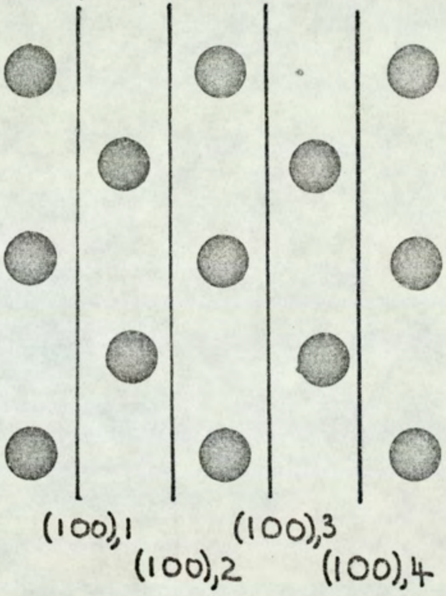

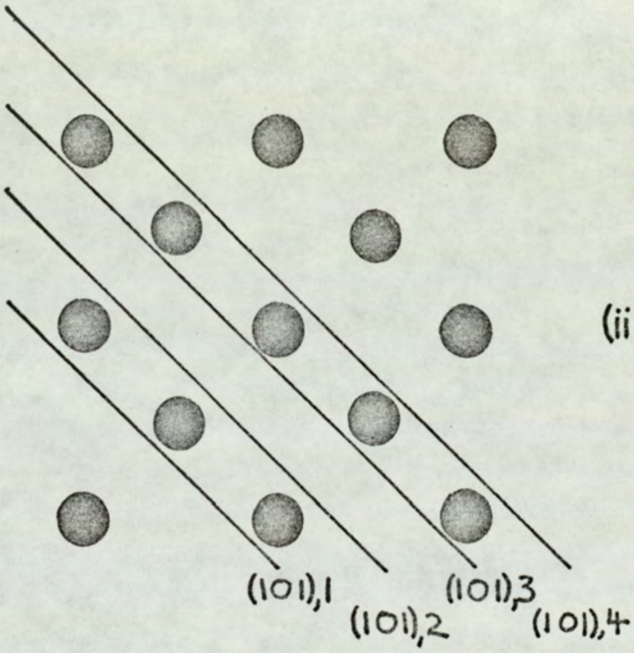

(ii) (101) boundary positions
[Structure represented by oxygen ions on (010) at $y \simeq -1/8$]

(iii) (111) boundary positions
[Structure represented by oxygen ions with corner A corresponding to $x \simeq y \simeq z \simeq -1/8$]

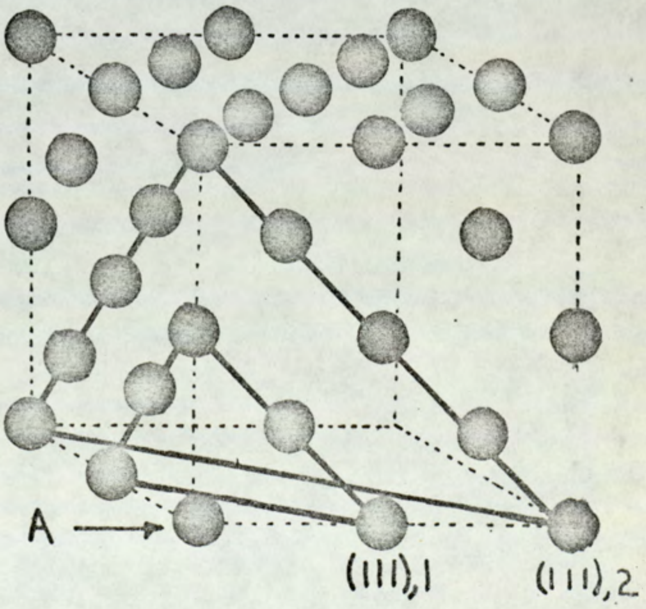

Fig.5.4 Illustration of anti-phase domain boundary positions in a unit cell of lithium ferrite.

intercepting the x axis at x = 0, x = $\frac{1}{4}$, x = $\frac{1}{2}$ or x = $\frac{3}{4}$. Starting from the boundary plane nearest the origin of a cell, the possible boundary planes have been designated (hkl), 1; (hkl),2 etc. For (110) type boundaries there are also four possible boundary positions, but for (111) type boundaries there are only two possible positions.

By simulating different domain structures either side of the possible (hkl), x boundaries, with the aid of a ball model of lithium ferrite, it was possible to determine those boundaries for which tetrahedral invariance is satisfied. At $\{111\}$ type boundaries, all combinations of adjacent domain structure violated the tetrahedral invariance condition. At $\{100\}$ type boundaries, tetrahedral invariance allows two of the three possible changes to occur. For example, an A type structure may change to a B or C type structure across a (100) boundary plane, but only one of the two possible changes may occur across a specific (100),x plane. All three possible changes may occur across $\{110\}$ type boundaries, but once again only specific changes are possible across individual (110),x boundaries. Only $\{110\}$ type boundaries allow domain growth to occur without high energy boundaries (i.e. tetrahedral invariance violated) being formed occasionally. The complete list of changes of domain structure which satisfy tetrahedral invariance across the $\{100\}$ and $\{110\}$ type boundaries are arrayed in tables 5.10 and 5.11, respectively.

The variation of J'(0)/J(0) as a function of (hkl) for low energy $\{100\}$ boundary planes in lithium ferrite has been previously derived by Wilson and Zsoldos (1966) as the restrictions imposed on the adjacent domains correspond to the case in Cu_3Au alloy where the $\{110\}$ boundaries are all of the high energy type (i.e. gold atoms in contact). Thus, defining T'_{100} as the average distance between adjacent (100) boundaries

Table 5.10 Changes of anti-phase domain structure across $\{100\}$ type boundaries satisfying the tetrahedral invariance condition.

(100),1	(100),2	(100),3	(100),4	Boundary planes
A → C	A → B	A → C	A → B	Possible changes
B → D	B → A	B → D	B → A	
C → A	C → D	C → A	C → D	
D → B	D → C	D → B	D → C	
(010),1	(010),2	(010),3	(010),4	Boundary planes
A → D	A → C	A → D	A → C	Possible changes
B → C	B → D	B → C	B → D	
C → B	C → A	C → B	C → A	
D → A	D → B	D → A	D → B	
(001),1	(001),2	(001),3	(001),4	Boundary planes
A → B	A → D	A → B	A → D	Possible changes
B → A	B → C	B → A	B → C	
C → D	C → B	C → D	C → B	
D → C	D → A	D → C	D → A	

Table 5.11 Change of anti-phase domain structure across $\{110\}$ type boundaries satisfying the tetrahedral invariance condition.

(101),1	(101),2	(101),3	(101),4	Boundary planes
A → C,D	A → none	A → B	A → B,C,D	Possible changes
B → C,D	B → none	B → A	B → A,C,D	
C → D	C → A,B,D	C → A,B	C → none	
D → C	D → A,B,C	D → A,B	D → none	
$(10\bar{1})$,1	$(10\bar{1})$,2	$(10\bar{1})$,3	$(10\bar{1})$,4	Boundary planes
A → B,C,D	A → C,D	A → none	A → B	Possible changes
B → A,C,D	B → C,D	B → none	B → A	
C → none	C → D	C → A,B,D	C → A,B	
D → none	D → C	D → A,B,C	D → A,B	
(110),1	(110),2	(110),3	(110),4	Boundary planes
A → B,D	A → none	A → C	A → B,C,D	Possible changes
B → D	B → A,C,D	B → C,A	B → none	
C → B,D	C → none	C → A	C → D,A,B	
D → B	D → A,B,C	D → A,C	D → none	
$(\bar{1}10)$,1	$(\bar{1}10)$,2	$(\bar{1}10)$,3	$(\bar{1}10)$,4	Boundary planes
A → B,C,D	A → B,D	A → none	A → C	Possible changes
B → none	B → D	B → A,C,D	B → A,C	
C → B,A,D	C → B,D	C → none	C → A	
D → none	D → B	D → A,B,C	D → A,C	
(011),1	(011),2	(011),3	(011),4	Boundary planes
A → none	A → D	A → B,C,D	A → B,C	Possible changes
B → C,D,A	B → A,D	B → none	B → C	
C → D,A,B	C → A,D	C → none	C → B	
D → none	D → A	D → A,B,C	D → B,C	
$(01\bar{1})$,1	$(01\bar{1})$,2	$(01\bar{1})$,3	$(01\bar{1})$,4	Boundary planes
A → D	A → B,C,D	A → B,C	A → none	Possible changes
B → D,A	B → none	B → C	B → A,C,D	
C → D,A	C → none	C → B	C → D,A,B	
D → A	D → A,B,C	D → B,C	D → none	

in the [100] direction, the variation of J'(0)/J(0) is given by

$$\frac{J'(0)}{J(0)} = -\frac{(h+2k+\ell)}{T'_{100}\sqrt{N}} \quad , \qquad h+\ell = 2n$$

$$\frac{J'(0)}{J(0)} = -\frac{(h+k+2\ell)}{T'_{100}\sqrt{N}} \quad , \qquad h+k = 2n$$

$$\frac{J'(0)}{J(0)} = -\frac{(2h+k+\ell)}{T'_{100}\sqrt{N}} \quad , \qquad k+\ell = 2n$$

where n is an integer.

To determine which anti-phase domain boundary model corresponded closest to the case of lithium ferrite, values for T, T_{100}, T'_{100}, T_{110}, and T_{111} were calculated from the measured values of J'(0)/J(0) given in tables 5.6 and 5.8 using the theoretical relations appropriate to each boundary model. Following this, the mean values $\langle T\rangle$, $\langle T_{100}\rangle$, $\langle T'_{100}\rangle$, $\langle T_{111}\rangle$ and $\langle T_{110}\rangle$ were calculated for each sample together with the mean deviations, expressed as percentages, due to the scatter in each set of T_{HKL} values,

$$\text{i.e. \% Mean deviation of } T_{HKL} = \frac{100}{n}\sum_{h,k,\ell}\left|(T_{HKL})_{hkl} - \langle T_{HKL}\rangle\right| / \langle T_{HKL}\rangle$$

where n is the number of lines analysed and $(T_{HKL})_{hkl}$ is the value of T_{HKL} determined from the (hkl) profile. The results of this analysis are presented in tables 5.12 and 5.13.

For all but four of the fifteen samples the {110} boundary model fitted best to the experimental variation of J'(0)/J(0). The fact that the results from samples CR1 and CR2 did not fit the {110} model was not considered to be significant because in these cases the super-

Table 5.12 Mean values of T, T_{100}, T'_{100}, T_{111} and T_{110} for each sample of quenched lithium ferrite together with the mean deviations, expressed as percentages, due to the scatter of the T values.

Sample Designation	T(Å)	Unrestricted {100}model T_{100} (Å)	Low Energy {100}model T'_{100} (Å)	{111} model T_{111} (Å)	{110} model T_{110} (Å)
LF725	109 ± 3.8%	155 ± 11%	148 ± 18%	211 ± 6%	333 ± 2.4%
LF735	154 ± 2.9%	224 ± 8%	216 ± 20%	298 ± 6%	470 ± 2.2%
LF740	102 ± 2.9%	149 ± 9%	140 ± 23%	199 ± 6%	313 ± 2.7%
LF745	139 ± 3.8%	201 ± 8%	192 ± 18%	268 ± 9%	424 ± 6.1%
LF700,0	77 ± 5.4%	111 ± 11%	100 ± 20%	150 ± 9%	234 ± 4.2%
LF700,1	92 ± 5.2%	133 ± 12%	120 ± 19%	180 ± 7%	282 ± 4.3%
LF700,5	96 ± 4.2%	136 ± 10%	125 ± 20%	186 ± 8%	290 ± 2.8%
LF700,60	112 ± 7.9%	161 ± 12%	147 ± 24%	219 ± 9%	342 ± 7.2%
LF700,140	128 ± 5.4%	183 ± 6.5%	197 ± 25%	251 ± 11%	391 ± 8.7%

Table 5.13 Mean values of T, T_{100}, T'_{100}, T_{111} and T_{110} for each sample of chromium substituted lithium ferrite together with the mean deviations, expressed as percentages, due to the scatter of the T_{HKL} values.

Sample Designation	T(Å)	Unrestricted {100}model T_{100} (Å)	Low Energy {100}model T_{100} (Å)	{111} model T_{111} (Å)	{110} model T_{110} (Å)
CR¼	502 ± 4.2%	723 ± 9%	655 ± 20%	982 ± 7%	1534 ± 2.3%
CR½	202 ± 3.2%	291 ± 9%	263 ± 19%	397 ± 6%	618 ± 2.3%
CR¾	173 ± 4.2%	270 ± 13%	227 ± 22%	338 ± 6%	528 ± 4.2%
CR1	116 ± 8.6%	165 ± 6%	149 ± 19%	228 ± 16%	354 ± 11%
CR1½	98 ± 2.0%	143 ± 12%	139 ± 23%	181 ± 8%	294 ± 0.6%
CR2	60 ± 5.5%	87 ± 4%	84 ± 17%	112 ± 13%	182 ± 8.6%

lattice lines were very weak, the background intensity levels were very high and the (210) and (211) lines were overlapping each other.

Further support for the boundaries being defined primarily by the $\{110\}$ planes was given by analysis of the relative magnitudes of the values of $J'(0)/J(0)$ determined from the more intense (110), (210), and (211) superlattice lines since:

(i) in 31 cases out of a total of 42 these values satisfied the inequalities of the theoretical $\{110\}$ model namely,

$$\left| \left[\frac{J'(0)}{J(0)}\right]_{210} \right| > \left| \left[\frac{J'(0)}{J(0)}\right]_{110} \right| > \left| \left[\frac{J'(0)}{J(0)}\right]_{211} \right|$$

(ii) the values of $(J'(0)/J(0))_{211}/(J'(0)/J(0))_{210}$, $(J'(0)/J(0))_{211}/(J'(0)/J(0))_{110}$ and $(J'(0)/J(0))_{110}/(J'(0)/J(0))_{210}$ averaged separately over the quenched lithium ferrite and chromium substituted lithium ferrite samples agreed, within the error due to scatter, with the values expected for the $\{110\}$ model - see table 5.14. Much better agreement was obtained for the chromium substituted samples when the results from samples CR1 and CR2 were omitted.

Table 5.14 Comparison of the average values for $((J'(0)/J(0)_{h'k'l'})/(J'(0)/J(0)_{hkl}))$ (= $R(h'k'l'/hkl)$ in the table) compared with the theoretical values for the $\{110\}$ model.

	Theory $\{110\}$ model	R(h'k'l'/hkl) Quenched Li-Ferrite	R(h'k'l'/hkl) Cr-Subst. Li-Ferrite	R(h'k'l'/hkl) Cr-Subst. without CR1,CR2
R(110/210)	0.948	0.967 ± 0.065	0.994 ± 0.090	0.965 ± 0.020
R(211/210)	0.912	0.944 ± 0.061	0.990 ± 0.090	0.925 ± 0.020
R(211/110)	0.962	0.978 ± 0.045	0.965 ± 0.020	0.960 ± 0.010

The possibility of the anti-phase domain boundaries in lithium ferrite being a combination of $\{110\}$ and $\{HKL\}$ planes was also examined. As $J'(0)/J(0)$ for such a combination of boundary planes is given by

$$\left[\frac{J'(0)}{J(0)}\right]_{hkl} = \frac{1}{T_{110}}\cdot f_{110}(hk\ell) + \frac{1}{T_{HKL}}\cdot f_{HKL}(hk\ell)$$

(Wilson and Zsoldos, 1966)

where the functions $f_{HKL}(hkl)$ correspond to the coefficients of $1/T_{HKL}$ in the single $\{HKL\}$ boundary model, a plot of $(J'(0)/J(0))_{hkl}/f_{110}(hkl)$ against $f_{HKL}(hkl)/f_{110}(hkl)$ will give a straight line with a positive slope if a second set of boundaries of the $\{HKL\}$ type tend to coexist with the $\{110\}$ boundaries. For individual samples the accuracy of the results was not good enough to justify the separation of two parameters from the observed values of $J'(0)/J(0)$. It was decided therefore to examine whether or not the average values $\langle (J'(0)/J(0))_{110} \rangle$, $\langle (J'(0)/J(0))_{210} \rangle$ and $\langle (J'(0)/J(0))_{211} \rangle$, formed by averaging over all the samples except CR1 and CR2, contained contributions other than those arising from the $\{110\}$ set of planes. An analysis of the suggested plots using these results (see Fig.5.5) for four combinations of boundaries indicated that,

(i) models consisting of $\{110\}$ boundaries with either $\{111\}$ or low energy $\{100\}$ were inconsistent with the experimental results.

(ii) a few per cent of the boundaries may possibly be of the unrestricted $\{100\}$ type or the type in which the mean domain thickness is independent of direction.

Possible explanations for $\{110\}$ boundaries being preferred over restricted $\{100\}$ boundaries are

(i) the interfacial energy of a $\{110\}$ boundary is less than a $\{100\}$ boundary,

(ii) the energy required for growth on the $\{110\}$ planes is less than that for growth on the $\{100\}$ planes.

5.4 Relation of experimental pseudo-variance results to the domain thickness distribution

Since the anti-phase domain boundaries in the present samples are described satisfactorily by a $\{110\}$ model in which there are no restrictions on the possible types of adjoining domain, $J''(0)/J(0)$ may be expressed in terms of the domain thickness distribution $f(t)$ at $t = 0$,

i.e. $$\frac{J''(0)}{J(0)} = \frac{16 f(0)}{9 D_{hkl}}$$ (Wilson (1963a), Roessler and Flinn (1967)

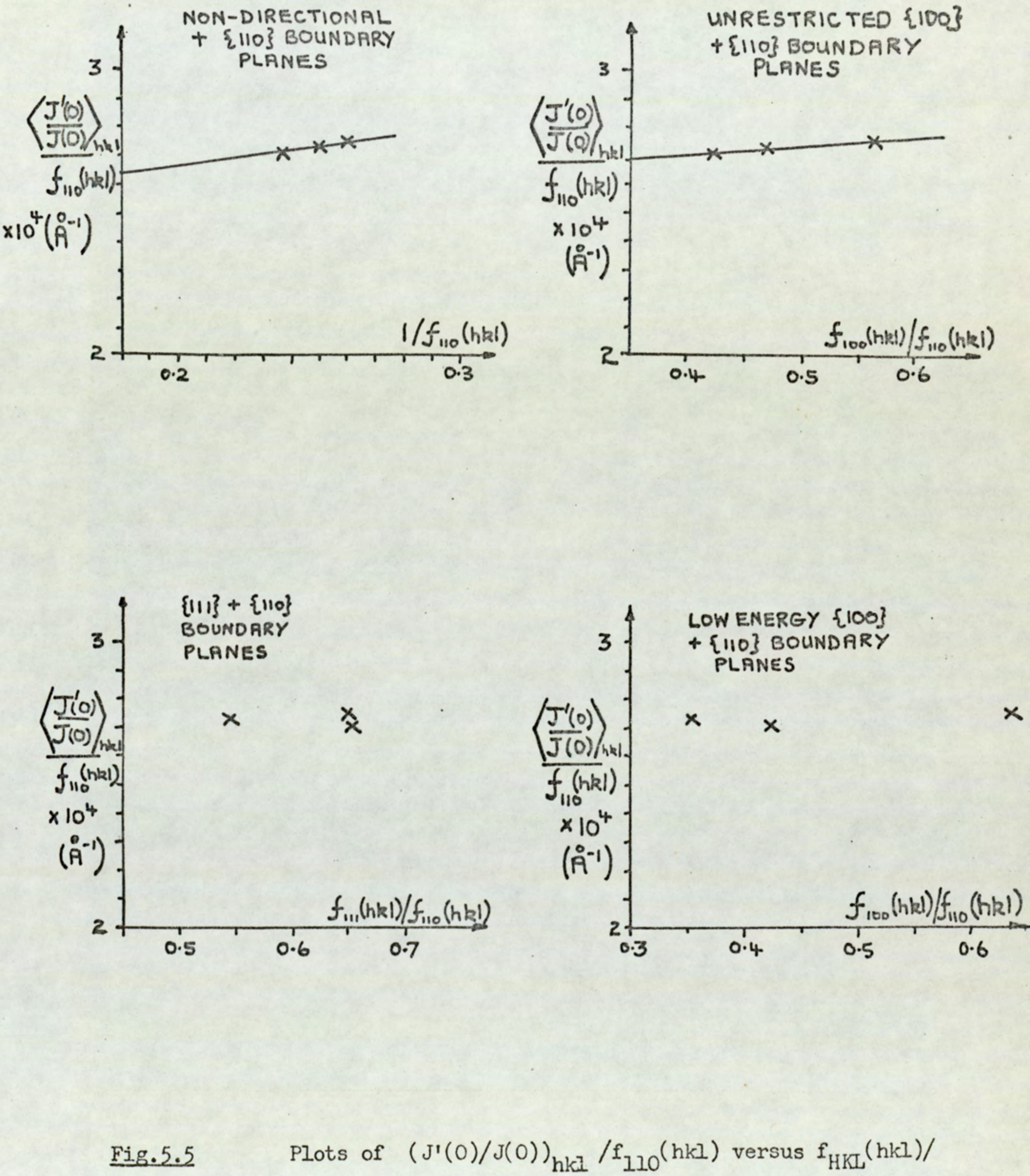

<u>Fig.5.5</u> Plots of $(J'(0)/J(0))_{hkl}/f_{110}(hkl)$ versus $f_{HKL}(hkl)/f_{110}(hkl)$ for various combinations of anti-phase domain boundary planes.

where $$\frac{J'(0)}{J(0)} = -\frac{4}{3D_{hkl}}$$

If the domain thickness distribution satisfies the random model (i.e. $f(t) = (1/D_{hkl})e^{-t/D_{hkl}}$) the average domain thickness D_{hkl}, determined from $J'(0)/J(0)_{hkl}$, and the apparent average domain thickness D'_{hkl}, given by $4(J(0)/J''(0))^{\frac{1}{2}}/3$, will agree. Comparisons of these values for the present results, carried out by plotting D_{hkl} against D'_{hkl}, are given in Figs. 5.6 and 5.7 for the quenched and chromium substituted samples of lithium ferrite, respectively. Also given in each of these plots is the relation between D_{hkl} and D'_{hkl} when the domain thickness distribution is described by the Gaussian distribution

$$f(t) = \frac{2}{\pi D_{hkl}} \cdot e^{-t^2/\pi D_{hkl}^2} \quad , \text{ i.e. } \frac{J''(0)}{J(0)} = \frac{32}{9\pi D_{hkl}^2} .$$

Within ±30% all the experimental results were in agreement with the random model; closest agreement being obtained with samples LF725, LF735, LF745 in which the results were scattered evenly about $D'_{hkl} = D_{hkl}$. Most of the sets of results however, did exhibit definite uniform trends away from the random model. The consistency of trends in the chromium substituted lithium ferrite and lithium ferrite samples LF700,1 to LF700,140 and the size of the deviations for the lithium ferrite sample LF740 demonstrated that these trends are not the outcome of random errors. That these trends were related to the type of domain thickness distribution was indicated by a rough analysis of the intensity profiles. The low angle superlattice reflexions from samples LF725, LF735, LF745 gave reasonably

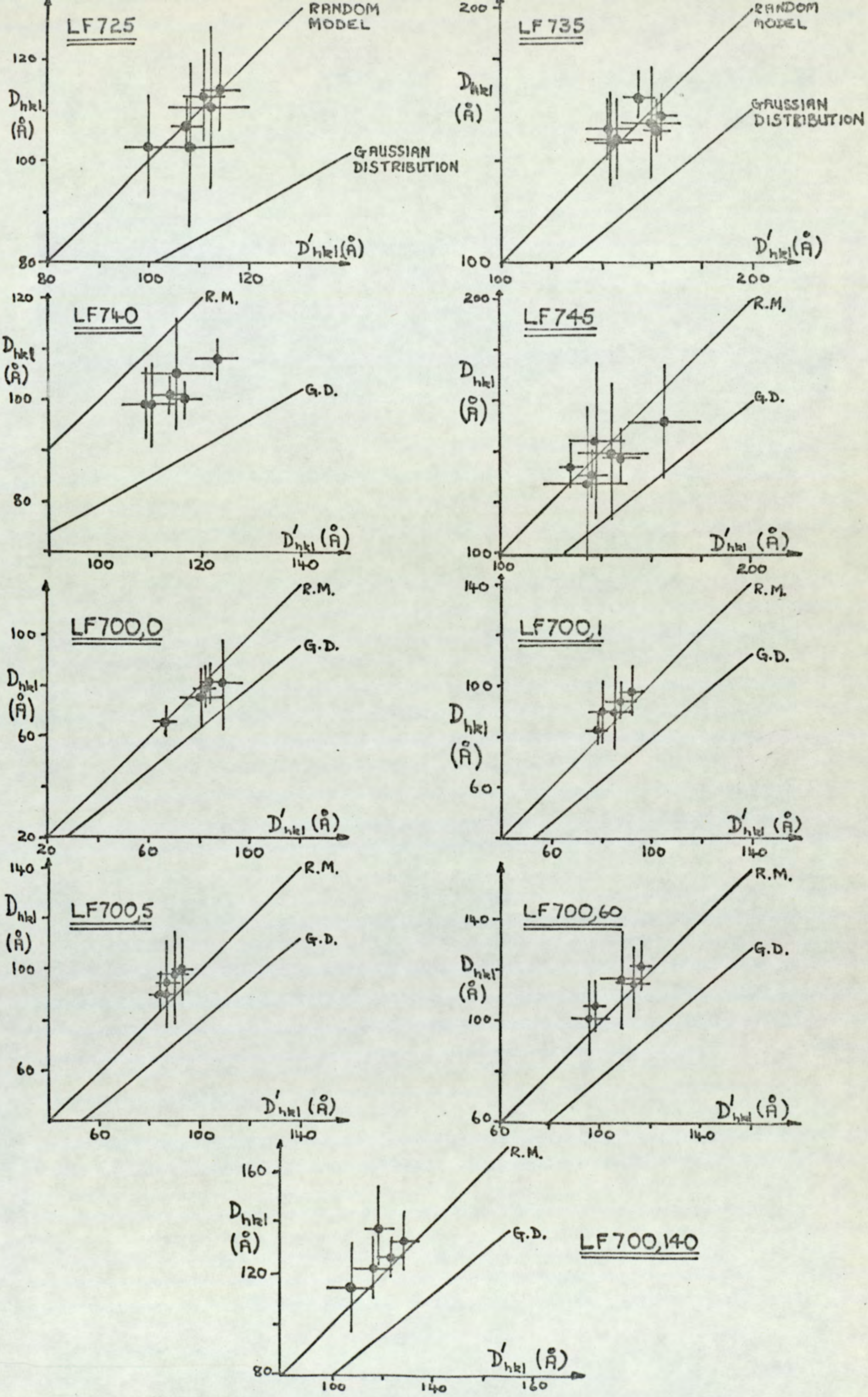

Fig.5.6 Comparison of D_{hkl} and D'_{hkl} values for the quenched samples of lithium ferrite.

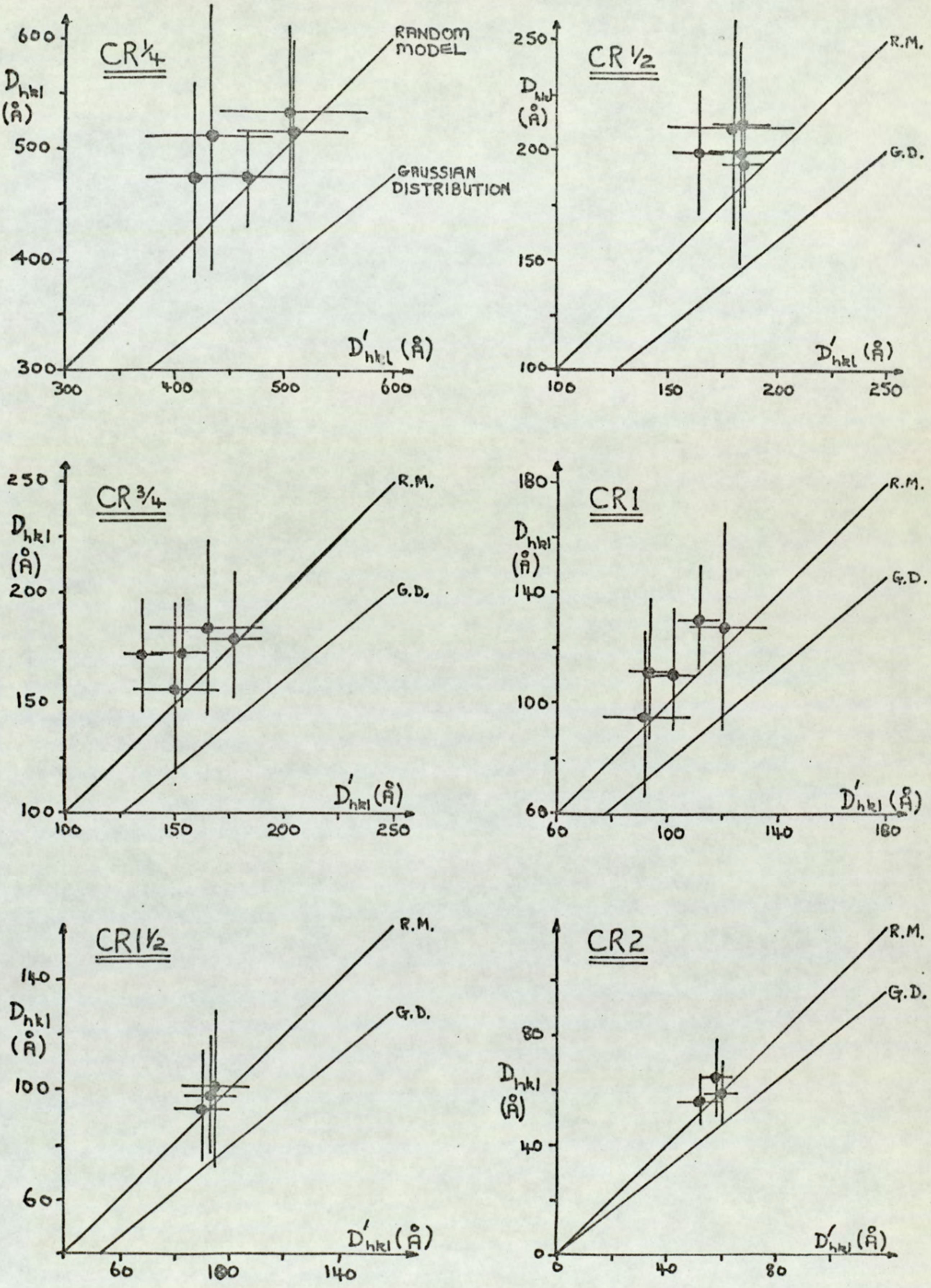

Fig.5.7 Comparison of D_{hkl} and D'_{hkl} values for the chromium substituted lithium ferrite samples.

comparable values of D_{hkl} when estimated by half width analysis (corrected $\Delta 2\theta = 4\lambda/3\, D_{hkl}\cos\theta$ rads.) and variance analysis thus indicating that the random model appears to be appropriate to these samples. When a similar comparison was carried out on the remaining samples, all of which exhibited trends away from $D_{hkl} = D'_{hkl}$, consistent discrepancies were observed between the two estimates of the mean domain thickness D_{hkl}. In the case of the (210) line from the lithium ferrite sample LF700,140 for instance, D_{hkl} was estimated as approximately 130Å by variance analysis and approximately 300Å by half width analysis.

To establish the degree to which the trends in Figs.5.5 and 5.6 could be attributed to the type of domain thickness distribution the influences of systematic errors of measurement and distortion at the anti-phase domain boundaries were examined. Possible sources of systematic error in the measurement of $J'(0)/J(0)$ and $J''(0)/J(0)$ are as follows:-

(i) wrongly estimated satellite correction,

(ii) non-linear terms in the (pseudo-variance)-range function $SW(2\phi)$,

(iii) wrongly estimated background level.

<u>(i) Wrongly estimated satellite correction</u>

An analysis of the underestimates of the apparent particle sizes determined from the variance slope and intercept when the satellite distribution is not corrected for, has been carried out by Edward and Toman (1970a). When their results are extrapolated to line profiles corresponding to an apparent particle of approximately 100Å (the average apparent particle size for the present results) the errors in the variance slope and intercept estimates are not only small, but also of the same sign and magnitude. Thus the effect of not correcting for the satellites will be to shift the results in a direction almost parallel to the line $D_{hkl} = D'_{hkl}$. As the satellite distribution used for correction purposes in the present work is at least approximately correct, the error in the relative magnitudes of D_{hkl} and D'_{hkl} will be small.

(ii) Non-linear terms in SW(2$\emptyset$)

By measuring $J'(0)/J(0)$ and $J''(0)/J(0)$ with the aid of SW(2$\emptyset$) as opposed to the variance-range function W(2$\emptyset$), the effect of the hyperbolic term in $\frac{1}{2\emptyset}$ is eliminated. Therefore, only terms in $(1/2\emptyset)^2$ and higher order will affect the reliability of the measurements. To estimate the influence of these terms the pseudo-variance-range function of a Cauchy profile of unit half width was calculated and the values of the variance slope and intercept estimated by fitting a straight line between the ranges of 2$\emptyset$ corresponding to 3 and 4 half widths of the intensity profile. The equivalents of D_{hkl} and D'_{hkl} determined from this analysis, were both smaller than the correct value by approximately 0.2%. Although experimental profiles may give larger absolute errors than 0.2% as a result of non-linear terms the ratio D_{hkl}/D'_{hkl} will tend to remain constant.

(iii) Effect of wrongly estimated background levels

Although background errors were shown earlier (chap.3.section 5.6) to be small it was nevertheless of interest to consider the sensitivity of the D_{hkl}-D'_{hkl} plots to these errors. This was done by determining values for D_{hkl} and D'_{hkl} from variance results of profiles into which background errors had been deliberately introduced. The

(110) profiles ($2\theta \simeq 22^\circ$) from samples LF725, LF735 and LF740 were chosen for this analysis and because their background levels were comparatively higher than the other superlattice lines a measure would be obtained for the case in which the optimized levels are least reliable. The range of background levels examined was such that the maximum and minimum values differed from the optimum values by 2.(Optimum Background)$^{\frac{1}{2}}$; this value representing two standard deviations according a Poisson distribution of the optimum background levels. The results of this analysis are given in Fig.5.8 as D_{hkl} - D'_{hkl} plots.

Two important features are illustrated in these results:

(i) D_{hkl} and D'_{hkl} tend to move in a direction which is approximately parallel to $D'_{hkl} = D_{hkl}$ as the mean background level is changed,

(ii) the slopes dD_{hkl}/dD'_{hkl} are all slightly less than 1 and the higher background levels correspond to larger values of D_{hkl} and D'_{hkl}. Consequently, as the variance optimised backgrounds tend, if anything, to be slightly higher than the correct levels (see chap.3, sec.5.6) the observed D_{hkl} - D'_{hkl} plots will be shifted relative to their corrected values in a direction which is away from the D_{hkl} axis and towards the D'_{hkl} axis. As these plots for the chromium substituted samples and most of the lithium ferrite samples lie above the random model line $D_{hkl} = D'_{hkl}$, the removal of any background errors can only increase the deviations from the random model.

Effect of distortions at the anti-phase domain boundaries

In lithium ferrite the ordering process involves rearrangement of the lithium and iron ions on the octahedral sites and also small shifts

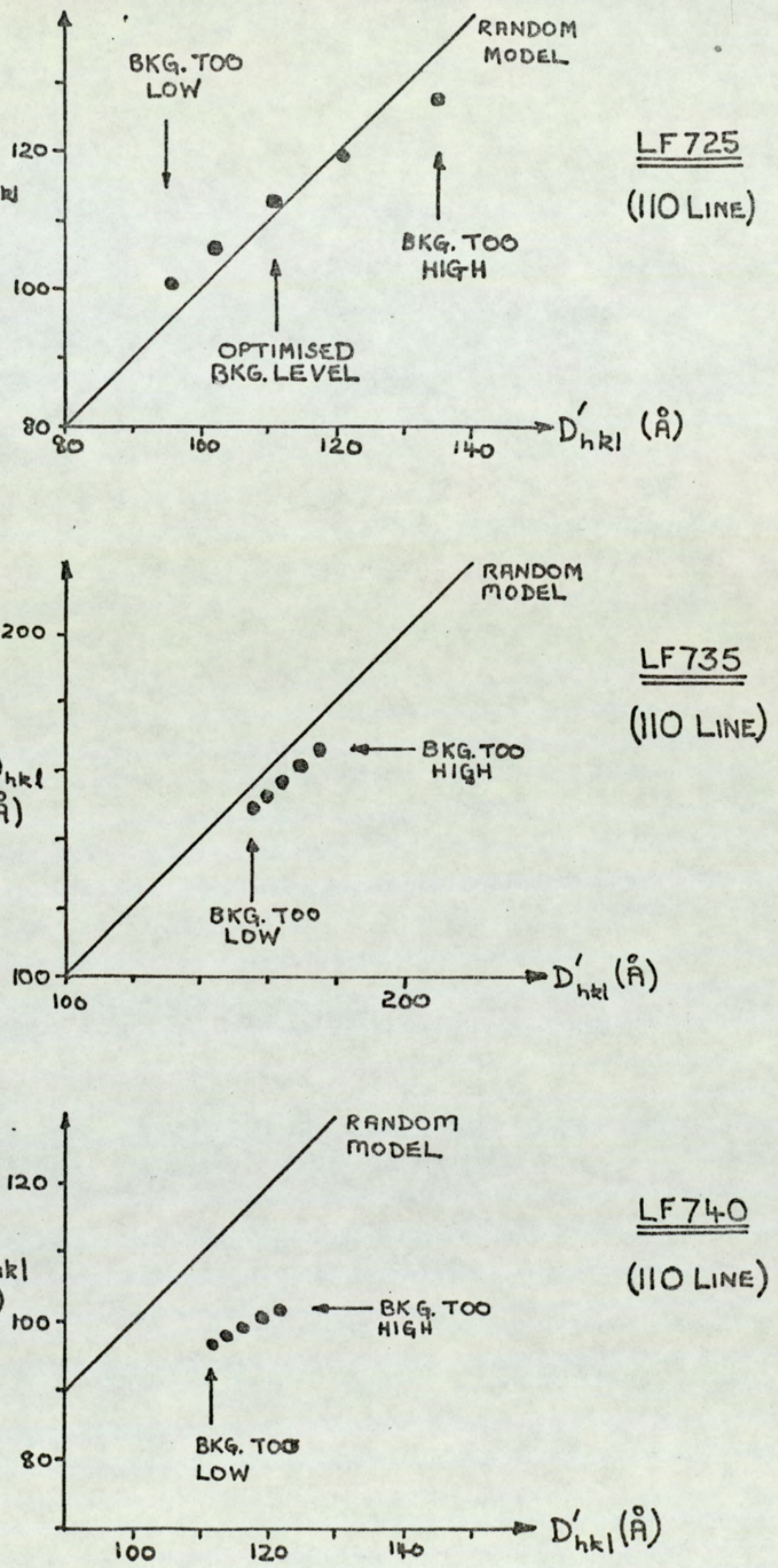

Fig.5.8 Variation of D_{hkl} and D'_{hkl} as a function of the background level.

of the iron and oxygen ions relative to their average positions in the disordered structure. Because these shifts are different in the neighbourhood of the positions $(0,0,0)$, $(0,\frac{1}{2},\frac{1}{2})$, $(\frac{1}{2},0,\frac{1}{2})$ and $(\frac{1}{2},\frac{1}{2},0)$, the atomic co-ordinates at a boundary between two anti-phase domains will not match up unless distortions occur in the boundary structure. In order to derive equations for $J'(0)/J(0)$ and $J''(\theta)/J(0)$ which include this effect the assumption was made that the crystal structure at the domain boundaries resembles the disordered structure so that distortions may be approximated by local increases in the interplanar spacing. Approximate values for these increases were assumed to be given from the increase in lattice parameter of lithium ferrite at its transition temperature.

According to Wilson (1963a), $J'(0)/J(0)$ and $J''(0)/J(0)$ are given by

$$\frac{J'(0)}{J(0)} = \frac{J_a - J_s}{J_s D_{hkl}}$$

and $$\frac{J''(0)}{J(0)} = \frac{(J_s - 2J_a + J_n)\,f(0)}{D_{hkl} J_s}$$

where J_s, J_a and J_n are the mean values of the real part of FF^* for cells in the same domain, adjacent domains and next but one domains, respectively. If u, the relative phase shift in the structure factors of adjacent domains due to boundary distortion, is the same and small for each type of structural change, J_a and J_n for the superlattice lines are given by

$$J_a = -\frac{|F|^2}{3}\cos u \simeq -\frac{|F|^2}{3}\left(1 - \frac{u^2}{2}\right)$$

and $$J_n = \frac{|F|^2}{9}\cos 2u \simeq \frac{|F|^2}{9}\left(1 - 2u^2\right)$$

Hence, $$\frac{J'(0)}{J(0)} \simeq -\frac{4}{3D_{hkl}}\left(1 - \frac{u^2}{8}\right)$$

and $$\frac{J''(0)}{J(0)} \simeq \frac{16f(0)}{9D_{hkl}}\left(1 - \frac{5u^2}{16}\right)$$

From graphical data given by Vishnevskii et al. (1969), the fractional increase in the lattice constant $\Delta a/a$ was estimated as 3.10^{-4} so that $u = \pi(\Delta d)/d \sim 10^{-3}$. Clearly, on the basis of this model of boundary distortions the absolute errors in the estimated values of D_{hkl} and D'_{hkl} will be negligible. Even for larger distortions (e.g. $\Delta d/d \sim 10^{-2}$) the absolute errors will still be small, besides which the overestimates of D_{hkl} and D'_{hkl} will be comparable.

Discussion of results

Of the systematic errors discussed none of them affects the relative values of D_{hkl} and D'_{hkl} to any great extent. The observed trends in the D_{hkl} - D'_{hkl} plots were therefore assumed to be significant. To represent these trends quantitatively, the average value of $f(0)_{\text{measured}}/f(0)_{\text{random}}$ $(= (D_{hkl}/D'_{hkl})^2)$ for each sample were determined. These values together with their mean deviations due to scatter are given in table 5.15.

Table 5.15 Average values of $(f(0))_{measured}/(f(0))_{random}$ for each lithium ferrite sample together with the mean deviations due to scatter (given in brackets).

Sample	LF725	LF735	LF740	LF745	LF700,0
$f(0)_m/f(0)_r$	0.995(0.030)	1.005(0.075)	0.775(0.030)	0.973(0.095)	0.910(0.045)
Sample	LF700,1	LF700,5	LF700,60	LF700,140	CR$\frac{1}{4}$
$f(0)_m/f(0)_r$	1.160(0.050)	1.130(0.030)	1.100(0.040)	1.160(0.090)	1.170(0.140)
Sample	CR$\frac{1}{2}$	CR$\frac{3}{4}$	CR1	CR1$\frac{1}{2}$	CR2
$f(0)_m/f(0)_r$	1.350(0.140)	1.225(0.150)	1.240(0.130)	1.110(0.020)	1.110(0.075)

For the lithium ferrite samples LF740 and LF700,0 the appropriate domain thickness distributions would appear to lie between a Gaussian distribution and a geometric distribution (i.e. random model). The standard deviations of these distributions, assuming similar mean domain thicknesses, are

$$\sigma(D_{hkl}) = D_{hkl}(\pi/2 - 1)^{\frac{1}{2}} \qquad \text{for the Gaussian case}$$

and $$\sigma(D_{hkl}) = D_{hkl} \qquad \text{for the geometric case}$$

Thus, the spread of domain sizes for an intermediate case is smaller than that for the equivalent random model.

For the lithium ferrite samples LF700,1 to LF700,140 and the chromium substituted lithium ferrite samples, the results indicate a marked tendency towards the formation of small domains (i.e. $f(0)/f(0)_{random} > 1$). In the cases of samples LF700,1 to LF700,140 the superlattice lines tended to display well resolved peaks and long tails (see Fig.5.9). For this condition to arise, large volume fractions of the crystallite must be accounted for by large domains. Thus the domain thickness distributions in these samples would appear to be described by a few large domains coexisting with a large number of small domains. The question of domain thickness distributions is given further consideration in chapter 6.

5.5 Time and temperature dependence of anti-phase domain growth

In the unsubstituted lithium ferrite samples the anti-phase domains were assumed to be of an unstable variety since isothermal annealing just below the transition temperature served, amongst other things, to increase the mean domain thickness. This is demonstrated in Fig.5.9 by the decrease in breadth of the (210) superlattice line as a function of the annealing time of the samples quenched from 700°C. If it is assumed that the energy associated with the instability of the domains (i.e. the configurational energy) is specified principally by the number of 'wrong' bonds at the boundaries then it follows that this energy will be proportional to the total surface area of the boundaries (Flinn, 1960). In this respect it is fortunate that the reciprocal of the mean domain thickness obtained from the variance slope is also approximately proportional to the total surface area of the boundaries (as demonstrated below).

Consider a column of unit cells along the [100] direction in which the anti-phase domain boundaries are of the {110} type (see Fig. 5.10); each member of the {110} set of boundaries being equally abundant. Assuming interactions between boundaries to be small the

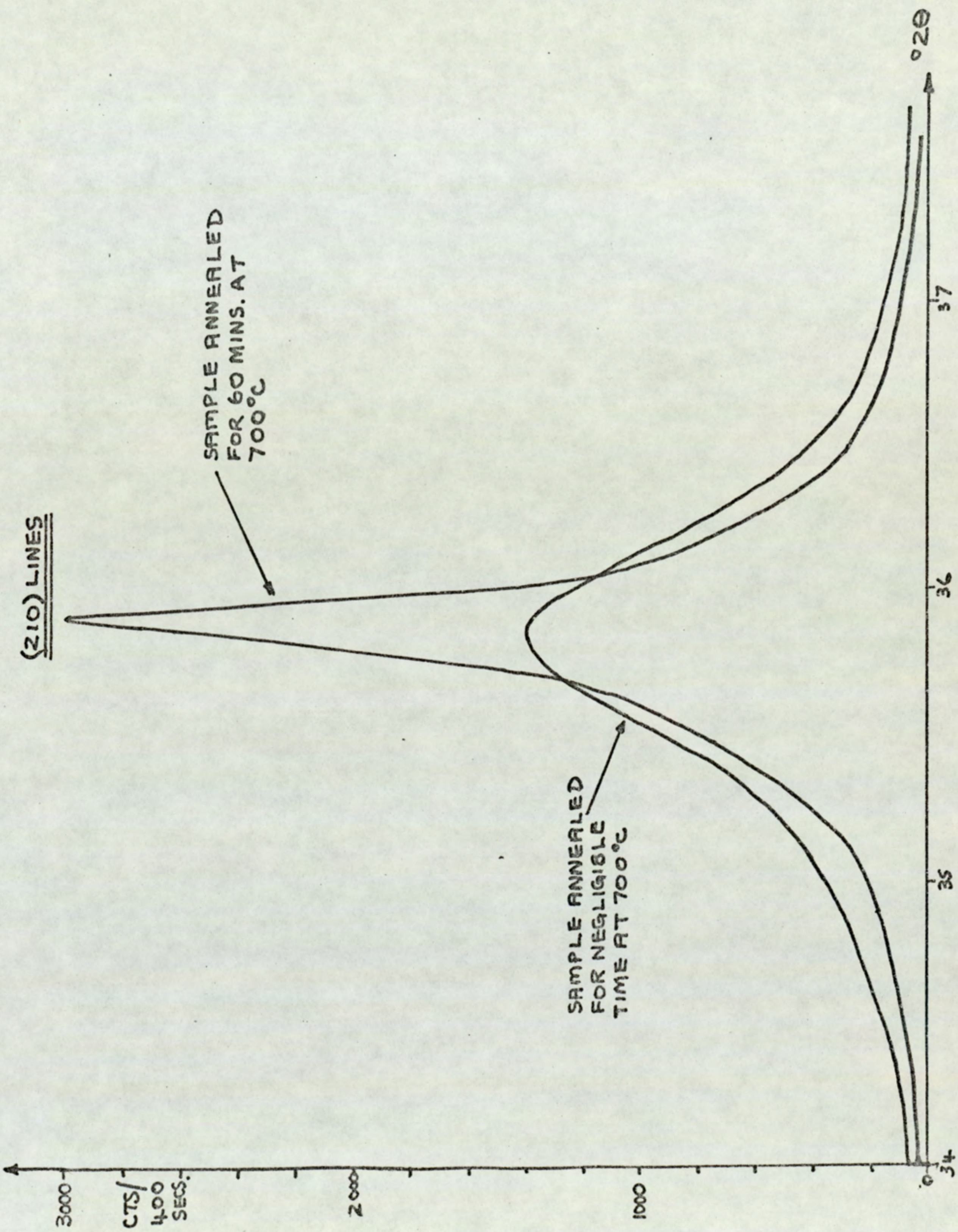

Fig.5.9 (210) profile from samples annealed 700°C for times of 0mins. and 60mins. (profiles normalised to the same integrated intensity).

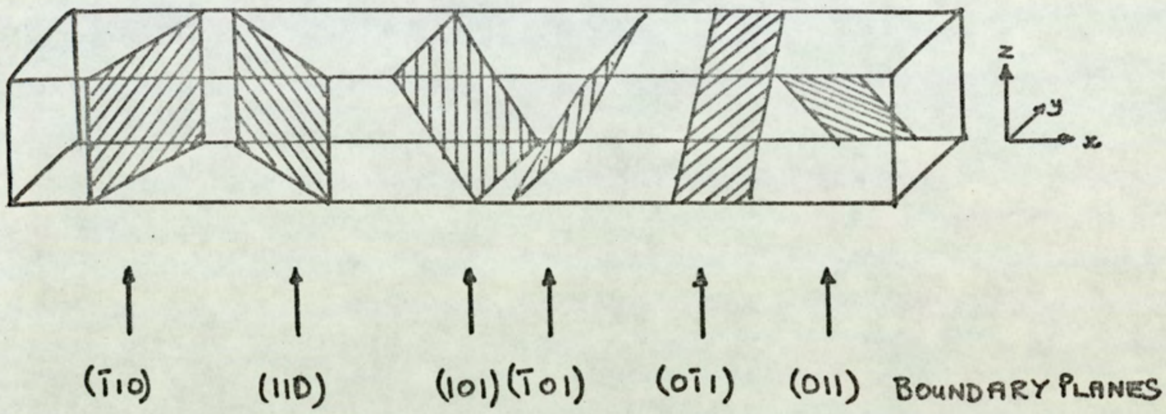

Fig.5.10 Illustration of column of cells along [100] direction containing each possible type ⟨110⟩ domain boundary.

mean total boundary area in the column will be

$$A = \frac{1}{T_{110}\sqrt{2}}\left[a^2 4\sqrt{2} + 2(\text{Mean Area Of (011) Boundaries})\right]$$

where T_{110} is the mean distance between adjacent (110) boundaries in the [110] direction. Thus the mean total boundary area/unit volume A' will be of the form $A' = K/T_{110}$ where K is a constant. As a consequence of this relation the net rate of decrease in the number of 'wrong' bonds dn/dt will be proportional to $d(1/T_{110})/dt$.

The mean value of $1/T_{110}$ for each sample annealed at 700°C (determined from the $J'(0)/J(0)$ results given in table 5.6) is plotted as a function of the annealing time in Fig.5.11. Also included in

Fig.5.11 are

(a) values of $1/T_{110}$ determined from the (210) superlattice lines of lithium ferrite samples prepared in a manner similar to the LF700, x type samples, but quenched from 730°C after times of 1, 10 and 30 minutes. These samples were prepared and investigated by Richard Bruce of this laboratory working under the author's supervision.

(b) the variation of the relative long range order parameter S as a function of the annealing time at 700°C; sample LF740,140 being used for reference purposes. Each value of S given in the figure represents an average of the values determined from the (110), (210) and (211) lines of each sample. The latter values were obtained from the relation

$$(S^2)_{hkl} = \left[\frac{I_{hkl}}{I_{220}}\right]_{LF700,x} \Bigg/ \left[\frac{I_{hkl}}{I_{220}}\right]_{LF700,140}$$

Samples LF700,10; LF700,20 and LF700,40 are not included in these results because their (220) lines were not measured. It is also worth remarking that as the LF700,x group of samples were prepared to be stoichiometrically equivalent the observed variation of S represents the variation of the degree of order and not the varying effects of Fe^{2+} ions.

The rather small change of the long range order parameter between the annealing times of 1 minute and 140 minutes coupled with the sharp decrease in the rate of growth of the domains in the neighbourhood of t = 1 minute indicates that a state of extremely high local order exists in the samples and that the volume fraction of disordered material is small and probably associated with the domain boundaries. It was

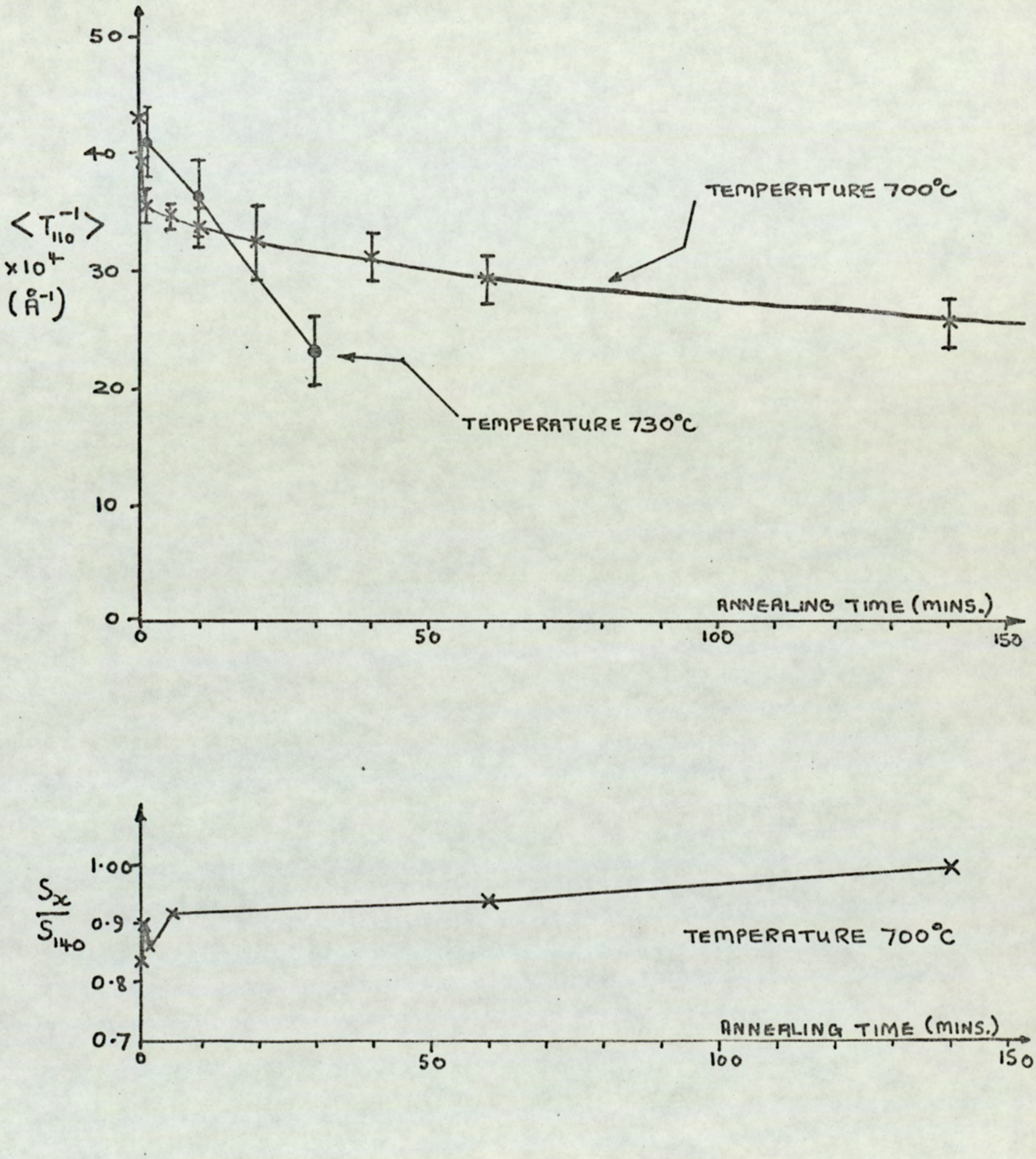

Fig.5.11 Mean values of $1/T_{110}$ and the relative long range order parameter as a function of time.

inferred therefore that the growth of the domains occurred only at the expense or loss of other domains (hereinafter referred to as growth by mutual absorption). These conclusions probably also apply to the samples annealed at 730°C and those annealed at 700°C for less than a minute as

(i) electron micrographs of small anti-phase domains in Cu_3Au (Yamaguchi et al.,1961) indicated highly ordered domains in close contact,

(ii) the difference in electrostatic energy/formula unit ($LiFe_5O_8$) between the ordered and disordered structures is approximately 9.8 e.v. (de Boer et al.,1950). This value is rather large compared with the ordering energy of Cu_3Au which is approximately 0.1 e.v/formula unit (Guttman,1956). Thus the attainment of local order in lithium ferrite should be extremely rapid below the transition temperature,

(iii) short range ordering of nearest neighbours and probably next nearest neighbour octahedral ions exists above the transition temperature of lithium ferrite (Brunel and Bergevin (1966), Yoshimori and Yamada (1967)),

(iv) the annealing times given in the present results correspond to the times the samples were held at 700°C and not the times of ordering which are probably (t + 2 to 5 minutes) if allowance is made for the cooling of the samples from the transition temperature to 700°C,

(v) the smallest measured mean domain thickness was $\sim 70\text{Å}$ (i.e. sample LF700,0).

Poquette and Mikkola in their analysis of anti-phase domain growth in Cu_3Au alloy concluded that the growth rate could be described by the equation governing classical grain growth in metals (see for instance

Cahn, 1970),

$$\text{i.e.} \quad D^2 - D_0^2 = Kt$$

where D_0 and K are constants and D and t are the average domain thickness and time variable, respectively. Owing, however, to lack of contrast in the present results it was only possible to conclude that anti-phase domain growth in lithium ferrite for $t \geqslant 1$ min is consistent with the above equation as good linear fits were obtained with plots of D^n against t for values of n ranging from -2 to +3. The fact that for both regions (i.e. $t \leqslant 1$ minute and $t \geqslant 1$ minute) $1/T_{110}$ could be fitted to a straight line is interesting because this would mean that the rate of loss of configurational energy is constant. This also applies to the results from the samples quenched from 730°C. The sharp decrease in the rate process after 1 minute in the former group of samples was found to be correlated with a decrease in the rate of change of the long range order parameter and also with the variation of $f(0)/f(0)_{\text{random}}$ which was <1 for sample LF700,0 and $\geqslant 1$ for the remaining samples of this group (see table 5.15). As the mean domain thickness can only be increased by a reduction of the mean number of domains/unit length, the initial high growth rate may be attributable to the fact that small domains are more easily absorbed than larger domains and that at $t \sim 1$ minute the volume fraction of small domains is reduced to a level which automatically decreases the rate of growth. In making this suggestion it is assumed that the migration of a domain boundary resembles a random walk process (i.e. the probability of the boundary moving to the right in a time dt is equal to the probability of moving to the left) since there would appear to be no a priori reason why a domain should grow or diminish in size.

Besides clarifying the time dependence of domain growth Poquette and Mikkola (1969) were also able to demonstrate, by examining the growth rate at four different temperatures, that the temperature dependence of domain growth in Cu_3Au is diffusion controlled with an activation energy Q of 1.9 e.v. (44 Kcals/mole). In the present work, unfortunately, the growth has been examined only at two temperatures, but even so the higher rate of growth at 730°C does appear to be consistent with a diffusion mechanism. By assuming that $d(1/T_{110})/dt$ is proportional to $e^{-Q/k\Theta}$ (Θ in °K) for $t>1$ minute which is not unreasonable as $d(1/T_{110})/dt$ is proportional to the net rate at which the number of 'wrong' bonds decrease, a comparison of the present results for $d(1/T_{110})/dt$ at 700°C and 730°C and at similar values of $1/T_{110}$ indicated an activation energy of 2.7 ± 0.7 e.v. for domain growth by mutual absorption.

Further support for a diffusion mechanism is given by other properties of lithium ferrite, but first it is necessary to consider the migration routes the Li^+ and Fe^{3+} ions might follow in going from one octahedral site to another octahedral site. Any octahedrally

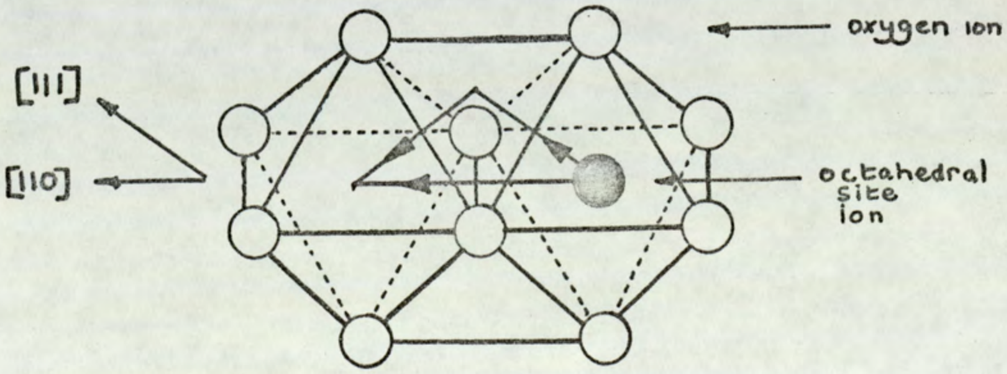

Fig.5.12 Migration routes from one octahedral site to another octahedral site.

co-ordinated ion in a spinel structure which is about to migrate from its site has the choice of passing through either the edge (⟨110⟩ type direction) or the face (⟨111⟩ type direction) of the octahedral arrangement of oxygen ions as demonstrated in Fig.5.12. In the former case the ion would arrive at the adjacent octahedral site, distant $\sim\frac{a\sqrt{2}}{4}$ away, whilst for the latter the ion would occupy an adjacent tetrahedral site distant $\sim\frac{a\sqrt{3}}{8}$ away. From the tetrahedral site, the ion may return to an octahedral site by a further jump through one of the faces of the tetrahedron of oxygen ions (⟨111⟩ type direction). Of the 12 octahedral sites surrounding each occupied octahedral site 6 will normally be occupied. The eight nearest tetrahedral sites, on the other hand, will normally be unoccupied. For approximate close packing of the oxygen ions the route octahedral-tetrahedral-octahedral site should be preferred as the alternative requires a greater displacement of the oxygen ions (i.e. higher activation energy).

According to the harmonic approximation, the mean square amplitude of motion $\langle u^2 \rangle$ of an atom, at high temperatures, is given approximately by

$$\langle u^2 \rangle = \frac{3k\Theta}{m(2\pi f)^2}$$ (see for instance, James 1948)

where f is the frequency of the atomic motion and m the atomic mass. In view of this relation it would appear that the order-disorder transition is most likely to be initiated by a migration of the Li^+ ion owing to its small mass. If it is specified that a jump of a Li^+ ion takes place when the mean amplitude is half the jump distance (i.e. $\frac{a\sqrt{3}}{16}$ for oct-tet or $\frac{a\sqrt{2}}{8}$ for oct-oct) then the vibration mode predominantly associated with the jump at the transition temperature ($\Theta \simeq 1020^{\circ}K$) should approximate to either

$$f = 3.36 \times 10^{12}\,\mathrm{sec}^{-1} \quad \text{for oct-tet jump}$$

or $$f = 2.04 \times 10^{12}\,\mathrm{sec}^{-1} \quad \text{for oct-oct jump}$$

To determine whether either mode was present, infra-red absorption analysis was carried out over the wave number range 40 cms^{-1} to 1000 cms^{-1}. The spectrum recorded for the lithium ferrite sample LF-S is given in Fig.5.13. To within experimental error this spectrum agrees with that given by Tarte (1962). At first sight it would appear that neither of the expected frequencies ($\cong 68\mathrm{cms}^{-1}, 112\mathrm{cms}^{-1}$) are present. Grimes (1971b) has demonstrated however, that the absorption of infra-red radiation in spinel structures is a two phonon process which means that the observed infra-red absorption frequencies are double the actual vibration frequencies of the modes in the solid. On this basis therefore the observed absorption frequency at 184 cms^{-1} will correspond to a vibration mode of 92 cms^{-1} in the solid. This value lies approximately mid-way between the expected frequencies. However, there is good reason to believe that the calculated frequencies are overestimates of the true frequencies as no account was taken of:

(i) the movement of the surrounding group of O^{2-} ions which will be in phase with the Li^+ ion if the vibration mode associated with the jump is the predominant mode describing the amplitudes of motion.

(ii) the extra energy required by the lithium ion to force its way through the space between the oxygen ions.

Under the circumstances therefore, the observed vibration mode appears to be consistent with the Li^+ ion jumping from an octahedral site to a tetrahedral site at the transition temperature. Moreover, it has also been shown with the aid of elastic constants (Grimes,1971b) that the observed mode in spinel structures corresponds to transverse waves in the $\langle 111 \rangle$ directions which gives even more support to a diffusion

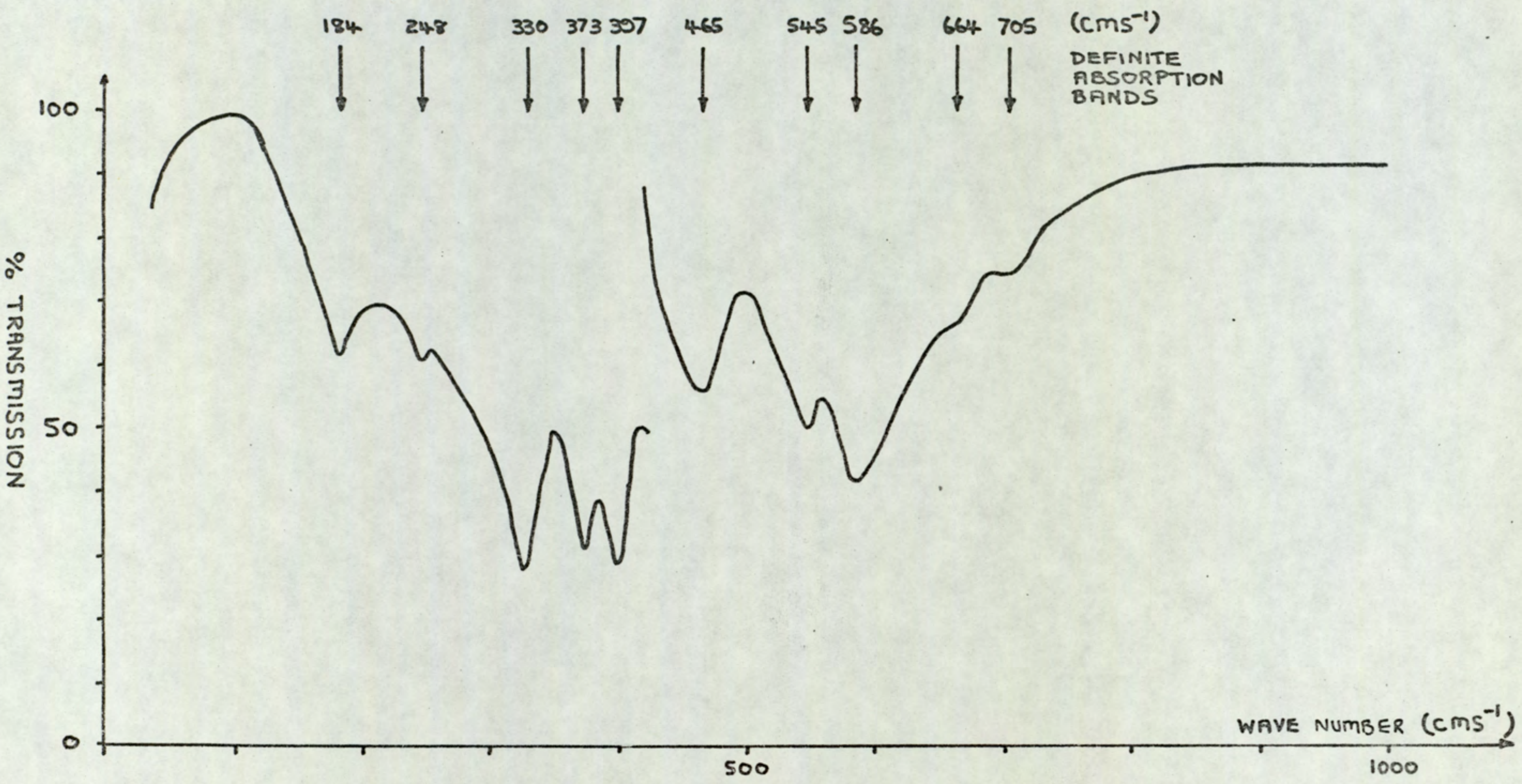

Fig.5.13 Infra-red spectrum of lithium ferrite from 40 to 1000cms^{-1} - sample LF-S.

controlled order-disorder transition in which the initial jump is from an octahedral to a tetrahedral site.

Having established that the order-disorder transition is most likely to be diffusion controlled it would not be unreasonable to assume that anti-phase domain growth by mutual absorption is also diffusion controlled. Recently, Glyde (1967) has shown that an approximate activation energy Q for self diffusion in face centred cubic metals is given by

$$Q = 9.12\times10^{-28} f^2 md^2 (\text{e.v.})$$

where m is the mass of the diffusing atom in atomic mass units, f is the frequency of atomic motion and d is the jump distance in Å. Further, Grimes (1971a) has demonstrated that this relation is also applicable to self diffusion in spinel structures. When applied to the Li^+ ion jumping from an octahedral site to a tetrahedral site an activation energy of 0.16 e.v. is obtained assuming $f = 2.76.10^{12}\,sec^{-1}$ ($\equiv 184 cms^{-1}$ absorption frequency). Clearly, as the Li^+ ion activation energy is small it would appear that the major contribution to the observed activation energy for domain growth is attributable to the Fe^{3+} ion activation energy. Self diffusion measurements of Fe in Fe_3O_4 (Himmel, Mehl and Birchenall, 1953) give a value for the activation energy of 2.39 e.v. which, according to Grimes (1971a), corresponds to a basic migration route of octahedral site - tetrahedral site - octahedral site. Now since the growth of the anti-phase domains in lithium ferrite is a process in which the Li^+ ions and Fe^{3+} ions have to interchange their positions in the tetrahedral group of octahedral ions, it would appear that the activation energy is accounted for by a diffusion mechanism in which both the Li^+ and Fe^{3+} ions follow the migration route octahedral-tetrahedral-octahedral site. Combining the estimated Li^+ ion activation energy with the published activation energy for Fe gives a total activation energy for the interchange $= 2.39 + 2 \times 0.16 = 2.71$ e.v. which agrees rather well with the measured value of 2.7 ± 0.7 e.v.

Although the above analysis is consistent with a diffusion mechanism experimental work at further temperatures is clearly desirable in order to confirm the details of the mechanism of domain growth by mutual absorption.

5.6 Chromium ion substitution in lithium ferrite

X-ray diffraction patterns of the lithium ferrite samples in which a small number of Cr^{3+} ions were substituted for Fe^{3+} ions (i.e. $LiCr_{x/4}Fe_{5-x/4}O_8$ where x = mean number of Cr^{3+} ions/unitcell) exhibited broadened superlattice lines and sharp lattice lines in spite of the fact that the samples were cooled relatively slowly (approx. 20°C/hr) from their preparation temperature to room temperature. It was concluded therefore that anti-phase domains are formed and that growth is inhibited by the presence of the Cr^{3+} ions as unsubstituted lithium ferrite prepared under similar conditions exhibits sharp superlattice and lattice lines. The behaviour of the superlattice lines with increasing Cr^{3+} ion content is shown in Fig.5.14 with the aid of (110) profiles ($2\theta \approx 22.4^\circ$) from samples containing substitutions of $\frac{1}{4}$, $\frac{3}{4}$ and $1\frac{1}{2}$ Cr^{3+} ions/unitcell. Also given are the (111) lattice line profiles ($2\theta \approx 27^\circ$) from the same samples.

An X-ray investigation of the cation distribution in these samples by Gorter (1954) showed that the Li^+ ions, for substitutions of less than $4Cr^{3+}$ ions/unitcell, do not enter the tetrahedral sites and that the Cr^{3+} ions probably occupy the octahedral sites. The likelihood of

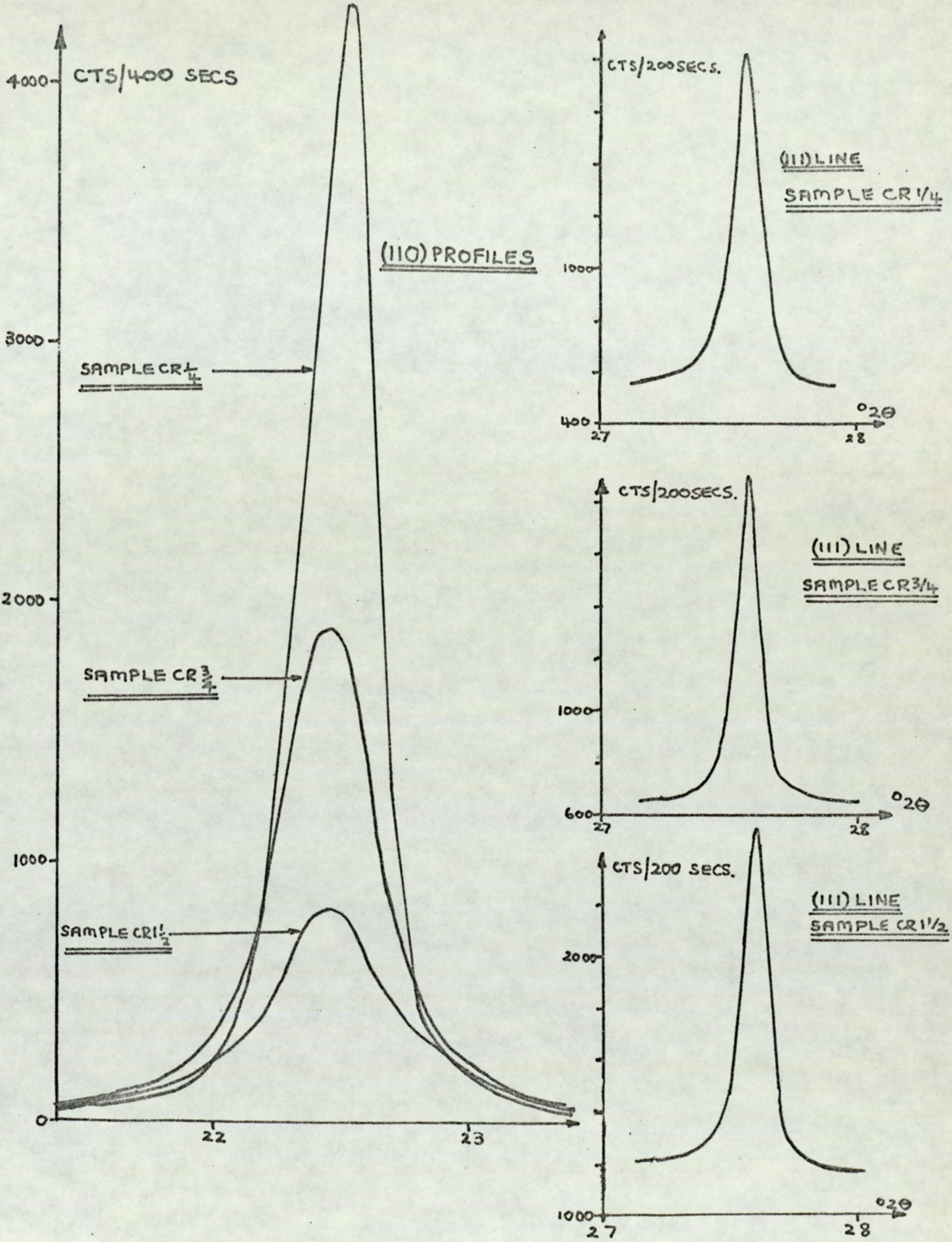

Fig.5.14 Effect of Cr^{3+} ion substitution on the breadth of the (110) profile from lithium ferrite.

any of the Cr^{3+} ions occupying tetrahedral sites is very remote as this ion has a high octahedral site preference energy, calculated to be approximately 2 e.v. (McClure, 1957), as a result of the symmetry of its outer 3d orbitals; the Fe^{3+} ion exhibits no such preference as its ground state has spherical symmetry.

The present X-ray diffraction results from these materials were examined in three parts:-

(i) Lattice parameters

Not all the lattice line profiles were measured. However, a point was made of measuring at least the (220), (400), (440) and (533) lines so that accurate lattice parameters could be determined by extrapolation methods. The graphs of a_{hkl} versus $f(\theta)$, the extrapolation function, are given in Fig. 5.15. The variation of the lattice parameter as a function of the Cr^{3+} ion concentration is given in Fig.5.16a.

(ii) $J'(0)/J(0)$ values determined from variance analysis

It was assumed that the $\{110\}$ boundary model was appropriate to these samples. The average value of $1/T_{110}$ for each sample (determined from the results in table 5.9) is plotted, together with the mean deviations due to scatter, in Fig. 5.16b.

(iii) Long range order parameters

As the constitution of the tetrahedral sites is unchanged by the Cr^{3+} ion substitutions, the integrated intensity of the (220) line will be the same for each sample. Consequently, the long range order parameters were determined from the

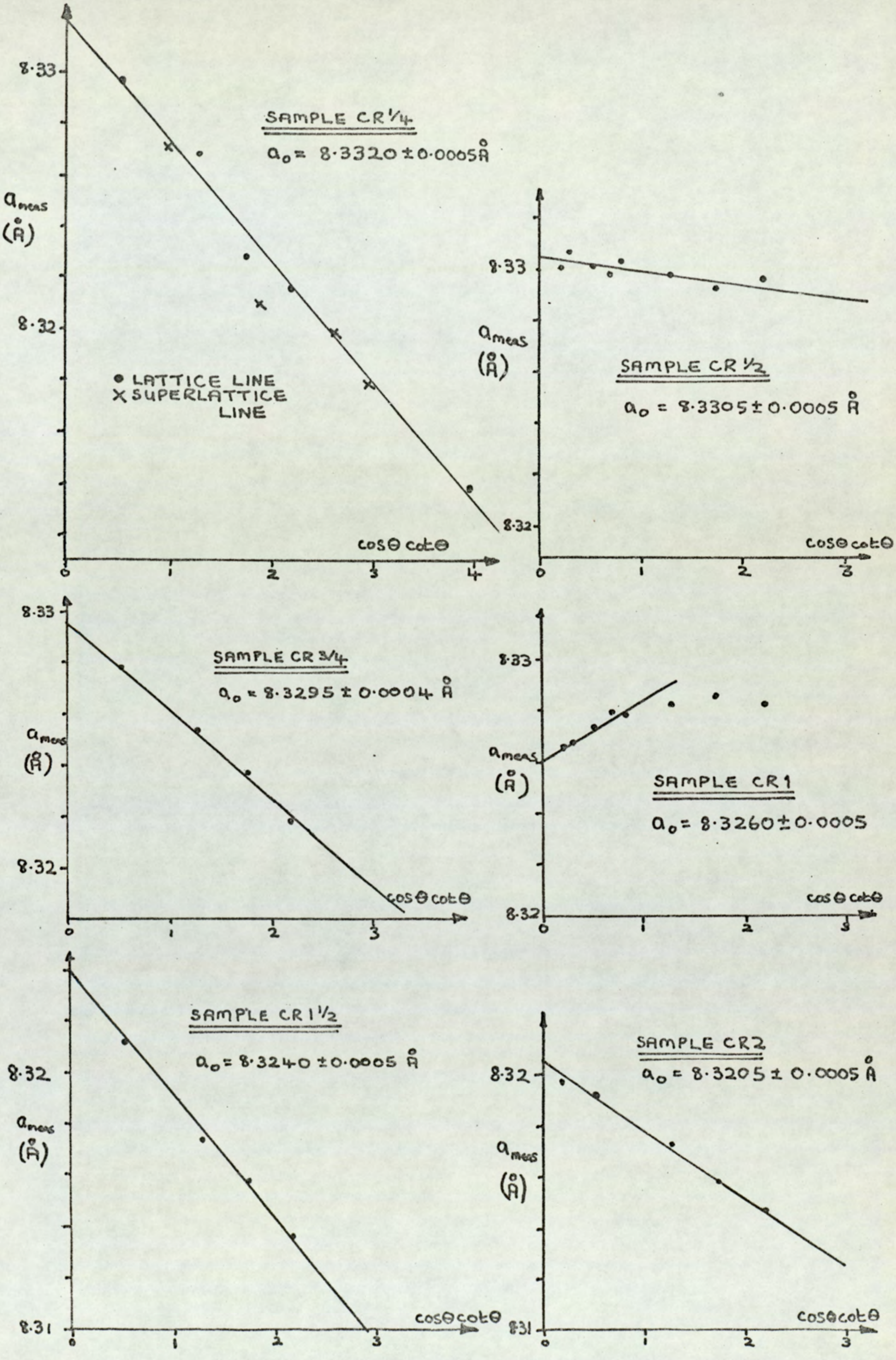

Fig.5.15 Graphs of a_{hkl} versus f(θ), the extrapolation function, for the chromium substituted samples of lithium ferrite.

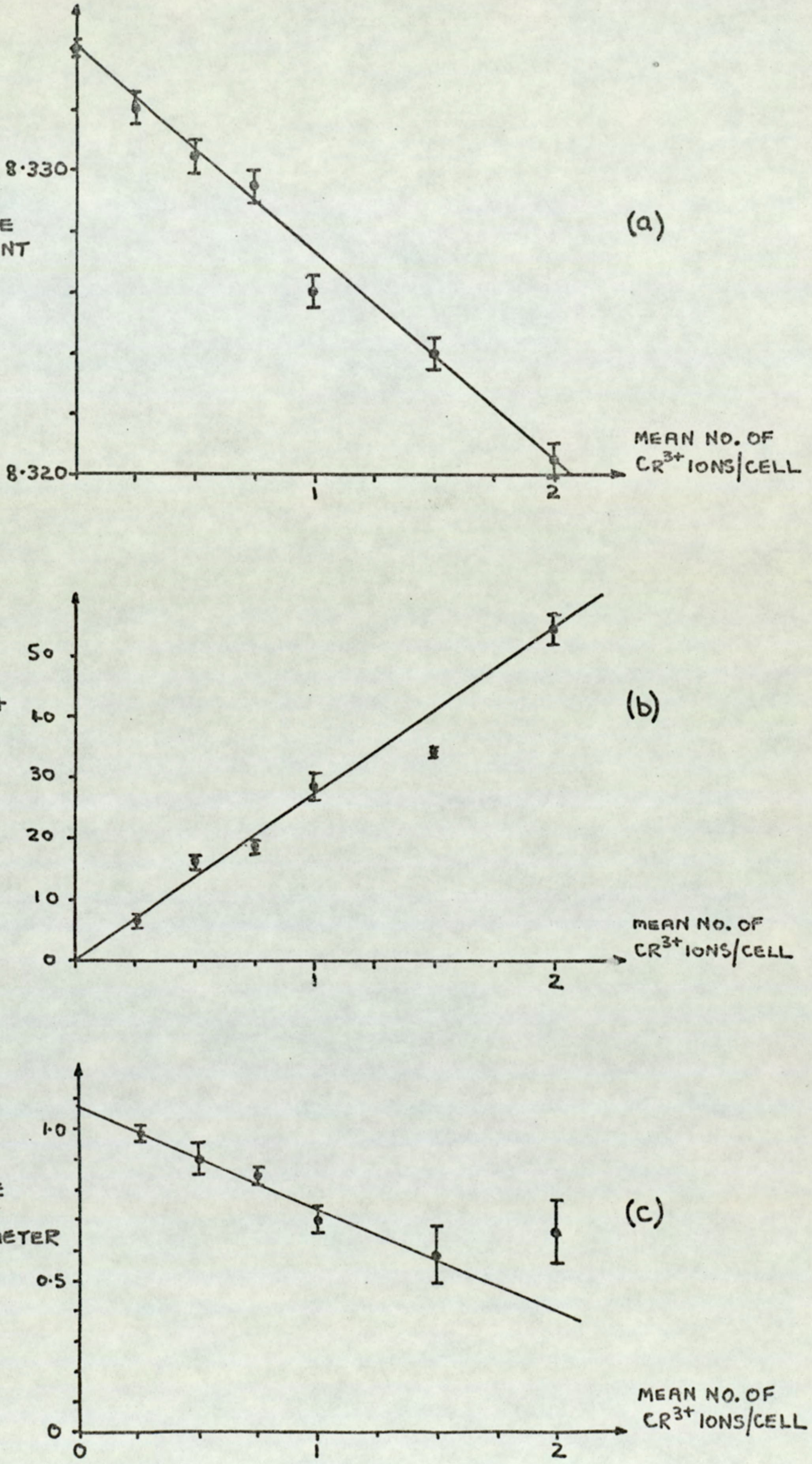

Fig.5.16 Variations of lattice parameter, $1/T_{110}$ and long range order parameter as a function of Cr^{3+} ion concentration.

relation,

$$S^2 = \left[\frac{I_{hkl}}{I_{220}}\right]_{CRx} \Big/ \left[\frac{I_{hkl}}{I_{220}}\right]_{\substack{\text{STANDARD}\\ \text{SAMPLE}}}$$

Unfortunately, the background intensity levels from these samples were high owing to CrKα fluorescence. All such values for S were therefore determined by averaging the (110), (210) and (211) values. These average values together with their mean deviations due to scatter are illustrated in Fig.5.16c as a function of the Cr^{3+} ion concentration.

The graphs given in Fig.5.16 indicate that each of the parameters is a substantially linear function of the Cr^{3+} ion concentration. The linearity of the lattice parameter variation shows that the Cr^{3+} ions were accepted into the lithium ferrite structure with a certain degree of homogeneity. As $1/T_{110}$ also exhibits linearity this indicates that the surface area of the anti-phase domains is proportional to the Cr^{3+} ion concentration. Finally, the linearity of the long range order parameter indicates that, on average, a fixed fraction of the Li^+ ions relative to the Cr^{3+} ion concentration are displaced from their ordered positions. The argument for the latter interpretation is given below.

The modulus of the structure factor F for the superlattice lines is approximately proportional to the difference in the average atomic scattering factors of the ions associated with the "Fe^{3+}" and "Li^+" octahedral sites of unsubstituted lithium ferrite. Let x be the average number of Cr^{3+} ions/unitcell and assume for the present approximation that the atomic scattering factors of Fe^{3+} ions and Cr^{3+} ions are the same (i.e. f_m). Also, let k be the average number of Li^+ ions which enter the "Fe^{3+}" octahedral sites relative to x, the Cr^{3+} ion content (i.e. k = 1 when x Li^+ ions enter the "Fe^{3+}" sites). Ignoring the scale factor,

$$|F| = \text{Average}\left(f_{\text{"}Fe^{3+}\text{"}} - f_{\text{"}Li^{+}\text{"}} \right)$$

$$= \left[\left(1 - \frac{kx}{12}\right) f_m + \frac{kx}{12} f_{Li^+}\right] - \left[\frac{kx}{4} f_m + \left(1 - \frac{kx}{4}\right) f_{Li^+}\right]$$

$$= \left(f_m - f_{Li^+}\right) - \frac{kx}{3}\left(f_m - f_{Li}\right)$$

Thus, the order parameter S is given by

$$S = \frac{|F|}{|F|_{LiFe_5O_8}} \simeq 1 - \frac{kx}{3}$$

Clearly, as the measured order parameter is linear in x the fraction of Li^+ ions entering the "Fe^{3+}" octahedral sites relative to the Cr^{3+} ion concentration must be constant. From the slope of S, the value of k was found to be 1.02 ± 0.15 where the error was estimated from the range of possible linear fits. This result means that the number of Li^+ ions displaced from their ordered positions is equal to the number of Cr^{3+} ions added. As the Fe^{3+} ions do not normally enter the Li^+ ion sites in unsubstituted lithium ferrite it would appear that all the Cr^{3+} ions occupy positions normally occupied by Li^+ ions.

Conclusions

That substitution of Cr^{3+} ions in lithium ferrite impedes the growth of anti-phase domains indicates that

(i) the Cr^{3+} ions are present at the domain boundaries otherwise the normal growth process would occur. This is supported by the observation that the surface area of the domain boundaries is directly proportional to the Cr^{3+} ion concentration,

(ii) the crystal field stabilisation energy of Cr^{3+} ions is probably the source of energy impeding the growth process as this, essentially, is the only difference between Fe^{3+} ions and Cr^{3+} ions. Substitution of spherically symmetric Al^{3+} ions or Ga^{3+} ions into lithium ferrite does not destroy the long range order (Schulkes and Blasse (1963), Kapitnova (1965)).

Anti-phase domains, by definition, are regions where the crystal structure is perfectly ordered. Clearly, if this concept is to be retained for the present samples together with the observed condition that each added Cr^{3+} ion puts a Li^{+} ion in a wrong position, it must be accepted that all the Cr^{3+} ions occupy boundary positions.

To relate T_{110} to x, the average number of Cr^{3+} ions/cell, under these circumstances, consider a column of unit cells of parameter a along the [100] direction in which the domain boundaries are {110} type (shown previously in Fig.5.10). Also let n be the average number of Cr^{3+} ions/boundary/unit cell cross section. The domain boundary planes which are not parallel to the [100] direction are the $(\bar{1}01)$, (101), (110) and $(\bar{1}10)$ planes therefore the average observed domain thickness T in the [100] direction will be given by

$$n.\frac{1}{T} = \frac{2}{3}.\frac{x}{a}$$

i.e. $n = 2Tx/3a$

and since $T = \sqrt{2}T_{110}/4$ (Wilson and Zsoldos, 1966) n becomes

$$n = \sqrt{2}T_{110}x/6a$$

Values for n calculated from the experimental values of x, T_{110} and a are given in table 5.16. According to these results an average of approximately 9 Cr^{3+} ions must occupy each domain boundary plane in a unit cell in order to satisfy the model of all Cr^{3+} ions at the boundaries.

Table 5.16 Calculated values of n, the number of Cr^{3+} ions/boundary/unit cell cross-section.

n/Bdy/cel	9.05	7.30	9.35	8.35	10.44	8.55
x/cell	$\frac{1}{4}$	$\frac{1}{2}$	$\frac{3}{4}$	1	$1\frac{1}{2}$	2
T_{110} Å	1534	618	528	354	294	182

From an inspection of a unit cell model of lithium ferrite it appears that each possible $\{110\}$ boundary passes through three tetrahedral groups of octahedral ions/unit cell which, assuming the tetrahedral charge invariance principle, corresponds to three Li^+ ions and nine 3^+ ions. Also each of the boundary groups is linked to single and different tetrahedral groups either side of the boundary which, including the boundary groups, amounts to a total of nine tetrahedral groups. Thus, the value of n = 9 would appear to be very significant.

Collecting various results together it would seem that the suggested model (i.e. all Cr^{3+} ions at the boundaries) has a great deal of support. In particular:-

(i) the measured values for the order parameter could possibly be accounted for if it was assumed that the nine boundary tetrahedral groups are each occupied by at least on Cr^{3+}ion,

(ii) the initial values for the domain thickness distribution f(0) exceed the random model distribution values by 10 to 30%. As the boundary layer according to (i) will be approximately a unit cell in thickness this would be equivalent to an increase in the number of domains of "zero" thickness.

(iii) for domain growth to be completely impeded by the presence of Cr^{3+} ions it is necessary that a large fraction of these ions segregate on the boundaries. To demonstrate this

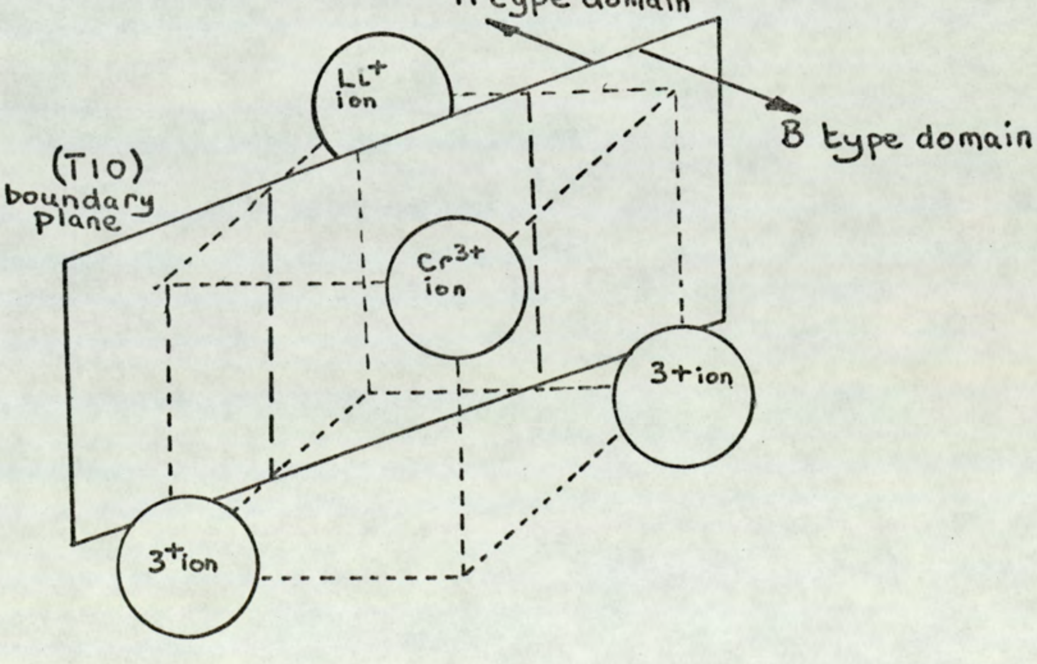

Fig.5.17 Illustration of an anti-phase domain boundary at one of the tetrahedral groups.

point consider the example of an A type - B type anti-phase domain boundary at one tetrahedral group and suppose a Cr^{3+} ion occupies the position in the B type domain which the Li^{+} ion would occupy if the A type domain were to grow (for a simplified illustration see Fig.5.17). Because the Cr^{3+} ion is relatively immobilised by its stabilisation energy, the tendency will be for the B type domain to grow at the expense of the A type domain. The observed state of the anti-phase domains however, is that domain growth is impeded in all directions. Hence, a large fraction of the Cr^{3+} ions must exist at or adjacent to the boundary in order to impede the growth of both the A and B type domains.

(iv) a somewhat similar problem to the present one, namely long range order in $Cu_{3+x}Au_{1-x}$, has been examined by Gehlen and Cohen (1969). They reached the conclusion, after studying computer simulated models of structures which matched up to their experimental short range and long range order parameters, that the excess atoms above Cu_3Au tend to segregate leaving most of the structure as fully ordered Cu_3Au.

(v) by placing the Cr^{3+} ions at the domain boundaries, the structure would appear to take on a fairly low energy configuration in that the ordered form of lithium ferrite is retained inside the domains whilst the positive energy normally associated with the domain boundaries is compensated for by the stabilisation energy of the Cr^{3+} ions.

CHAPTER 6.

ANALYSIS OF THE ANTI-PHASE DOMAIN STRUCTURE BY FOURIER TECHNIQUES

6.1 Introduction

By itself variance analysis only provides enough information for speculating on the nature of the domain thickness distribution. Fourier analysis, on the other hand, is potentially capable of providing the whole of the domain thickness distribution. However, even if all the effects of systematic errors are eliminated from the measured transform function J(t) the form of the domain thickness distribution f(t) is not directly interpretable unless the random model describes the distribution. This does not mean that Fourier analysis is of little value because it is nearly always possible to obtain the function g(t), the probability of two cells separated by a distance t in the [hkl] direction being similar, as J(t) for an anti-phase domain structure in which no restrictions are placed on the types of adjacent domain is given by

$$\frac{J(t)}{J(0)} = \frac{4}{3} g(t) - \frac{1}{3} \qquad \text{(Wilson, 1943)}$$

where $g(0) = 1$ and $g(\infty) = \frac{1}{4}$. The function g(t) in fact, has the particularly useful property of being more sensitive than the domain thickness distribution f(t) to the presence of large anti-phase domains as the latter represents a distribution of numbers of domains rather than a distribution of the volume fractions taken up by domains.

A unique feature of the present analysis compared with previous published analyses on X-ray line broadening due to anti-phase domains is that a method has been evolved for determining the domain thickness distribution f(t). The theory for this determination is based on the method of deriving the intensity distribution across a line profile by expressing the structure amplitude diffracted from a crystallite as the sum of the structure amplitudes diffracted by each domain (Landau(1937a), Lifschitz(1937)). By taking this approach not only are the results of Roessler and Flinn (1967) recovered more readily, but also the domain thickness distribution is expressable, indirectly, in terms of J"(t)/J(0).

6.2 Theory of X-ray diffraction from an anti-phase domain structure with domain thickness distribution f(t).

The intensity distribution across an X-ray diffraction line profile is given, within a scale factor, by

$$I(s) = \int_0^\infty \left[J(t)\cos 2\pi st - K(t)\sin 2\pi st \right] dt$$

where t is a vector length in the [hkl] direction and J(t) is the mean value of FF* for cells separated by a distance t in the [hkl] direction. As a consequence of the definition of J(t) the derivation of an intensity distribution across a powder diffraction line profile reduces to a one dimensional problem.

Consider, therefore, a columnar section, aligned in the [hkl] direction, from a crystallite which has anti-phase domains. Let the boundaries of the nth domain be y_{n-1} and y_n and the structure factors of the unit cells in that domain be F_n (see Fig.6.1)

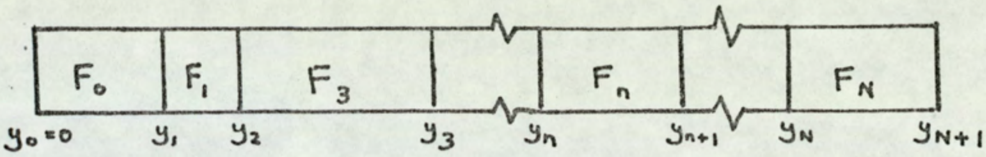

Fig.6.1 Columnar section comprising anti-phase domains.

By analogy to the general equation for I(s), the amplitude A(s) diffracted by an (hkl) plane may be expressed as

$$A(s) = \int_0^\infty F(t)\, e^{2\pi jst}\, dt$$

where F(t) is the structure factor of the cell at distance t in the [hkl] direction from the origin which in this instance corresponds to $t = y_0 = 0$. For the domain structure defined in Fig.6.1,

$$A(s) = \sum_{n=0}^{N} F_n \int_{y_n}^{y_{n+1}} e^{2\pi jst}\, dt$$

$$= \sum_{n=0}^{N} \frac{F_n}{(2\pi js)} \left(e^{2\pi jsy_{n+1}} - e^{2\pi jsy_n} \right)$$

The intensity function I(s), therefore, will be given by

$$I(s) = A(s)A^*(s)$$

$$= \sum_{n=0}^{N}\sum_{m=0}^{N} \frac{F_n F_m^*}{(2\pi s)^2}\left(e^{2\pi j s y_{n+1}} - e^{2\pi j s y_n}\right)\left(e^{-2\pi j s y_{m+1}} - e^{-2\pi j s y_m}\right)$$

$$= \sum_{n=0}^{N}\sum_{m=0}^{N} \frac{F_n F_m^*}{(2\pi s)^2}\left(e^{-2\pi j s(y_{m+1}-y_{n+1})} - e^{-2\pi j s(y_m - y_{n+1})} - e^{-2\pi j s(y_{m+1}-y_n)} + e^{-2\pi j s(y_m - y_n)}\right)$$

Making the substitutions p = m - n and q = n, I(s) may be expressed by the single summation

$$I(s) = \sum_{p=-N}^{+N} \frac{(N-|p|)}{(2\pi s)^2}\left(2J_p - J_{p+1} - J_{p-1}\right)\left\langle e^{-2\pi j s x_p}\right\rangle$$

For large N and rapid decay of J_p,

$$I(s) = \sum_{p=-N}^{+N} N\left(\frac{2J_p - J_{p+1} - J_{p-1}}{(2\pi s)^2}\right)\left\langle e^{-2\pi j s x_p}\right\rangle$$

where J_p is the mean value of FF* for cells separated by p domain boundaries,

x_p is the column length of p adjoining domains,

and $\left\langle e^{-2\pi j s x_p}\right\rangle$ is the mean value of $e^{-2\pi j s x_p}$.

If the thickness of a domain is t_i then x_p may be expressed as a sum of p domain thickness,

i.e. $x_p = \sum_{i=1}^{p} t_i$ and $x_o = 0$

and for the situation in which the sizes of the different domains are uncorrelated

$$\left\langle e^{-2\pi j s x_p} \right\rangle = \left\langle e^{-2\pi j s t_i} \right\rangle^p = m^p$$

where m is the characteristic function of the domain thickness distribution f(t),

$$\text{i.e.} \quad m = \int_0^\infty f(t)\, e^{-2\pi j s t}\, dt$$

It is also worth remarking that m^p will be characteristic function of the thickness distribution of p domains, $f_p(t)$

$$\text{i.e.} \quad m^p = \int_0^\infty f_p(t)\, e^{-2\pi j s t}\, dt = \left[\int_0^\infty f(t)\, e^{-2\pi j s t}\, dt \right]^p$$

Calculation of J_p

When each type of adjacent domain is equally probable the difference equation defining the probability Q_p of two domains separated by p boundaries being similar will be given by

$$Q_{p+1} = (1-Q_p)/3$$

which from the condition $Q_o = 1$ gives

$$Q_p = \tfrac{1}{4}(1+3(-\tfrac{1}{3})^p)$$

By formulating J_p in a manner similar to the formulation of $J(t)$ (Wilson, 1943) the result obtained is

$$J_p = FF^*(-\tfrac{1}{3})^p$$

On substituting J_p into the expression for $I(s)$ the result is

$$I(s) = \frac{8NFF^*}{3(2\pi s)^2} + \frac{16NFF^*}{3(2\pi s)^2}\sum_{p=1}^{N}\left(-\frac{1}{3}\right)^p\left(m^{*p} + m^p\right)$$

When multiplied by $(2\pi s)^2 e^{2\pi jst}$ and integrated with respect to s between the limits $-\infty$ to ∞, this expression becomes

$$\int_{-\infty}^{\infty} I(s)\,(2\pi s)^2 e^{2\pi jst}\,ds = \frac{8NFF^*}{3}\,\delta(t) + \frac{16NFF^*}{3}\sum_{p=1}^{N}\left(-\frac{1}{3}\right)^p\int_0^{\infty} f_p(x)\left(\delta(x-t)+\delta(x+t)\right)dx$$

$$= \frac{8NFF^*}{3}\,\delta(t) + \frac{16NFF^*}{3}\sum_{p=1}^{N}\left(-\frac{1}{3}\right)^p f_p(t)$$

where the terms of the form $\delta(t-x)$ are Dirac delta functions. (For the properties of these functions see Irving and Mullineux(1966)).

If the formulation of $I(s) = 2\int_0^\infty J(t)\cos(2\pi st)dt$ is substituted into the left hand side of the above equation and NFF* is replaced by J(0)/D, where D is the average domain thickness, it is possible to show by comparing coefficients that

$$J'(0) = -\frac{4J(0)}{3D}$$

and
$$J''(t) = -\frac{16J(0)}{3D}\sum_{p=1}^{N}\left(-\frac{1}{3}\right)^{p} f_p(t)$$

One obvious feature of these results is the physical impossibility of a 'hook' effect in J(t) as f(0) would have to be negative. The equation for J"(t) also demonstrates, quite clearly, the erroneous nature of the relation

$$\frac{J''(t)}{J(0)} = \frac{16f(t)}{9D}$$

obtained by Roessler and Flinn (1967)

To obtain an expression for f(t) let

$$Z(s) = \int_0^\infty \frac{J''(t)}{J(0)}e^{-2\pi jst}dt = H(s) - jG(s)$$

so that

$$Z(s) = -\frac{16}{3D}\sum_{p=1}^{N}\left(-\frac{m}{3}\right)^{p}$$

which on summing the right hand side becomes

$$Z(s) = \frac{16}{3D} \cdot \frac{m}{3+m}$$

or,
$$m = \frac{3\,Z(s)}{(16/3D - Z(s))}\,.$$

The expression for the domain size distribution f(t) is then given by performing a cosine transform on m + m*

i.e. $$f(t) = \int_{-\infty}^{\infty} (m + m^*) \cos 2\pi st \, ds$$

$$= \int_{-\infty}^{\infty} \left[\frac{3\,Z(s)}{(\gamma - Z(s))} + \frac{3\,Z^*(s)}{(\gamma - Z^*(s))} \right] \cos 2\pi st \, ds$$

where $\gamma = 16/3D$

Substituting $Z(s) = H(s) - jG(s)$ and utilizing the evenness of the integrand about $s = 0$,

$$f(t) = 12 \int_0^{\infty} \frac{(\gamma H(s) - (G^2(s) + H^2(s))}{(G^2(s) + (H(s) - \gamma)^2)} \cos 2\pi st \, ds$$

$$= \int_0^{\infty} R(s) \cos 2\pi st \, ds \qquad \text{say},$$

where $R(0) = 4$ as $H(0) = \gamma/4$ and $G(0) = 0$.

As the function f(t) will tend to have a similar shape to the J"(t) or J(t) characteristics, the function R(s), by analogy, will tend to behave similar to an intensity profile. This is also shown by the fact that as H(s) may be expressed as a series in $1/s^{2n}$ for $|s|>0$, the behaviour of R(s) at large values of s will be given by

$$R(s) \simeq \frac{12}{\gamma} H(s) \simeq -\frac{12}{\gamma}\frac{J'''(0)}{J(0)} \cdot \frac{1}{(2\pi s)^2}$$

(For large s, $\gamma H(s) > H^2(s)$ and $G^2(s)$).

To substantiate the theory given here, f(t) was derived for the random model. For this model $J(t)/J(0) = e^{-4t/3D}$ so that

$$Z(s) = \frac{16}{9D^2}\frac{(4/3D - 2\pi js)}{((4/3D)^2 + (2\pi s)^2)}$$

and subsequently

$$m + m^* = \frac{2}{(1+(2\pi sD)^2)}$$

The domain thickness distribution f(t), therefore, is given by

$$f(t) = \text{REAL PART}\left[\int_{-\infty}^{\infty} \frac{2e^{2\pi jst}\,ds}{(1+(2\pi sD)^2)}\right]$$

which after integration around an infinite semi-circle in the upper half of the complex plane gives $f(t) = (1/D)e^{-t/D}$, the domain thickness distribution for the random model.

Unless the Fourier transform results are accurate and reliable the evaluation of the domain thickness distribution will serve little purpose. If the operation of one Fourier transform on an intensity profile results in large errors in the $J(t)$ characteristic, which is frequently the case, further Fourier transform operations together with a double differentiation procedure on $J(t)$ will probably result in much larger errors in the final domain thickness distribution. Even reliable crystallite size distributions have proven immensely difficult to determine, because of systematic errors (see for instance Langford, 1968b), and they only require $V''(t)$ for their evaluation.

6.3 Experimental analysis and results

The Fourier transforms $J(t)$ were evaluated for the (210) profiles of the lithium ferrite samples LF725;LF735;LF740;LF745;LF700,0; LF700,$\frac{1}{2}$;LF700,1;LF700,5;LF700,60; and LF700,140. Good agreement, as shown earlier, (see chapter 3, section 5.6) was obtained between the values of $J'(0)/J(0)$ determined by pseudo-variance analysis and the values determined from the initial slope of $J(t)$. Although the above agreement is a necessary condition for the preclusion of systematic errors it is not a sufficient condition. Unfortunately, this was borne out by the fact that for some of the characteristics $J''(t)$ was negative at small values of t. For the purpose of determining domain thickness distributions the results as computed were therefore unsuitable.

However, as a knowledge of the domain thickness distributions is desirable, at least in qualitative terms, and as the observed $J(t)$

characteristics did not exhibit the signs of extensive systematic errors, the determination of the domain thickness distributions in the present samples seemed worth continuing with, but on an alternative basis. To improve the consistency of the J"(t) characteristics and also to reduce the effects of random errors on J(t), a curve fitting procedure was adopted with use being made of results from pseudo variance analysis.

As the pseudo-variance results indicated approximate agreement with the random model the form of each J(t) characteristic was represented at small values of t (<30Å) by

$$J(t) = J(0)e^{-(at+bt^2)}$$

where a was obtained from the Fourier estimated values for J'(0)/J(0) and b with the aid of the pseudo-variance estimated values for $f(0)/f(0)_{\text{random}}$ given in table 5.15. To curve fit the remainder of a J(t) characteristic, the $\log_e(J(t)/J(0))$ curve given by the computed results was subdivided into a series of connected straight lines (see Fig.6.2a) the slopes of which were used to express J(t) as a series of connected exponential function (see Fig.6.2b). This procedure was adopted because pseudo-variance results indicated approximate agreement with the random model (i.e. log(J(t)) = linear function of t). As the analytic differential coefficient of a fitted J(t) function at the junction of two exponentials will be discontinuous, J"(t)/J(0) was computed by a seven point numerical differentiation formula,

$$\text{i.e. } \frac{J''(t)}{J(0)} = \frac{5(J(t+15) - J(t-15)) - 4J(t) - 3(J(t+5) + J(t-5))}{1050}$$

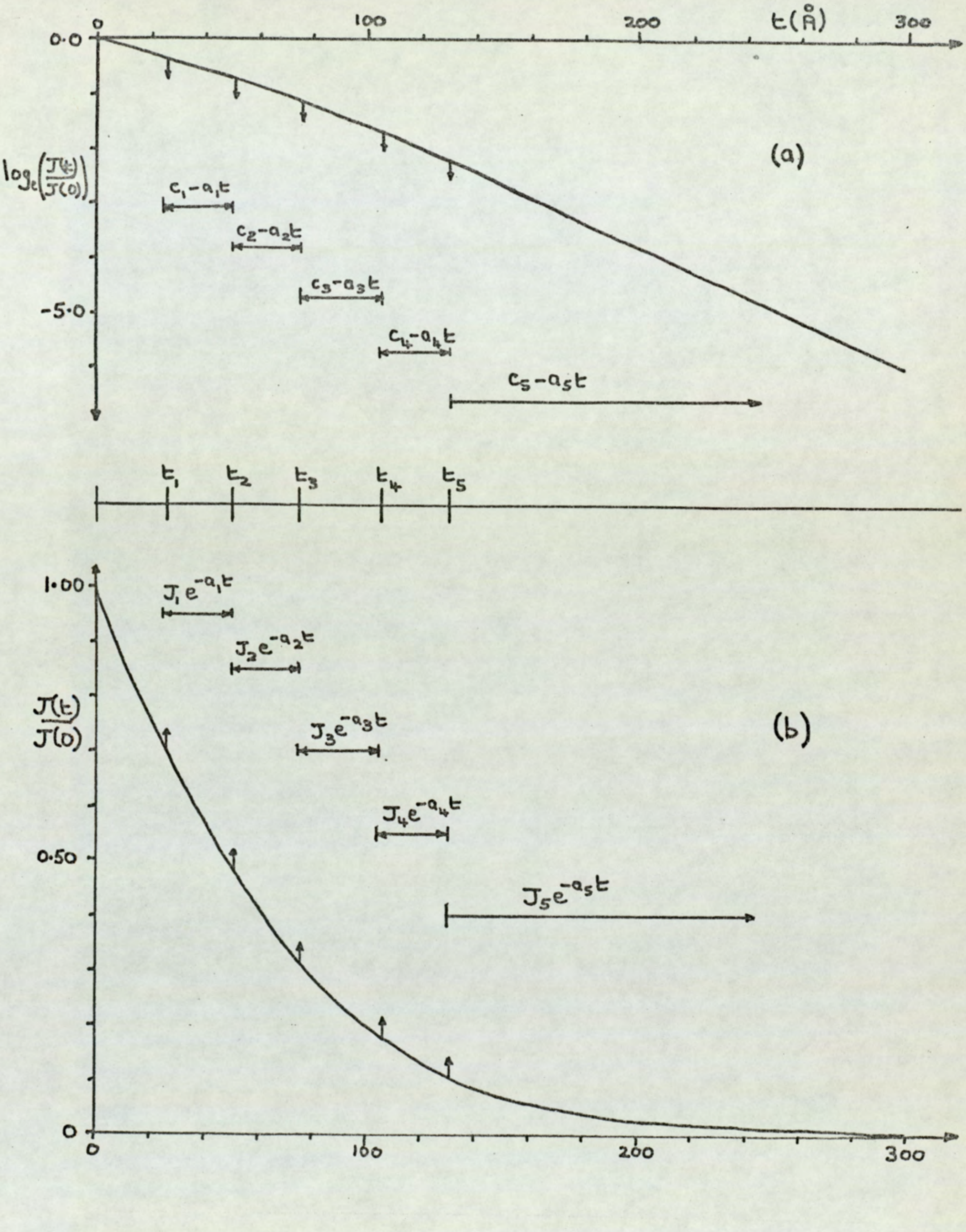

Fig.6.2 Illustration of curve fitting procedure to J(t) - sample LF740. Plots of log(J(t)/J(0)) versus t are sub-divided into linear regions, the slopes of which give the decay factors of the corresponding exponential regions in J(t).

which smoothed away much of the discontinuous effect.

Even after smoothing however, the changes in the gradient of $J''(t)/J(0)$ brought about by the curve-fitting procedure were still sufficiently large to propagate substantial systematic errors into the eventual domain thickness distribution. Fortunately, these errors exhibited themselves in an apparently simple form and as a result it was possible to reduce their influence by making simple subtractive corrections to the intermediate function $R(s)$ and the domain thickness distribution $f(t)$. Because of the sharp changes in each smoothed $J''(t)/J(0)$ function, $R(s)$ not only tended to be too large at small values of s, but also oscillated about a constant value at large values of s (see Fig.6.3a). Consequently, when $R(s)$ was subjected to Fourier transformation the value for $f(0)$ tended to be larger than the pseudo-variance estimated value, the initial variation of $f(t)$ resembled a $\sin(tk)/t$ function superposed on a smooth function, the value of $f(t)$ at $t \rightarrow \infty$ was constant and the area under $f(t) \neq 1$ (for an illustration see Fig.6.3b). The behaviour of $f(t)$ at small values of t was attributed to the lack of convergence of $R(s)$ whilst the lack of convergence of $f(t)$ was attributed to the oscillations in $R(s)$ and the discrepancy of the measured value of $R(0)$.

On this basis the following corrections were made to obtain representative domain thickness distributions:-

(i) the average value of $R(s)$ at large values of s was subtracted from all the $R(s)$ values before performing the Fourier transform operation,

(ii) the average value of $f(t)$ at large values of t, as determined from the corrected $R(s)$ function, was subtracted from all the values of $f(t)$.

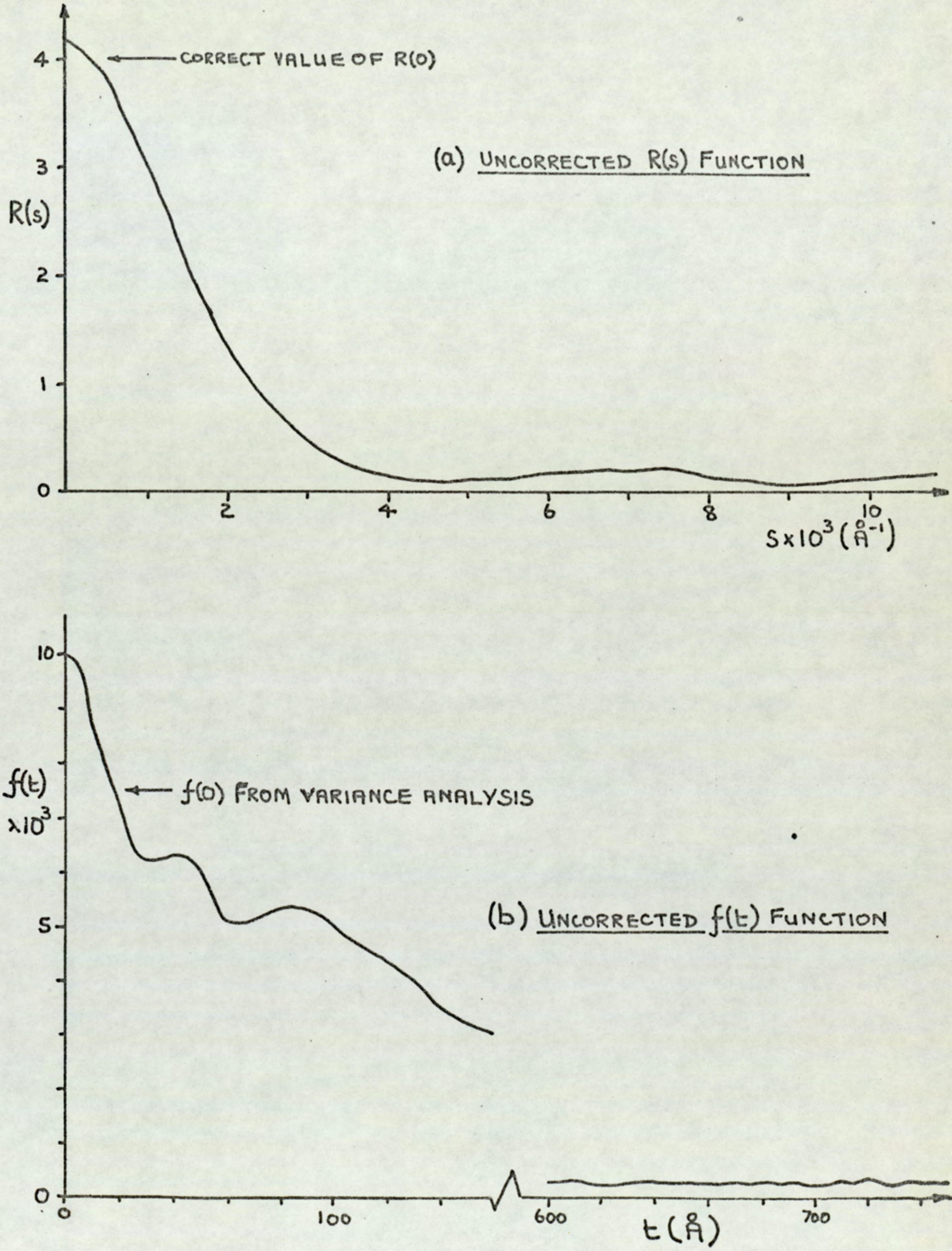

Fig.6.3 Illustration of behaviour of uncorrected R(s) and f(t) functions - sample LF740.

Further justification for making these corrections was given by the internal consistency of the modified distributions in that the following conditions were approximated to

(i) $\int_0^\infty f(t)\,dt \simeq 1$

(ii) $\int_0^\infty t f(t)\,dt \simeq D$, the mean domain thickness estimated from $J'(0)/J(0)$,

(ii) $f(0) \simeq$ value of $f(0)$ estimated from pseudo-variance analysis.

The Fourier computations involved in the determination of $f(t)$ were performed in a manner similar to the determination of $J(t)$, the step sizes between each value for $J''(t)/J(0)$ and $R(s)$ being 5Å and $1/7500\text{Å}^{-1}$ ($\equiv \Delta 2\theta = 0.02^\circ$ for a low angle diffraction profile). To minimise truncation errors in the determination of $R(s)$, the Fourier contribution from $J''(t)/J(0)$ at large t was estimated analytically by assuming the exponential dependence of $J''(t)/J(0)$, corresponding to the highest practically considered values, continues to $t = \infty$.

The results of Fourier analysis (i.e. $J(t)$ and $f(t)$) are presented in Figs.6.4a to 6.4j together with the domain thickness distributions expected for the random model (D given by values of $J'(0)/J(0)$). The values of a_i and t_i (defined in Fig.6.2) evaluated from the curve fitting of each $\log(J(t))$ function are presented in table 6.1 together with the values for b which were calculated from the average values for the ratio $(f(0)/f(0)_{\text{random}})$ given in table 5.15.

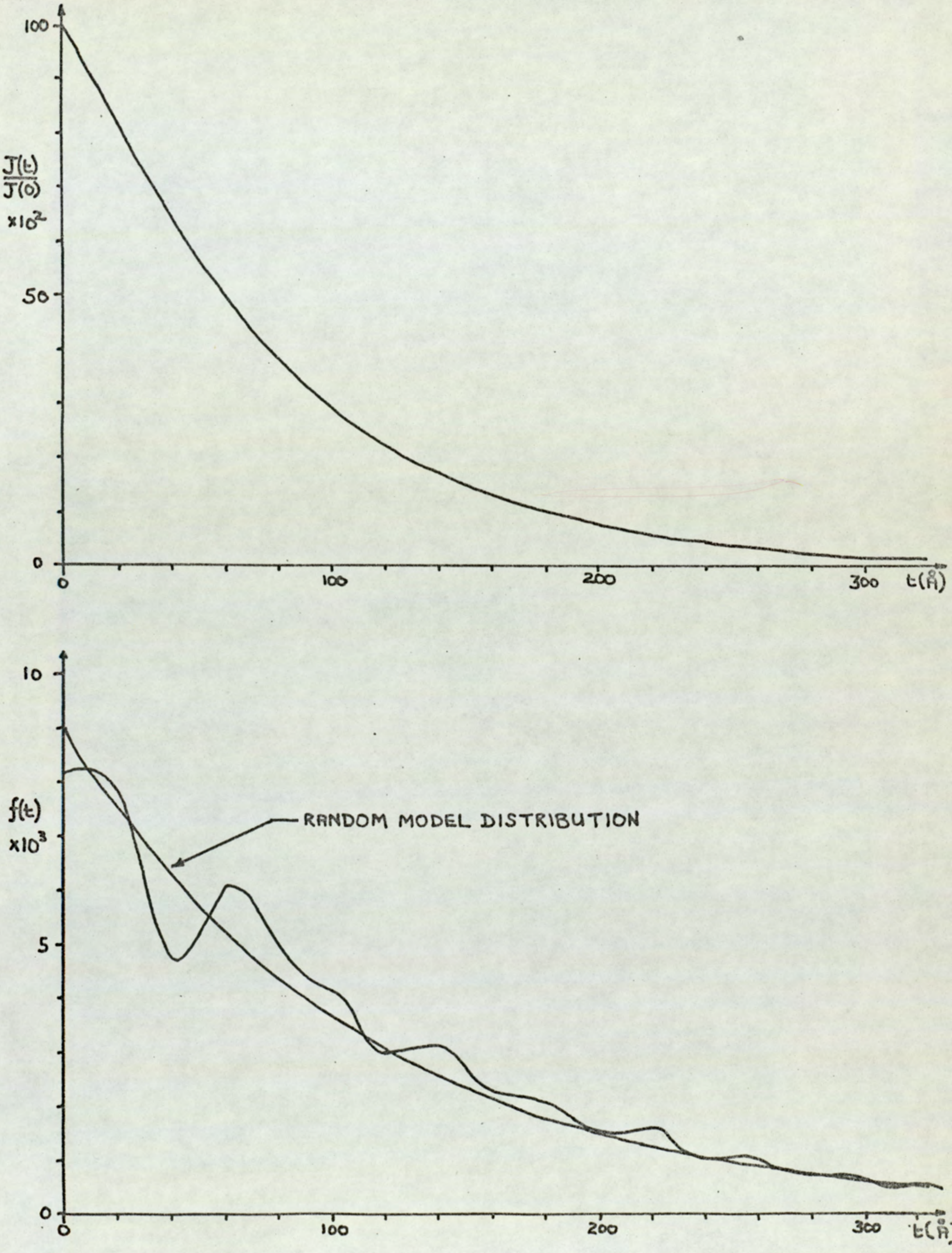

Fig.6.4a Fourier transform J(t) and domain thickness distribution f(t) - sample LF725.

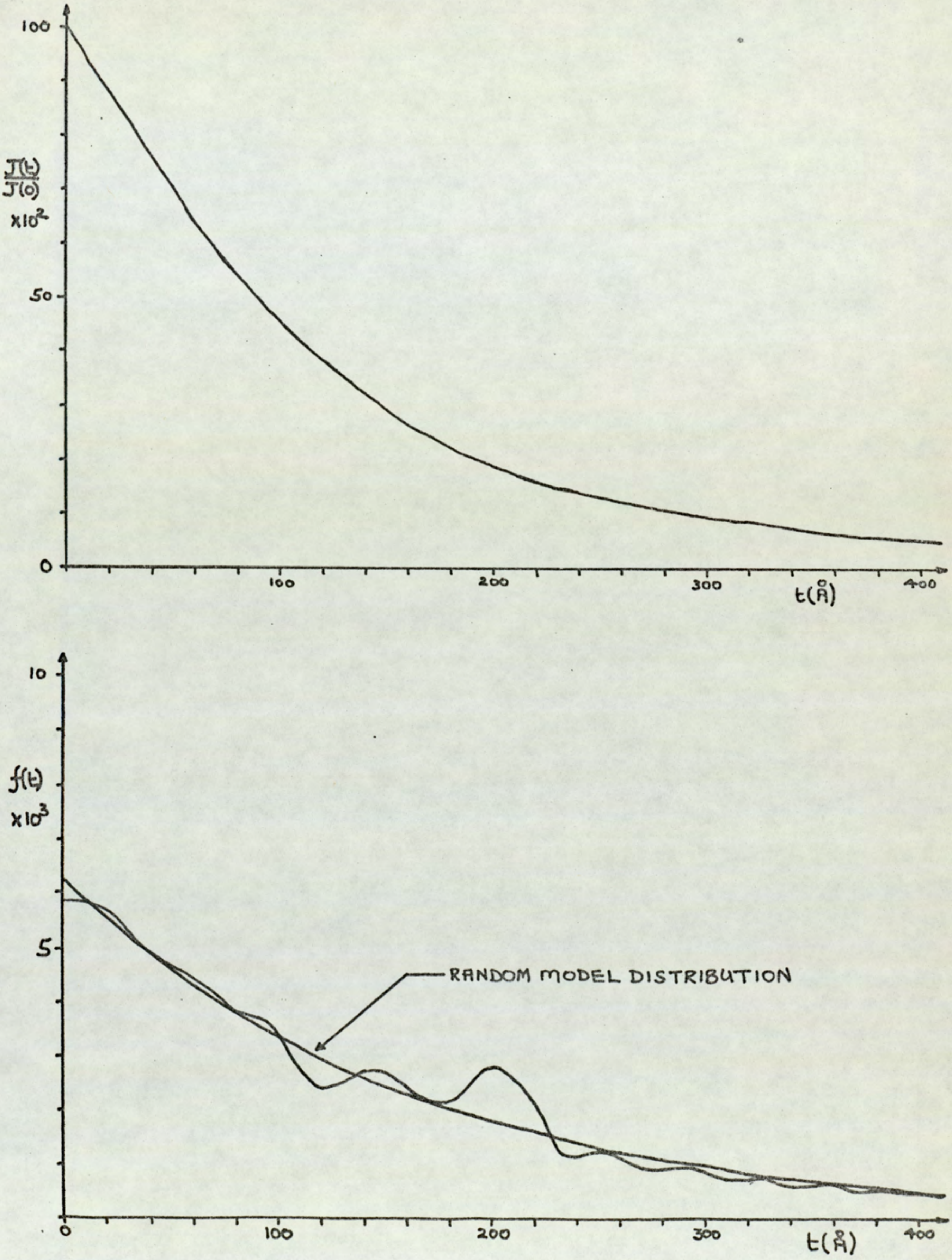

Fig.6.4b Fourier transform J(t) and domain thickness distribution f(t) - sample LF735.

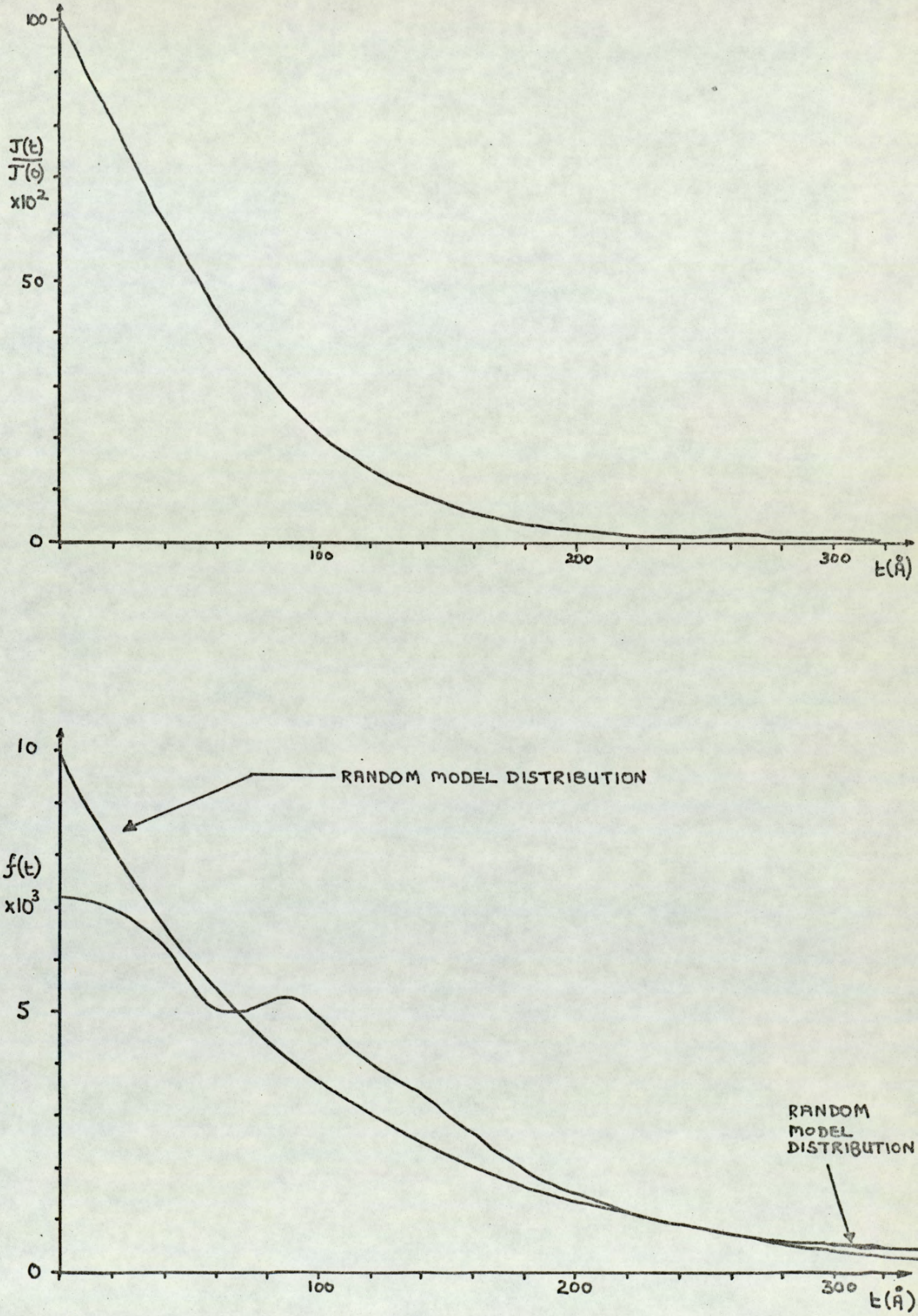

Fig.6.4c Fourier transform J(t) and domain thickness distribution f(t) - sample LF740.

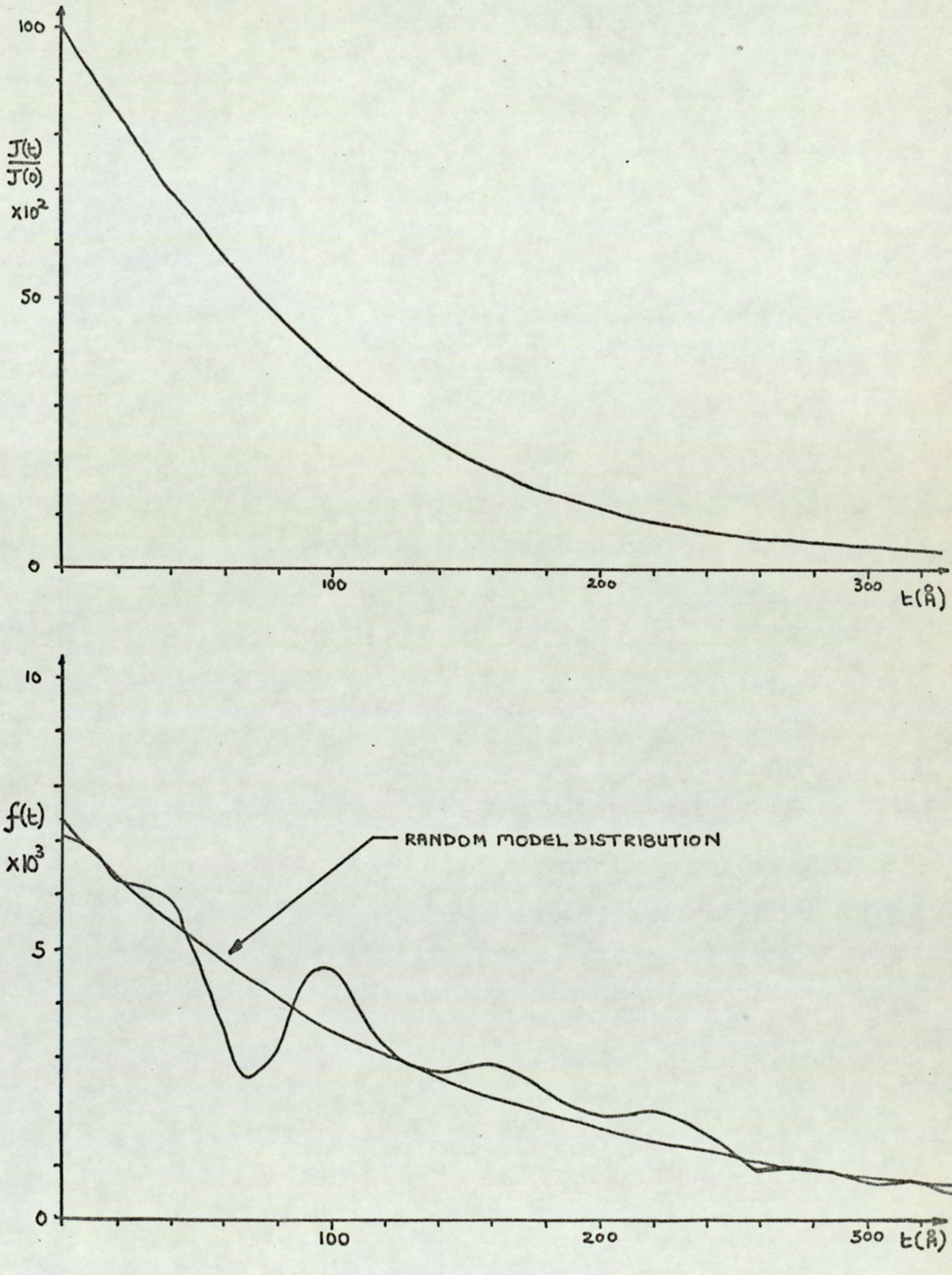

Fig.6.4d Fourier transform J(t) and domain thickness distribution f(t) - sample LF745.

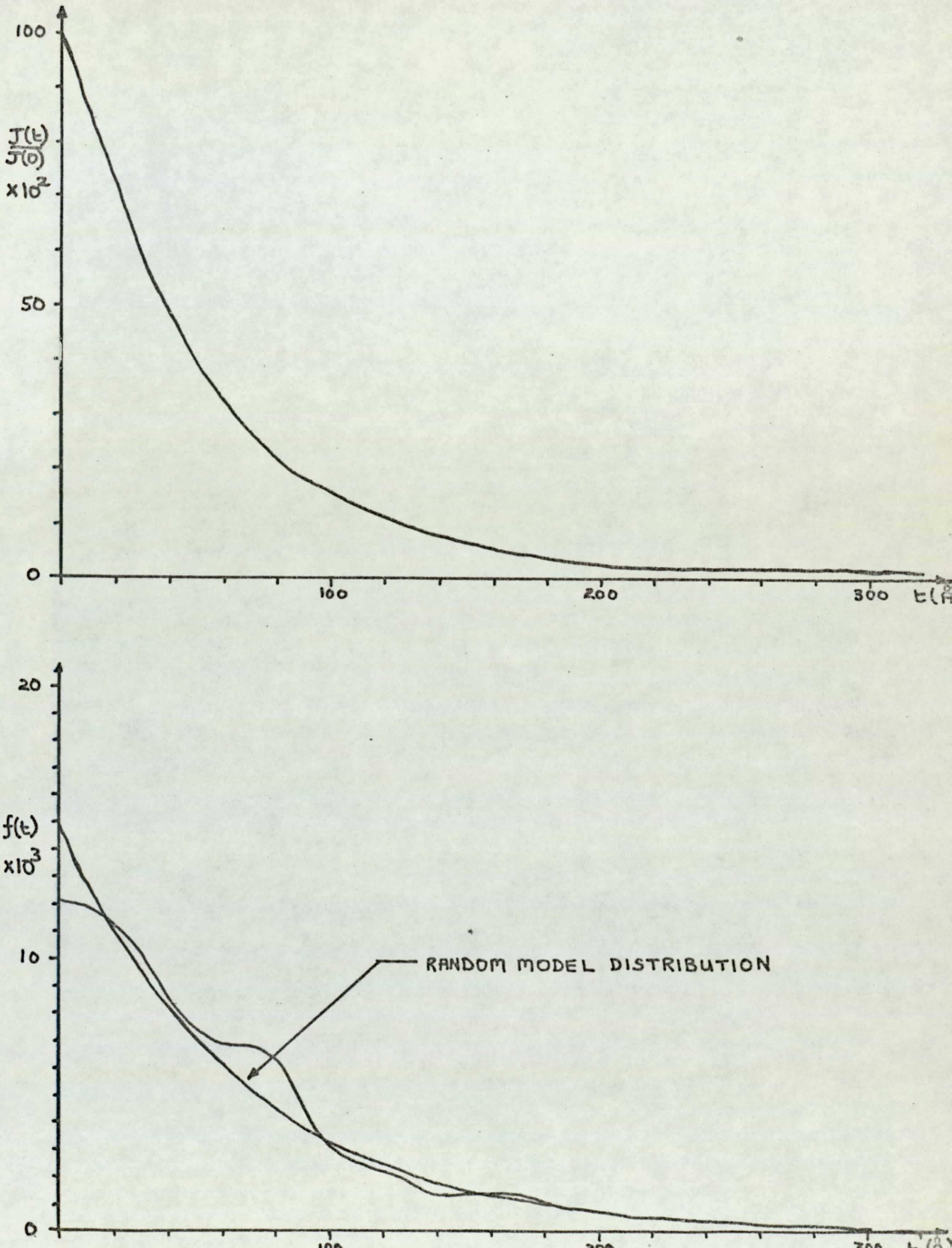

Fig.6.4e Fourier transform J(t) and domain thickness distribution f(t) - sample LF700,0.

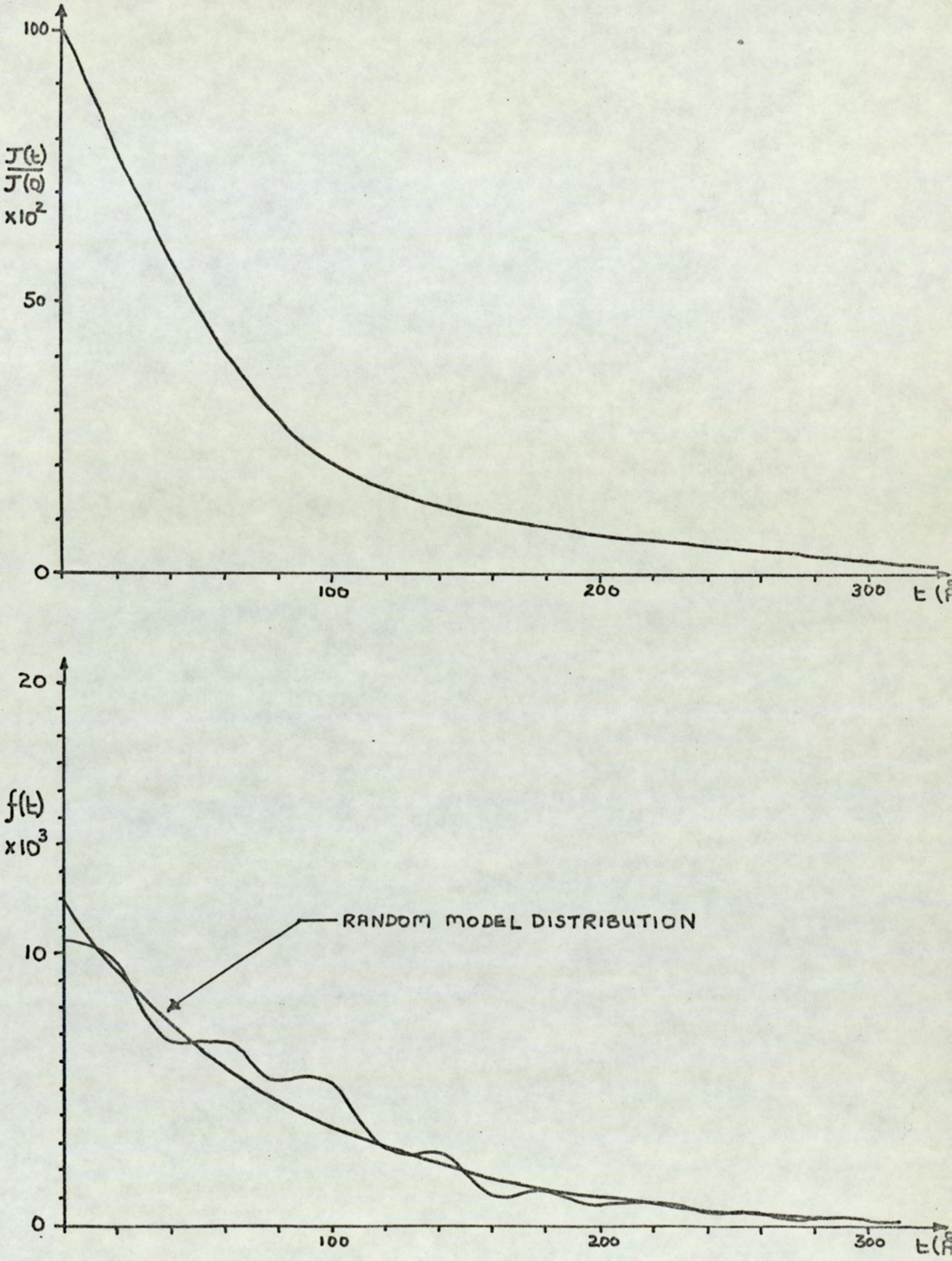

Fig.6.4f Fourier transform J(t) and domain thickness distribution f(t) - sample LF700,$\frac{1}{2}$.

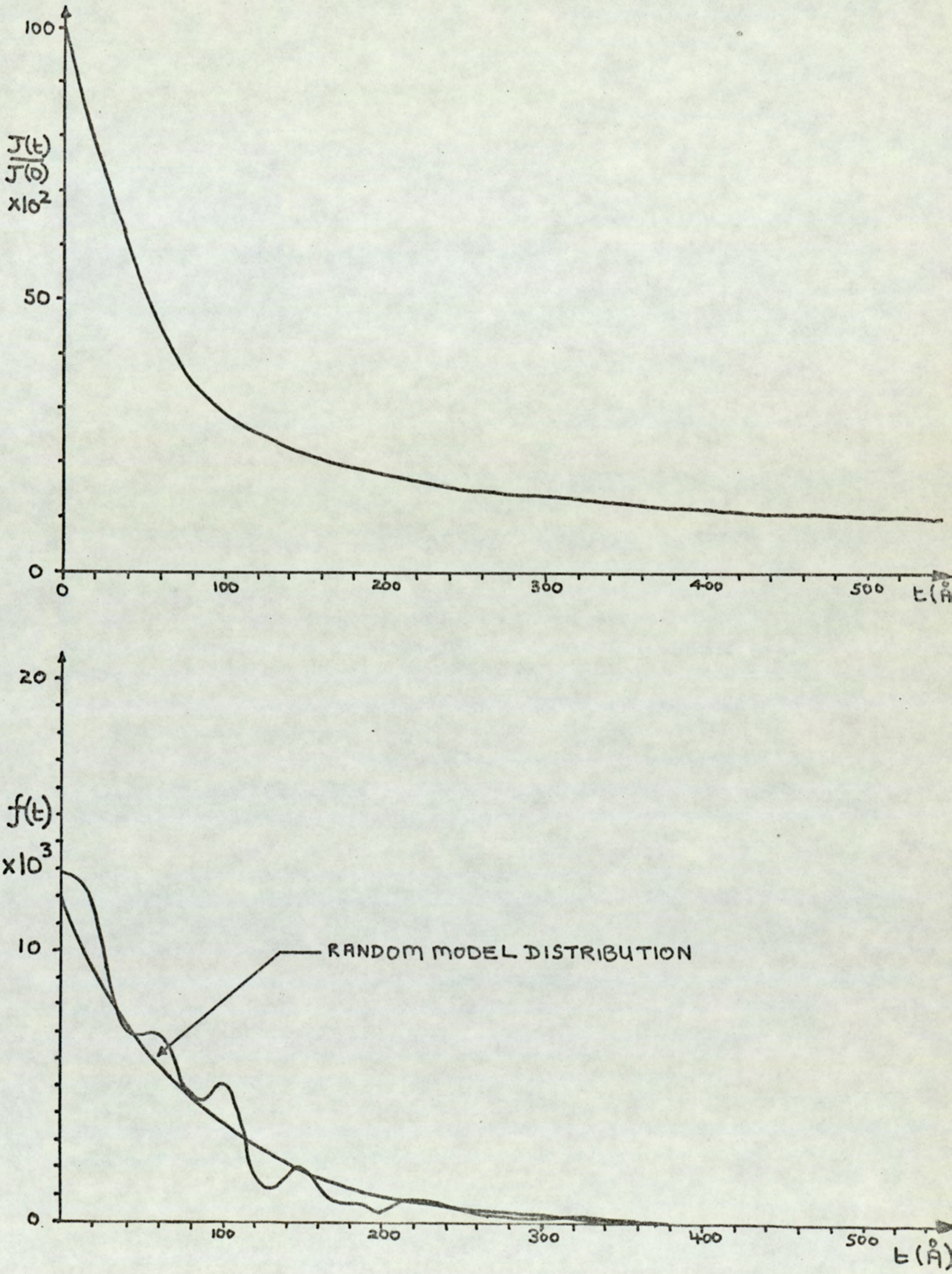

Fig.6.4g Fourier transform J(t) and domain thickness distribution f(t) - sample LF700,1.

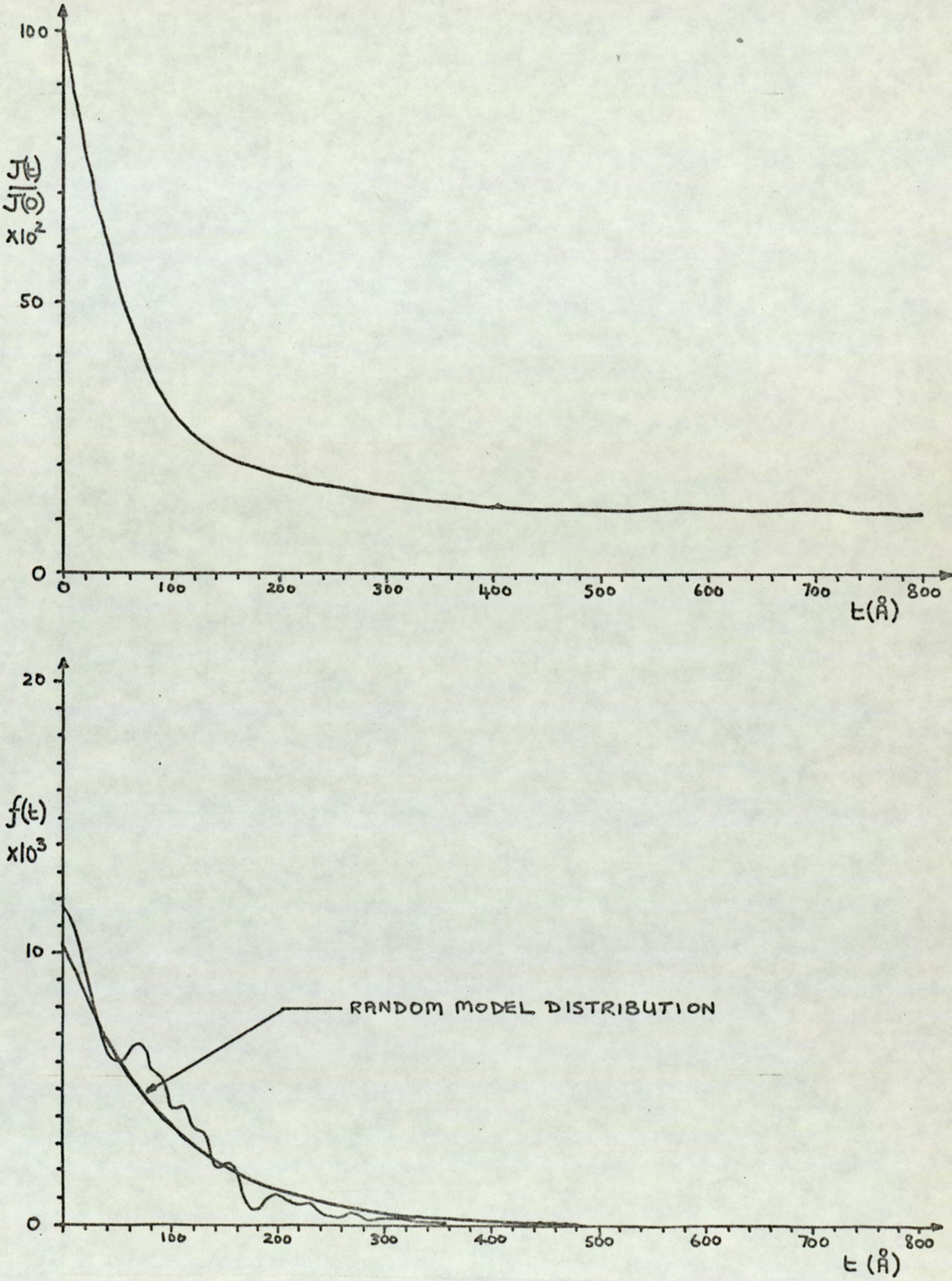

Fig.6.4h Fourier transform J(t) and domain thickness distribution f(t) - sample LF700,5.

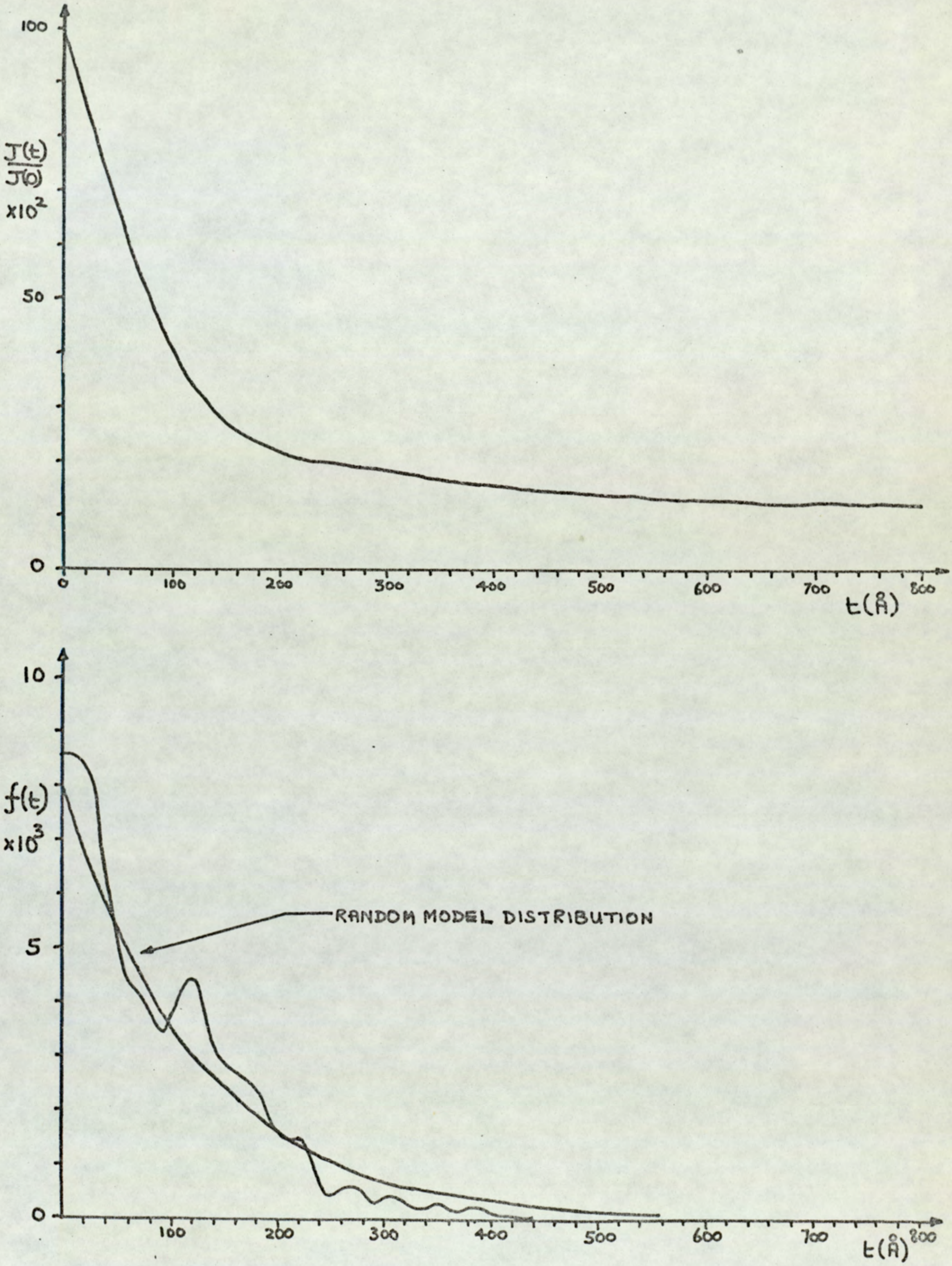

Fig.6.4i Fourier transform J(t) and domain thickness distribution f(t) - sample LF700,60.

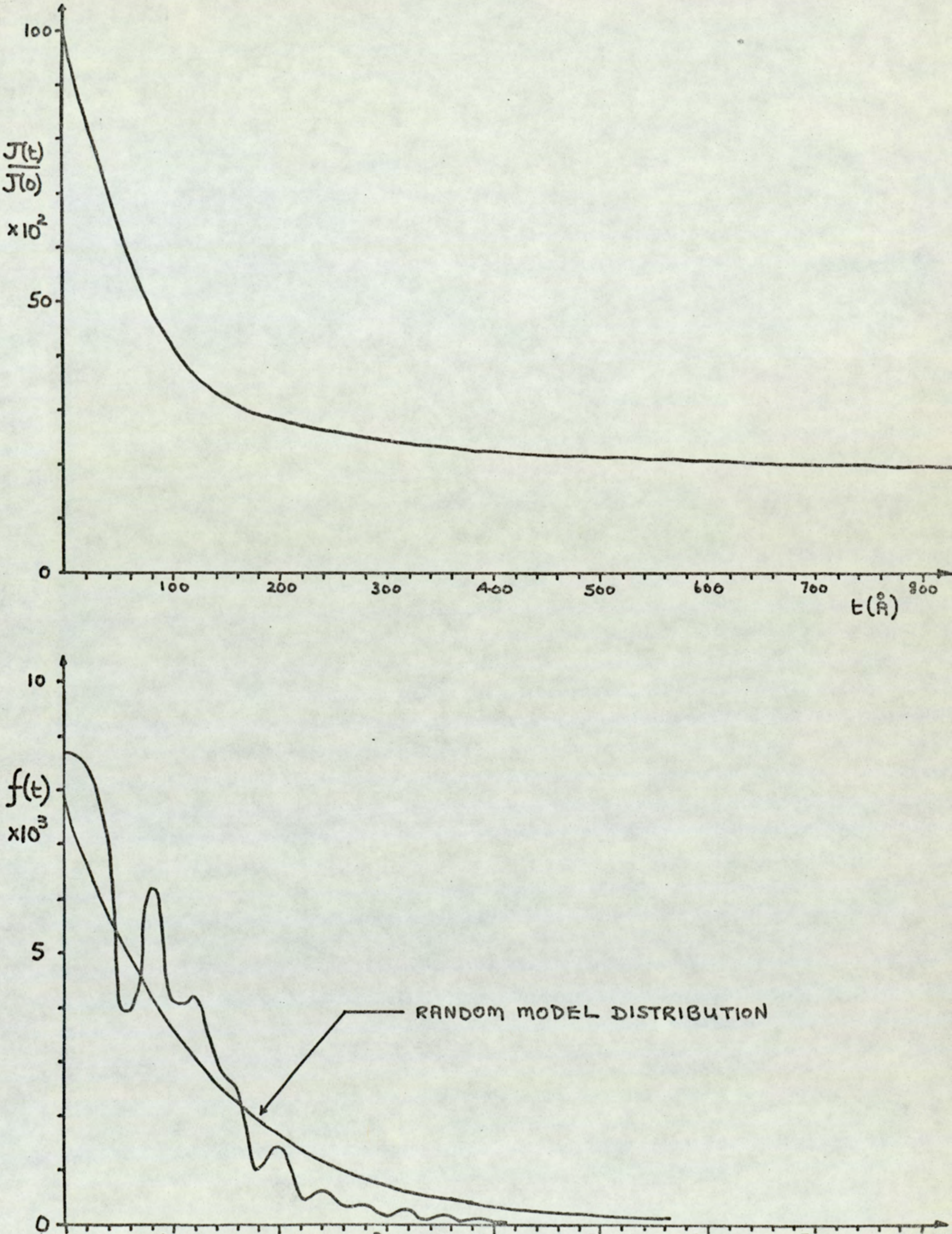

Fig.6.4j Fourier transform J(t) and domain thickness distribution f(t) - sample LF700,140.

Table 6.1 Parameters a_i, t_i and b obtained from curve fitting $\log_e(J(t)/J(0))$

SAMPLE	b	a_o	$a_1 - (t_1)$	$a_2 - (t_2)$	$a_3 - (t_3)$	$a_4 - (t_4)$	$a_5 - t_5$
LF725	0	0.0123	0.0132(40)	0.0138(115)	-	-	-
LF735	0	0.0084	0.0088(120)	0.0071(205)	-	-	-
LF740	19.10^{-6}	0.01321	0.01475(25)	0.0168(50)	0.0193(75)	0.0212(105)	0.0224(130)
LF745	0	0.0098	0.01139(70)	0.0122(135)	0.0099(230)	-	-
LF700,0	18.10^{-6}	0.0202	0.0168(80)	0.0204(140)	-	-	-
LF700,½	7.10^{-6}	0.0156	0.0175(40)	0.0126(100)	0.0092(85)	-	-
LF700,1	-15.10^{-6}	0.0163	0.0140(25)	0.0109(65)	0.0056(100)	0.0038(150)	0.0020(230)
LF700,5	-15.10^{-6}	0.0140	0.0130(25)	0.0100(75)	0.0060(110)	0.0035(145)	0.0024(210)
LF700,60	-6.10^{-6}	0.0107	0.0096(30)	0.0073(120)	0.0053(150)	0.0031(180)	0.0016(215)
LF700,140	-6.10^{-6}	0.0108	0.0092(25)	0.0069(85)	0.0043(120)	0.0024(150)	0.0016(195)

Although the domain thickness distributions still contain undulations as a result of the nature of the curve fitting procedure, their effect was not strong enough to obscure the general shapes of the distributions. The effect of errors in the a_i values on the measured distribution f(t) is demonstrated in Fig.6.5 where the distribution curves A and B were determined from a_i values deliberately chosen to be ± 2% in error (see table 6.2). To avoid these errors, each fitted J(t) function was recomputed from the values of a_i, t_i and b so that the subsequent log(J(t)) function could be compared with the original log(J(t)) function.

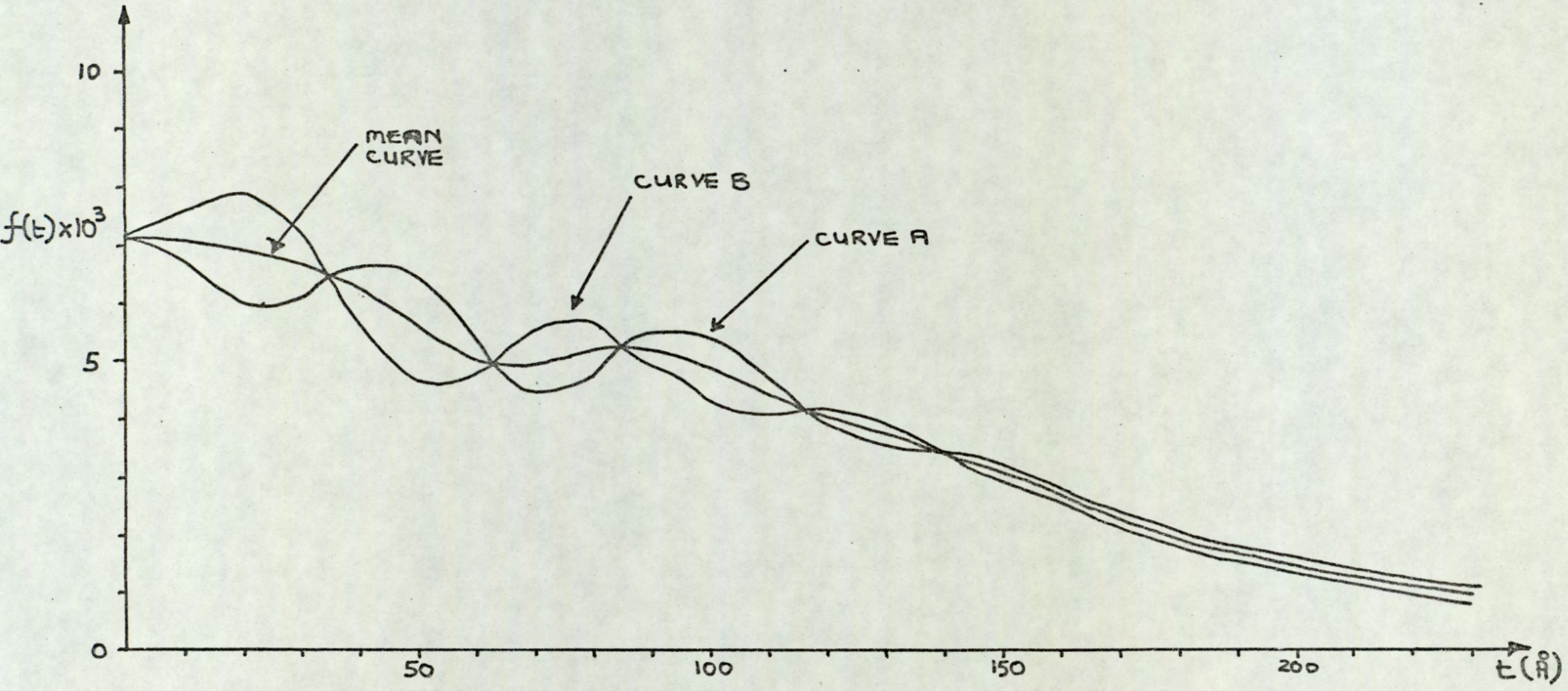

Fig.6.5 Effect on f(t) of 2% error in a_i values.

Table 6.2 Values of a_i, t_i and b appropriate to Fig.6.5

$b = 19.10^{-6}$	a_o	a_1	a_2	a_3	a_4	a_5
Curve A	0.01290	0.01505	0.01645	0.01970	0.0208	0.02285
Mean	0.01320	0.01475	0.01680	0.01933	0.0212	0.02240
Curve B	0.01345	0.01445	0.01715	0.01890	0.0216	0.02190
		$t_i = 25$	$t_2 = 50$	$t_3 = 75$	$t_4 = 105$	$t_5 = 130$

The following parameters were calculated from the domain thickness distributions,

(i) the sum of all the probabilities,

(ii) the mean domain thickness,

(iii) the standard deviation of the domain thickness about its mean value ($\sigma(D)$).

The values obtained for these parameters are given in table 6.3 together with the expected values for the mean domain thickness estimated from the initial slopes of the J(t) curves, the observed and expected values for f(0) and the ratios of observed standard deviations to those expected from the equivalent random models.

Table 6.3 Parameters obtained from domain thickness distributions.

SAMPLE	$\int_0^\infty f(t)dt$	f(0) OBSERVED ($Å^{-1}$)	f(0) FROM a_1 & b ($Å^{-1}$)	MEAN DOMAIN THICKNESS (Å)	MEAN DOMAIN THICKNESS FROM J(t)	STANDARD DEVIATION σ(D) (Å)	$\frac{\sigma(D)}{\sigma(D)_{random}}$
LF725	1.041	0.0082	0.0090	111	108	111	1
LF735	1.021	0.0059	0.0063	157	159	156	0.99
LF740	1.033	0.0074	0.0099	102	101	91	0.89
LF745	1.030	0.0071	0.0074	136	135	129	0.95
LF700,0	1.045	0.0122	0.0150	69	66	65	0.94
LF700,½	1.051	0.0104	0.0120	85	85	85	1
LF700,1	1.063	0.0128	0.0120	77	82	104	1.35
LF700,5	1.058	0.0118	0.0105	89	95	113	1.27
LF700,60	1.038	0.0085	0.0080	108	124	120	1.10
LF700,140	1.022	0.0087	0.0079	100	123	124	1.24

6.4 Discussion of results

Values for J'(0)/J(0) determined from J(t) were in good agreement, as shown earlier, with similar values obtained from pseudo variance analysis. This was only true however, when the former values were estimated by numerical differentiation based on the assumption that for $5 \leqslant t \leqslant 20$Å, $J(t) = a + bt + ct^2$. When J'(0)/J(0) was estimated by the normal method (Warren, 1959) of graphically fitting a straight line over a similar region, say 5 to 35Å, the subsequent values for

J'(0)/J(0) were always a good deal smaller than the other J'(0)/J(0) values (see table 6.4). This difference was attributed to the fact that the graphical values included a systematic error arising from terms in t^2 and higher order in the initial variation of J(t).

Table 6.4 Comparison of J'(0)/J(0) determined by different methods (Units $\mathring{A}^{-1}$)

SAMPLE	FOURIER (NUMERICAL)	FOURIER (GRAPHICAL)	PSEUDO-VARIANCE
LF725	-0.0123	-0.0091	-0.0125
LF735	-0.0084	-0.0063	-0.0088
LF740	-0.0132	-0.0096	-0.0132
LF745	-0.0098	-0.0073	-0.0099
LF700,0	-0.0202	-0.0139	-0.0202
LF700,½	-0.0156	-0.0110	-0.0166
LF700,1	-0.0163	-0.0105	-0.0160
LF700,5	-0.0140	-0.0100	-0.0146
LF700,60	-0.0107	-0.0072	-0.0110
LF700,140	-0.0108	-0.0070	-0.0105

To a large degree, the shapes of the measured J(t) and f(t) function confirm earlier deductions. The slow convergence of the J(t) characteristics appropriate to the samples LF700,x(x=1,5,60 and 140) indicates that large volume fractions of the crystallites are taken up by large domains (i.e.>800Å) even though the mean domain thickness is only ~100Å. The domain thickness distributions however, give the impression that all the domains are less than ~300Å in size. It would appear therefore, that domain growth occurs primarily through the activity of a few of the larger domains. The J(t) characteristics for samples LF740 and LF700,0 exhibit a rapid convergence to zero which indicates a very narrow range of domain sizes. Midway between these extremes are the samples LF725, LF735, LF745, and LF700,$\frac{1}{2}$,the J(t) curves for which agree quite well with the random model curves as previously indicated by the variance results in Chapter 5, section 4.

Despite the marked contrast in the shapes the measured J(t) characteristics, the shapes of the subsequent domain thickness distributions are not very different from their equivalent random model distributions. There are however, trends in the shape of f(t) which appear to be a function of the state of growth. In the earlier stages of growth, as for instance in sample LF700,0, the distribution tends to be flat initially ($f(0)<f(0)_{\text{random}}$) and as a result resembles a Gaussian curve. As growth proceeds (e.g. samples LF725;LF735;LF745; and LF700,$\frac{1}{2}$) the values for f(0) increase and the distributions approach those corresponding to the random model. Further domain growth (e.g.LF700,x;x=1,5,60,140) results in $f(0)> f(0)_{\text{random}}$ and a distribution which converges relatively slowly (i.e. similar to a Cauchy curve). Although the mean domain thicknesses for the latter set of samples are somewhat smaller than the mean domain thickness for the sample LF735 for instance, their equivalent stage of growth was considered advanced as sample LF735 had not reached the stage in which one or two domains governed the rate of growth. The domain thickness distributions suggested for the three stages of domain growth are illustrated more clearly in Fig.6.6. Additional support for the earlier and later

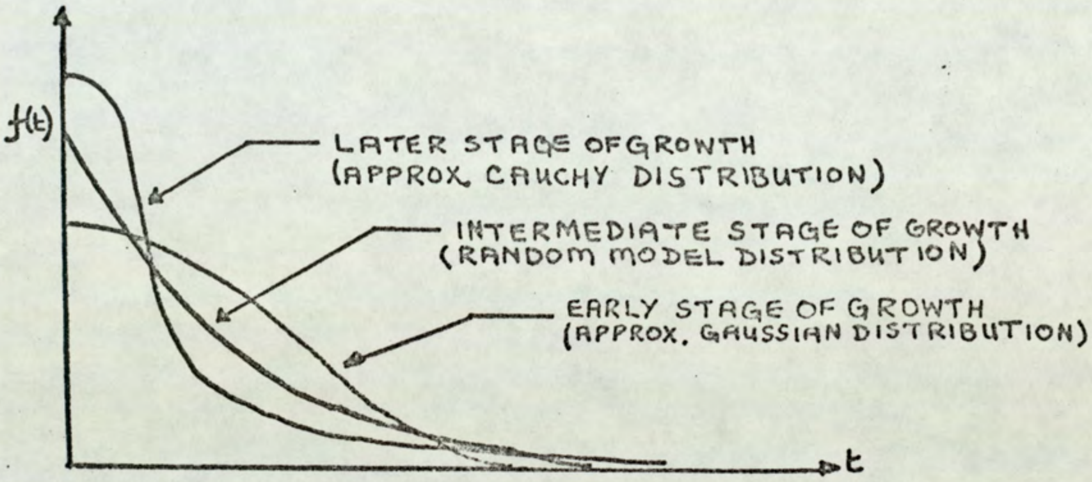

Fig.6.6 Domain thickness distributions for the three stages of domain growth (each curve normalised approximately to the same mean domain thickness).

stages being described by distributions approximating to Gaussian and Cauchy curves respectively is given by the changes in the standards deviations of the domain sizes relative to the random model (see table 6.3), as

(i) $\sigma(D)/\sigma(D)_{\text{random}} < 1$ for samples LF740 and LF700,0; a property of Gaussian curves,

(ii) $\sigma(D)/\sigma(D)_{\text{random}} \sim 1$ for samples LF725, LF735, LF745 and LF700,$\frac{1}{2}$

(iii) $\sigma(D)/\sigma(D)_{\text{random}} > 1$ for samples (LF700,1), (LF700,5), (LF700,60) and LF700,140; a property of curves approximating to a Cauchy shape.

Describing the early stages of growth by an approximate Gaussian distribution does seem consistent with proposed models of the initial growth process (i.e. multiple nucleation and growth till domains meet (Jones (1936), Lifschitz (1937)) or increase in local order through atomic rearrangement (Taylor, Hinde and Lipson (1951))) as the spread of domain sizes expected from these models would appear, from a qualitative point of view, to be small.

CHAPTER 7

SUMMARY OF CONCLUSIONS AND SUGGESTIONS FOR FURTHER WORK

7.1 Summary of conclusions

Lithium ferrite has been shown to possess an anti-phase domain structure when quenched from just below its transition temperature and also when a small number of Cr^{3+} ions are substituted for Fe^{3+} ions. The observed variations of the Wilson parameter $J'(0)/J(0)$ as a function of the planes of reflection were satisfactorily accounted for by anti-phase domain boundaries on the $\{110\}$ planes. Considerations of the interfacial energies based on the principle referred to as tetrahedral charge invariance showed that only these boundaries satisfy the principle for all possible types of adjoining domains. $\{110\}$ boundaries may also be favoured because the volume to surface ratio of the domains is greater than that for domains bounded by higher symmetry planes. It is of interest to remark in this respect that X-ray topographic analysis carried out on fully ordered single crystals of lithium ferrite (Belt, 1967) showed up defects on the $\{110\}$ planes.

Measurements of the long range order parameter indicated that a high degree of local order is established very rapidly in the unsubstituted specimens of lithium ferrite and that the volume fraction of disordered material is probably associated with the domain boundaries. These conclusions are given further support by the following:-

(i) the mean domain thickness was ~70Å after annealing for negligible time at 700°C,

(ii) the (210) superlattice line could still be detected in the diffraction patterns of specimens quenched from above the transition temperature,

(iii) short range ordering exists above the transition temperature (Brunel and Bergevin, 1966),

(iv) the ordering energy is large (de Boer et al.,1950).

It was concluded therefore, that the growth observed was of the type in which some domains grow at the expense of others.

The rate of growth of the domains as a function of annealing time was found to be very rapid during the first few minutes of growth. After this period however, the growth rate decreased quite sharply. In this region the time dependence of growth was similar to that of grain growth in metals whilst for the initial period the growth appeared to be such that the rate of loss of configurational energy was constant. It is suggested that the migration of the domain boundaries is a random walk process and that the initially high growth rate is attributable to the large volume fraction of small domains. Changes of the mean domain thickness were correlated with changes in the shape of the measured domain thickness distributions. During the earlier stages of growth this distribution resembled a Gaussian distribution and as such the spread of domain sizes was relatively small. Further growth led to an increasing spread of domain thicknesses relative to the mean domain thickness. At the same time, the thickness distribution changed, first of all to a geometric type distribution (i.e. random model), and later to a distribution whose shape resembled a Cauchy curve. During the later stages it would seem that growth occurs primarily through the action of a few domains. In this connection it is interesting to note that the Fourier transform results of Edmunds and Hinde (1952) for Cu_3Au and Steeple and Edmunds for Mg_3Cd are similar to the present results for the earlier stages of growth.

The mechanism of growth in lithium ferrite is probably diffusion controlled. Although the growth rate was examined only for two temperatures it was encouraging to find that the calculated value for the activation energy of domain growth, assuming a process in which the Li^+ and Fe^{3+} ions exchanged positions through the migration route octahedral site-tetrahedral site-octahedral site, agreed rather well with the experimental value of 2.7 ∓ 0.7 e.v.

In view of the instability of the domains in the unsubstituted specimens it was surprising that the results for $J'(0)/J(0)$, when considered collectively, indicated only a small proportion of boundaries other than the $\{110\}$ variety. On the basis of the diffusion mechanism envisaged (i.e. probability of an interchange independent of other possible interchanges) the development of planar boundaries would not be expected. Thus, if the concept of a diffusion mechanism is to be retained, the process of interchange must occur co-operatively over a domain boundary. In the case of the chromium substituted specimens the anti-phase domains are of an apparently stable variety and as such the boundaries should be planar (Bragg, 1940).

The lack of growth of the anti-phase domains in the latter group of compounds seems to arise from an inhibition of the ordering process by the Cr^{3+} ions. Measurements of the long range order parameter and line breadth parameters indicated a model in which all the substituted Cr^{3+} ions lie on the domain boundaries. Support for this model is given by the fact that the configurational energy of the boundaries is reduced by the stabilisation energy of the Cr^{3+} ions whilst fully ordered $LiFe_5O_8$ is retained inside the boundaries.

7.2 Suggestions for further work

From an experimental as well as a theoretical point of view the present analysis of anti-phase domain growth in lithium ferrite is incomplete. Much experimental work remains to be done on the time and temperature dependence of domain growth through investigation of the superlattice lines, preferably from stoichiometric lithium ferrite. For example, the present experiments were only concerned with samples in which the mean domain thicknesses ranged from 70 to 135Å whereas a much larger range of mean thicknesses would provide a firmer basis for theoretical models. In addition, it would be desirable to confirm the existence of $\{110\}$ boundaries by alternative techniques such as X-ray topography or electron microscopy. It is evident that an improved practical method for determining the domain thickness distribution is also needed as the present method, based on the representation of $J(t)$ as a series of connected exponential functions, propagates substantial systematic errors. If time had permitted, the Fourier transform functions would have been curve fitted to the form $J(t)/J(0) = \sum_i A_i e^{-u_i t}$ since the first stage of transformation on $J''(t)/J(0)$ could then have been carried out analytically. It is suggested that a curve fitting procedure always be adopted as fluctuations in experimental data tend to be magnified quite considerably in going through the Fourier transformation operations.

Information given by experimental domain thickness distributions brings nearer the possibility of testing the various theories of anti-phase domain formation from the disordered structure. It is suggested therefore, that further work be done on the determination of theoretical domain thickness distributions. In this respect, computer simulation, similar to that of Chernov and Lewis (1967), would appear to be a possible approach. Unfortunately, the experimental analysis of anti-phase domain formation in lithium ferrite could prove to be difficult as the initial growth rate is extremely rapid. Cu_3Au alloy would be preferred because not only is the initial growth rate in this material less rapid, but also its lattice constant is only 3.75Å and as such the diffraction pattern displays well separated lines (i.e. using CuKα radiation), a particularly useful property when measuring very broad lines.

Investigations into the next stage of growth (i.e. growth in which some domains grow at the expense of others) could also be carried out by comparison of experimental and theoretical domain thickness distributions with the concept of growth based on a random walk process being suggested as a possible physical model. Analytical work would appear to be more practicable with respect to the behaviour of the mean domain thickness as a function of time and temperature. The possibility of applying the dynamical theory of diffusion (Glyde,1967) and infra-red data in this connection is particularly interesting. This could also be said of the migration behaviour during the order-disorder transition. It is interesting to note that the approximate equation for the transition temperature given in chapter 5, section 5 (i.e. $T_c \propto f^2/a$) is at least qualitatively correct as the infra-red spectrum of $LiAl_5O_8$ (transition temperature 1295°C) is shifted towards higher frequencies (Hafner and Laves (1961), Tarte (1962)) relative to that of $LiFe_5O_8$ (note: it was not possible to test the relation quantitatively as the published spectra did not extend to low enough frequencies).

One of the uncertainties of the present analysis was the stability or otherwise of the anti-phase domains in the chromium substituted samples of lithium ferrite as a lower energy structure would seem to be that in which there are no anti-phase domains, the Cr^{3+} ions occupying octahedral sites other than those corresponding to the ordered positions of the Li^+ ions. Clearly, this could be checked by extensive annealing of the specimens just below their transition temperatures. It would also be desirable to verify that the source of energy impeding domain growth arises from the large octahedral site stabilisation energy of the

Cr^{3+} ions. This might be achieved by investigating the influence of substitutions of other 3+ transition metal ions which have large octahedral site stabilisation energies. Unfortunately, most of the transition metal ions which have this property are either unstable in the 3+ state or subject to the Jahn-Teller effect. The only comparable ion to chromium is the rhodium ion of the second transition series.

APPENDIX

Estimation of the statistical errors of the measured variance slopes (k) and intercepts (Wo)

The standard error of a function of several random variables (i.e. $(F(x_1, x_2, \ldots n_n))$ is given approximately by

$$\sigma^2(F(x_1, x_2, \ldots\ldots, x_m) = \sum_{i=1}^{m} \left(\frac{\partial F}{\partial x_i}\right)^2 \sigma^2(x_i)$$

where $\sigma^2(x_1)$ is the statistical variance of x_i (see for instance Wilson, 1967). To simplify the calculation of $\sigma(k)$ and $\sigma(Wo)$ the background correction is assumed to be a non-random variable so that

$$\sigma^2(k) = \sum_{n} \left(\frac{\partial k}{\partial G_n}\right)^2 \sigma^2(G_n)$$

$$\sigma^2(W_0) = \sum_{n} \left(\frac{\partial W_0}{\partial G}\right)^2 \sigma^2(G_n)$$

where G_n represents the measured intensity at an angle $n\Delta$ relative to the profile centroid, Δ is the step size between intensity measurements, $\sigma^2(G_n) = G_n$ (Wilson, 1967) and the summations are carried out over the intensity measurements used in the determination of k and Wo.

The slope k and the intercept Wo, as determined from least squares analysis, are given by

$$k = \frac{\langle W(2\phi_j).2\phi_j\rangle - \langle W(2\phi_j)\rangle\langle 2\phi_j\rangle}{\langle 2\phi_j^2\rangle - \langle 2\phi_j\rangle^2}$$

and $$W_o = \frac{\langle W(2\phi_j)\rangle\langle 2\phi_j^2\rangle - \langle W(2\phi_j).2\phi_j\rangle\langle 2\phi_j\rangle}{\langle 2\phi_j^2\rangle - \langle 2\phi_j\rangle^2}$$

where $\langle Y\rangle$ represents the average value of Y over the linear region of the variance-range function $W(2\phi_j)$ (i.e. $2\phi_s$ to $2\phi_z$), and the variance-range function is given approximately by

$$W(2\phi_j) = \sum_{n=-j}^{n=+j} (n\Delta)^2 (G_n - B_n) / IT$$

where B_n is the estimated background level at $(n\Delta)$ and IT is the sum of the intensities over all the profile (i.e. $\sum_{-\infty}^{\infty}(G_n - B_n)$) which is also assumed to be a non-random variable. As the statistical errors of B_n and IT are normally quite small the assumptions made in the present calculation are not expected to influence to any great extent the final results for $\sigma(k)$ and $\sigma(Wo)$.

The problem therefore, is to express $\langle W(2\phi_j)\rangle$ and $\langle 2\phi_j.W(2\phi_j)\rangle$ as simple functions of G_n. This is done as follows,

$$\langle W(2\phi_j)\rangle = \sum_{j=S}^{Z}\left[\sum_{n=1}^{j}(n\Delta)^2(G_n + G_{-n} - B_n - B_{-n})/IT\right]\Big/Q$$

where Q = Z - S + 1, or on rearranging the series,

$$\langle W(2\phi_j)\rangle = \left[\sum_{n=1}^{s}(n\Delta)^2(G_n+G_{-n}-B_n-B_{-n})\,Q + \sum_{n=s+1}^{z}(n\Delta)^2(G_n+G_{-n}-B_n-B_{-n})(z-n+1)\right] \Big/ Q \cdot IT$$

Similarly on rearranging the expression for $\langle W(2\phi_j).2\phi_j\rangle$ the result obtained is

$$\langle W(2\phi_j).2\phi_j\rangle = \left[\sum_{n=1}^{s}(n\Delta)^2(G_n+G_{-n}-B_n-B_{-n})\left(\sum_{j=s}^{z}2j\Delta\right) + \sum_{n=s+1}^{z}(n\Delta)^2(G_n+G_{-n}-B_n-B_{-n})\left(\sum_{j=n}^{z}2j\Delta\right)\right] \Big/ Q.IT$$

Thus,

$$\frac{\partial\langle W(2\phi_j).2\phi_j\rangle}{\partial G_n} = \frac{\Delta(n\Delta)^2(s+z)}{IT}, \quad n \leqslant s$$

$$\frac{\partial\langle W(2\phi_j).2\phi_j\rangle}{\partial G_n} = \frac{\Delta(n\Delta)^2(z-n+1)(n+z)}{Q \cdot IT.}, \quad z \geqslant n > s$$

$$\frac{\partial\langle W(2\phi_j)\rangle}{\partial G_n} = \frac{(n\Delta)^2}{IT}, \quad n \leqslant s$$

$$\frac{\partial\langle W(2\phi_j)\rangle}{\partial G_n} = \frac{(n\Delta)^2(z-n+1)}{Q \cdot IT}, \quad z \geqslant n > s$$

It is now a simple matter to formulate expressions for $\sigma^2(k)$ and $\sigma^2(Wo)$.

REFERENCES

Abrahams,S.C. and Calhoun,B.A. (1953). Acta. Cryst. 6,105.

Anderson,P.W. (1956). Phys. Rev. 102,1008.

Andrews,T. (1869). Phil.Trans.R.Soc. 159,575.

von Aulock,W.H. (1965). "Handbook of Microwave Ferrite Material", Academic Press (New York). p.407ff.

Batterman,B. (1956). Thesis, M.I.T., Cambridge, Massachusetts.

Bearden,J.A. and Shaw,C.H. (1935). Phys. Rev. 48,18.

Bertaut,E.F. (1950). Acta. Cryst. 3,14.

Bertaut,E.F. (1952). Acta. Cryst. 5,117.

Belt,J. (1967). Mat. Res. Bull. 2,919.

Bethe,H.A. (1935). Proc. Roy. Soc. 150,552.

Betteridge,W. (1949). J.Inst. Metals 75,559.

Blasse,G. (1963). J.Inorg. Nucl. Chem. 26,1473.

Blasse,G. (1964). Philips Res. Repts. Supplement 3.

de Boer,F.,van Santen,J.H. and Verwey,E.J.W.(1950). J.Chem. Phys. 18,1032.

Bragg,W.H. (1915). Phil. Mag. 30,305.

Bragg,W.L. and Williams,E.J. (1934). Proc. Roy. Soc. 145,699.

Bragg,W.L. (1940). Proc. Phys. Soc. 52,105.

Braun,P.B. (1952). Nature 170,1123.

Brunel,M. and de Bergevin,F. (1964). C.R.Acad. Sci. 258,5628.

Brunel,M. and de Bergevin,F. (1966). Solid State Comm. 4,165.

Cahn,R.W. (1970). In "Physical Metallurgy" edt. by R.W.Cahn, North Holland, P1181.

Chernov,A.A. and Lewis,J. (1967). J.Phys. Chem. Solids 28,2185.

Chipman,D. and Warren,B.E. (1950). J.Appl. Phys. 21,696.

Chipman,D. and Paskin,D.R. (1959). J.Appl. Phys. 30,1992.

Cowley,J.M. (1950). Phys. Rev. 77,667.

Datta,R.K. and Roy,R. (1963). J.Amer. Ceram. Soc. 46,388.

Domb,C. (1971). Physics Bulletin 25,323.

Dunitz,J.D. and Orgel,L.E. (1957). J.Phys. Chem. Solids 3,20.

Edmunds,I.G. and Hinde,R.M. (1952). Proc. Phys. Soc. 65,716.

Edwards,H.J. and Toman,K. (1969). J.Appl. Cryst. 2,240.

Edwards,H.J. and Toman,K. (1970a). J.Appl. Cryst. 3,157.

Edwards,H.J. and Toman,K. (1970b). J.Appl. Cryst. 3,165.

Edwards,H.J. and Langford,J.I. (1971). J.Appl. Cryst. 4,43.

Ehrenfest,P. (1933). Proc. Kon. Akad. Amsterdam 36,153.

Flinn,P.A. (1960). Trans.T.M.S. A.I.M.E. 218,145.

Gehlen,P. and Cohen,J.B. (1965). Phys. Rev. 139,A844.

Gehlen,P. and Cohen,J.B. (1969). J.Appl. Phys. 40,5193.

Glyde,H.R. (1967). J.Phys. Chem. Solids 28,2061.

Goodenough,J.B. (1963). "Magnetism and the Chemical Bond", Wiley (New York).

Gorter,E.W. (1954). Philips Res. Repts. 9,403.

Grimes,N.W. (1971a). Phil. Mag. In the press.

Grimes,N.W. (1971b). Private communication.

Guttman,L. (1956). Solid State Physics 3,189.

Hafner,F. and Laves,F. (1961). Z.Krist. 115,321.

Hendricks,S. and Teller,E. (1942). J.Chem. Phys. 10,147.

Hilliard,R.J. (1969). Private communication.

Himmel,L., Mehl,R.F. and Birchenall,C.E. (1953). Trans.A.I.M.E. 197,827.

Hoffman,A. (1938). Naturw. 26,431.

"International Tables for X-ray Crystallography" (1952). Vol.I. The Kynoch Press (Birmingham).

"International Tables for X-ray Crystallography" (1962). Vol.III. The Kynoch Press (Birmingham).

Irving,J. and Mullineux,N. (1966). "Mathematics in Physics and Engineering", Academic Press (New York). p.209,214.

James,R.W. (1948). "Optical Principles of the Diffraction of X-rays" G.Bell and Sons (London).

Jones,F.W. and Sykes,C.(1936). Proc. Roy. Soc. A157,213 and J.Inst. Metals 59,257.

Jones,F.W. (1938). Proc. Roy. Soc. A166,16.

Jones,F.W. and Sykes,C. (1938). Proc. Roy. Soc. A166,376.

Joubert,J.C. and Durif,A. (1964). C.R. Acad.Sci. 258,4482.

Kapitnova,N.P. (1965). Soviet Physics-Solid State 6,2111.

Kato, E. (1958). Bull. Chem. Soc. Jap. 31,113.

Keating, D.T. and Warren,B.E. (1951). J.Appl. Phys. 22,286.

King,G.S.D. (1962). Acta. Cryst. 15,512.

Klug,H.P. and Alexander,L.E. (1954). "X-ray Diffraction Procedures" Wiley (New York).

Krivoglaz,M.A. and Smirnov,A.A. (1964). "The Theory of Order-Disorder in Alloys" Macdonald (London).

Kukol,V.V. (1962). Soviet Physics - Solid State 4,528.

Landau,L.D. (1937a). Phys.Z.Sowjet. 12,579.

Landau,L.D. (1937b). Zh. Eksperim. i.Teor. Fiz. 7,19.

Langford,J.I. and Wilson,A.J.C. (1963). In "Crystallography and Crystal Perfection" edt. by G.N.Ramachandran, Academic Press (London), pp207 - 222.

Langford,J.I. (1965). Thesis, University of Wales (Cardiff).

Langford,J.I. (1968a). J.Appl. Cryst. 1,48.

Langford,J.I. (1968b). J.Appl. Cryst. 1,131.

von Laue,M. (1926). Z.Krist. 64,115.

Lifschitz,I.M. (1937). Phys.Z.Sowjet. 12,623.

MacGillavry,C.H. and Strijk,B. (1946). Physica 12,129.

Marcinkowski,M.J. and Fisher,R.M. (1960). J.Appl. Phys. 31,1687.

McClure,D.S.(1957). J.Phys. Chem. Solids 3,311.

Mikkola,D.E. and Cohen,J.B. (1966). In "Local Atomic Arrangements Studied by X-ray Diffraction", Gordon and Breach (New York) p289.

Moss,S.C. (1966). In "Local Atomic Arrangement Studied by X-ray Diffraction", Gordon and Breach (New York) p95.

Nishikawa,S. (1915). Proc. Tokyo Math. Phys. Soc. 8,199.

van Oosterhout,G.W. and Rooymans,C.J.M. (1958). Nature 181,44.

Owen,E.A. and MacArthur Sim,G. (1947). Phil. Mag. 38,342.

Parratt,L.G. (1936). Phys. Rev. 50,1.

Parrish,W. (1965). In "X-ray Analysis Papers" edt. by W.Parrish. Centrex (Eindhoven).

Pike,E.R. and Wilson,A.J.C. (1959). Brit.J.Appl. Phys. 10,57.

Pippard,A.B. (1964). "Elements of Classical Thermodynamics", Cambridge University Press.

Pointon,A.J. and Saull,R.C. (1969). J.Amer. Ceram. Soc. 52,157.

Pollack,S.R. and Atkins,K.R. (1962). Phys. Rev. 125,1248.

Poquette,G.E. and Mikkola,D.E. (1969). Trans. T.M.S. A.I.M.E. 245,743.

Ridgley,D.H., Lessoff,H. and Childress,J.D. (1970). J.Amer. Ceram. Soc. 53,304

Rooymans,C.J.M. (1959). J.Inorg. Nucl. Chem. 11,78.

Roessler,B. and Flinn,P.A. (1967). Phys. Stat. Sol. 24,263.

Scherrer,P. (1918). Nach. Ges. Wiss. Göttingen 26 Sept.,p98.

Schulkes,J.A. and Blasse,G. (1963). J.Phys. Chem. Solids 24,1651.

Shannon,R.D. and Prewitt,C.T. (1969). Acta Cryst. B25,925.

Steeple,H. and Edmunds,I.G. (1956). Acta Cryst. 9,934.

Stokes,A.R. and Wilson,A.J.C. (1942). Proc. Camb. Phil.Soc. 38,313

Stokes,A.R. and Wilson,A.J.C. (1944a). Proc. Camb. Phil.Soc. 40,197.

Stokes,A.R. and Wilson,A.J.C. (1944b). Proc. Phys. Soc. 56,174.

Stokes,A.R. (1948). Proc. Phys. Soc. 61,382.

Suortti,P. and Jennings,L.D. (1971). J.Appl. Cryst. 4,37.

Sykes,C. and Wilkinson,H. (1937). J.Inst. Metals 61,223.

Tarte,P. (1962). C.R. Acad. Sci. 254,2008.

Taylor,C.A., Hinde,R.M. and Lipson,H. (1951). Acta Cryst. 4,261.

Tournarie,M. (1956a). C.R. Acad. Sci. 242,2016.

Tournarie,M. (1956b). C.R. Acad. Sci. 242,2161.

Trucano,P. and Batterman,B.W. (1970). J.Appl. Phys. 41,3949.

Verwey,E.J.W., de Boer,F. and van Santen,J.H. (1948). J.Chem. Phys. 3,311.

Vishnevskii,I.I., Alapin,B.G., Lysak,S.V. and Skripak,V.N. (1969). Soviet Physics-Crystallography 13,940.

van der Waal,J.D. (1873). Thesis,Leiden.

Wagner,C.N.J. and Aqua,E.N. (1964). Advances in X-ray Analysis 7,46.

Wagner,C.N.J. (1966). In "Local Atomic Arrangements Studied by X-ray Diffraction", Gordon and Breach (New York) p219.

Warren,B.E. and Biscoe,J. (1938). J.Amer. Ceram. Soc. 21,49.

Warren, B.E. (1959). Prog. in Metal Phys. 8,147.

Warren,B.E. (1969). "X-ray Diffraction", Addison Wesley (Reading).

Waters,W.J. (1969). Private communication.

Wilson,A.J.C. (1943). Proc. Roy. Soc. A181,360.

Wilson,A.J.C. (1958). Acta Cryst. 11,227.

Wilson,A.J.C. (1962a). Nature 193,568.

Wilson,A.J.C. (1962b). Proc. Phys. Soc. 80,286.

Wilson,A.J.C. (1962c). "X-ray Optics", Methuen (London).

Wilson,A.J.C. (1963a). Proc. Phys. Soc. 81,41.

Wilson,A.J.C. (1963b). "Mathematical Theory of X-ray Powder Diffractometry", Centrex (Eindhoven).

Wilson,A.J.C. (1965). Proc. Phys. Soc. 85,807.

Wilson,A.J.C. and Zsoldos,L. (1966). Proc. Roy. Soc. A290,508.

Wilson,A.J.C. (1967). Acta Cryst. 23,888.

Wilson,A.J.C. (1969). Acta Cryst. A25,S15.

Wilson,A.J.C. (1970). J.Appl. Cryst. 3,71.

Yamada,K. and Yoshimori,A. (1967). Prog. Theor. Phys. 37,473.

Yamaguchi,S., Watanabe,D. and Ogawa,S. (1961). J.Phys. Soc. Jap. 17.1030.

Young, R.A., Gerdes,R.J. and Wilson,A.J.C. (1967). Acta Cryst. 22.155.

ACKNOWLEDGEMENTS

This research was carried out at the University of Aston in Birmingham during the tenure of an S.R.C. Research Studentship.

I would like to thank my supervisor, Mr. N.W. Grimes, for his advice, encouragement and assistance during the course of this work.

I would also like to thank the following persons.

Messrs. G.V. Cochrane and A. McKenzie for assistance with graphical work.

Mr. A.J. Collett for carrying out the infra-red analysis of lithium ferrite.

Finally, my thanks are due to my wife for her patience and understanding.